Università Politecnica delle Marche
Scuola di Dottorato di Ricerca in Scienze dell'Ingegneria
Corso di Dottorato in Ingegneria Industriale

Indoor Air Quality: Study, Optimization and Implementation of a Novel Hybrid Air Cleaning Process

Supervisor:
Prof. Maria Letizia Ruello
Assistant Supervisor:
Prof. Gabriele Fava

Ph.D. Dissertation of:
Mattia Pierpaoli

Ph.D. Course coordinator:
Prof. Ferruccio Mandorli

XVII edition - new series

Università Politecnica delle Marche
Dipartimento di Scienze e Ingegneria della Materia, dell'Ambiente ed Urbanistica
Via Brecce Bianche — 60131 - Ancona, Italy

Introduction

Clean air is an essential requirement of life, together with food and water. Although the latter two have been a primary concern for many civilizations for multiple centuries, especially in more industrialized countries, shaping new lifestyles and driving new economies, air is something imposed, with no possibility of choice. Since the industrial revolution, as people started to spend most of their time in confined environments, clean air should have been considered a prerogative, as indoor air had become a leading exposure for humans. Therefore, in places of life and work, it is necessary to monitor the urban environment. For this reason, as major environmental concerns, policy directives and guidelines have recently highlighted energy use, sustainable buildings, outdoor air quality, and indoor air quality (IAQ).
It is generally recognized that Europeans spend 90% or more of their time *indoors*. Despite this, the quality of air is considered a secondary problem, often ignored; while it is possible to choose what to eat and what to drink, it is difficult to choose *which* air to breathe. However, indoor air pollution may cause serious health problems such as respiratory diseases, allergies, and lung cancer.

The most common indoor pollutants can be classified by their form: particulate or gaseous. Conventional strategies to combat the formers are source removal, dilution through ventilation and air treatment. While indoor emissions are ubiquitous and it is not always possible to remove the source, dilution through mechanical and natural ventilation and air cleaners are the generally preferred. As sustainability and energy-efficiency are becoming prerogatives in many countries, ventilation may imply energy losses, and therefore it can not be the only applicable strategy. For these reasons, air cleaners constitute a solution for removing harmful indoor pollutants.

Common indoor air treatment technologies are classified according to the type of pollutant removed: filters, electrostatic precipitators, inertial collectors, scrubbers are generally used for the removal of particles, while adsorptive media, (photo)catalysts, and plasma-operated reactors are adopted for the removal of gases.
In this thesis, a combination in situ of the three previously reported methods (adsorption, photocatalysis and electrostatic precipitation) was deeply studied for the enhanced removal of indoor pollutants. The synergistic effect between each coupled process was investigated, in order to highlight the *novelty* of operating photocatalysis, adsorption and electrostatic precipitation in the single *hybrid* reactor.

Structure of the Thesis

The present thesis is divided into 3 chapters:
Chapter 1: Motivation; the Indoor Air Quality topic has been introduced both with a more general bibliometric analysis, both with a particular focus on the treatment technologies adopted to control the former.
Chapter 2: Experimental; the different combinations of the three technologies considered were deeply studied, and the main parameters affecting the process were optimized. At the end of each subchapter, a comprehensive discussion of the results was reported.
Chapter 3: Conclusion; the main findings, in relation to each paired process or to the combined process, were reported, and its implementation was discussed. A critical review of the process, including strength and limitations of the process has been redacted, as well as a brief discussion about economic costs.

Acknowledgments

First and foremost I wish to thank my tutor, professor Maria Letizia Ruello, giving me free reins for my research and for having offered me many opportunities in these years. Maybe I took too seriously her motto "*fai il pane con la farina che hai*" which brought me many times to go crazy, building by myself the instrumentation that I needed. However, I have to say that it helped me a lot to understand *how stuff works*.
This is also thanks to professor Gabriele Fava, who has been a mentor for me since my bachelor. He always supported my curiosity, and often, when I came out with a new finding (or, more often, with a new unsuccess), he was ready to listen and to discuss it (or saying "I told you!"). Fueling my desire to know and my *wunderlust*, I convinced myself that in order to fully understand the process that I was investigating, I had to move from a macroscopic to a microscopic approach and to use different tools. This brought me to collaborate with professor Robert Bogdanowicz, from the Gdansk University of Technology, that I thank so much for the all the work about carbon nanowalls and for making me feel at home in his *Nanodiamond Team*.
Surely this work would not have been possible without the help of Orlando Favoni, Mirco Marcellini, Roberto Mancini, Aneta Lewkowicz, Tiziano Bellezze and Carla Conti, for having been of amazing help all this time. Since substance cannot exist without form, I have to thanks a special teacher, Ewa, for her time and for being patient with me.
Although not strictly related to this work, I'd like to give special thanks to professor Aneta Łuzkiewicz and dr. Sylwia Fudala-Książek for working together and for the trust given. As well, a good part of the knowledge about adsorbent materials is thanks to professor Antonina Bondarenko, who taught me a lot at the Lipetsk State Technical University.
Not less important, I would like to thank all my PhD colleagues, with whom I have shared moments of stress and joy, for bearing with me and for not having pummeled me about my enormous ego.
I especially thank my parents and my family, for the unconditional love and care provided my whole life.
The greatest achievement from these past four years, was not only my academic journey, but as well the special person with whom I succeed in it. I'm not only thankful for the thousands cakes prepared for me, but for having taught me to be patient and for giving me the strength to achieve what I love.
At last, I would like to thank those who did not understand me, who criticized me and the reviewers who rejected my works, because it is only thanks to the obstacles encountered and to my failures that I *learned it after knowing it all*.

List of publications

M. Pierpaoli, M.L. Ruello, **Indoor Air Quality: A Bibliometric Study** Sustainability 2018, 10(11), 3830;
doi:10.3390/su10113830

M. Pierpaoli, Lewkowicz, A., Ficek, M., Ruello, M. L., & Bogdanowicz, R. (2018). **Preparation and characterization of TiO_2/carbon nanowall composite on a transparent substrate**. Photonics Letters of Poland, 10(2), 54-56.
doi:10.4302/plp.v10i2.825

M. Pierpaoli, M., Favoni, O., Fava, G., & Ruello, M. (2018). **A Novel Method for the Combined Photocatalytic Activity Determination and Bandgap Estimation**. Methods and Protocols, 1(2), 22.
doi:10.3390/mps1020022

M. Pierpaoli, M. L. Ruello, G. Fava - **Enhanced Adsorption of Organic Compounds over an Activated Carbon Cloth by an External-Applied Electric Field**. Environments 4.2 (2017): 3.
doi:10.3390/environments4020033

M. Pierpaoli, C. Giosuè, M. L. Ruello, G. Fava - **Appraisal of a hybrid air cleaning process**. Environmental Science and Pollution Research, Vol. 24 No14, pp. 12638-12645.
doi:10.1007/s11356-016-7880-x

G. Fava, M. Pierpaoli. - **A Hybrid Photocatalytic-Electrostatic Reactor for Nitrogen Oxides Removal**. American Journal of Environmental Engineering and Science. ISSN: 2381-4691 Vol. 2, No. 1, 2015, pp. 7-13.

G. Fava, M. Pierpaoli. - **Volatile Organic Compounds Removal in a Hybrid Photocatalytic-Electrostatic Reactor**. American Journal of Environmental Engineering and Science. ISSN: 2381-4691 Vol. 2, No. 2, 2015, pp. 14-17.

M. Pierpaoli, M. Ficek, M. Rycewicz, M. Sawczak, J. Karczewski, M. L. Ruello and R. Bogdanowicz, **Tailoring electro/optical properties of transparent boron-doped carbon nanowall grown on quartz** *Submitted to Materials*

Other publications

G. Fava, T. Naik, and M. Pierpaoli. "**Compressive Strength and Leaching Behavior of Mortars with Biomass Ash.**" Recycling 3.3 (2018): 46.
doi:10.3390/recycling3030046

Fudala-Ksiazek, S., Pierpaoli, M., & Luczkiewicz, A. (2018). **Efficiency of landfill leachate treatment in a MBR/UF system combined with NF, with a special focus on phthalates and bisphenol A removal.** Waste Management, 78, 94-103.
doi:10.1016/j.wasman.2018.05.012

C. Giosuè, M. Pierpaoli, A. Mobili, M. L. Ruello, F. Tittarelli **- Influence of Binders and Lightweight Aggregates on the Properties of Cementitious Mortars: From Traditional Requirements to Indoor Air Quality Improvement Materials** 2017, 10(8), 978;
doi:10.3390/ma10080978

S. Fudala-Ksiazek, M. Pierpaoli, A. Luczkiewicz. - **Fate and significance of phthalates and bisphenol A in liquid by-products generated during municipal solid waste mechanical-biological pre-treatment and disposal**. - Waste Management Vol. 64 (2017): pp.28-38.
doi: 10.1016/j.wasman.2017.03.040

M. Pierpaoli, G. Fava - **A Passive Opportunity for Improving Air Quality in the Schools Environment: A Real-World Scale Testing**. American Journal of Environmental Sciences ISSN: 1553-345X, Vol.12, No. 3, pp. 206-212
doi:10.3844/ajessp.2016.206.212

S. Fudala-Ksiazek, M. Pierpaoli, E. Kulbat, A. Luczkiewicz **- A modern solid waste management strategy – the generation of new by-products.** Waste Management. ISSN: 0956-053X Vol. 49, March 2016, pp. 516–529.
doi:10.1016/j.wasman.2016.01.022

Act of conferences

M. Pierpaoli, M. Ficek, M.Rycewicz, M. Sawczak, J. Karczewski, M. L. Ruello and R. Bogdanowicz - **Transparent carbon nanostructures for conductive electrodes**, Nanosmat: International Conference on Surfaces, Coatings and Nanostructured Materials, 11-14 Semptemebr 2018, Gdansk, Poland

M. Pierpaoli, M. L. Ruello, G. Fava - **Electrosorption of gaseous volatile organic compounds onto technical ad-sorbents**, Indoor Air, 22-27 July 2018, Philadelphia, USA

M. Pierpaoli, L. Riderelli, S. Palmieri, G. Fava, M. L. Ruello **-Transparent electrospun PLA-nanofibers on 3D-printed honeycomb for a high-efficient air filtration**; Indoor Air, 22-27 July 2018, Philadelphia, USA

M. Pierpaoli, M. L. Ruello, R. Bogdanowicz - **Growth of boron-doped carbon nanowalls on quartz glass** – FEMS Junior Euromat, 8-12 July 2018, Budapest, Hungary

M. Pierpaoli, A. Lewkowicz, M. L. Ruello, R. Bogdanowicz **- Preparation and characterization of TiO_2/carbon nanowall composite on transparent substrate**, OPTO 2018, 4-7 July 2018, Gdansk, Poland

M. Pierpaoli, D. Forconi, S. Monosi, M. L. Ruello - **Can VOC adsorption be enhanced by an external electric field**? XIV AIMAT National Congress, 13-15 July 2017, Ischia Porto

M. Pierpaoli, M. L. Ruello, G. Fava - **SiO_2/TiO_2 composites for real scale application: adsorptive and de-polluting properties**. Healthy Buildings Europe 2017, 2-6 July 2017, Lublin (Poland)

M. Pierpaoli, Z. Xu, V. Bondarenko, R. Wang, G. Fava. M. L. Ruello - **Silica-Titania Composites for the Air De-Pollution**. 5th Sino-French Joint Workshop on Atmospheric Environment, 11-14 October 2016, Xi'An (China).

M. Pierpaoli, C. Giosuè, M.L.Ruello, G.Fava - **Appraisal of a Multitasking Air Cleaner Process Based on Multiple Combined Techniques**. 9th European Meeting on Solar Chemistry and Photocatalysis: Environmental Applications, 13-17 June 2016, Strasbourg (France)

Summary

It is what you learn after you know it all that counts.

Chapter 1:
Motivation

1.1 Indoor Air Quality: a bibliometric study
1.2 Indoor Air Treatment: a comparison between scientific and patent literature

In paragraph 1.1, the Indoor Air Quality (IAQ) topic, in the last 38 years, is presented through a scientometric approach;

- *More than 7000 publications have been clustered into few significant research field. Among these, indoor air treatment technologies and processes account for the 3% in the IAQ-related scientific literature;*
- *Scientometric tools can be useful to analyze, categorize, and identify milestone and turning points if the scientific literature. However, these tools cannot be considered exhaustive and scientific advances will probably be driven by new multidisciplinary contaminations into the discipline.*

1.1 Indoor Air Quality: a bibliometric study

1.1.1 Introduction

Bibliometrics is the application of quantitative analysis and statistics to publications using different parameters, such as author co-citation, document co-citation, co-word analysis, and journal mapping, in order to understand emerging trends and the knowledge structure of a research field. Jointly with science mapping tools, it is possible to start from a large dataset of scientific publications in order to generate straightforward visual representations of complex structures for statistical analysis and interactive data exploration.

Using bibliometric tools to analyze the scientific literature collected by Web of Science, this article provides, firstly, an overview of the IAQ topic from 1990 to 2018, by reporting the most important publications and by collocating the existing literature in a finite number of clusters and, secondly, the latest developments and future trends. Although this work is not structured as an exhaustive review of the related literature, it does illustrate the opportunity of bibliometric techniques for exploring research gaps and new frontiers.

1.1.2 Materials and Methods

1.1.2.1 Data collection

All data were obtained from the Web of Science Core Collection (WoSCC) by Thomson Reuters prior to 1 May 2018. In this study, the keywords used for the data retrieval strategy were as follows: TS: (“Indoor air quality” OR “IAQ”). English-only document types were articles, letters, and reviews, ranging from 1990 to 2018, from the following indexes: SCI-EXPANDED, SSCI, A&HCI, CPCI-S, CPCI-SSH, and ESCI. The final dataset contained 7389 bibliographic records of Article or Letters or Review in English.

1.1.2.2. Data analysis

We utilized several scientific and visual analytic methods. The statistical results are displayed in CiteSpace V [1], visualization software used for analyzing data by network modeling.

For the first analysis, the overall time span adopted was 1990 through 2018, with a 1-year time slice. The Term Source included Title, Abstract, Author Keywords, and Keyword Plus; Node Type was selected according to the type of analysis conducted; and Selection Criteria included the top 50. No pruning was selected. For the second part, in order to focus on the actual and future trends, a restricted dataset, in which only papers selected with the same criteria from 2010 to 2018, was used. A different thresholding method was adopted: Instead of selecting the top 50 articles of each time slice, CiteSpace thresholding parameters (citation, co-citation, and the cosine coefficient thresholds, shortened as: c, cc, and ccv) were set at 8;8;40, 6;6;30, and 2,2,10, respectively. This choice was justified by the three thresholding being respectively referred to: Begin, middle, and end of the selected period of time and, by applying more selective parameters for the first years, only the most relevant publications are reported. In the last period, a wider number of publications are reported.

1.1.3 Results

1.1.3.1. Data description

The distribution of yearly outputs is shown in Figure 1. The publishing trend increased from 13 publications in 1990 to 786 publications in 2017, highlighting the increased global focus on the topic. In particular, since 1990, it is possible to distinguish between two different phases. During the first phase from 1990 to 2009, a slow increase in publications occurred. The second phase occurred from 2010 to 2017, with a higher growth rate, indicating the growing interest in the topic. This distinct separation coincides with the publication of the World Health Organization (WHO) guidelines for indoor air quality [2].

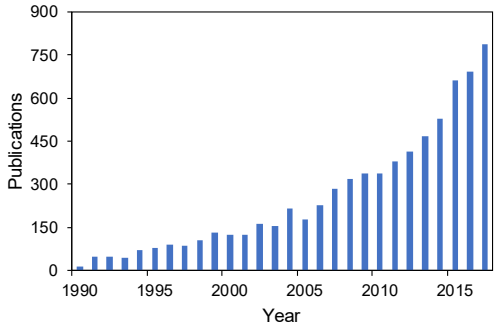

Figure 1 - *Temporal distribution of the bibliographic set.*

Almost 30% of the publications in the dataset were published by five scholarly journals (2102, 28.45%), each one accounting for about 350 publications. This trend is reported in Figure 2.

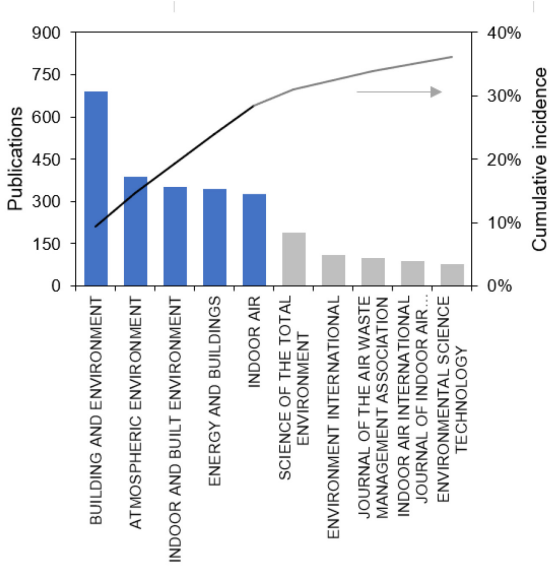

Figure 2 - *Top 10 journals with the highest number of publications. The line represents the cumulative incidence of the entire dataset.*

The top 15 contributing institutes are listed in Table 1. The University of California (3.71%) ranked first, followed by two Chinese universities: Tsinghua University (2.64%) and Hong Kong Polytechnic University (2.56%). Among the top 25 institutions, 11 are American, followed by 7 European, and 3 Chinese. However, more than one-quarter of the total records are American, followed by People's Republic of China (PRC) (14.12%).

Table 1 - *Top 15 contributing institutions.*

Organizations	Records	% of 7389	Country
University of California System	274	3.71%	USA
Tsinghua University	195	2.64%	China
Hong Kong Polytechnic University	189	2.56%	China
University of California Berkeley	186	2.52%	USA
United States Department of Energy DOE	158	2.14%	USA
Technical University of Denmark	141	1.91%	Denmark
United States Environmental Protection Agency	127	1.72%	USA
Lawrence Berkeley National Laboratory	126	1.71%	USA
Harvard University	123	1.67%	USA
Centre National de la Recherche Scientifique CNRS	91	1.23%	France
Chinese Academy of Sciences	85	1.15%	China
University of London	82	1.11%	UK
Finland National Institute for Health Welfare	80	1.08%	Finland
Uppsala University	77	1.04%	Sweden
Centers for Disease Control Prevention USA	71	0.96%	USA

The top 10 contributing countries, in terms of publications, are reported in Table 2. In first place, the USA accounts for 27.5% of the total literature, with 2032 records, followed by China with 1043 records (14.12%). England, Canada, and South Korea ranked third, fourth, and fifth place, respectively, with a cumulative number of

publication equal to the total number of publications in 1990, followed by four European countries and Australia.

Table 2 - *Top 10 contributing countries.*

Country	Records	% of 7389
USA	2032	27.50%
China	1043	14.12%
England	444	6.01%
Canada	375	5.08%
South Korea	371	5.02%
Italy	369	4.99%
France	355	4.80%
Germany	288	3.90%
Denmark	282	3.82%
Australia	241	3.26%

The top 10 categories are reported in Table 3. However, only the first four constitutes the major fields. The top four categories, in order of importance, are: “Engineering”, “environmental sciences ecology”, “construction building technology”, and “public environmental occupational health”.

Table 3 - *Top 10 categories.*

Field	Record Count	% of 7389
Engineering	2839	38.42%
Environmental Sciences Ecology	2426	32.83%
Construction Building Technology	2285	30.92%
Public Environmental Occupational Health	1748	23.66%
Energy Fuels	719	9.73%
Meteorology Atmospheric Sciences	627	8.49%
Chemistry	458	6.20%
Thermodynamics	374	5.06%
Science Technology Other Topics	280	3.79%
Toxicology	275	3.72%
Materials Science	184	2.49%
Agriculture	142	1.92%
Allergy	104	1.41%
Instruments Instrumentation	104	1.41%
Mechanics	102	1.38%

1.1.3.2 Categories and Journal co-occurring networks

The network of co-occurring subject categories (Web of Science categories), reported in Figure 3, highlights the relationship between the main subjects and disciplines in the field. The thickness of each link represents the density of the co-occurring category and the color map refers to the average year of the node. The color of a category ring denotes the time of corresponding utilization. The thickness of a ring is proportional to how many times the category has been used in a specified time slice. Lighter colors (yellow) correspond to newer nodes, while darker colors (blue)

are related to older nodes. This method enabled us to highlight the multidisciplinary and temporal evolution of the subject. We found that environmental sciences and engineering, construction and building technology, and public, environmental, and occupation health were the main subjects in the IAQ field. Minor categories, constituted mainly by unlabeled nodes because of their lower amount, have been grouped into larger areas. "Material science" is a linking node between chemistry, physics, and environmental studies and "public, environmental, and occupational health" belongs to the highest burst, as it connects the most populous nodes (construction and building engineering with environmental sciences).

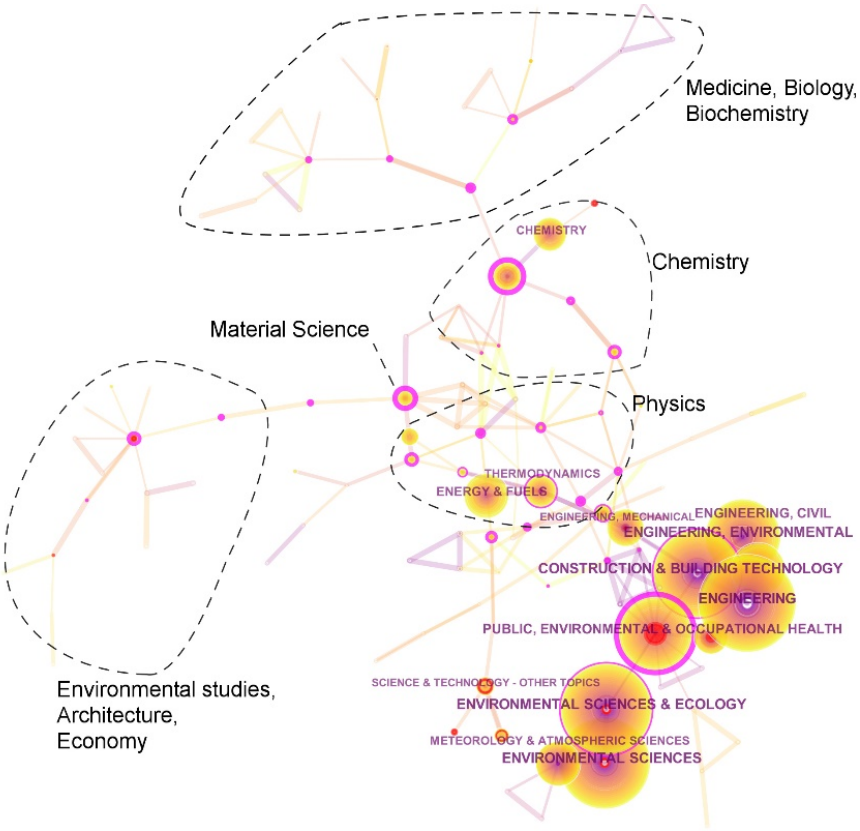

Figure 3 - *Network of co-occurring subject categories.*

In order to outline the set of journals that are connected to the IAQ topic, the co-citation network at the journal level is shown in Figure 4. Like the previous figure, color and thickness reflect the temporal distribution of the cited journals. It was possible to categorize the journals into four macro areas: Medicine-related (center), energy-related (left), building-related (bottom), and environment-related (top). The biggest circles correspond to the most cited journals. The most-cited journals were the ones reported in Figure 2 but, while "Building and Environment", "Atmospheric Environment", "Indoor and Built Environment" are, the top three journals in terms of number of publications, the most-cited were "Indoor Air", "Energy and Buildings", and "Environmental Health Perspective". Unlabeled nodes are minor journals given their number of citations.

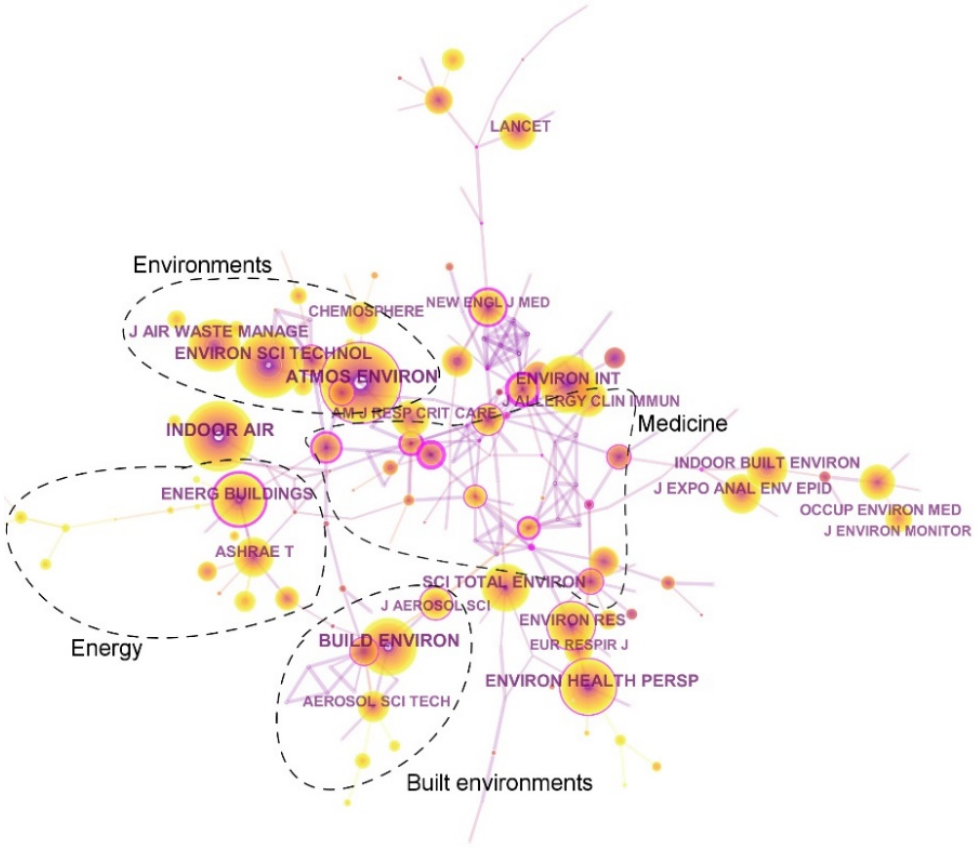

Figure 4 - *Network of co-occurring Journals.*

1.1.3.3. Term burst

Citation burst is an indicator of the most active part of the research. CiteSpace's citation burst is based on Kleinberg's algorithm [3], and it provides evidence that a particular publication (or keyword) has attracted an extraordinary degree of attention from its scientific community. The keywords in the literature can reveal the main research content, and literature citation frequency can reflect research heat. The terms (title, abstract, and keywords) having the strongest citation bursts in the dataset are reported in Table 4. The time intervals are represented by the blue line, while the periods of the burst are highlighted in red, indicating the beginning and end of each burst interval. The full list is reported in the supplementary material.

Table 4 - Terms having high citation burst strengths.

Terms	Strength	Begin	End	1990–2018
Indoor Air-Quality	47.64	1990	1995	
Sick Building Syndrome	27.26	1991	2006	
Office Workers	10.43	1991	2004	
Environmental Tobacco Smoke	33.26	1991	2004	
Outdoor Level	9.54	1991	2008	
Nitrogen Dioxide	11.89	1996	2002	
Personal Exposures	10.57	1998	2005	
Fungal Spores	8.63	1998	2006	

Respiratory Symptoms	8.79	1999	2008	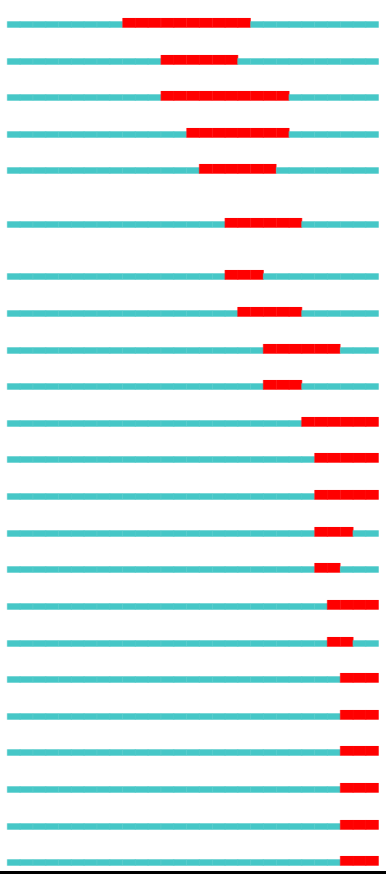
Displacement Ventilation	9.68	2002	2007	
Airborne Bacteria	10.56	2002	2011	
Air-Conditioning System	10.19	2004	2011	
Health Effects	9.02	2005	2010	
Computational Fluid Dynamics	9.48	2007	2012	
Air-Conditioned Offices	13.81	2007	2009	
Fresh Air	12.19	2008	2012	
Ultrafine Particles	11.36	2010	2015	
Practical Implications	12.12	2010	2012	
Indoor Environmental Quality	16.88	2013	2018	
CO_2 Concentration	22.72	2014	2018	
Indoor $PM_{2.5}$	19.85	2014	2018	
Air Conditioning System	8.00	2014	2016	
Indoor Temperature	8.81	2014	2015	
Energy Efficiency	8.86	2015	2018	
Public Health	9.11	2015	2016	
Air Temperature	9.50	2016	2018	
Residential Buildings	15.25	2016	2018	
Indoor Air Temperature	14.62	2016	2018	
Energy Saving	12.56	2016	2018	
Thermal Comfort	11.83	2016	2018	
Outdoor PM2.5	15.36	2016	2018	

From Table 4, the initial “IAQ” burst was coincident with the “sick building syndrome”, “office workers”, “environmental tobacco smoke”, and “outdoor level” term bursts. The term “sick building syndrome” (SBS) is used to describe when building occupants experience acute health and comfort effects that can be linked to the time spent in a building. The first studies were conducted in offices [4,5] in which tobacco smoke was the major pollutant [6,7], as the smoking ban in working and public places had not yet been implemented, together with the presence of contaminants from the outdoor air. By that time, several specific pollutants, like nitrogen dioxide (NO_2), fungal spores, and airborne bacteria, were present as strong citation bursts for the 1996–2011. Notably, volatile organic compounds (VOCs) appeared with burst strength lower than the threshold (arbitrarily set to 7.0, which is equal to the median value of the citation burst distribution) in different time intervals; for this reason, they are not reported in Table 4.

All the citation burst still active started after 2013. The introduction of other physical and psychological aspects of indoor life led to the definition of Indoor Environmental Quality (IEQ), within which IAQ occurs. In this last time interval, pollutants with a strong, still active burst are related to fine particulate matter ($PM_{2.5}$), carbon dioxide (CO_2), and “energy saving” fields. Also, the “residential buildings” term appears, which may indicate the shift of academic attention from the work place to private homes, together with increased attention focused on building energy saving and thermal comfort of occupants

1.1.3.4. Document co-citation network

A document co-citation network represents a network of references that have been co-cited by a set of publications. Time was divided into a number of one-year slices, and an individual co-citation network was derived from each time slice. In order to reduce the dimension of every single slice, the top 50 most-cited publications in each year were used to build a network of cited references in that particular year. Subsequently, individual networks were merged. The merged network reported in Figure 5 depicts a spatial visualization of the network, which represents the development of the IAQ topic over time, showing the most important footprints of the related research activities. Each colored node represents a cited reference.

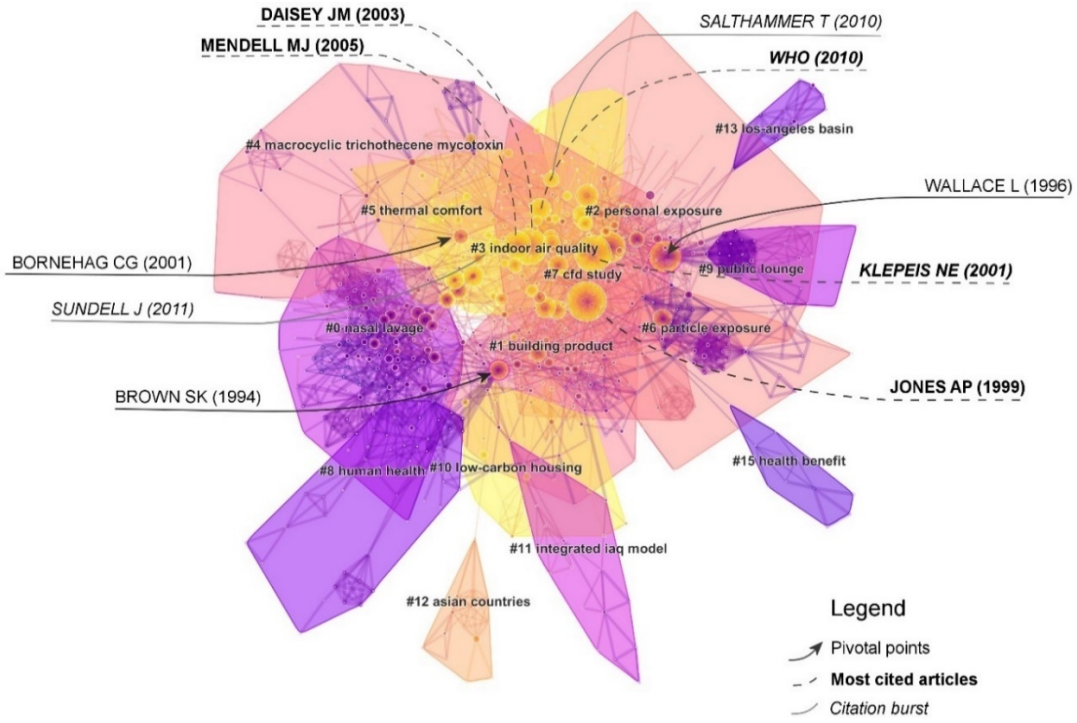

Figure 5 - *Landscape views of the resulted network. The arrow indicates the pivotal points; the most cited articles are written in bold and the citation bursts in italic.*

The network in Figure 5 is divided into 19 co-citation clusters. These clusters are labeled by index terms from their own citers. The numbers in front of the cluster's name are identifiers rank the size of the clusters. The "silhouette" value is a descriptor of the homogeneity of a cluster, and it ranges between −1 and 1; higher values indicate meaningful clusters [8], while the "modularity" measures the extent to which a network can be divided into independent blocks, which ranges from zero to one [9]. The network has a modularity of 0.7437, which is considered to be high, suggesting that the specialties in IAQ are clearly defined in terms of co-citation clusters. The average silhouette score of 0.2579 is low mainly because of the presence of numerous small clusters. Different colors indicate the time when co-citation links in those areas appeared for the first time. Purple areas were generated earlier than yellow areas. Important publications have been reported in the network visualization.

The importance of clustering publications lies in identifying the most important thematic macro areas and to see how they are related to each other. Cluster descriptors in Figure 5 are reported in Table 5. The "size" column refers to the number of

publications within the cluster. The "name" tag was generated by the Log-likelihood algorithm from the articles' indexing terms [10]. The Log-likelihood algorithm was chosen as it better reflected the cluster topic. The "description" column was manually filled after analyzing the top articles of each cluster having high coverage value. The "range" is the period in which the cluster evolves, or the period covered, by the various publications within the cluster. A straightforward visual representation of this parameter is reported in Figure 6.

Table 5 - *Clusters description.*

#	Size	Silhouette	Name	Description	Range (Years)
0	145	0.866	Nasal Lavage	Correlation between physical/chemical parameters and occupants symptoms.	1980–1999
1	125	0.725	Building Product	Gaseous pollutants: Source, modeling, concentrations. Indoor sources.	1973–2010
2	109	0.766	Personal Exposure	Personal exposure to particulate matter.	1981–2006
3	105	0.753	Indoor Air Quality (IAQ)	Air quality in school and residential homes.	1992–2017
4	63	0.908	Macrocyclic Trichothecene Mycotoxins	Asthma, bacterial and fungal aerosols.	1958–2011
5	43	0.884	Thermal comfort	Thermal comfort, relative humidity, HVAC.	1970–2016
6	41	0.916	Particle exposure	Risk assessment. Environmental tobacco smoke.	1982–2013
7	41	0.94	CFD study	Ventilation. CFD modeling.	1980–2009
8	35	0.962	Human Health	Epidemiology of SBS and related symptoms	1975–1995
9	27	0.912	Public Lounge	Environmental tobacco smoke.	1969–1996
10	17	0.971	Low-Carbon Housing	Air purification techniques. Numerical modeling.	1974–2011
11	16	0.974	Integrated IAQ Model	VOC emissions.	1960–2001
12	14	0.999	Asian countries	*	1998–2010
13	11	0.997	Los Angeles Basin	*	1975–1990
15	10	0.989	Health benefit	*	1974–1989

* The cluster shows a high silhouette, but it's difficult to identify a common topic. VOC, volatile organic; HVAC, Heating, Ventilation and Air Conditioning; CVD, Computational Fluid Dynamics.

Cluster #0 is the largest cluster, containing 145 publications and having a silhouette value of 0.866. It is labeled as "nasal lavage". The first five publications, with the highest coverage in this cluster, are by Wieslander [11,12], followed by Brooks [13], and Nordstorm [14]. They all investigated the health effects (nasal and ocular) of sick building syndrome in hospitals and public facilities. This cluster collects the first comprehensive studies between built environments through monitoring of chemical and physical parameters (pollutants concentrations, temperature, and humidity) and symptoms of indoor occupants. Publications ranged between 1980 and 1999.

The second largest cluster (#1) has 125 members and a silhouette value of 0.725. While it is the lowest among all clusters, it had a relatively high level of homogeneity.

The cluster is labeled “building product”. This second cluster is related to the factors are connected to the presence of gaseous pollutants. The top five, in order of citations, are: Ozone [15], VOC emission from building products [16], NOx and O_3 concentration [17], terpene/ozone mixtures [18], and carbonyl compounds [19]. It ranges from 1973 to 2010.

The third largest cluster (#2) has 109 members and a silhouette value of 0.766. It is labeled “personal exposure”. It is representative of the personal exposure to fine particulate matter ($PM_{2.5}$ and PM_{10}). Articles with the highest coverage are by Bahadori [20], Janssen [21], and Micallef [22]. This cluster, as with the previous one, started after the previous one, but it terminated more recently. It covered 1981–2015.

The fourth largest cluster (#3) has 105 members and a silhouette value of 0.753. It is labeled “indoor air quality”. This cluster collects studies of indoor pollution in schools. While all the population is vulnerable to air pollution, the children are the most at risk. This constitutes a trend of actual interest, starting in 1992 up to current. The measurement of pollutant concentrations [23–25] and the risk assessments [26–28] are the main topics in this cluster.

The fifth largest cluster (#4) has 63 members and a silhouette value of 0.908. It is labeled “macrocyclic trichothecene mycotoxin”. The trichothecene mycotoxins are a group of toxins produced by some fungi. Some of these substances may be present as contaminants in mold and transported through aerosols. This cluster is representative of bacterial and fungal aerosols, as well the role of environmental factors in asthma. This cluster extends from 1958 to 2011.

The sixth largest cluster (#5) has 43 members and a silhouette value of 0.884. It is labeled “thermal comfort” and includes research papers on thermal personal comfort, Heating, Ventilation and Air Conditioning (HVAC), and the effect of relative humidity. This cluster extended from 1970 to 2016.

The seventh largest cluster (#6) has 41 members and a silhouette value of 0.916. It is labeled as “particle exposure” and collects publications about the environmental tobacco smoke. This cluster started in 1982 and ended in 2013, probably due to the implementation of non-smoking laws, which reduced the exposure to these pollutants.

Figure 6 shows the timeline visualization in CiteSpace, in which clusters are distributed along the horizontal timeline, reported in the top view. In black are the top two items ranked by centrality, while the colors represent the top three most cited articles. The full list of articles, ordered by coverage for each cluster, is reported in the supplementary file.

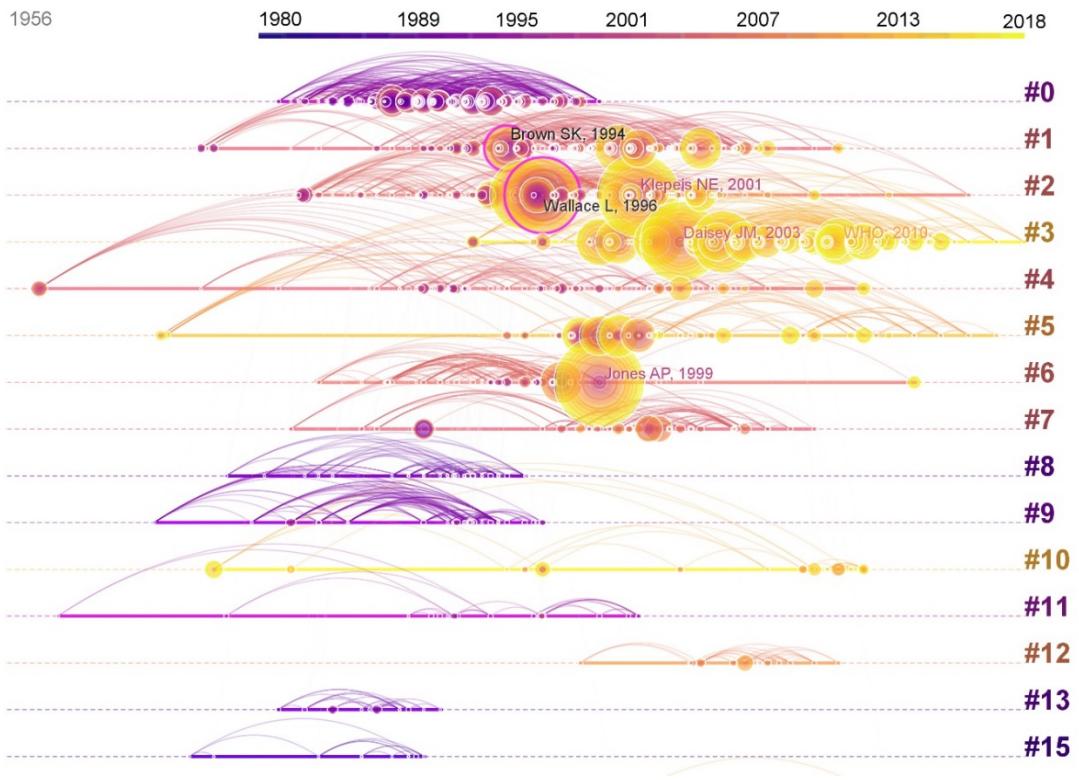

Figure 6 - *Timeline view of the clusters.*

Most-cited articles

The top-ranked item by citation counts is a comprehensive review of the relationship between indoor air pollution and health by Jones [29] in Cluster #6, with 262 citation counts. The second most-cited article is by Klepeis [30] in Cluster #2, with the publication of the National Human Activity Pattern Survey (NHAPS): A two-year probability-based telephone survey, sponsored by the U.S. Environmental Protection Agency (EPA), to assess the population exposure to environmental pollutants, with 261 citation counts. The third most-cited article is by Daisey [31] in Cluster #3, with 233 citation counts. In this review, data about ventilation rates, pollutants concentrations, and symptoms related to indoor air contaminants in schools were collected. The results highlighted the limited knowledge on the topic and it was a starting point for all current research on IAQ in schools, as shown in Figure 6, Cluster #3. The fourth is the "Indoor Air Quality Guidelines" by the World Health Organization (WHO) in 2010 [2] (Cluster #3) with 151 citation counts. The guidelines identified in benzene, carbon monoxide, formaldehyde, naphthalene, nitrogen dioxide, polycyclic aromatic hydrocarbons, radon, trichloroethylene, and tetrachloroethylene the selected indoor pollutants. The choice was made for three reasons: (1) These compounds have indoor sources, (2) they are known because of their hazardousness to health, and (3) they are often found indoors in concentrations of health concern. Particulate matter (PM) was exempt from the list, as it appears into the WHO guidelines on particulate matter were updated in 2005 [32], which also apply to indoor spaces. Mendell [33] in Cluster #3, who reviewed the literature on school environments and performance, had the same number of citations.

Citation bursts

As previously reported, citations bursts are a strong indicator of scholarly impact in terms of the attention of the research community. Table 6 reports the first five citation bursts. The top-ranked item by citation bursts is the WHO guideline for indoor air quality [2], in Cluster #3. The second is a multidisciplinary review of the scientific literature on ventilation rates and occupant health by Sundell [34] and the third is by Klepeis [30]. Following these are two reviews about the relationship between indoor and outdoor particles by Chen et al. [35] and about formaldehyde by Salthammer [36]. These first five publications bursts belong to Clusters #2 and #3. Clusters with numerous nodes with strong citation bursts can be considered an emerging trend, so for this reason, Cluster #3 is of a particular interest.

Table 6 - Top 5 citation bursts.

Bursts	References		Cluster
44.37	World Health Organization (WHO) Guidelines For Indoor Air Quality	[2]	3
37.81	Ventilation rates and health: Multidisciplinary review of the scientific literature	[34]	3
33.83	The National Human Activity Pattern Survey (NHAPS): A resource for assessing exposure to environmental pollutants	[30]	2
28.03	Health Effects of Fine Particulate Air Pollution: Lines that Connect	[37]	3
27.76	Formaldehyde in the Indoor Environment	[36]	3

Pivotal points

Nodes that have high betweenness centrality scores, as defined by Freeman [38], are an indicator of how strongly a reference connects references associated with two or more clusters. Centrality is normalized to the unit interval of [0, 1]. The sigma score (Σ) of a node is a composite metric of the betweenness centrality and the citation burstness of the node, computed as $(centrality + 1)^{burstness}$ [9].

The 1994 Brown paper (centrality = 0.14, Σ = 3.22) [39] is a typical pivot node; it is a strong contact point mainly between the two biggest clusters, and to a lesser extent between Cluster #8 and Cluster #10, as shown in Figure 5. This review systematically compared the concentration of VOCs in the indoor air of buildings of different classifications and categories, drawing mainly from the articles in Cluster #0 (1980–1999). Results suggested that indoor concentrations were significantly elevated above those outdoors, indicating that they were emitted from indoor sources. The aspect of source emission and modeling was afterward deepened by the publications gathered in Cluster #1 (as reported in Table 5).

Contemporary to the work of Brown about the analysis of the relationships between VOCs is the work of Wallace (centrality = 0.13, Σ = 9.05) [40], in which particle concentrations and sources in homes and buildings were summarized in detail. The conclusions suggested tobacco smoking as the leading source of indoor PM and secondary, cooking. Many links to Cluster #9 (topic—environmental tobacco smoke) highlight this aspect. Different from the previous study, PM infiltrations from the outdoors were found to contribute significantly to indoor PM. These first two papers have the highest centrality for Clusters #1 and #2, respectively.

The work of Bornehag (centrality = 0.06, Σ = 2.47) [41] is part of Cluster #5 (topic—"thermal comfort, relative humidity, HVAC"). In this study, the relationship

between “dampness” in building and health was considered, concluding that there is evidence for a strong association between them. Dampness is usually related to the presence of microbial agents (supporting the closeness to Cluster #4) as airborne molds and bacteria. However, due to the limited knowledge about the mechanisms behind the association between ‘dampness’ and health effects, it is difficult to intervene to limit this problem, unlike other known major pollutants.

1.1.3.5. Actual and future trends

In the second part of the analysis, a restricted dataset (from 2010 to 2018) was used. The results of the selection are reported in Table 7. For each year slice, in the “Criteria” column, the interpolated citation, co-citation, and the cosine coefficient thresholds are reported [42]. The “Space” column reports the number of articles having at least one citation within the related year-slice.

Table 7 - *Description of the new restricted dataset, resulting from the thresholding.*

1-Year Slices	Criteria	Space	Nodes	Links/All
2010–2010	8 | 8 | 0.4	6116	4	0/2
2011–2011	7 | 7 | 0.38	7577	22	8/86
2012–2012	7 | 7 | 0.36	7352	24	8/80
2013–2013	6 | 6 | 0.34	9311	46	26/187
2014–2014	6 | 6 | 0.32	9511	87	103/841
2015–2015	6 | 6 | 0.3	13675	109	218/1497
2016–2016	4 | 4 | 0.23	14241	404	808/7267
2017–2017	3 | 3 | 0.17	16496	1001	2002/19654
2018–2018	2 | 2 | 0.1	7117	618	1236/7066

In this last period, the most active institutions are reported using a geographical distribution map, which was created using “Generate Google Earth Maps” in CiteSpace (Figure 7). The colors on the maps show the institution that published papers about IAQ during the last eight years. The most active areas are colored in red. Notably, this map only highlights the quantity and not the quality of the publications.

Figure 7 - *Geographical distribution of published paper in the 2010–2018 dataset.*

Figure 7 shows that countries and territories in Europe, Northeast U.S., and East Asia participated actively in IAQ research in the recent years. The results of the actual geographical map were consistent with the total contribution by country, reported in Table 2, which referred to the complete dataset.

Articles with high citation bursts in the development of IAQ, between 2010 and 2018 are reported in the following list, ordered in ascending initial burst date. References with strong values in the "Strength" column can be considered relevant in the last eight years for the IAQ field. The "Topic" column summarizes the content of the publication. The "Begin" and "End" columns report, respectively, the beginning and end of the citation burst.

The first milestone, in the last eight years of study, is the IAQ guidelines published by the WHO. Notably, 10 of the 25 publications reported in Table 8 are related to the school environment, and this constitutes a major topic. Another topic common between articles having a strong citation burst is the relationship between indoor and outdoor pollutants, followed by studies on ventilation.

Table 8 - *A list of 25 articles having a strong ("strength">5) citation burst*

References		Topic	Strength	Range	2010–2018
Yu, C.W.F., 2010	[43]	VOCs and formaldehyde emissions	15.73	2011–2014	
WHO, 2010	[2]	IAQ: WHO guidelines	23.65	2012–2015	
Yu, C.W.F., 2011	[44]	IEQ assessment: Standards and certifications	13.93	2012–2013	
Chen, C., 2011	[35]	Indoor/outdoor particles relation	11.44	2013–2015	
Dimitroulopoulou, C., 2012	[45]	Ventilation in European dwellings	8.58	2013–2015	
Zhang, Y.P., 2011	[46]	A review on fan-driven air cleaning technologies	7.18	2013–2015	
Salthammer, T., 2010	[36]	Indoor Formaldehyde	8.76	2013–2015	
Sundell, J., 2011	[34]	Ventilation rates and health	16.36	2013–2015	
Almeida, S.M., 2011	[47]	Children exposure to PM in primary schools	19.63	2013–2015	
Lim, S.S., 2012	[48]	Risk assessment of disease burden caused by different risks	11.43	2014–2015	
Hospodsky, D., 2012	[49]	Human occupancy as a source of indoor airborne bacteria	5.41	2014–2015	
Satish, U., 2012	[50]	Effects of CO_2 on human decision-making performance	5.93	2014–2015	
Geiss, O., 2011	[51]	VOC in public buildings, schools, kindergartens	5.15	2014–2015	
Pegas, P.N., 2011	[52]	Outdoor/indoor air quality in primary schools	8.67	2014–2015	
Guo, H., 2010	[53]	$PM_{2.5}$ in school	9.39	2014–2015	
Logue, J.M., 2011	[54]	Hazard assessment of chemical air contaminants in houses	5.14	2014–2015	

Pegas, P.N., 2010	[55]	Outdoor/indoor air quality in primary schools	10.06	2014–2015	
Qian, J., 2012	[56]	Emission rates of airborne bacteria and fungi in classroom	6.31	2014–2015	
Wichmann, J., 2010	[57]	$PM_{2.5}$, soot and NO_2: Indoor/outdoor relationships	6.54	2014–2015	
Branis, M., 2011	[23]	PM in school gyms	6.69	2014–2015	
Pegas, P.N., 2011	[58]	Indoor air quality in schools	9.93	2014–2015	
Pegas, P.N., 2012	[59]	Pollutants inside school	6.43	2014–2015	
Annesi-Maesano, I., 2013	[60]	IAQ in school	5.20	2014–2016	
Fabi, V., 2012	[61]	Occupants' window opening behavior	5.38	2015–2016	
Mendell, M.J., 2013	[62]	Classroom ventilation and reduced illness absence	6.77	2015–2016	

1.1.4 Discussion

The categories and journals co-occurrence analysis showed the multidisciplinary nature of the IAQ topic and the most relevant categories. Although only a few journals are now the most active, the network of co-occurring journals reported an articulated structure, groupable into four macro thematic areas: Medicine, energy, buildings, and environments. Temporal patterns showed IAQ is a theme that has changed over time, often due to new external stimuli (different sources of pollution, different environments, and new emerging countries), and the result of new laws enacted, due to a greater awareness of the topic, such as non-smoking laws. Cluster analysis found 15 well-defined clusters, of which two (Cluster #2, “personal exposure” and Cluster #5, “thermal comfort”) are still active.

This study, although not comparable to a systematic and in-depth study of the issue, has allowed us to delineate the past and present of IAQ research. The analysis of when the meaningful terms had a citation burst, together with the study of the cluster timeline, shows how the concept of IAQ has blossomed, starting from a medical point of view, i.e., from the study of the symptoms of SBS in places of work. Over the years, the focus has shifted to the characterization of pollutants and risk assessment. With the introduction of the ban on smoking in public places and workplaces, one of the prevailing indoor sources has been greatly reduced.

At the same time, academic attention initially focused on workplaces, and then moved to public buildings, especially schools and hospitals. The implementation of non-smoking laws has reduced the focus on the Environmental Tobacco Smoke (ETS), despite the recent introduction of electronic cigarettes on the market.

Although many studies have been completed on indoor and outdoor sources of pollutants and risk assessments on poor air exposure, in many parts of the world, these sources have been abruptly reduced (ETS, for example), so IAQ remains important.

From the presence of new sources, ignored until a few years ago as niche or because they were non-existent (3D printers, electronic cigarettes), the field has

evolved from the need to make workplaces as appropriate and pleasant as possible (by thinking of a broader concept of Indoor Environmental Quality, in which more environmental parameters are considered to increase productivity), due to the ubiquitous use of new available technologies (low-cost sensors and DNA sequencing techniques), to the new frontiers in indoor chemistry and transformation of indoor pollutants. These are just a few examples of the challenges that the scientific community working on the issue of IAQ has encountered in recent years, without considering the research based on non-major fields. These challenges range from the impact of clothing on exposure, to smart technologies, from the study of phytoremediation and materials able to passively improve air quality [63–65] to new technologies and purification processes [46,64,66–68]. The monitoring of indoor airborne pollutants is a necessary step for assessing personal exposure to pollutants not previously considered. Many of the chemicals presently found in indoor environments were not present in the past, and concentrations have varied over time due to the use of different building materials, new consumer products, electrical appliances, and cleaning products. For this reason, new monitoring campaigns, as well as new sampling methods, are required. Passive samplers are popular and convenient for distributed and long-term exposure assessment, but they cannot provide a short time-resolved picture of the indoor air, which can be completed by using more expensive analyzers. Widespread low-cost sensors are valuable resource that could be coupled with well-established monitoring techniques because, even if they have recently shown an improvement in power consumption, sensitivity, and resolution, they still have problems in selectivity. So, at the time of writing the present article, only laser scattering-based sensors for PM measurement provide acceptable results [69,70].

The collection of big data obtained from ubiquitous sensor networks [69,71,72] requires determining how to process and extract useful information from the raw data, and semantic frameworks can be a useful tool to address this challenge [73].

From another point of view, 1.2 billion people from developing countries are without access to electricity, while nearly 3 billion people worldwide are exposed to the threat of household air pollution every day from the use of solid fuel for cooking, heating, and lighting [74,75].

These are only a few aspects the indoor air community has to consider. Scientometric tools can be useful to analyze, categorize, and identify milestone and turning points in the scientific literature. However, these tools cannot be considered exhaustive and scientific advances will probably be driven by new multidisciplinary contaminations into the discipline.

In Paragraph 1.2, a comparison between scientific production and patent literature about indoor air quality control techniques has been conducted;

- *despite the presence of many different technologies for the removal of pollutants, out of 111 registered patents, the majority comprised of filtration and adsorption processes;*
- *photocatalysis is the major topic in the scientific literature, starting in 1990, dramatically increasing in 1998, reaching a peak in 2008 and decreasing up to nowadays, while its presence in the patent literature starts in 2010;*
- *non-thermal plasma oxidation, botanical filtration, and phytoremediation are novel treatment technologies. Around the latter two, it is shown an intense and recent patent activity.*

1.2 Indoor Air Treatment: a comparison between scientific and patent literature

1.2.1 Introduction

1.2.1.1 Indoor pollutants

Indoor air pollution is a complex issue, consisting of a multitude of pollutants, occurring in confined environments, which may pose threats to human health. As a result of the bibliometric study, presented in the previous chapter, pollutants' studies can be clustered into three macro areas: particulate pollutants, gaseous pollutants, and microbiological pollutants. This type of classification is particularly useful from a control technology perspective, as different technologies are more effective on a specific class of pollutants.

Gaseous pollutants

Organic compounds

Both the European and the American definition of VOC is an organic compound having an initial boiling point less than or equal to 250° C, measured at a standard atmospheric pressure of 101.3 kPa [76,77].

VOCs are ubiquitous in indoor environments. They are commonly present in consumer products, cleaning products, furnishing and building materials, paints, office equipment, and they are generated by human activities, such as cleaning, tobacco smoking, and cooking.

The World Health Organization (WHO) categorizes indoor organic pollutants by how easily they are emitted:

- Very volatile organic compounds (VVOCs)
- Volatile organic compounds (VOCs)
- Semi-volatile organic compounds (SVOCs)

While the VOC and VVOC indoor emission are generally easily assessed, SVOC, (including pesticides, plasticizer and fire retardants), require a much longer monitoring period, and only recently the public attention focused on this last type of pollutants.

Gallego et al. [78] identified 113 VOCs in indoor environments, with a total VOC concentration of 1.33 ±1.53 mg/m^3 in a case study where the primary source was outdoor. Previous studies reported similar results, with the total volatile organic compound (TVOC) concentration of about 1.1 mg/m^3 average [39] and the mean concentration of each VOC is generally between 5 μg/m^3 and 50 μg/m^3.
Among the variety of VOCs occurring in indoor environments, alkanes and aromatic compounds comprise the major classes.
To some VOC have been associated with adverse respiratory effects [43], and to others have been classified as known human carcinogens [79].

Inorganic compounds

Inorganic gases are mainly represented by gaseous compounds such as NO_2, SO_2, O_3, CO, and they are generally traffic-related pollutants, and the presence in the indoor environments is due to their penetration from the outdoor. Many activities involving combustion (i.e., cooking, heating, incense burning, tobacco smoke), may dramatically increase indoor levels.

The NO_2 natural background means concentrations are in the range 0.4–9.4 μg/m^3, while indoor average, with unvented gas combustion appliances, may reach 200 μg/m^3, with short-term episodes up to 2000 μg/m^3. Normal healthy people experienced pronounced decrements in pulmonary function for concentration equal to 4700 μg/m^3 (2.5 ppm), for short-term NO_2 exposure [80].

In the last decades, SO_2 concentration in the environments showed a decline, mainly due to changes in fuel use. However, the coal-burning activity can result in local episodes of higher concentrations. WHO guidelines [32] report as 24-hours limit concentration 125 μg/m^3, while for the annual 50 μg/m^3.

Ground-level ozone (O_3) is a pollutant. In the environment, O_3 is formed by the action of short-wavelength radiation from the sun on nitrogen dioxide, and it can be enhanced by the presence of VOCs. Background levels of O_3, are in the range 40–70 μg/m^3. Indoor ozone concentrations can be significantly increased by many sources, such as ozonizers, electrostatic filters, and photocopying machines. Short-term acute effects for ozone exposure, in healthy adults, have been observed at a concentration threshold of 160 μg/m^3. The health risk to prolonged exposition includes respiratory symptoms, pulmonary function changes, and airway inflammation [80].

Carbon monoxide (CO) is produced by the incomplete combustion of carbon-containing fuels; indoor concentrations are generally comprised between 1 and 10 mg/m^3 [2,81]. Among the health effect of exposure to CO, fatigue, reduced brain function, cause eye irritation, headaches, confusion, it can be fatal at very high concentrations because of its oxygen intake inhibition.

Particulate/fibrous pollutants

According to the aerosol science terminology, dust is defined as solid particles larger than 0.5 μm, which can deposit on surfaces. The majority of house dust particles are of biological origin in the order of tens of micrometers [23,49,82].
Fibers, instead, are characterized by a length-to-diameter ratio of a least 3:1, by a length of more than five μm and a diameter of fewer than three μm [82]. They can be classified in natural or artificial and organic or inorganic.
Their diameter-based classification is of particular interest when we want to compare them with their effect on the human body. The inhalable fraction remains in the mouth and head area, while the thoracic fraction penetrates the airways of the respiratory system. At last the respirable particulates, the smallest fraction, can infiltrate most deeply into the alveolar region and penetrate the organism.

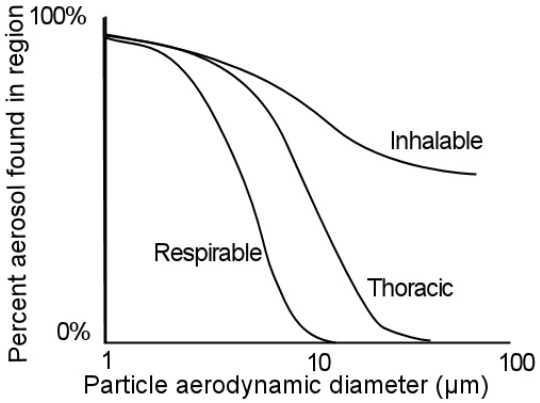

Figure 8 *– Distribution of the particulate found in the region*

One of the most known pollutants within this family is asbestos, which, in the past, has been widely used in materials construction. This particular mineral (exhibiting roughly a 1:20 aspect ratio) has been found to cause mesothelioma and several types of cancer.
However, particulate matter can be not hazardous by itself, but for the molecules, they can vehicle. For instance, SVOC or endocrine disruptors can be adsorbed on the surface of dust and particles, even in appreciable amounts [83].

Biological pollutants

Biological pollutants found indoor comprise animal allergens, viruses, bacteria, and related endotoxins, molds, which release spores and microbial volatile organic compounds (MVOC). Allergens produced by house dust mites are considered to be the most important causes of hypersensitivity pneumonitis, allergic rhinitis and some types of asthma. Bacteria and fungi, present in damp areas, may cause building-related severe disease as well, (e.g., the Legionella bacteria).

1.2.1.2 Indoor treatment technologies

Three basic strategies may be applied to reduce indoor pollution, in order to improve IAQ: source reduction, dilution ventilation, and active control systems. While the first one is not always actable, increasing ventilation does not necessarily involve the reduction of pollutant concentrations above a safe limit; nevertheless it may imply

to bring in more pollutants from the outside, and it is inconsistent with energy saving policies. For these reasons, purification/treatment technologies deserve special attention nowadays. Their effectiveness widely varies, because both of the implemented process, both of the used material. Zhang et al., from the analysis of 59 literature study, come to the point that none of the reviewed technologies was able to effectively remove all indoor pollutants, that some of them are mostly ineffective, and may produce harmful by-products [46].
In the follow section are reported the commont techniques to remove pollutants from the indoor air and they are summarized in Table 10.

Mechanical filtration

Mechanical filtration is one of the most widely used air purification technique for removing suspended particles because of its simplicity of use most economical means. The minimum requirement is defined as a "fan-filter unit," where a filter media is placed upstream the fan. This technique is effective on particles, which are captured by interception, impact, diffusion, electrostatic deposition or gravitational settling; for this reason, filter media undergoes to a progressive decrease of the removal efficiency, jointly with an increase of the pressure drop. A typical filter efficiency for individual filtration mechanisms and total filtration efficiency is reported in Figure 9. It is possible to observe that three fundamental mechanisms act concurrently and with different intensity, according to the particle size.

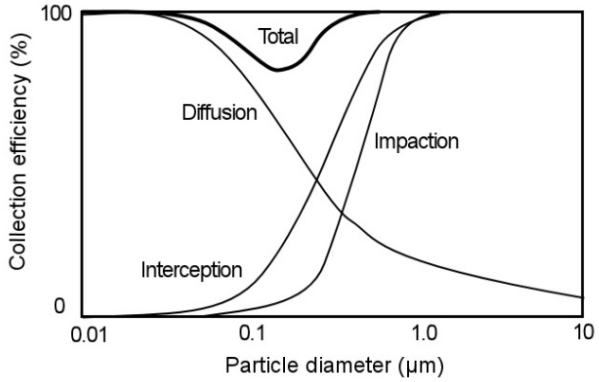

Figure 9 *– Mechanisms defining the collection efficiency of a typical filter media*

Mechanical filter efficiency generally depends on the type and the material of the filter; from the air flow and the size of the particulate. The three most commonly used operating parameters that characterize an air filter are the filtration efficiency, the pressure drop across the filter and the dust-holding capacity. Filtration efficiency is defined as

$$\eta = 1 - C_{down}/C_{up} \qquad \textit{Equation 1}$$

Here, C_{up} and C_{down} represent the particle concentrations (particles/cm^3) upstream and downstream of the filter, respectively.

HEPA filters are characterized by high filtration efficiency near 100% for particles having a diameter equal to 0.3µm.

Aerodynamic air cleaners

Cyclones and scrubbers are apparatus for the removal of suspended particles in which, respectively, a centrifugal force is impressed to the airstream and droplets, having specific kinetic energy, collect the particles.
This mechanism is effective for larger particles because of their relatively large masses (and so greater inertia), and it does not need a media substitution. A drawback is that fine particles remain suspended in the air stream.

Electrostatic filtration

Electrostatic precipitators (ESPs) have been used since a century for the collection of particulate matter present in the gas streams of many industrial processes. ESPs are based on Coulombic attractions between charged particles and a collecting plate. That gives the principle of operation: the particulates are passed through an electric field, where they receive an electric charge. Afterward, particles are deflected by the electric field to the collector electrode [84,85] (Figure 10).

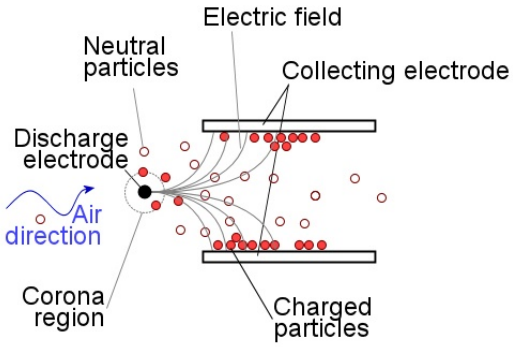

Figure 10 *– Schematic representation of the process underlying an ESP*

An electric field is formed from the application of an electric potential difference to the ESP discharge electrodes; the strength of this electric field is a critical factor in ESP performance. Despite the higher setup costs, if compared to conventional mechanical filters, due to high-voltage transformation unit, ESPs are characterized by a small pressure drop, a high-collection efficiency of small-size particles and low operating and maintenance costs. A known drawback is the production of ozone by the discharge electrode [86], which is harmful to the health [87].

Adsorption

There are many definitions of the term “adsorption” focusing on different aspects of the same phenomena: from a thermodynamic approach to a macroscopic perspective. However, all these nuances arise from the attractive forces between molecules, in which molecules from an ambient fluid phase tends to adhere to the surface of a solid because of the creation of a low potential energy region near the solid

surface, resulting in an increased molecular density close to the surface compared to the counterpart in the bulk phase [88].

Figure 11 and Table 9 reports the terminology adopted for describing the adsorption process.

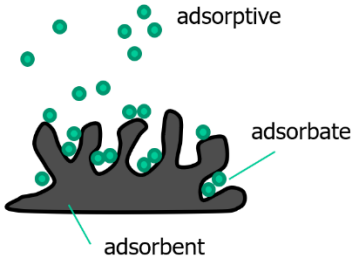

Figure 11 *- Schematic representation of the adsorption process*

Table 9 *– Terms related to the adsorption process*

Term	Definition
Adsorptive	The adsorbable substance in the fluid phase
Adsorbent	Solid on which adsorption occurs
Adsorbate	The substance in the adsorbed state
Adsorption	The increase of the concentration of species in the vicinity of an interface
Chemisorption	Adsorption involving chemical bonding
Physisorption	Adsorption without chemical bonding

The adsorption process is a common technique for removing various pollutants from a fluid stream. Many adsorptive materials are widely used for filters application; for instance, activated carbon has the ability to reduce ozone, selected volatile organic compounds (VOCs) and other pollutants over long periods [89], as well as zeolites, alumina, silica gel, clay. The adsorption process, over an appropriate media, it is considered effective also for little concentration of pollutants, even if they are merely transferred from the gaseous to the solid phase, instead of being destroyed.

Photocatalysis

The environmental photocatalysis enthusiasm in scientific literature was driven by the extensively cited publication of Fujishima and Honda [90], even if the study of light-driven reaction at semiconductor surfaces was already widely fuelled by the 1973 oil crisis. However, due to long-term catalyst stability problems and difficulties in applying such process in real scale, the scientific interest decreased.

Photocatalytic oxidation (PCO) over titanium dioxide (TiO_2) is widely reported as a promising technique for decomposition of various hazardous compounds, among energy applications and synthesis of various compounds.

The principle underlying the photocatalytic process is the formation of an electron-hole pair by the absorption of a photon having energy equal or greater than the semiconductor's bandgap (Figure 12).

$$Photocatalyst \xrightarrow{h\nu} e^-_{CB} + h^+_{VB}$$

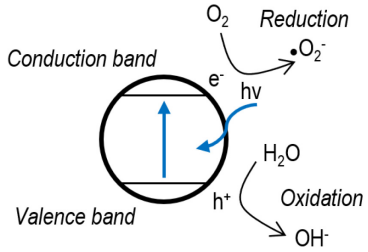

Figure 12 *- Schematization of the photocatalytic process*

The formation of the electron/hole couple on the catalyst surface induces the formation of active species, including $O_2^{\bullet-}$, $^{\bullet}OH$, $O^{\bullet-}$ radicals, as well as H_2O_2, O_3, ${O_2}^1$, ${O_3}^{\bullet-}$,$HO_4^{\bullet}$, $HO_3^{\bullet}$ radicals, which take part in the oxidative process. However, most of the photogenerated electron-hole couple rapidly recombine after excitation [91], while only 10% is supposed to start the formation of Reactive Oxygen Species (ROS) [92,93].
TiO_2-PCO is a non -selective air cleaning technology, which can degrade the majority of the contaminants (organic, inorganic, odors) and combining TiO_2 with an adsorbent, make possible to enhance the PCO degradation of target pollutants. Doping (introducing defects into the catalyst lattice) and realizing new bond in TiO_2-composites are the most common techniques to lower the bandgap, in order to enhance the quantum yield. However, PCO can generate by-products, such as formaldehyde, acetaldehyde, etc., which are more harmful to human health than the original pollutant. Combining TiO_2 with adsorption material (ie. activated carbon) may lower the generation of the by-products and enhance the mineralization into final compounds.

Non-thermal plasma

Plasma-based oxidation technology refers to a process in which a high voltage discharge is used for the destruction of pollutants. Non-thermal plasma (NTP) refers to a weakly-ionized plasma, in which electrons temperature (1-25eV) is higher than the average gas temperature, at ambient temperature [94]. The most commons reactor configuration are dielectric barrier discharge (DBD), corona discharge and ferroelectric packed bed reactor. The reactive species formed in the plasma region can directly react with the VOCs, leading to a more or less complete mineralization. Best results have been obtained when plasma was coupled with a catalyst [95,96]. Plasma air cleaners have been reported to remove particles effectively. However, NTP-technology alone may produce a wide range of unwanted byproducts, as well as ROS, for this reason, it is often found coupled downstream with an adsorbent or a catalyst.

Ion generators

A corona charges particle by an ion generator, in order to remove them on collector plates or indoor surfaces. However, the effectiveness of such a device has been questioned as many studies demonstrate a secondary production of nanoparticles due to the reaction of ozone with terpenes [97,98] and a wide range of efficiencies.

UV-photolysis

Gas-phase oxidation of volatile organic compounds was initially studied by McGregor et al. in 1988 [99]. Direct photolysis is a technique to remove VOC by providing photons which induce chemical changes in the pollutant structure. The irradiation of oxygen, with a light characterized by a wavelength shorter than 185nm, leads to the ozone formation. Many studies on the photolysis of chlorinated organic compounds [100,101], α-Pinene [102], 27 typical indoor-found VOCs [103], were made, showing a wide spectrum of mineralization rate to CO_2 (from 9% and 90%). However, due to the ozone emission and its reaction with the VOC, this technique may generate, as well, particulate matters [103].

Ozonation

In the market, some ozone generators are sold as air cleaners. Ozone is a strong oxidizer, and it is known for inactivating viruses and bacteria [104,105]. However, ozone is a pollutant, and ozonizer-only devices are not considered air-purifiers.

Table 10 *– Conclusive remarks on indoor air control technologies*

Technology	Target pollutant	Advantage	Disadvantage
Mechanical filtration	PM	No by-products Easy to implement	Medium/high pressure-drop; filter replacement;
Aerodynamic air cleaner	PM	No by-products Easy to implement	Medium pressure-drop; Medium/low efficiency
Electrostatic filtration	PM	Low pressure-drop; Low maintenance Effective $PM_{0.02}$	By-products generation High setup cost
Adsorption	VOCs Inorganic compounds	No by-products No energy consumption Easy to implement	Medium pressure-drop; Adsorbent replacement; Target-compound specific Negatively affected by water vapor
Photocatalysis	Inorganic compounds VOCs Microbes	Low pressure-drop; low energy consumption	By-products generation Photocatalyst inactivation Optimal in 20-60% RH
UV-photolysis	Microbes VOCs	Low pressure-drop; Effective for microorganism (UVGI)	By-products generation Lamp replacement
Non-thermal plasma	VOCs Microbes PM	Low pressure-drop;	By-products generation; High setup cost High energy consumption Negatively affected by water vapor
Ion generators	PM	Low pressure-drop;	By-products generation Low efficiency

1.2.2 Materials and methods

In order to collect the related scientific literature, article data were obtained from the Web of Science Core Collection (WoSCC) by Thomson Reuters before 1 October 2018. In this study, the keywords used for the data retrieval strategy were as follows:

indoor AND (air OR gas) AND (removal OR oxidation OR purif OR adsor*)*

English-only document types were articles, letters, and reviews, ranging from 1990 to 2018, from the following indexes: SCI-EXPANDED, SSCI, A&HCI, CPCI-S, CPCI-SSH, and ESCI. The final dataset contained 2935 bibliographic records of Article or Letters or Review in English.

Patent data was obtained from two different sources: the USPTO database, by using the PatentsView library written in R and from Lens.org.
According to the WIPO classification, subclasses indexes for gas separation processes are reported in Table 11:

Table 11 *– WIPO subclasses for gas separation processes*

LIQUID/LIQUID, LIQUID/GAS OR GAS/GAS SEPARATION	
Method	
General operations	B01D
by centrifugal force, using centrifuges or free-vortex apparatus	B01D
using magnetic or electrostatic effect	B03C
Apparatus	
General operations	B01D
by centrifugal force, using centrifuges or free-vortex apparatus	B04B, B04C
using magnetic or electrostatic effect	B03C

SOLID/LIQUID OR SOLID/GAS SEPARATION	
Method	
General operations	B01D
by centrifugal force	B01D
using centrifuges or free-vortex apparatus	B01D
using magnetic or electrostatic effect	B03C
Apparatus	
General operations	B01D
by centrifugal force	B01D
using centrifuges or free-vortex apparatus	B04B, B04C
using magnetic or electrostatic effect	B03C

The statistical analysis of articles was conducted in CiteSpace V [1], while the patents analysis were made in R [106], using the patentsview package [107] and the dataset obtained from the USPTO database. Despite Lens.org hosts a higher number of references, from different sources, some database fields are missing (i.e., abstract). For this reasons, in the following analysis, only the dataset from the USPTO was considered. The analysis conducted on the Lens.org database is reported in Annex 1.
Relevant data from the PatentsView API was obtained by the following query:

```
query <- with_qfuns(
  or (
   and(begins(cpc_subgroup_id = 'B01D'), text_all(patent_abstract = "indoor")),
   and(begins(cpc_subgroup_id = 'B03C'), text_all(patent_abstract = "indoor")),
   and(begins(cpc_subgroup_id = 'B04C'), text_all(patent_abstract = "indoor"))
  ))
```

The query results in 111 patents. These patents cite 2005 patents and are cited by 1066 patents. Although the list is comprehensive only of the US patents, it is a starting point for being compared with the existing scientific literature.

1.2.3 Results

1.2.3.1 Patent analysis

Geographical distribution of the patent dataset is reported in Figure 13. Figure 14a shows the citations network among the resulted patents, while in Figure 14b and Figure 14c are reported two major patents sub-networks. The cluster B (Figure 14b) collects many patents characterized by the most widely-adopted technologies: filtration, adsorption, oxidation and electrostatic precipitation. Cluster C, instead, gathers patents about phytoremediation and botanical filtration. The unconnected dots cloud are representative of patents which do not have anteriority within the dataset.

Figure 13 *- Geographical distribution of the patent dataset*

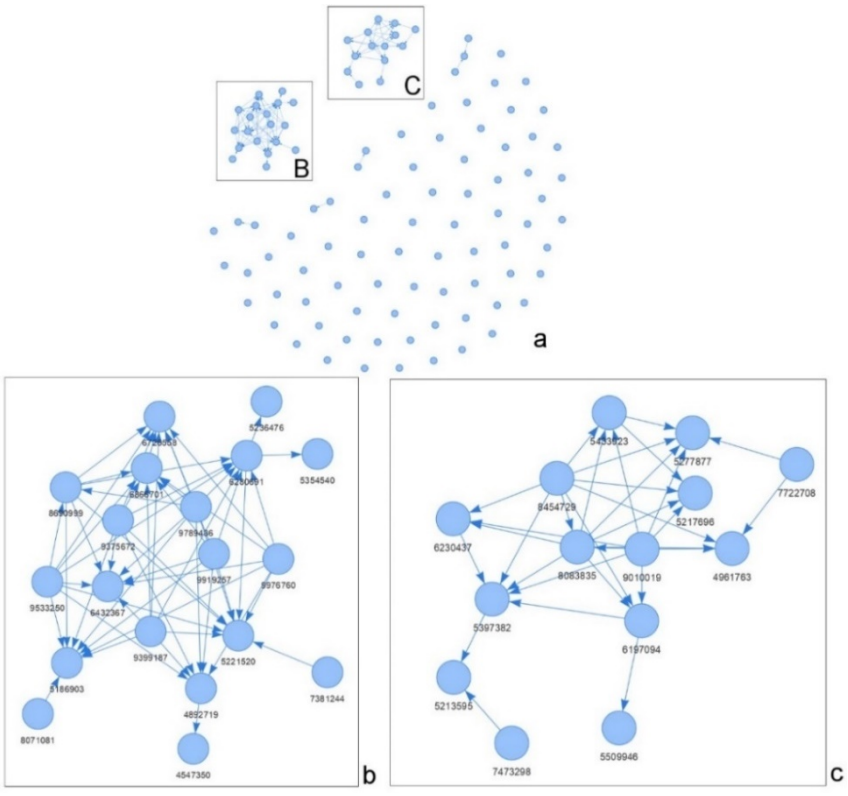

Figure 14 *– a) Patents citation network; b,c) major patents sub-networks*

Table 12 reports the patents which have the highest number of patent citations, that are contained within the clusters B-C.

Table 12 *- Patents with the highest number of patent citations*

Cluster B **Patent #**	**Citing patents**	**Title**
5221520	8	Apparatus for treating indoor air
6432367	7	Indoor air quality gas phase return air cleaner
5186903	7	Apparatus for treating indoor air
6280691	7	Indoor air purification system
6866701	7	Oxygen enrichment of indoor human environments
6726558	7	Oxygen enrichment of indoor human environments
4892719	6	Removal of aldehydes and acidic gases from the indoor air

Cluster C **Patent #**	**Citing patents**	**Title**
5397382	5	Bio regenerating air filter
5277877	5	Room air purifier
4961763	4	Indoor air purifier
5217696	4	Combined lamp and indoor air purification apparatus
6197094	3	Device for improving the quality of indoor air
5433923	3	Indoor humidifier and air purifier
6230437	3	Plant stand

In Table 13 are reported the top organizations patenting in the indoor air quality control group (IAQC). In "IAQC patents" column is reported the number of patents pertinent to the query, in the "total patents" column, is reported the total number of patents belonging to an Assignee, and in the last column the ratio between the two previous columns.

Table 13 *- Top patenting organization in the IAQC dataset*

Assignee	**IAQC patents**	**Total patents**	**IAQC patents / total patents**
Daikin Industries, Ltd.	10	2543	0.004
ENVERID SYSTEMS, INC.	8	16	0.5
Brown University	4	134	0.03
Carrier Corporation	3	2404	0.001
G.B.D. Corp.	2	112	0.018
North Carolina Center for Scientific Research, Inc.	2	3	0.667
NovelAir Technologies, L.L.C.	2	7	0.286
Space Biospheres Ventures	2	12	0.167
WMA Ranger, Inc.	2	2	1

A further step in the patent analysis is reported in Figure 15, in which, the patent count, identified as the Cooperative Patent Classification (CPC) group are plotted against the year. More than one CPC may classify a single patent.

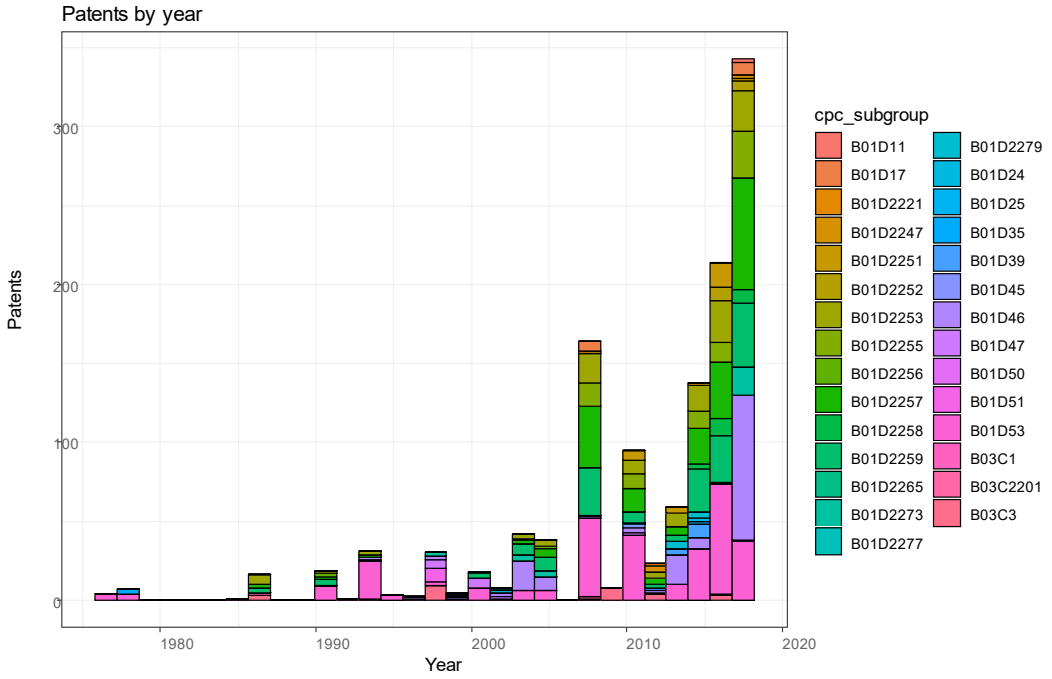

Figure 15 *- CPC groups in the IAQC dataset*

In Table 14 are reported the largest CPC groups reported in Figure 15. It is possible to observe in Figure 15 that the group B01D225 is correlated to the "Components to be removed" through a separation process (B01D) and it is, generally, linearly related to the number of patents. Patents belonging to the CPC B01D46 (Filters for PM) appeared around the year 2000, as before the PM was recognized mostly as a nuisance pollutant. B01D53 is a wide group of separation techniques designed for separating gases and B01D39 is related to the material which filters are realized.

Table 14 *- Most occurring CPC groups in the IAQC dataset*

CPC code	Description
B01D2257	Components to be removed
B01D46	Filters or filtering processes specially modified for separating dispersed particles from gases or vapors
B01D53	Separation of gases or vapors; Recovering vapors of volatile solvents from gases; Chemical or biological purification of waste gases, e.g., engine exhaust gases, smoke, fumes, flue gases or aerosols
B01D39	Filtering material for liquid or gaseous fluids

Through a more detailed investigation of the group B01D2257, reported in Figure 16, it is possible to highlight how different target pollutants have changed during the last decades. While the odorous compounds have always been present as a target species, other pollutants, such as VOCs and ozone, became part of it, only recently. This aspect is in agreement with the bibliometric analysis presented in the previous paragraph.

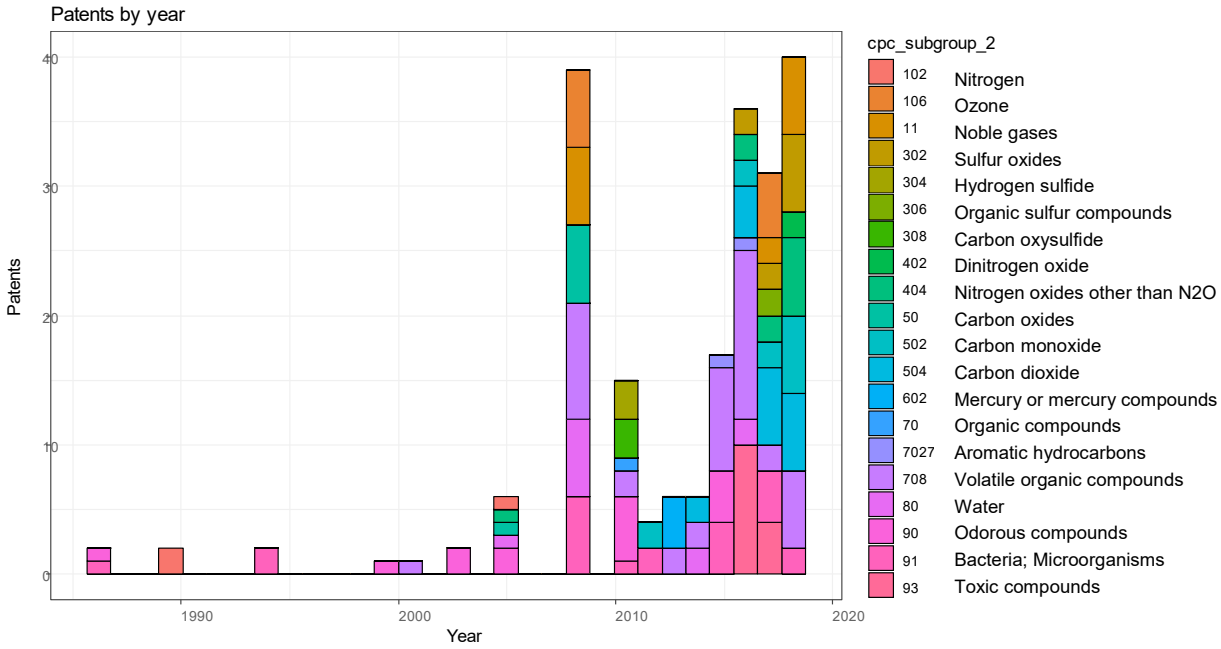

Figure 16 *- Time distribution of the target pollutants reported within the CPC B01D2257.*

Although CPC groups are descriptive of a particular process, to further enhance the analysis, a new variable has been introduced. Its value is related to the process adopted to remove the target pollutants, among the ones reported in Paragraph 1.2.2. The assignment of the corresponding value has been made by scraping the abstract and title text of each patent and looking for specific keywords, reported in Table 15.

Table 15 *- List of keywords used to "label" the type of process described.*

Process	Keywords
Filter	"HEPA", "ULPA", "filter", "filters", "filtration", "filtering"
Aero	"Cyclone", "scrubber"
ESP	"electrostatic filtration", "electrostatic precipitation", "electrostatic filter"
Ads	"adsorption", "adsorbent", "adsorbing"
PCO	"photocatalysis", "photocatalyst", "semiconductor"
UV	"UVGI", "photolysis", "UV-C"
NTP	"NTP", "plasma", "dielectric barrier discharge"
Ion	"ionizer", "ionization", "ions"
Plant	"plant", "botanical", "plants"

In order to assess the goodness of the clustering process, Figure 17 reports the correlation plots between the patent year, the CPC subgroup related to the patent (the B01D2257 group was removed, as it is indicative of the target pollutant removed) and the new variable "process." Despite the low correlation value (0.22) between the process and the cpc_subgroup, by manually analyzing a significant sample of patents, in most of the cases, the classifier algorithm succeeded in correctly labeling the process.

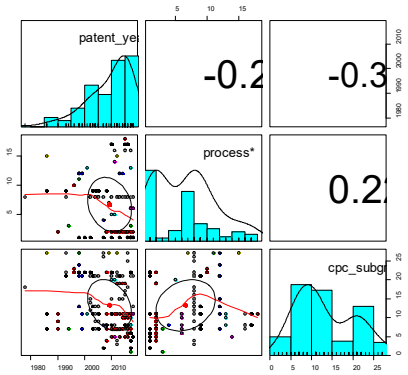

Figure 17 *- Correlation plot between the year, the cpc_subgroup and the process*

The number of patents, identified using the same technology, versus the year, are reported in Figure 18. It is possible to notice that adsorption and filtration are, since 1980, the most adopted processes for removing pollutants from the indoor; only recently photocatalysis became commercially available, as well as phytoremediation/botanical filtration.

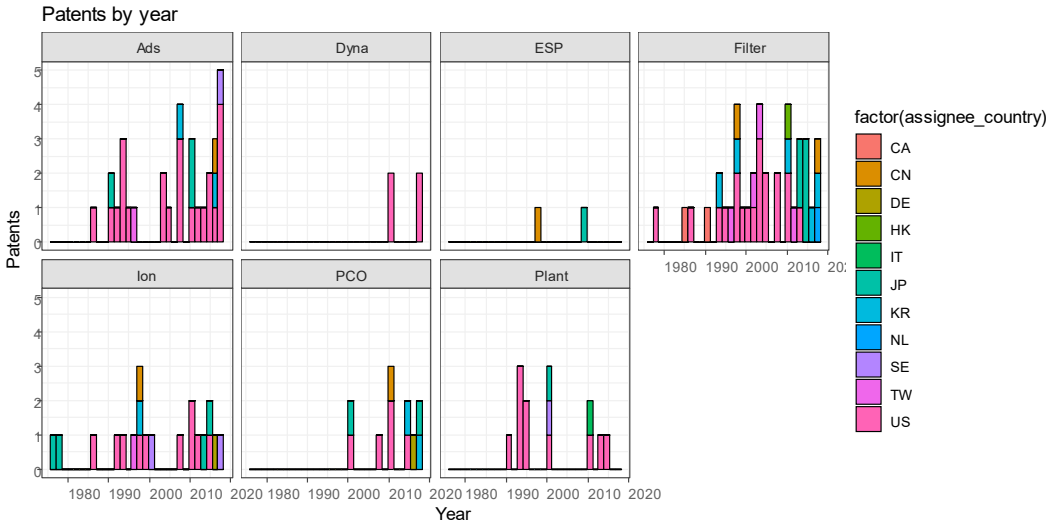

Figure 18 *- Number of patents, using different control techniques, published by year*

1.2.3.2 Scientific literature analysis

The co-citation network (see paragraph 1.1.3.4. for an exhaustive description) of the selected dataset is reported in Figure 19.

The presence of two macro-groups is easily appreciable. By analyzing the articles present in each cluster, it was found that in the left macro-group, were present many articles on the impact of reaction products from building materials and furnishings and, therefore, they were considered not relevant to the current research. On the other hand, in the right macro-grouping, studies relating to processes, technologies, and materials for the "active" removal of indoor pollutants are reported.

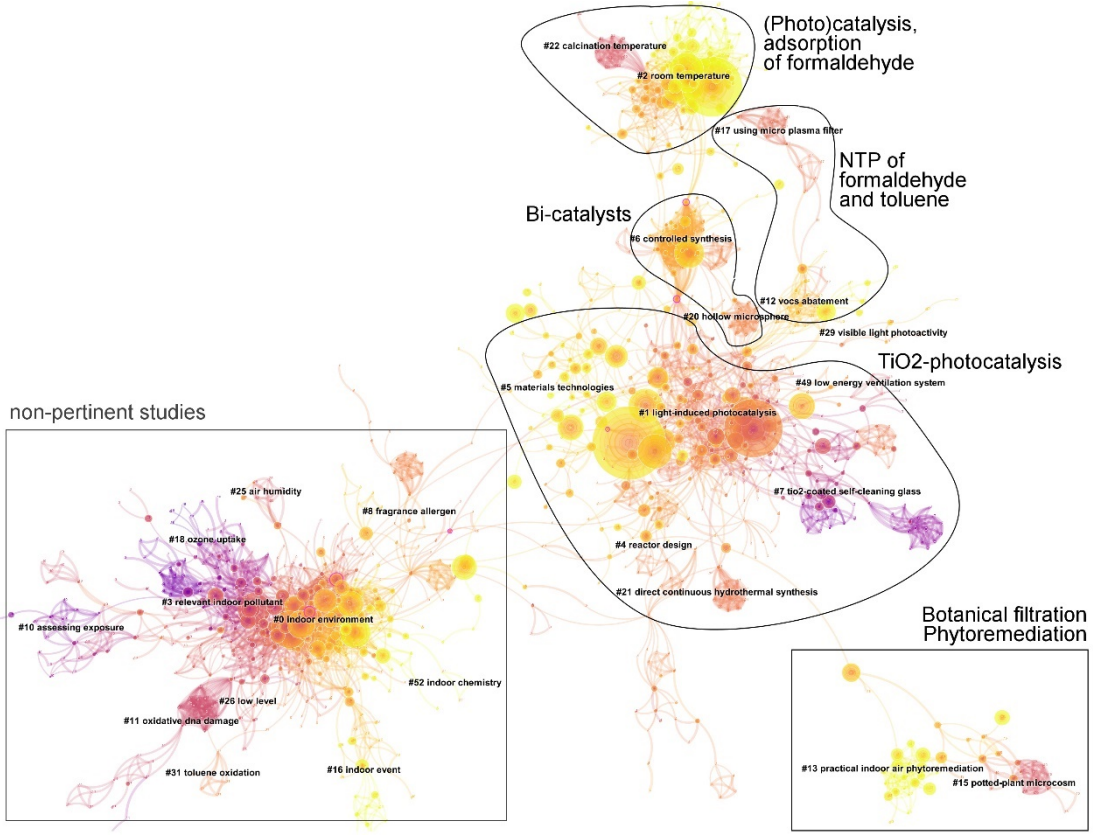

Figure 19 - *Landscape views of the resulted co-citation network*

The largest group collects the Clusters #1,4,57,21,49, and it is related to the TiO_2 photocatalysis.

Bismuth-based catalysts, grouped in Clusters #6,20, is a recent study line and they are considered a valid alternative to TiO_2, due to their reduced bandgap, and therefore, they are suitable for real-scale applications, without the need for UV irradiation.

In Clusters #2,22, the main character is the formaldehyde, and the processes collected in this group are photocatalysis and adsorption. Formaldehyde is an indoor pollutant of great concern, due to its carcinogenicity. However, in literature are reported both cases of photocatalytic oxidation of formaldehyde, conducted by TiO_2, both cases of photocatalytic air purifiers in which the formaldehyde production was monitored.

Clusters #12,17 report the use of NTP (with and without catalyst) for the effective removal of formaldehyde and toluene.

To conclude, in the bottom right, a group containing the Clusters #13,15 collects publications about botanical filtration/phytoremediation. In order to have a straightforward visualization of the trend of the previously cited groups, Figure 20a reports the number of publications during the considered period. It is possible to observe a dramatic growth of publications about TiO_2-photocatalysis, starting from 1998, reaching a maximum in 2007 and, then, a decrease. A similar trend is for the Bi-based catalyst, but no publications were found before 2002.

NTP is a relatively new control technique, the interactions are more complex and it is less interdisciplinary if compared to the PCO. It started in 1998 and an average of 10 publications for year were found. To conclude, phytoremediation and botanical

filtration were studied only recently (1997). Figure 20-b reports the extracted term by the article analysis; the font size is proportional to the single word occurrence.

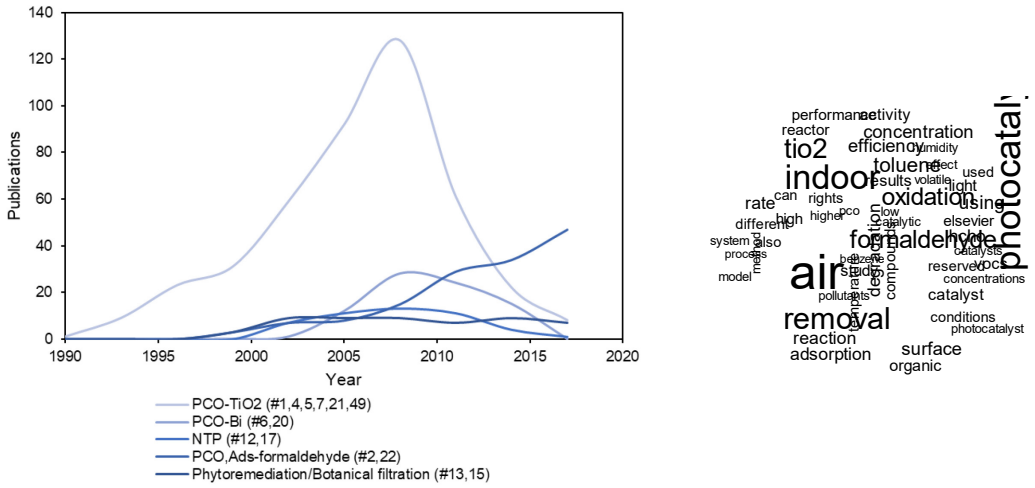

Figure 20 *- a) Publications occurrence by year in different research areas. b) extracted term from the publication abstract, title, and keywords.*

1.2.4 Discussion

In this paragraph, after listng the most widespread technologies for the control of the IAQ, a comparison between the patent and the scientific literature has been made. It is possible to report a few observations:

- Filtration and adsorption have always been the leading technology to remove particles, widely reported in the patent literature; however, as a well-established technique, not many advances are reported in the recent scientific literature;
- In the scientific literature, photocatalysis has been subjected to tremendous growth until 2010, followed by a decrease. However, photocatalysis (alone or coupled with other processes), in patents literature, accounts for less than 10%. This aspect reflects how the photocatalysis cannot be considered a mature technology;
- The coupling of a PC with an adsorbent material is of current interest;
- Botanical filtration and phytoremediation (often coupled with adsorption) are a novel alternative to traditional IAQ control technologies, found both in the patent and scientific literature.

Chapter 2:
Experimental

In this second chapter, a combined process for the removal of different pollutants has been described and studied. The simultaneous application, on-site, of three control technologies (adsorption, photocatalysis and electrostatic precipitation) enhance the process efficiency and lower the drawbacks of the singles.

- *In paragraph 2.1 an overview of the coupled processes and how the research has organized is provided;*
- *In paragraph 2.2, the effect of an external applied electric field (such as the one present in electrostatic precipitators) to an adsorbent, is described;*
- *In paragraph 2.3, the coupling of a photocatalyst with an adsorbent material is described;*
- *In paragraph 2.4, the coupling of photocatalysis with an external applied electric field is described;*
- *In paragraph 2.5, the application of the three processes simultaneously and locally has been studied.*

2.1 Introduction

The application of many control technologies, within a commercial air-purifier device, is a common technique to improve the efficiency of the process. The most common configuration is in a sequential manner, in which the first process (i.e., filtration) is followed by the second process (i.e., adsorption), and so on. This type of configuration, even if simpler, may results that each stage may lose efficiency differently, leading to a not-perfect synergy and a higher pressure drop across the device, which turns in a more powerful mechanical air extraction system (and higher electrical consumption).

In literature, there are many examples of synergies coming from the coupling of, at least, two processes. Among these, one of the most investigated is the coupling of a photocatalyst with an adsorbent material, with the aim of enhancing photocatalytic activity by increasing the concentration of the target pollutant in the vicinity of the catalyst. The confinement of a plasma in the proximity of a catalyst is, as well, an emerging technique with the aim of increasing the mineralization rate of gaseous pollutants. The highly ionized gas is produced by high voltage electrical discharges, such as dielectric barrier or corona discharges, which also produce ozone and other radicals. The application of an electric field to an adsorbent, in the air, has never been deeply investigated; while there are few references in which technical adsorbents were treated with ozone, or other oxidizing species, in order to alter the surface functional groups.

2.1.1 Synergies and the "hybrid" process

Each pollution control technique has pro and cons; by the simultaneous application of two processes, different synergies can develop. For instance, the harmful excess ozone, generated by a corona discharge, may enhance the photocatalytic activity of a photocatalyst by increasing the production of •OH radicals [93] or modify the surface functional groups of an absorbent [108,109]. Anyway, the same synergy may be considered positive or negative: the change of surface functional groups may "regenerate" the adsorbent for certain pollutants and inhibit the adsorption of others. Few synergies may be applied to the different system (air and liquid), while others are strictly related to a specific one (e.g., the "electrosorption" requires the presence of a solvent in which ions are migrating).

For these reasons, the simultaneous application of two processes can be named accordingly the type of system considered, the configuration and the intended purpose. Figure 21 report a scheme in which are reported the terms adopted in literature to describe the coupled process under investigation.

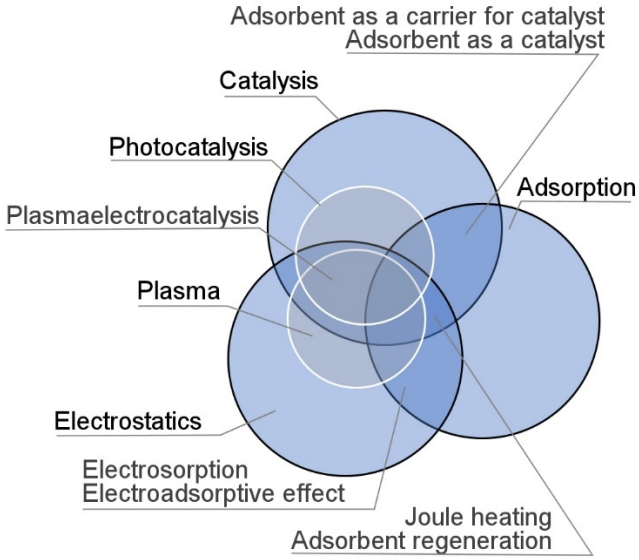

Figure 21 *- Terminology found in the literature to describe the coupled process under investigation*

2.1.2 Current work

Firstly, given the lack of information in the literature about coupling an adsorbent material with an external applied electric field (Ads+ESP), the coupled process was investigated. Technical and unconventional adsorbents were tested in order to highlight how the electric field affects the kinetic of adsorption of a selected volatile organic compound. Then, relying on these test results, the two best-performing adsorbents were selected, and they were coupled with a photocatalyst, under different deposition methods (Ads+PCO). Jointly, the study of the effect of an electric field applied on a photocatalyst has been carried out (ESP+PCO).

The roadmap about the conducted investigation is briefly reported in Figure 22.

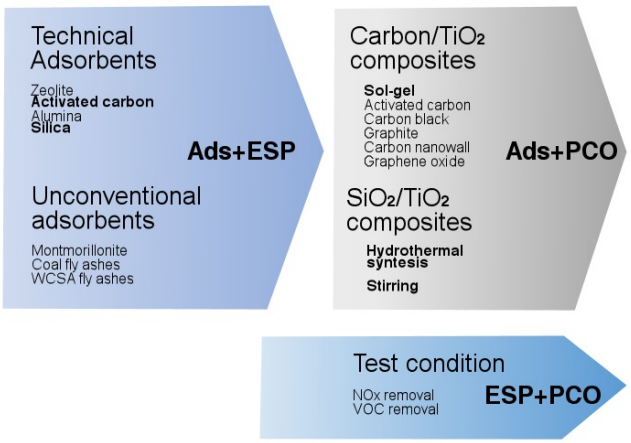

Figure 22 *- Roadmap of the conducted work.*

Adsorption is a consequence of the surface energy. The existence of electrostatic bonding means that the presence of an external electric field may affect the adsorbate/adsorbent interaction. Nevertheless, this aspect has been poorly studied in the literature, except for the use of non-thermal plasma or corona discharge for the modification of the adsorbent. The main findings in this section are:

- *the positive corona, formed at the discharge electrode, generates ionized and active species which interact both with the sorptive in the gas phase, both on the surface, with the adsorbed species (Section 2.2.3.1);*
- *the adsorbent is modified by the ionized gas(Section 2.2.3.2);*
- *the ionic wind, produced by the corona discharge, affect the transport of the sorptive towards the adsorbent, resulting in more efficient adsorption kinetic (Section 2.2.3.3).*

2.2 Adsorption and Electrostatic

2.2.1 Introduction

As the term “adsorption” is defined by the IUPAC as “An increase in the concentration of a dissolved substance at the interface of a condensed and a gaseous phase due to the operation of surface forces,” it is impossible to think that an alteration of the distribution of the surface charges of the adsorbent, due to the external-applied electric field, may not impact the adsorption process. As well, the generation of “active species and radicals may play a role in the adsorption or/and in altering the adsorbent characteristics.

2.2.1.1 Electrosorption

In 1989 Grevillot defined “electrosorption" as the reversible adsorption or the reversible retention of ions, molecules, or particles from a liquid phase on or near an electronic conducting surface as a function of the electric potential difference between the surface and the liquid [110]. From this first definition, which was related only to the liquid-solid adsorption, Su and Hatton broaden the definition to all those phenomena in which this surface-binding process is promoted or aided by the presence of an electrical field [111]. However, while this definition seems to cover every scenario in which a polarization of a conductive substrate (due to an application of an electrical current) induces an attraction of oppositely charged species to the surface, a literature research highlights that this process is mainly used in capacitive and pseudocapacitive deionization for separation [112–115], and energy storage [116,117]. Other applications are the removal of dangerous contaminants such as organic ions and heavy metals, or for enhanced liquid chromatography sensing techniques [118]. The scope of application of electrosorption is, therefore, closely linked to the presence of a liquid phase and a solid phase.

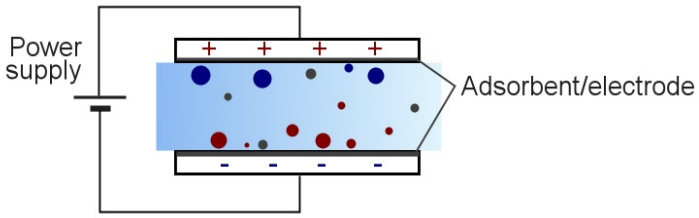

Figure 23 *- Schematic of the electrosorption process*

Difference between electrosorption and adsorption from the gas phase are well described by Gileadi [119], Bockris [120] and Chue [121]. Table 16 briefly reports these differences. However, this term has never been used to define the phenomenon in the gas phase. The main reasons are because the air is not electrically conductive and the species in the electrodes are barely adsorbed and not solvated. However, in case of a weakly-ionized plasma, the charged species in the air gap between the electrodes can conduct electricity, and the electric field may displace molecules previously adsorbed.

Table 16 *- Differences between gas-phase adsorption and electrosorption.*

	Adsorption from gas-phase	**Electrosorption**
Adsorbent surface	Bare	Solvated
The standard free energy of adsorption	Higher	Lower
Potential difference at the interface	Is constant	Can be varied
Adsorbent	-	Electrically conductive
Solute	-	Electrically conductive

2.2.1.2 Electroadsorptive effect

Not to be confused with the previous term, the electroadsorptive effect consists of applying an external electric field to the sensitive layer of a semiconductor gas sensor, in order to alter its sensing behavior.
When an electronegative molecule approaches the surface of a thin metal conductor, the free electrons are attracted from the solid surface. A fortiori, if dealing with a semiconductor (such as activated carbon) which has a lower number of available displaced charges, the thickness of the layer involved by the electrostatic attraction will be larger, and, the electrical conductivity, will be lower. This change in the electrical performance of the semiconductor is the fundamental operation of the metal oxides (MOS) gas sensors. If the described system is placed between an electric field, induced, for instance, by applying a voltage between two electrodes, the field may force the electrons towards (or in the opposite way), the (semi)conductor surface, decreasing (or increasing) the adsorption of certain gas species [122]. The application of this idea in gas sensing applications was firstly described by Wolkenstein [123] in 1960 but, up to nowadays, no application, exploiting the same principle, has been reported regarding pollution control technology.

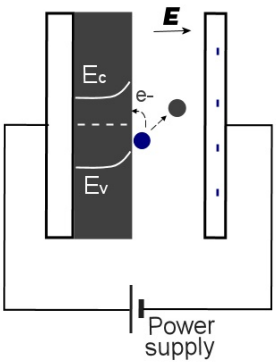

***Figure 24** - Schematic diagram of the electroadsorptive effect. Adapted from [122]*

However, few examples are reported in the literature in which an electric field is applied to a carbonaceous adsorbent material (Table 17), but with different purposes. It is interesting to notice that the main purposes of those studies are different, as well as the main findings are sometimes contradictory and an unequivocal explanation of the phenomenon has not yet been produced. For these reasons, this chapter will focus mainly on providing greater insight of the possible occurring physical phenomena.

2.2.1.3 By-products generation

Air consists of a mixture of oxygen (O_2) and nitrogen (N_2). When air is overstressed electrically, the oxygen molecule is split into O, and it becomes very chemically reactive [124]. Electron-impact reactions mainly occur in the corona plasma region. However, produced radicals may be transported outside of the corona plasma region.
The atoms can combine into O_2 or ozone, and if the electrical stress is very high, the oxygen enters chemical combination with the nitrogen, forming nitrogen oxides.
An exhaustive list of reaction mechanisms for ozone and nitrogen oxides production in positive corona discharges has been compiled by Chen et al. [125] but, by way of simplification, we can summarize the overall reaction in several steps. The initial step for the formation of O_3 and NO_x is given by the dissociation of molecular O_2 and N_2 by electron impact:

$$e + O_2 \rightarrow O + O + e$$
$$e + N_2 \rightarrow N + N + e$$

Then, the atomic nitrogen reacts with O_2 and O_3 to form NO:

$$N + O_2 \rightarrow NO + O$$
$$N + O_3 \rightarrow NO + O_2$$

moreover, NO_2 is formed by the further reaction of NO:

$$NO + O_3 \rightarrow NO_2 + O_2$$

thus, different forms of nitrogen oxides are expected to form, only NO and NO_2 were monitored in our study.

***Table 17** - Summary of publication in which an electric field was applied to a carbonaceous adsorbent material*

Objective	Coupled process		Main findings	Author	Ref
Regeneration of GAC exhausted with acid orange 7	Adsorption/ DBD plasma	Activated carbon (GAC)	• Decrease of surface area of GAC • O_2 is favorable for the regeneration of GAC	Qu et al. 2008	[126]
p-nitrophenol degradation by the simultaneous operation of AC and electrocatalysis in a single reactor sparged with O_2	Electrocatalysis/ adsorption	Activated carbon (AC)	• Formation of AC microelectrodes under the EF. • AC acted not only as adsorbent but also as catalyst. • Partial electrochemical regeneration of AC adsorption capacity	Wu et al. 2004	[127]
SO_2 and NO adsorption using AC, followed by microwave radiation desorption	Adsorption/ microwave irradiation	Activated carbon (AC)	• SO_2 and NO are desorbed from AC under microwave heating • SO_2 and NO under microwave irradiating over AC are decomposed • AC is regenerated	Ma et al. 2012	[128]
The effect of an applied electric field on hydrogen physisorption isotherm on carbonaceous sorbents	Electric field/ Adsorption	Activated carbon (AC)	• Application of EF to enhance hydrogen adsorption • The enhancement is distinctive on Pt-supported carbon samples. • No enhancement of carbon samples only. • Effect due stronger interaction between electrical charges in AC and the dissociated hydrogen.	Shi et al 2010	[129]
Electronic structure calculations on how electric field influences the hydrogen adsorption on graphene.	Electric field/ Adsorption	Graphene	• A linear relationship between the EF intensities and chemisorption energies • The chemisorption energy values increased with the EF • The chemisorption bond distance did not show a significant change with the EF intensity.	Cab et al. 2015	[130]
Electric Field Swing Adsorption (EFSA) for CO_2 capture	Electric field/ Adsorption	Activated carbon pellet	• EF creates favored adsorption sites • Negative charges serve as electron donating centers on sorbent surface, driving the formation of dative bonds by supplying electron density to Lewis acid center	Finamore et al. 2011	[131]

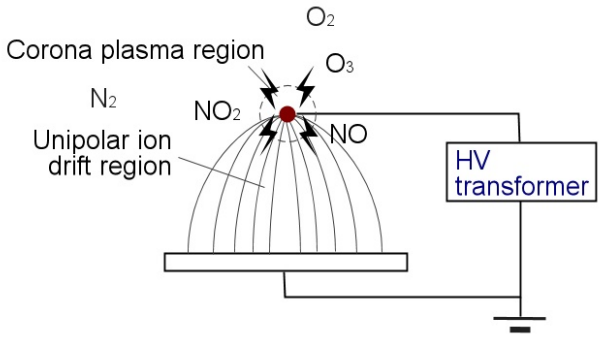

Figure 25 *- Schematic of the production of by-products by corona discharge*

NO_2 can be adsorbed on the activated carbon surface through a different mechanism: physisorption, chemisorption, and reduction; however, when NO_2 is adsorbed on carbonaceous materials, a significant amount of NO can be released [132]. The adsorbed species, once leached with ultrapure water, can be found in the form of nitrates and nitrites, which can be quantified using liquid ionic chromatography.

O_3, in low concentrations, can be effectively removed by activated carbon[133]. The ozonation of activated carbon is reported as a technique for modifying its surface functional groups (Paragraph 2.2.1.5).

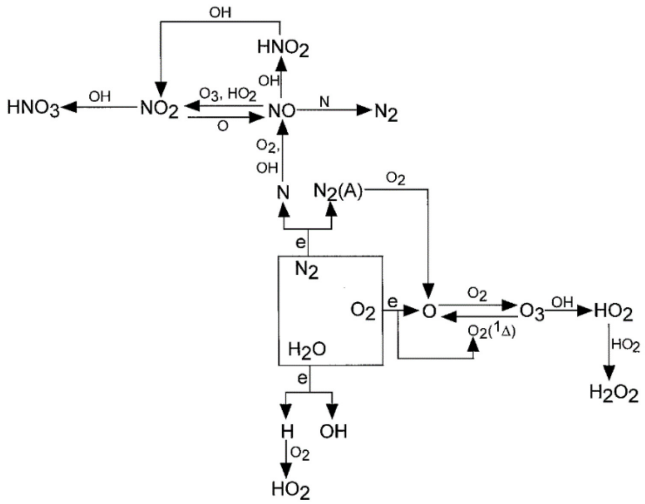

Figure 26 *- Atmospheric gas-phase corona-induced reaction. From* [134]

2.2.1.4 Electrohydrodynamic effect

The creation of electric wind due to the electrohydrodynamic force is a known effect due to the charged/neutral particles interaction in electrically charged fluids, which occurs in DC corona discharge and surface dielectric barrier discharge.

The electrohydrodynamic (EHD) phenomena, using a pair of asymmetrical electrodes having a potential difference of the order of few of kilovolts, was first studied by Brown in 1928 [135]. However, while the efficiency of such devices for moving air flow is few unit percents, EHD devices receive interest mainly because of the absence of moving parts and for their potential for miniaturization.

Numerical modeling of the electro-induced flow by a filamentary discharge electrode on a plate is a topic that has already been discussed in the literature [136–138].

The gas ions, formed in the corona discharge area, are accelerated by the electric field, which results in a drag force of the bulk fluid. An ionic wind, which includes neutral molecules, is formed. For the sake of simplicity, only three generic charged particles will be considered: electrons, positive ions, and negative ions.
The EHD flow generated by the positive corona discharge is described by the Poisson's equation, in which the electric field intensity, $\vec{E}$, and the electric potential V are related according to the Equation 2:

$$\vec{\nabla} \cdot \vec{E} = \nabla^2 V = -\frac{q}{\varepsilon_0} \qquad \textit{Equation 2}$$

In which q is the space charge density (C m^{-3}) and $\varepsilon_0$is the vacuum permittivity.
The electron density is then computed by solving the drift-diffusion equation for the electron density (Equation 3), with using the local field approximation (Equation 4), in order to relate the mean electron energy to the reduced electric field [139].

$$\frac{\partial \mathrm{n_e}}{\partial \mathrm{t}} + \nabla \cdot \overrightarrow{\Gamma_e} = \mathrm{R_e} \cdot (\vec{u} \cdot \nabla)\mathrm{n_e} \qquad \textit{Equation 3}$$

$$\varepsilon = \mathrm{F}\left(\frac{\mathrm{E}}{\mathrm{N}}\right) \qquad \textit{Equation 4}$$

The EHD force acting on the neutral gas can be approximated, according to the Boeuf approach [140], by the following equation

$$\mathbf{F} = \mathrm{e_0}\left(\mathrm{N_p} - \mathrm{N_n} - \mathrm{N_e}\right)\mathbf{E} \qquad \textit{Equation 5}$$

In which N_i is the i-charged species density, e_0 is the elementary charge, towards the same direction of the electric field.
When charged molecules, generated in the corona plasma region, are accelerated by the electric field and gain kinetic energy, due to their collision with other neutral species, their momentum is transferred to the adjacent molecules, resulting in a bulk gas flow.

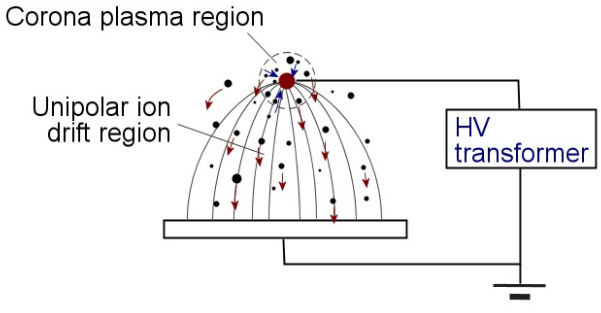

***Figure 27** - Schematic of the generation of ionic wind by corona discharge*

In particular, according to Boeuf [140], electric wind velocity increases with the square root of both the electrode gap and the discharge current, according to Equation 6:

$$v_G = D\sqrt{\frac{dI}{\mu}} \qquad \textit{Equation 6}$$

Where d is the electrode gap, I is the discharge current, μ is the ion mobility and D is a constant. This simplified equation is valid for the hypothesis that the cross-section area of the corona discharge and the gas density are constant.
The discharge current is then evaluated as follows [85]:

$$I = CV(V - V_0) \qquad \textit{Equation 7}$$

Where V is the applied voltage, V_0 is the onset voltage and C a constant depending on the electrode geometry and ion mobility. The corona onset voltage is the lowest voltage at which continuous corona occurs, and it is described by the Peek's law. Equation 7 highlights that the discharge current increases in a quadratic manner with the applied voltage. The wire electrode thickness also affects the electric wind velocity. Debien [141] showed how decreasing the wire radius it is possible to attenuate the presence of micro-discharges on the wire, inducing an increase in the maximum electric wind velocity.

2.2.1.5 Adsorbent modification

Few authors suggested that it is possible to enhance the adsorbability of activated carbon by surface modification. Alongside traditional methods of modification, dielectric barrier discharge [142,143] and ozonation [108,144] have been used as well to introduce functional groups on the surface. The surface of carbonaceous materials, reacting with O_3, may obtain many oxygen-functional groups, such as: -OH, -CHO, -COOH, CO. These groups are characterized by a high polarity, which involves a higher adsorption capacity of polar adsorbates. Deitz [145] studied the rate of adsorption of water vapor by ozone-treated activated carbon, and he attributed the enhanced kinetic to the formation of highly-polar sites on the carbon, although the BET area decreases.

2.2.2 Materials and methods

2.2.2.1 Adsorbents

Technical and unconventional adsorbents

Different technical and unconventional adsorbents were characterized and studied, in order to study the coupled processes with different materials having different properties and to find the best candidates regarding cost, efficiency, and stability. For these reasons, technical and widely adopted adsorbents, such as activated carbon (AC), silica (S), alumina (A), zeolite (Z) and unconventional ones, as montmorillonite (M) and fly ashes (FAC, from coal burning and FAB, from biomass burning), were investigated.

The list of the adsorbent is reported in Table 18. The different composition between the two fly ashes is reported in Table 19. The main difference is the amount of aluminum oxide, which is expected to affect the electric property of the fly ashes.

Table 18 *- List and reference of the adsorbent investigated*

Adsorbent	Brand (producer)
Activated carbon	205 E (BMD), from mineral coal
Silica	Silica gel 60A 6 - 35μm (Carlo Erba Reagents)
Alumina	Activated basic alumina (Jansen Chimica)
Montmorillonite	Montmorillonite KSF (Fluka Chemie)
Coal-Fly Ashes	From coal [146]
Biomass-Fly Ashes	From wood, corn stover, and corncob ash (WCSA) [147]

Table 19 *- Fly Ashes oxide composition comparison (%)*

FA type	Na	Mg	Al	Si	P	S	Cl	K	Ca	Fe
WCSA	5.6	4.0	8.2	39.9	3.3	6.0	2.6	7.1	16.5	5.0
Coal	0.1-06	0.2-3	22-36	36-52		0.2-2		0.2-2	1-10	2-10

All the tested materials were grinded, and the material passing through a 0.42mm sieve was dispersed in deionized (DI) water, sonicated for 15 minutes, coated on a 50x100mm glass slide and dried under an IR lamp.

Activated carbon cloth (ACC)

Air filtration and adsorption require good control over the containment of the adsorbent material, and the use of activated carbon clothes meets this requirement [148]. Moreover, ACC is ubiquitous, and it is used in the automotive sector, in kitchen hoods, and aircraft.

Two activated carbon clothes (ACC), commercially available, were tested. If not otherwise indicated, the sample used for all tested materials was provided by Purification Products Limited. For few tests, ACC was provided by Rema Filtration. Their characteristics are reported in Table 20.

Table 20 *- Activated carbon fiber clothes characteristics.*

Parameter	Rema Filtration	Purification Products Limited
Specific weight	280 g/m^2	280 g/m^2
Thickness	17 mm	13 mm
Average particle diameter		352 μm
Carbon content (w/w%)	32%	44%
Carbon *BET surface area*	n.a.	400 m^2/g

Chemicals and reagents

All of the organic compounds used (Acetone, Acetaldehyde, Benzene, Cyclohexane, Ethanol, Methyl Ethyl Ketone, Toluene, 1-Propanol) are of a lab-grade purity and were purchased from Carlo Erba reagents S.A.S. These selected compounds have been chosen as representative for common organic pollutants.

2.2.2.2 Apparatus

Experimental setup

The test apparatus consists of a sample holder, on which the adsorbent specimens takes place (Figure 28), positioned inside a 13-L box with borosilicate glass walls. To a thin (180 µm diameter) tungsten wire electrode (discharge electrode) it has been applied a positive potential, whereas the opposite electrode (collector) is earthed by two grounded connections at the ends of the activated carbon cloth sample, or the glass is placed over an aluminum plate. A fan, with trough apposite deflectors, induces an air flux parallel to the sample (direction 1). The applied electric field yields a driving force to the charged particles and a vertical velocity component in the direction of the potential gradient (direction 2).

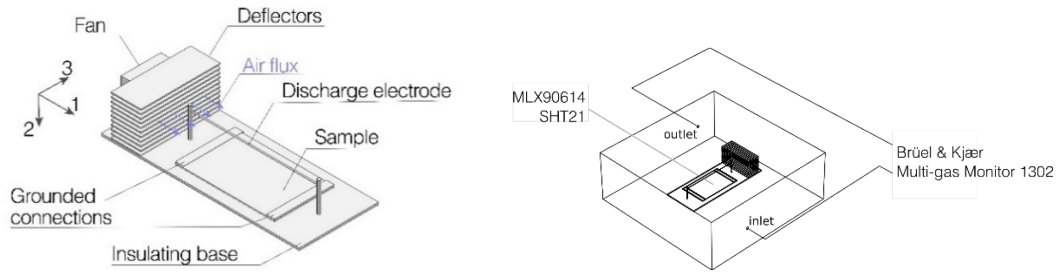

a) b)

Figure 28 - *(a)The sample holder for the experimental setup. (b), the full test apparatus is reported. The selected compound is injected between the outlet and the fan.*

Inside the glass box, temperature and relative humidity are monitored (R.H. = 59 ± 6% T = 24 ± 2 °C) through a SHT21 (±0.3 °C ± 2%) sensor. Sample temperature is also monitored by using an MLX90614 IR thermometer (±0.5 °C) (Melexis NV, Ieper, Belgium).
Air velocity measurements were conducted using a hot wire anemometer and a metal net instead of the sample. The anemometer was placed under the metal net, in order to measure the intensity of the ionic wind toward the sample, as a function of the applied electric field and fan speed.

For evaluating the VOC adsorption kinetic, an initial amount of 0.33 mmol was injected into the test box is. Data collection starts 30 s after the initial injection, in order to account for its full vaporization.

Determination of water vapor adsorption isotherms

Water vapor adsorption is a standard characterization method, in which the partial pressure of water vapor is varied, and the adsorbed mass measured. By using an appropriate model, such measurements make possible to estimate the internal surface area and the pore size distribution, by the hysteresis between adsorption and desorption isotherms.
From the desorption isotherm, it is possible to estimate the cumulative pore volume and surface area, by means the Kelvin equation [149,150]:

$$RT \ln \frac{P_0^K}{P_0} = -\frac{2\gamma V_m}{r_C} \qquad \textit{Equation 8}$$

Where the constant $2\gamma Vm/RT$ is 1.05 nm for Water (γ = 0.072 N/m, Vm = 18 cm^3/mol) at 25◦C.
Adsorption isotherms of tested samples were carried out in a constant temperature and humidity glass desiccator. The humidity was controlled by using a set of saturated solutions of salts. Humidity and temperature were recorded continuously by using an SHT21 (Sensirion) digital temperature sensor. Before each test, samples were dried at 105°C in an oven for 4 hours. Weights of the samples were recorded every 24h by an electronic balance with an accuracy of 0.00001g.

SEM and EDX analysis

Sample morphology was investigated by Scanning Electron Microscopy (SEM), using a ZEISS 1530 SEM, equipped with a Schottky emitter, with two different secondary electrons (SE) detectors (the in-lens and the Everhart-Thornley), operating at ten keV, coupled with an energy dispersive microanalysis (EDX).

Boehm titration

The Boehm titration [151] is a technique that allows quantifying acidic or basic functional groups on the surface of activated carbons. This method is supported by the existence of oxygen surface groups having different acidities that can be neutralized by bases having different strengths, like $NaHCO_3$ (pKa = 6.4), Na_2CO_3 (pKa = 10.2) and NaOH (pKa = 15.7). In ascending order of strength, $NaHCO_3$ neutralizes only the carboxylic groups, Na_2CO_3 neutralizes the lactonic and carboxylic groups, and NaOH neutralizes the phenolic, lactonic, and carboxylic groups.
Two samples of activated carbon cloth were exposed for one hour in the apparatus previously described, with an applied potential of, respectively, 3 and 7kV. The method adopted follows the procedure described by Kim et al. [152]. Briefly, each sample was divided into smaller pieces, and two of these (weighing approximately 60mg) were weighted and placed in a flask with a 10ml of an alkali solution (0.1M). Then, the flasks were sealed and sonicated for 10 minutes, and an aliquot of 10 mL from the sample solution was taken and titrated using 0.1M HCl.

Raman Spectroscopy

The Raman spectra were obtained with an integrated confocal micro-Raman system with a LabRam Aramis (Horiba Jobin Yvon) 460 mm spectrometer equipped

with a confocal microscope. The light source was a laser emitting green light diode at 532 nm with 50 mW power.

FTIR analysis

Infrared spectra were collected at room temperature with a GX1 Perkin Elmer spectrophotometer, coupled with Autoimage microscope and U_ATR accessory (SensIR Technologies) for measurements in Total Attenuated Reflectance Acquired spectra were elaborated with Spectrum 5.3 by Perkin Elmer.

Electrical impedance measurement

Microporous carbons are capacitors, so they are used to store electrical energy if coupled with electrolytes. For this reason, a classical impedance meter is usually not convenient for measuring resistance (except if it has a very high internal impedance) because the capacitor is charging during the measurement. The I-V curves of the ACC were acquired in AC mode, by a Reference 3000 (Gamry) potentiostat, in the 10^5-10^1 Hz range, with 100mV rms. Measurements were taken at room conditions (temperature equal to 27°C and relative humidity equal to 70%), in the air, by directly attaching the electrodes on Hoffman clamps at both ends of a 2x3cm ACC sample.

O_3, NOx, VOC, CO_2, CO concentration measurements

Air samples inside the box were collected and analyzed every 3 min by an automatic photoacoustic transducer system (Brüel and Kjaer Multi-gas Monitor Type 1302, Nærum, Denmark) equipped with UA0982, UA0984, UA0987, SB0527 filters, in order to determine concentrations of VOC, CO_2, CO, and water vapor.
To monitor the ozone concentration, a UV Photometric Ozone Monitor (API Ozone Monitor Model 450) has been used, while NOx concentrations were determined using a chemiluminescent analyzer (Monitor Labs, Nitrogen oxides analyzer model 8841).

Determination of the adsorbed ions

To determine the amount of nitrites and nitrates adsorbed, the sample was placed into an airtight container with approximately 40 mL of ultrapure water and subsequently mixed for 24 h on a suitable rotary shaker (Heidolph Reax 20, Schwabach, Germany), at a speed of 4 min^{-1}. Then, the aqueous solution was analyzed by liquid ion chromatography (IonPac Dionex AS23 Anion-Exchange Column, Waltham, Massachusetts) in the first three hours subsequent the extraction with water.

2.2.2.3 Data elaboration

The process efficiency is correlated with the kinetics of adsorption, described by several mathematical models, which can generally be classified as a reaction or diffusion models. In the diffusion model, it is possible to distinguish three subsequent steps, that are assimilated in few parameters into the reaction model. The adoption of a model has to be justified not only from a “goodness of fit” point of view but also from the adsorption process mechanism [153]. The classification of adsorption kinetic models is reported in Figure 29.

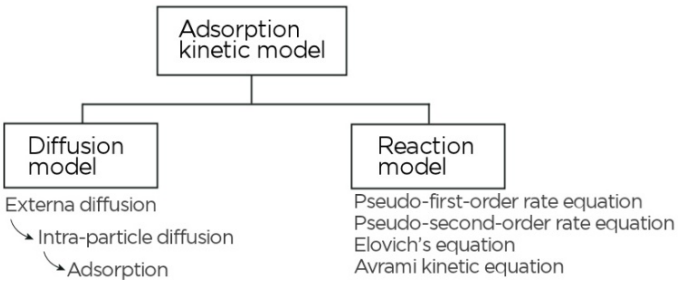

***Figure 29** - Classification of the kinetic model of adsorption*

In this work, a pseudo-second-order kinetic, [154,155] was adopted to fit the experimental data. The linearized equation is the following:

$$\frac{t}{q_t} = \frac{1}{h} + \frac{1}{q_e}t \qquad \textit{Equation } 9$$

where q_e is the amount of adsorbate (mg cm^{-2}) at equilibrium, q_t is the amount of adsorbate (mg cm^{-2}) at any time t, and h is the initial adsorption rate (mg cm^{-2} min^{-1}) as q_t/t approaches 0. In Equation 9, the pseudo-second-order model constants can be determined experimentally by plotting $\frac{t}{q_t}$ against t.

In order to quantify the enhanced kinetics of adsorption in the presence of an electric field, ε, the differential kinetic removal index has been introduced. It accounts for the different rate of adsorption with and without the application of the electric field. It is evaluated as follows:

$$\varepsilon = \frac{h_{HV} - h_{ads}}{h_{ads}} \qquad \textit{Equation } 10$$

2.2.3 Results

2.2.3.1 By-products generation

Table 21 shows the amounts of nitrogen as nitrites and nitrates accumulated on the adsorptive sample, resulted from the analysis of the sample leaching liquor, and the amount of nitrogen dioxide and ozone generated during the test at various electrical potential applied.

***Table 21** - Nitrites and nitrates in the ACC extraction liquor and NO_2, O_3 concentration in air during 90min of test*

Applied voltage	Extracted liquor		Air	
	NO^{2-}	NO^{3-}	NO_2	O_3
kV	µmol	µmol	µmol	µmol
0	0.00	0.00	0.02	0.00
3	0.00	0.02	0.02	0.01
7	0.25	0.24	0.14	0.07
11	0.69	0.17	0.35	0.41

It is possible to observe from Table 21 that, by increasing the applied electrical potential, the concentrations of ozone and nitrogen dioxide generated within the test box increases, jointly with the amount of nitrites and nitrates found in the leached ACC sample liquor.

However, the adsorption of some species generated by the corona-discharge, (as NOx, initially present in environmental concentrations) can play an important role into limiting the capacity of the adsorbent, while ozone may introduce functional groups on the adsorbent surface.

2.2.3.2 Adsorbent modification

SEM morphology

The SEM pictures of the untreated and treated ACC are shown in Figure 30. It is observed that the surface of the ACC after the process is similar as it was before the application of the electric field.

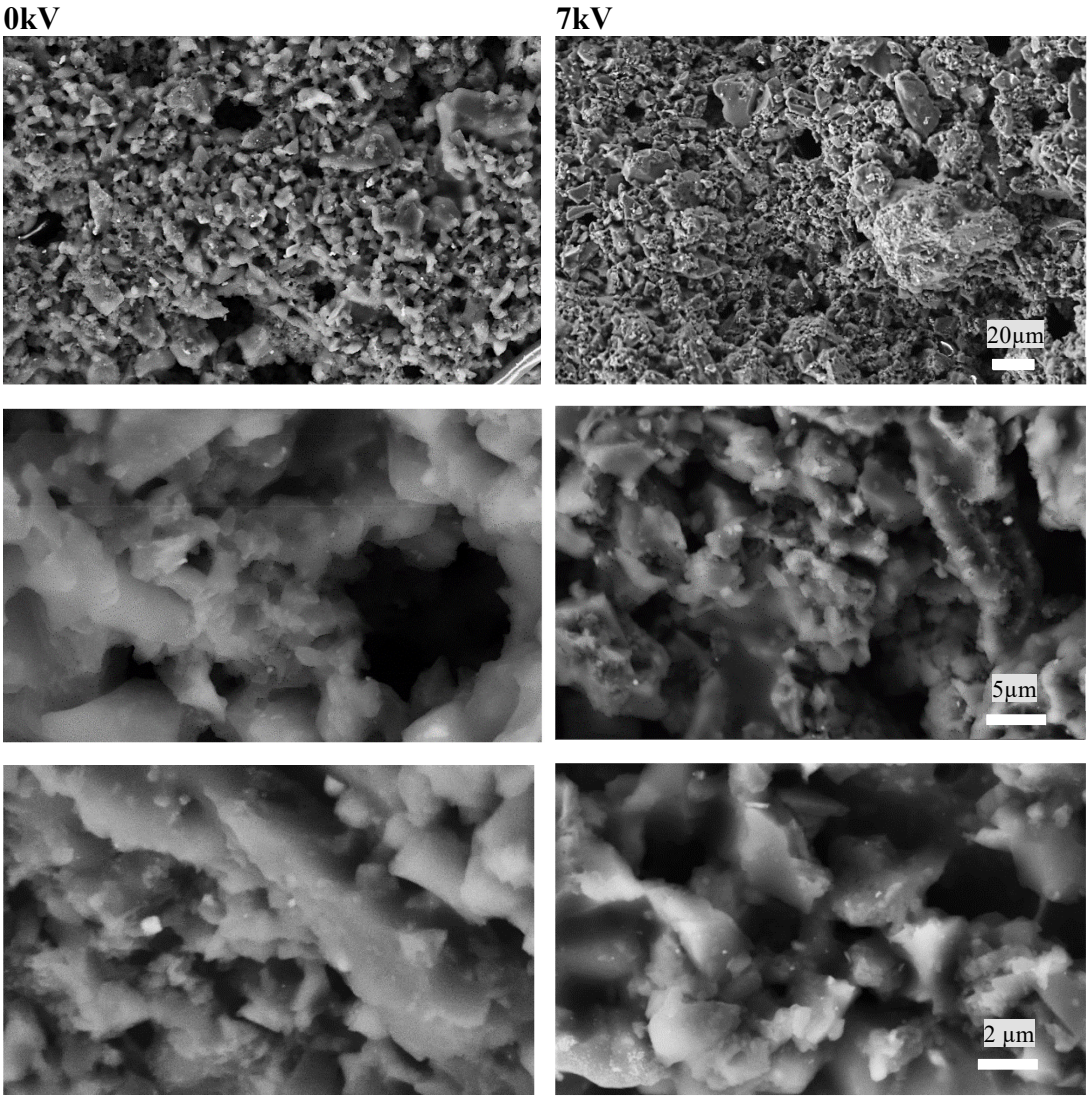

Figure 30 *- SEM pictures of the ACC before and after the application of 7kV for 3 hours*

Kodama [143] reported that activated carbon was etched by the DBD treatment: while the total surface area was decreased, a little increase in macropore was observed, while for Srinivasan et al. [156] functionalization does not affect the morphological properties of the activated carbon but it only increases the functional groups on its surface. This is in accordance with our results, where it is difficult to distinguish a clear difference in the morphology between the activated carbon sample before and after the application of the electric potential to the discharge electrode.

Boehm titration

The functional groups present on the ACC surface are involved in acid-base equilibrium. According to the data reported in Table 22, regarding the content of surface oxygen groups obtained to the Boehm's method, it is shown that the pristine ACC does not contain carboxyl groups and that the total number of the acidic group increases with increasing the applied potential.

Table 22 *– Functional groups determined by titration*

	Amount [mmol g^{-1}]		
Functional group	**0kV**	**3kV**	**7kV**
Carboxylic	0.0	22.8	14.5
Lactonic	0.0	2.3	11.8
Phenolic	51.0	47.3	60.6
Total acidic groups	51.0	72.3	86.9

The amount of phenol functional groups constitutes approximately a half of the total amount of all functional groups; carboxylic and lactone are found in the treated samples only

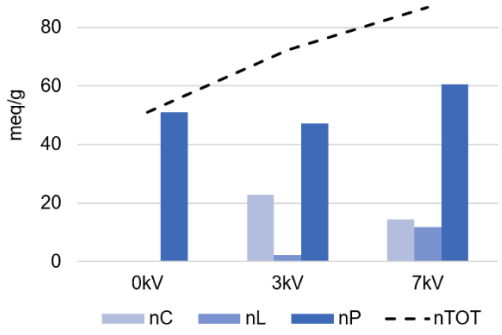

Figure 31 *– Amount of functional groups determined by titration*

Electrical resistivity

The module of the complex impedance, measured at different frequencies, is reported in Figure 32.

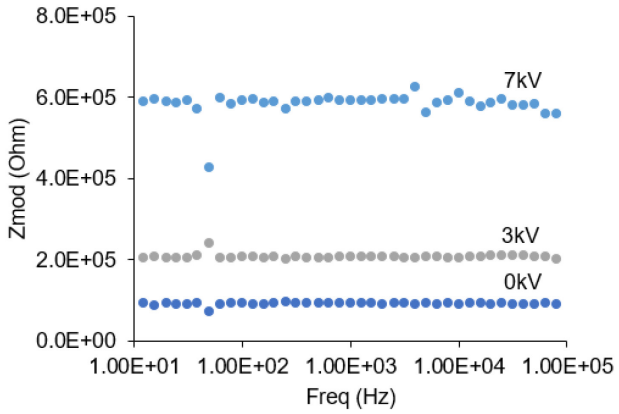

Figure 32 *– Impedance module vs. frequency for the ACC samples, under different applied potential (0kV, 3kV, and 7kV).*

All ACC samples show only a resistive behavior in the 10-10000Hz range. The outlier at 50Hz is due to the interference with the electric line. Treated samples exhibit a purely resistive behavior and an increase of the electrical resistivity from 9.77 kΩcm to 24.0 kΩcm for the 3kV-treated sample and 62.7kΩcm for the 7kV-treated sample. This change can be attributable to the formation of functional groups that alter the electron mobility within the carbon structure.

FTIR analysis

Fourier Transform Infrared Spectrometry (FTIR) is a technique to obtain structure information of a molecule, due to the specific molecular vibrational spectrum. As some functional groups can be detected by FTIR spectroscopy, FTIR spectra of the synthesized ACC are presented in Figure 33. The spectra were acquired in the 500 – 3000nm interval, but only the 500-1750nm region has been reported.

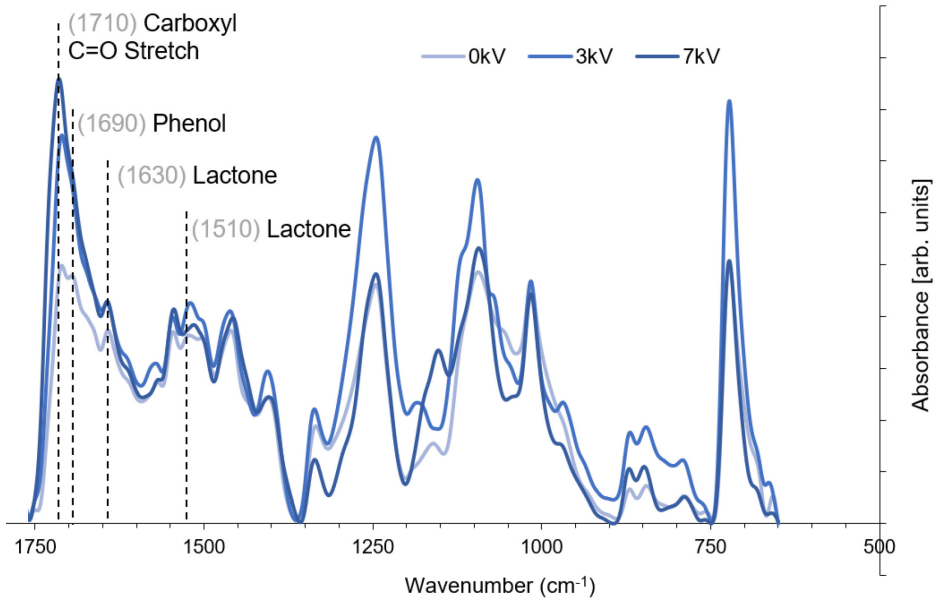

Figure 33 *- FTIR spectra of the ACC samples, under different applied potential (0kV, 3kV, and 7kV).*

Barkauskas and Dervinyte [157], investigated a batch of 20 different activated carbon in order to correlate the number of functional groups determined by Boehm titration with the peaks in the FTIR reflectance spectra. By comparing the obtained spectra with their results and with the available literature, it is possible to identify several peaks, which can be correlated with the acidic group, previously determined by Boehm titration. The peak at 1710 cm^{-1} is generally linked to a carboxylic C=O stretch, and it has been found to increase with the electric field intensity, as well as other smaller peaks at 1690 cm^{-1}, due to the phenolic groups and at 1630 and 1510 cm^{-1} due to lactone functional groups [157].

Raman Spectroscopy

Two main bands at ~1600 cm^{-1} and ~1350cm^{-1} are attributed to the G and D band of the carbon structure, respectively. In particular, Ferrari and Robertson have suggested that the G and D peaks are due to sp^2 vibration. In particular, the G-band is due to the bond stretching of all pairs of sp^2 atoms, while the D-band is attributed to the of sp^2 breathing modes of atoms in rings [158]. The sample subjected to the treatment shows the G-band shifted. A similar result was observed by Lota et al., who exposed an activated carbon to ozone [159]. This trend may be explained by the loss of C bonded in rings and the formation of chains due to the incorporation of oxygen and nitrogen atoms, which is consistent with the previous FTIR and Bohem titration results.

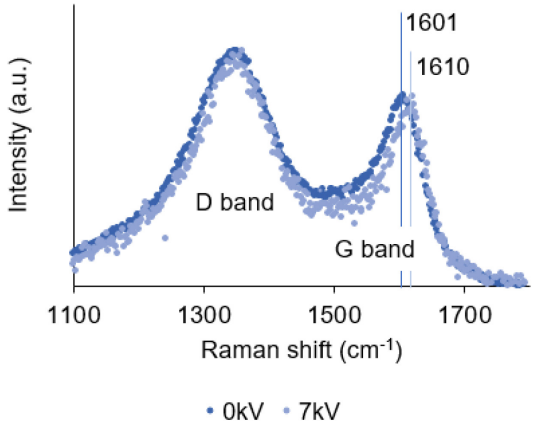

Figure 34 *– Raman spectra of the ACC samples, with and without the applied electric field*

The intensities ratio of the D and G bands, characteristics of carbonaceous materials, (I_D/I_G) is an important parameter to estimate the structural disorder of carbon sheets. The intensity ratios of the analyzed samples are 3.40, and 3.32 respectively. The lower I_D/I_G ratio of the treated ACC may suggest the amorphization of the carbon, as reported in the three-stage model reported by Ferrari and Robertson [158].

Table 23 *– Results of the peak fitting with Lorentzian function.*

	D band			G band			I_D/I_G
	Peak center	**FWHM**	**Height**	**Peak center**	**FWHM**	**Height**	
0kV	1345	199	1.58	1601	81	1.15	3.40
7kV	1348	184	1.60	1611	75	1.17	3.32

EDX analysis

Figure 35 shows the EDX results for the ACC specimens before and after the process. It is possible to notice a slight increase of the nitrogen amount, probably due to the adsorbed NO_2 (Section 2.3.3) and dissociated in nitrates, due to the moisture present in the sample, as the physical-only adsorbed species are likely to be degassed during the operation of the SEM-EDX apparatus. This trend is consistent with the amount of nitrogen-containing species leached by ultrapure water, previously reported in Table 21.

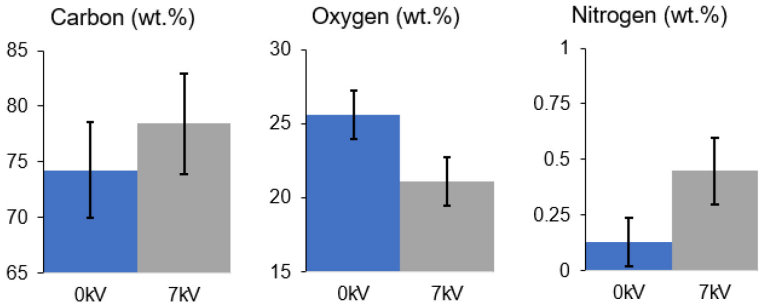

***Figure 35** - EDX results for the ACC before and after the treatment*

2.2.3.3 Enhanced transport of charged/neutral species

Effect of the ionic wind

Different horizontal air velocities (u) have been obtained by varying the voltage applied to the fan. In Figure 36 is reported the linear correlation between these two variables

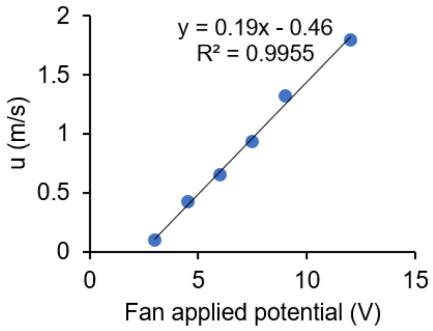

***Figure 36** - Correlation between the voltage applied to the fan and horizontal air velocity measured*

The vertical air velocity component (v) has been measured, just below where the sample is placed, by using at its place a metallic net as a grounded electrode. By varying both the fan speed, and the applied potential, measurements have been performed, and they are represented by the black dots in Figure 37. The surface is a piecewise cubic interpolant, normalized by the mean value of the two independent variables. It is possible to observe how the vertical velocity component depends on the intensity of the applied potential to the discharge electrode, but also the fan speed.

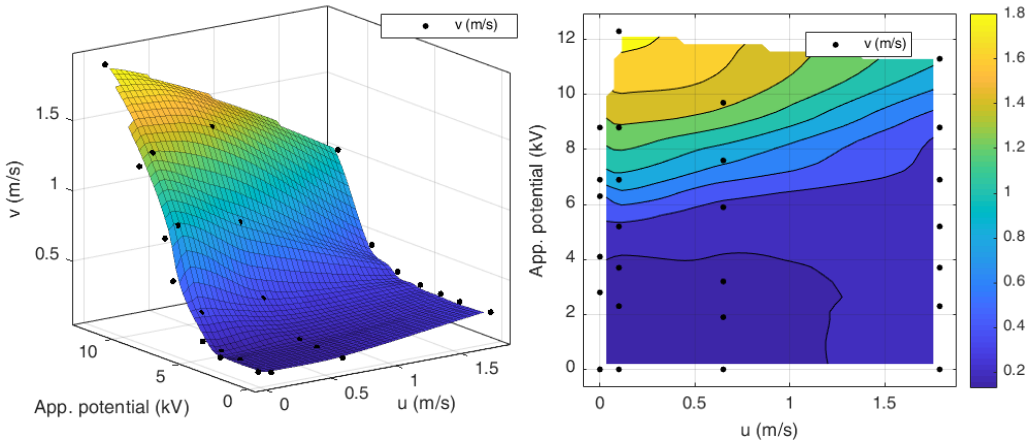

Figure 37 *- 3D fit (a) and contours plot (b) of the vertical wind speed, as both function of the horizontal applied speed and potential.*

In the absence of the horizontal air flux (with the fan switched off), or with a low speed, the experimental values of *v* follow the equation proposed by Boeuf (Equation 6). By merging Equation 6 with Equation 7, reported in Paragraph 2.2.1.4, it is possible to obtain Equation 11, which has been used to fit the experimental data:

$$v = \alpha\sqrt{V(V - V_0)} \qquad \textit{Equation 11}$$

In which α, the pre-square root factor, takes into account all the constants, and it depends on the electrode geometry, the ion mobility, the electrode gap, and V_0 is the corona onset voltage.

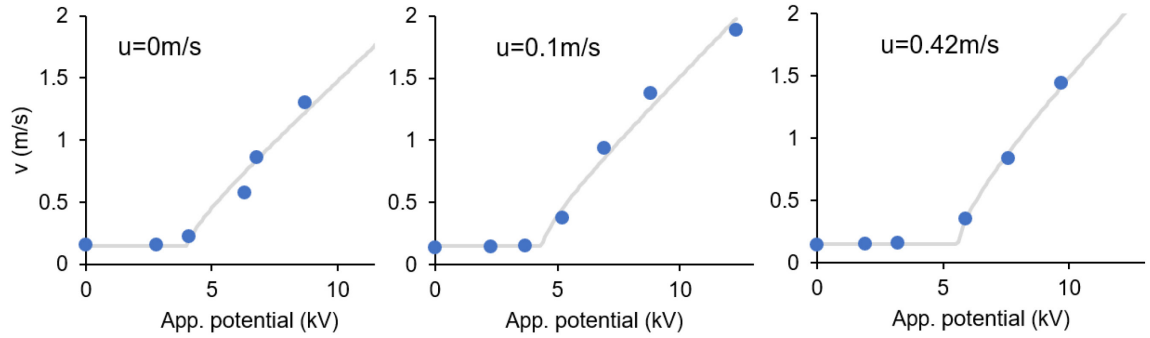

Figure 38 *- Experimental (blue dots) and fitted values (grey lines)*

Fitted values are reported in Table 24. Two trends are observable: a slight increase of the α and the corona onset voltage. The latter one, in particular, increases of about 2kV for an increase of the airspeed of 0.4m/s.

Table 24 *- Fitted values of the Equation 10*

u (m/s)	α	V_0 (kV)	R^2
0.00	0.19	3.84	0.9447
0.10	0.20	4.21	0.9714
0.42	0.22	5.50	0.9946

When the horizontal air velocity exceeds the 0.42 m/s, the transition between laminar and turbulent flow takes place. For flow over a flat plate, it is reported that transition occurs when Reynolds number should exceed 50,000. In the present case, the transition occurs earlier, at 11,200 because of the superficial irregularities presented by the metal grid. Similar behavior is expected to be present with the ACC, because of its high surface roughness. This aspect is also observed experimentally by the experimental points at a lower potential than the corona onset voltage ($V<V_0$), which possess a higher vertical velocity, even *a priori* the ionic wind formation, due to the turbulence eddy. In Figure 39 are reported the experimental data, at u=1.80m/s, and, on the background, is reported the fit at u=0.

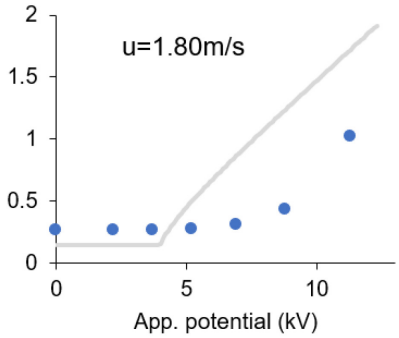

Figure 39 *- Comparison between the experimental data at u=1.8m/s (blue dots) and the fit at u=0 (grey line).*

Effect of the adsorptive

The differential kinetic removal index, evaluated by using Equation 10, in paragraph 2.2.2.2, was plotted against the specific heat of fusion of selected organic compounds. Figure 40 shows that the kinetics of adsorption of the organic compounds tested, under an external applied electric field, it is faster compared to the one in the absence of the electric field. This implies a positive ε, according to Equation 10.
A linear correlation fits the experimental data at different applied potentials, with the specific heat of fusion of the adsorptive; in particular, organic compounds having a low specific heat of fusion are more subject to such enhancement.

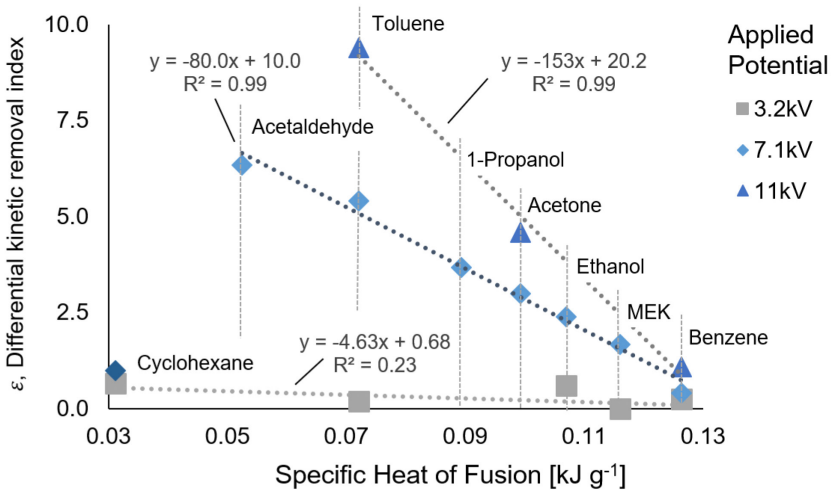

Figure 40 *- Plot of the differential kinetic removal index versus the specific heat of fusion of tested organic compounds.*

Considering a linear relation between the angular coefficient of the interpolant line and the applied potential, and by its substitution into the experimental relation found, the following interpolant function was determined and plotted in Figure 41.

$$\varepsilon(\lambda, \Delta) = a\lambda\Delta + b\lambda + c\Delta + d \qquad \textit{Equation 12}$$

Where λ is the specific heat of fusion, Δ is the applied potential and a, b, c, d are experimental coefficients. Cyclohexane kinetic at 7 kV was not included into the model. Fitted parameters are reported inTable 25.

Table 25 *- Fitted parameters for the Equation 12.*

Coefficients	Fitted value
a	−19.31
b	57.36
c	2.544
d	−7.394
Goodness of fit	
SSE*	1.336
R-square	0.9883

* The sum of squares due to error (SSE); § Root mean squared error (RMSE)

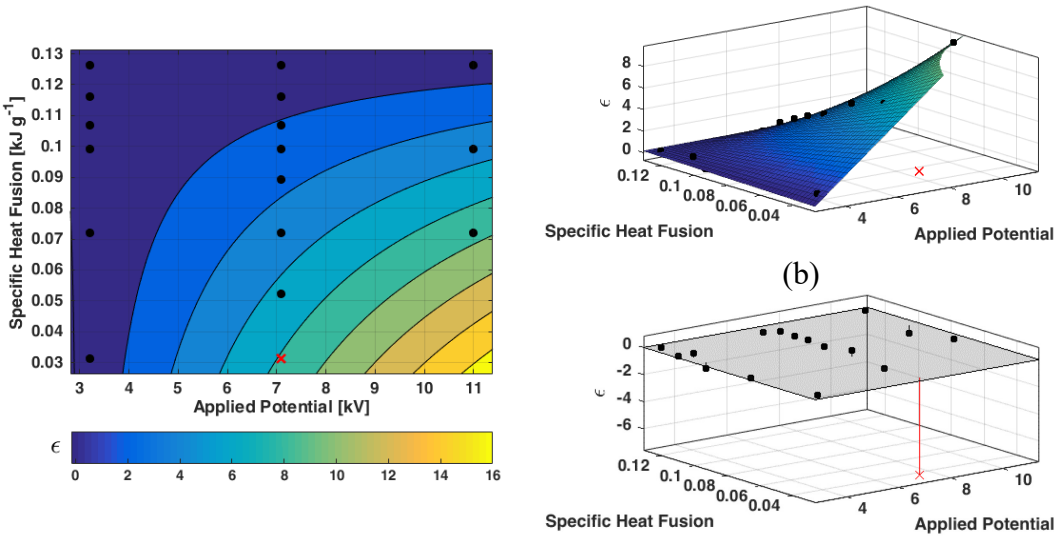

Figure 41 *- Fitted model; contour plot (**a**), main plot (**b**), residuals plot (**c**).*

In order to assess the long-term adsorption performance, in another test, the same amount of Methyl Ethyl Ketone (MEK, 30 µL) was injected inside the box every 60 min for seven times. Collected data were treated as previously described. Results are reported in Figure 42. Fitted parameters show that the adsorption rate under the electric field initially doubled the one without the electric field and decreased in subsequent tests (Figure 42-a). Moreover, the amount of adsorbate decreases slightly faster in the presence of the electric field (Figure 42-b).

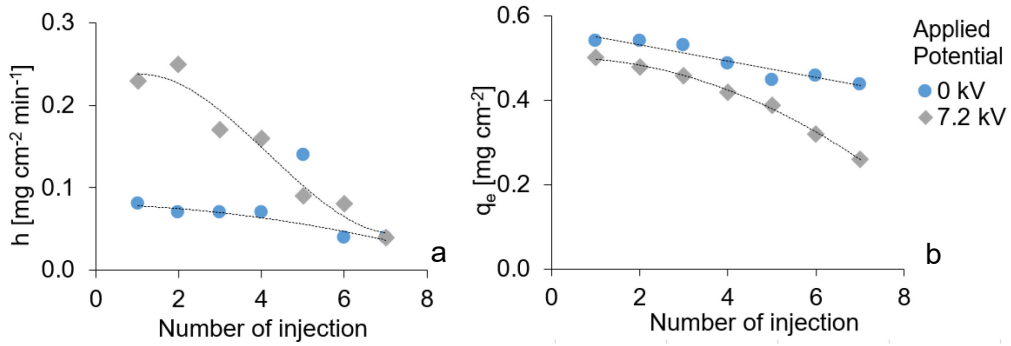

Figure 42 *- Variation of the adsorption parameter for subsequent injection of MEK: (a) h, initial adsorption rate and (b) q_e, amount of adsorbate at t=60min with and without the application of an external electric field.*

Effect of the adsorbent

Water vapor isotherms have been used to estimate the internal surface area and the pore size distribution. All samples, except for FAC and Z, exhibit a hysteresis between adsorption and desorption isotherms. The silica (S), activated carbon (AC) and alumina (A) isotherms have a low-pressure region convex to the pressure axis and a high-pressure concave region. These three adsorbent possess the highest water vapor adsorption capacity. Their shapes are a Type IV isotherm, typical for mesoporous solids, in which the adsorption is a multilayer. The hysteresis is related to the capillary condensation and the limiting uptake for high p/p_0.

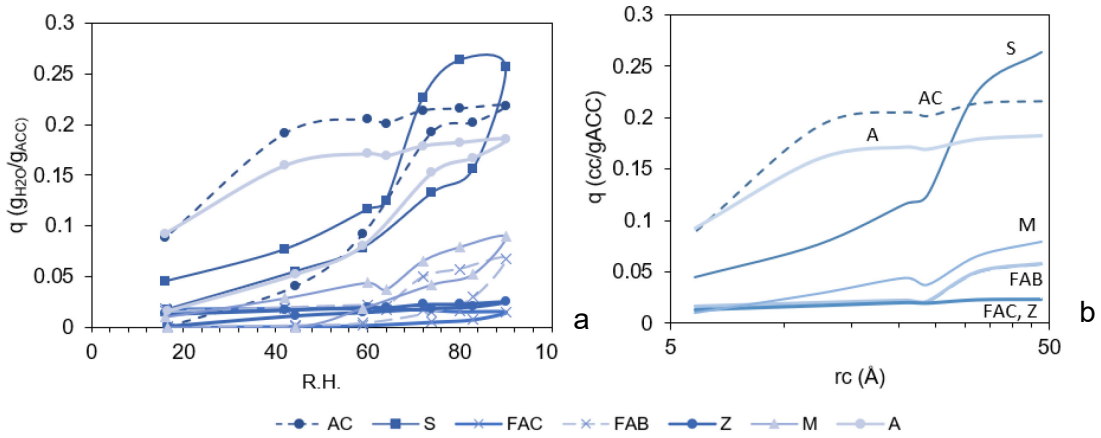

Figure 43 *– Water vapor isotherm (a) and pore distribution (b) of the tested adsorbent*

Figure 44 reports the MEK adsorption kinetic by the different adsorbent, with and without an applied electric field. Most of the adsorbents tested show an enhancement of the removal rate in the presence of the electric field. Only fly ashes (FAC, FAB) which are characterized by low capacity, were not affected by the electric field. For alumina (A), silica (S) and montmorillonite (M), the kinetics of adsorption

is lower, if compared to the one with activated carbon (AC), but they are all dramatically increased by the application of the electric field.

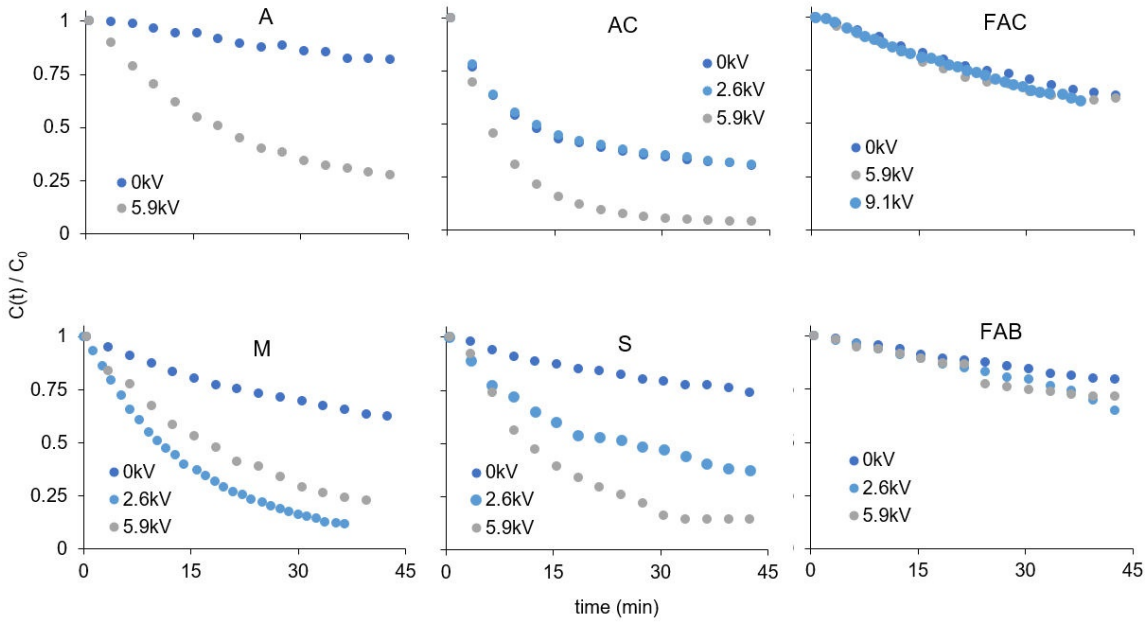

Figure 44 *– Kinetic of MEK adsorption onto six different adsorbents, with and without the application of an electric field.*

Ozone production, due to the corona discharge, was as well monitored. The ability to limit the release of ozone by the adsorbent is related to its chemical and physical structure. Figure 45 shows the concentration of ozone, measured in air, with different adsorbents. Activated carbon is known to decompose ozone into oxygen, for this reason, it has been often coupled downstream of an electrostatic precipitator, in order to limit the release of ozone. As well alumina is capable of decomposing O_3 into O_2 [160], and the activity of clay minerals in removing O_3 has been previously investigated [161].

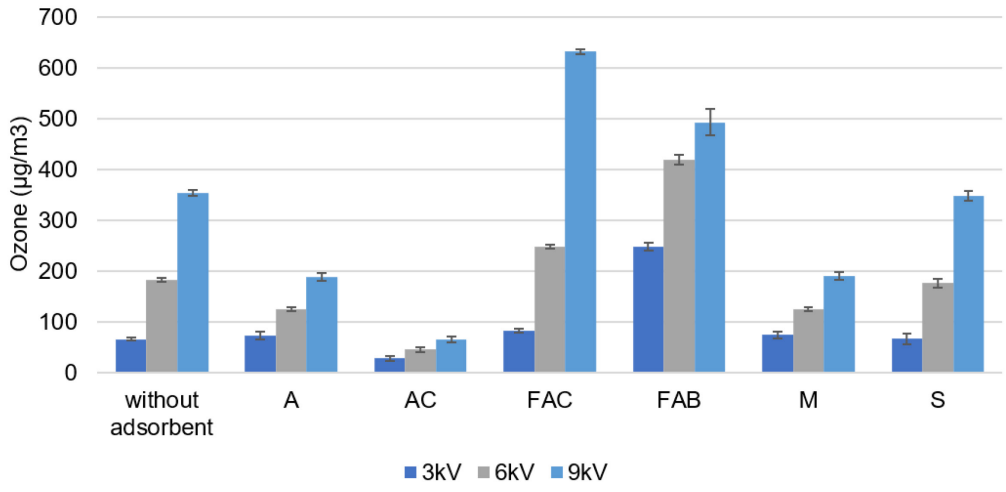

Figure 45 *- Ozone concentration measured with different adsorbent*

2.2.4 Discussion

2.2.4.1 O_3 and NO_2 generation

The corona discharge produces ozone. Ozone, by itself, it is considered a pollutant, but its production can be mitigated by using a proper adsorbent material. The destruction of O_3 by activated carbon is a process which happens at the molecular scale, involving the opening of the carbon rings into carboxylic and other functional groups [162]. This effect does not modify the overall morphology of the activated carbon but only its surface chemistry, by increasing the number of acid functional groups and making more favorable the adsorption of polar compounds.

NO and NO_2 are, as well, produced by the corona discharge. These nitrogen compounds can play a negative role in limiting the capacity (because of the competitive adsorption against a target compound). This aspect has been confirmed by the presence of nitrites and nitrates in the sample washing liquor, and their amount is proportional to the exposure time and the ozone produced.

O_3 and NOx production depends, primarily, on the voltage applied to the discharge electrode and, secondly, on the electrode geometry. The production of O_3 may be used, as well, to destroy or inactivate numerous bacteria present on the adsorbent media [104,105].

No production of CO_2 and CO was measured during the tests with the VOC; this indicates an absence (even partial) of the mineralization of the initially injected organic compounds.

2.2.4.2 Surface functionalization

Ozone plays an important role in the functionalization of the activated carbon. Raman and FTIR spectroscopies indicate, respectively, the loss of carbon bonded in rings with the formation of functional groups. Carboxylic, lactone and phenolic groups were also quantified by Boehm titration. This superficial alteration also has repercussions on the distribution of free charges, which are more constrained, increasing the electrical resistivity of the material.

2.2.4.3 Enhanced mass transport by ionic wind

The migration of the positive charged molecules and particles toward the collecting electrode results in an ionic wind, in which neutral particles are involved as well. In this study, this aspect has been considered to be the main process involved in the enhanced adsorption of VOC in the presence of an electric field. However, this effect starts only if the corona applied voltage is greater than the corona onset voltage, and it is dependent, to the air velocity perpendicular to the electric field.

The choice of different adsorbent materials has shown that the increase in efficiency is mainly kinetic: unconventional adsorbent materials, characterized by low capacities, do not benefit from the application of an electric field, while for long-established adsorbent materials, characterized by large capacity, the adsorption rate is drastically increased.

Since only the first layer of adsorbed molecules are in contact with the adsorbent, and the other layers are in contact with other adsorbates molecules only, a general assumption is that the evaporation-condensation properties of the molecules in

the second and higher adsorbed layers are the same as if the adsorbate would be in the liquid state. Since van der Walls forces are characterized by a short range of action, they are almost depleted after the first adsorbed layer, so all the other layers are bonded mainly by cohesion forces between the molecules. These forces, having an electrostatic nature, can be altered by the presence of an external electric field, favoring, or inhibiting, the adsorption. The correlation found suggests that VOC having the lower specific heat of fusion are positively affected by the electric field, probably because of the stronger induced electrostatic force.

In conclusion, the model should include both physical and chemical processes affecting the adsorptive, the adsorbate and the adsorbent. Figure 46 schematize the possible mechanism which can affect the process.

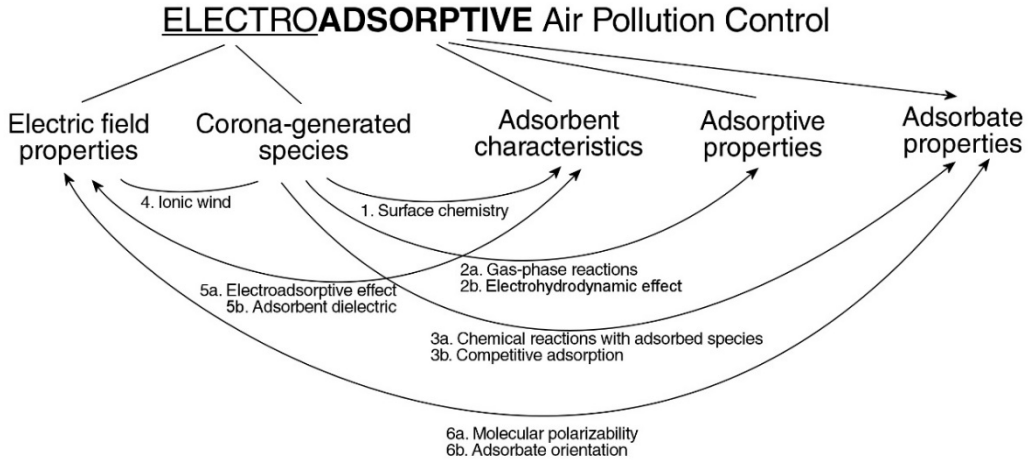

Figure 46 *– Schematization of the possible phenomena occurring when coupling an electric field with the adsorption process*

Coupling a photocatalyst with an adsorbent material is a common technique to improve photocatalysis. Because there are numerous studies in the literature on the subject, in this paragraph only a few highlights, focused on a specific goal, have been discussed:

- *Lower the cost. In paragraph 2.3.1.1 has been reported a facile route for coating silica with TiO_2, starting from metallic titanium powder. Both constituents may be of non-lab grade or recovered.*
- *Enhance photocatalysis. Combining TiO_2 with carbonaceous nanomaterials makes it possible to increase photocatalytic activity. The effect of using different allotropes of carbon has been investigated in paragraph 2.3.1.2.*
- *Tailor a nanocomposite. Differing from the first point, the realization of a nanostructured composite is essential to understand the mechanisms that take place at the molecular scale. For this reason, a TiO_2/carbon nanowall composite has been realized and studied in paragraph 2.3.1.3.*
- *Simplicity. Given the previously described results, to simplify the production of such adsorbent/photocatalytic composite, it was decided to utilize an activated carbon cloth on which a commercially available TiO_2 (P25, often used as a reference), was deposited by simple impregnation, in paragraph 2.3.1.4.*

2.3 Photocatalysis and Adsorption

2.3.1 Introduction

The adsorption of pollutants onto the photocatalyst surface plays a critical role in the efficacy of photocatalytic oxidation technology for air purification applications. For this reason, embedding a photocatalyst onto the surface of an adsorbent is reported to be a strategy to enhance the overall photocatalytic reaction performance. Rapid reactions may be achieved by using porous catalyst support, offering a high density of active surface sites and fast molecular transport to/from these. Moreover, as the photocatalytic activity takes place only on the titania surface, its required amount can be significantly lowered by coating porous materials, as silica [163–165] zeolite [92,166–168], clays [169–172], activated carbon [173–177]. Due to the large extent of photocatalyst/adsorbent composites, in this study, only a few of them were synthesized, characterized and studied.

2.3.1.1 A low-cost Silica/Titania composite

The most adopted method [163,165,178–182] to obtain a controlled growth of spherical silica particles of uniform size was reported by Stöber et al. (1968) [183]. However, the use of tetraethylorthosilicate (TEOS) as silica precursor constitutes a

limitation for large-scale production. Similarly, titanium precursors as titanium isopropoxide (TTIP)[163,179,181,184,185], tetrabutyl orthotitanate (TBOT) [165,178,185,186], titanyl sulphate ($TiOSO_4$) [179,180], titanium tetrachloride ($TiCl_4$) [187,188], titanium(III) trichloride ($TiCl_3$) [184] are unsuitable as well, due to their cost or difficulty in the preparation method. Few authors have investigated different methods for obtaining a cost-effective composite, by using sodium silicate [188,189], commercial silica [184,190] or a commercial TiO_2 P25 [64,189]. A short literature review is reported in Table 26.

Table 26 *- Precursors and surface area of many silica/titanium composites reported in the literature*

Authors	Year	Precursor		Surface area	Ref.
		Silica	Titanium	m^2/g	
This study	*2016*	*Silica*	*Ti*	*210 - 314*	
Wang L. & Jiang Z.	2016	SS/TEOS	$TiCl_4$	533 – 605*	[188]
Paušová Š. Et al	2014	Silica	$TiCl_4$		[187]
Dong W. et al.	2007	TEOS	TTIP	20 – 269$^{\$,T}$	[185]
Smitha V. S. et al	2010	TEOS	$TiOSO_4$	100 - 216	[182]
Alaoui O. T.et al.	2009	SS	TiO_2 P25		[189]
Houmard M. et al.	2007	TEOS	TTIP		[181]
Guan K.	2005	TEOS	TBOT		[165]
Hirano M. et al.	2004	TEOS	$TiOSO_4$	5 - 180 ^{T}	[179]
Hirano M. et al.	2004	Silica	$TiOSO_4$	533 – 703$^{\$}$	[190]
Hirano M. & Ota K.	2004	SS/TEOS	$TiOSO_4$/TTIP	58 - 1123	[180]
Guan K. et al.	2003	TEOS	TBOT	73 – 308$^{\$}$	[178]
Yu J. et al.	2001	TEOS	TBOT		[186]
Montes M. et al.	1997	Silica/TEOS	$TiCl_3$/TTIP	55 – 332^T	[184]
Anderson C. & Bard A.	1995	TEOS	TTIP	200 – 430$^{\$}$	[163]

*Depending on the Silica precursor; $^{\$}$ Depending on Si/Ti ratio; ^{T} Depending on temperature synthesis

2.3.1.2 The effect of Carbon type on Titania/Carbon composites

Nanostructured photocatalysts present several distinct advantages, compared to their bulk counterparts, because of their enhanced electronic conductivity, better stability, increased number of active sited and improved reaction kinetics [191–194]. Conventional carbonaceous materials such as carbon black, activated carbon, graphite, and graphitized materials have been extensively used in heterogeneous catalysis. Only in the last decades, the discovery of new nanostructured materials, such as carbon nanotubes, carbon nanowalls, fullerenes, and graphene have laid the foundations for a new line of research.

The adsorption of pollutants onto the photocatalyst surface plays a critical role in the efficacy of photocatalytic oxidation technology for air purification applications. For this reason, embedding a photocatalyst onto the surface of an adsorbent is reported to be a strategy to enhance the overall photocatalytic performance. Rapid reactions may be achieved by using porous catalyst support, offering a high density of active surface sites and fast molecular transport to/from these. Moreover, as the

photocatalytic activity takes place only on the titania surface, its required amount can be significantly lowered by coating porous materials, as silica [163–165] zeolite [92,166–168], clays [169–172], activated carbon [173–177]. Due to the large extent of photocatalyst/adsorbent composites, in this study, only a few of them were synthesized, characterized and studied.

2.3.1.3 Tailoring a nanocomposite: Carbon nanowall/Titania composite

A tailored nanostructured composite can hardly find the application on a real scale for environmental applications because of its high costs; however, its realization is necessary to study the mechanisms occurring at a nanometric scale.

In the last decade, hybrid catalysts based on both doped-carbon materials and transition metals compounds have received particular attention [194–197]. The nanoscale feature dimensions of catalysts are responsible for the very different properties of nano-engineered catalysts compared to their bulk counterparts, because of their enhanced electronic conductivity, better stability, increased number of active sited and improved reaction kinetics [191–194].

Carbon nanowalls are open boundaries, vertically-oriented few-layer graphene sheets [198–200]. They can grow on a substrate. For almost 20 years, scientific community interests in this type of nanostructures, because they can be used as field electron emitters [199], catalyst supports/templates [201], gas storage materials, hydrophobic coating, sensing media, capacitor, heat sink, electrodes [202] , filter, and bio-sensor [203,204].

Boron-doped carbon nanowalls attract attention thanks to their tunable band gap, high conductivity, high mechanical robustness, high absorption. To achieve a particular morphology and characteristic, it is possible to vary the synthesis parameters, like a level of boron doping, heating temperature, plasma intensity, substrate, deposition time and gas precursor.

Titanium dioxide photocatalysis enthusiasm was driven by the extensively cited publication of Fujishima and Honda [90], even if the study of light-driven reaction at semiconductor surfaces was already known [93]. However, due to long-term catalyst stability problems, the scientific interest decreased. Photocatalytic oxidation (PCO) over TiO_2 is nowadays widely reported as a promising technique for decomposition of various hazardous compounds, among energy applications and synthesis of various compounds. The formation of the electron/hole couple on the catalyst surface induces the formation of active species, such as OH radicals, and reactive oxygen species (ROS) that take part in the oxidative process. However, the enhancement of the photocatalytic efficiency of TiO_2 is still of current interest, because of the low quantum yield caused by the rapid recombination of photogenerated electrons and holes. A commonly adopted method is to form a heterojunction which can enhance the separation of the carriers. To date, only one attempt by Wang et al. is reported in the literature to realize a TiO_2/carbon nanowall composite [205]. Moreover, the possibility of doping the carbon nanowall with boron allows adding a further degree of freedom in creating a carbonaceous substrate having a predetermined bandgap and electrical conductivity.

Since carbon nanowalls can be considered as intermediate between this cited material, because of being constituted of free-standing, vertical aligned, graphene sheets, it is possible to imagine that they possess, as well, improved photocatalytic activity.

In this study, TiO_2 was deposited, by a simple sol-gel technique, on B-CNW grown, by microwave-plasma-enhanced chemical vapor deposition, on fused quartz glass. Boron doping in the CNW and CNW layer thickness was varied, in order to study the impact on the optical and photocatalytic properties. To our best knowledge, this is the first study in which TiO_2 was deposited on boron-doped carbon nanowalls.

2.3.1.4 A simple activated carbon cloth/titania composite

Due to its simplicity, the impregnation method is often used for the preparation of catalysts. In wet impregnation the support material, the activated carbon cloth (ACC), is brought into contact with a solution containing the metal precursors, or the metal oxide itself; after removing the solvent, the final catalyst is obtained.

In this section, an activated carbon cloth was characterized, and P25 titanium dioxide was deposited on the surface by a simple wet impregnation method, using water as a solvent. Graphene oxide is added with the aim of increasing the electrical conductivity and enhances the photocatalytic activity of TiO_2. As this composite is the one that will be used in the final combined process, results of the photocatalytic tests are reported in Paragraph 2.5.

2.3.2 Materials and Methods

2.3.2.1 Silica/Titania composites

A total of six samples, with different TiO_2 concentration, were prepared using two different methods. SiO_2- Silica gel (Carlo Erba Reagents Silica gel 60A 6 - 35μm) was used as purchased. TiO_2 – AEROXIDE P25® is a fine white powder with hydrophilic character caused by hydroxyl groups on the surface. It consists of aggregated primary particles, having a mean diameter of approximate 21 nm, which are several hundred nm in size. Their size and density of about 4 g/cm³ lead to a specific surface area (BET) of approx. 50±15 m^2/g. Titanium metal powder (325 mesh, 99.9% purity) was provided by Metalpolveri Srl.

Simple impregnation method (W)

A determined amount of TiO_2 was dispersed in 230g of ultrapure water and sonicated for one hour. Ten grams of silica was added to the solution and sonicated for another hour. Subsequently, the solution was mechanically stirred for two hours, vacuum filtered and oven-dried at 105°C for 24h.

High-temperature hydrolysis method (A)

Several samples of photoactive materials were obtained by the method of high-temperature hydrolysis of titanium precursors with the formation of titanium dioxide and its deposition on the matrix. For the preparation of the precursor, titanium powder has been dissolved in concentrated sulfuric acid. The resulting solution of titanium sulfate was filtered, hydrolyzed with water, and mixed with silica. The mixture was dried in a fume cupboard for 2 hours and calcinated at 600°C for 3 hours. In order to vary the sample titanium dioxide content, different solutions were prepared (see Table 27).

***Table 27** - SiO_2/TiO_2 composites description*

Sample name	Type of Treatment	SiO_2 g	Ti (m) g	TiO_2 (P25) g	Estimated TiO_2 amount
A3		10	0.40	-	3%
A7	A	10	0.95	-	7%
A12		10	1.63	-	12%
W3		10	-	0.30	3%
W7	W	10	-	0.70	7%
W12		10	-	1.20	12%

Microscopy and XRD analysis

Pictures of every sample have been obtained by using a Keyence Digital Microscope, VHX-5000 series, jointly with a VH-Z100T Wide-range Zoom Lens (100-1000X). SEM was performed with a Sirion200 Field-emission Scanning Electron Microscopy.
X-ray diffractometric analysis was performed using a Philips PW 1730 X-ray diffractometer. The XRD spectrum was taken from 5.0 to 50.0 2θ. The peaks in the new positions of the spectrum were marked, compared and identified.

Measurement of water vapor adsorption

Adsorption kinetics and isotherms of testing samples on water vapor were carried out in a constant temperature and humidity chamber. The chamber can supply constant air condition with deviations of ±0.5°C for temperature and ±3% for relative humidity. Before each test, samples were dried at 150°C in an oven for 4 hours. Weights of the samples were recorded at set intervals by an electronic balance with an accuracy of 0.001g.
To fit the experimental data, a pseudo-second-order kinetic, as described reported in Equation 9, was adopted [24].

Measurement of texture property

Texture properties such as surface area, pore volume, pore size distribution were tested and analyzed by an Accelerated Surface Area and Porosimetry System (ASAP2020). The system utilizes the static volumetric technique to obtain nitrogen adsorption/desorption isotherms at liquid nitrogen temperature. Surface area is calculated based on the BET (Brunauer-Emmett-Teller) equation, and pore size distributions are obtained according to the BJH (Barrett-Joyner-Halenda) theory. The experimental error of the ASAP apparatus is mainly caused by temperature and pressure transducers. The accuracy of the temperature transducer is ±0.02°C, while for pressure is about 0.1%.

NOx removal

The experimental apparatus is illustrated in Figure 1. The reactor has a volume of 3L, and it consists of a Pyrex glass cylinder. Inside is positioned a thin aluminum plate on which is placed the powder sample.

The UV lamp is located at the center of the reactor, over the sample, outside the reactor. The lamp is a UVA metal-halogen quartz lamp with mercury vapor, peak at 360 nm and adsorbed power of 400 W. Irradiance, which was measured with a photoradiometer Delta Ohm HD2102.2, is kept constant at 20W/m^2. The probe of the photoradiometer is centered in the field of UVA with a resolution of 0.001 W/m^2.
The NOx flux inside the reactor is kept constant with a permeation and dilution system (Calibrator 8188) which is alimented with a NOx tank (499ppb NO) at 430±25 ppbNO. Dilution is obtained by mixing with atmospheric air at room temperature (293K ±2K) and relative humidity between 40-60%. NOx concentrations are determined using a chemiluminescent analyzer (Monitor Labs, Nitrogen oxides analyzer model 8841).

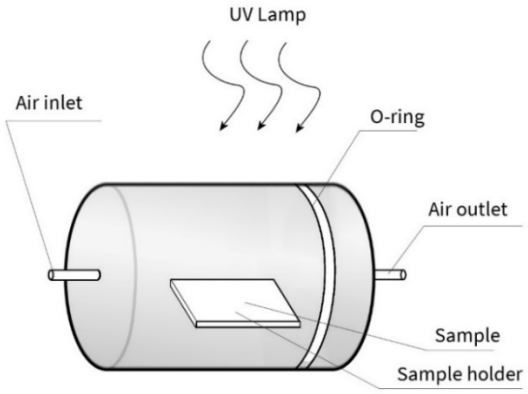

***Figure 47**- Schematic representation of the reactor used to determine the photocatalytic activity in NOx removal.*

Concentrations were monitored during dark and UV-light conditions. NO, and NO_x reduction efficiency weres evaluated as follow:

$$\text{NO removal} = \frac{S}{S_0}\frac{NO^{dark} - NO^{light}}{NO^{dark}} \qquad \textit{Equation 13}$$

$$NO_x \text{ removal} = \frac{S}{S_0}\frac{NO_x^{dark} - NO_x^{light}}{NO_x^{dark}} \qquad \textit{Equation 14}$$

Where NO^{dark}, NO_x^{dark} are the initial concentrations of NO and NOx in dark condition, NO^{light}, NO_x^{light} are the concentration of NO and NO_x while the UV light is turned on, and $\frac{S}{S_0}$ is the ratio between the powder surface and the sample dimensions.

MEK removal

Methyl-ethyl-ketone (MEK) oxidation experiments have been carried out in a batch reactor. The scheme of the reactor is reported in Figure 48.

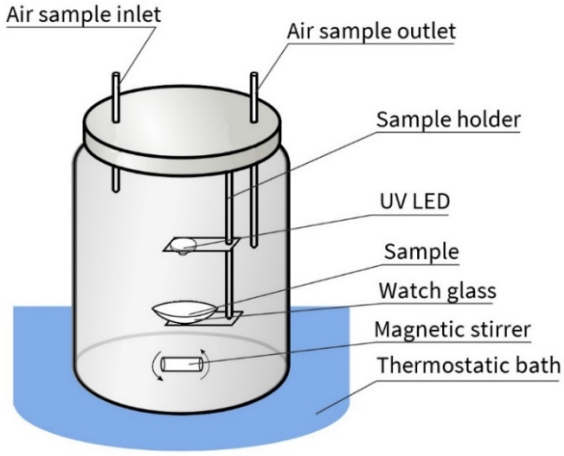

Figure 48 *- Schematic representation of the reactor used for the MEK removal efficiency in the batch test.*

The photocatalytic reactor consists of a glass chamber having a total volume of about 1.05L. Inside the reactor is present a UV LED with a peak at 365nm and adsorbed power of 1W. The distance between the LED and the sample was taken according to the value of irradiance fixed at $7W/m^2$. Magnetic stirring can guarantee continuous air recirculation. The temperature was kept constant by immersing the reactor in a thermostatic bath. The sample used as the powder is placed into a glass watch, below the LED. Air samples inside the box are collected and analyzed by a photoacoustic transducer system (Briiel and Kjaer Multi-gas Monitor Type 1302).
The initial amount of MEK injected into the test box is 5µL. Data collection starts 30sec after the initial injection, in order to account the full vaporization of MEK.
The test is conducted in dark and UV-light condition for every sample. Collected data was treated as apparent second-order kinetics, by using Equation *9*.

2.3.2.2 Carbonaceous nanomaterials/Titania composites

Five different carbon materials have been chosen: Graphite (G), Carbon Black (CB), Graphene Oxide (GO), Activated Carbon (CA) and Carbon Nanowalls (CNW); three of these, GO, CB, and CNW were already available in powder.

Deposition of TiO_2 by sol-gel method

By using a mortar, G and AC were crushed. All the materials were screened through a 0.075 mm sieve. Subsequently, an equal amount of 10 mg of each carbon powder was taken and suspended in Dimethyl sulfoxide (DMSO). The mixing was performed maintaining a constant ratio for each sample equal to 1 ml of DMSO for every 10 mg of carbonaceous particles. Except for GO, the remaining samples were poorly dispersed.

An organic precursor of TiO_2 in liquid phase, obtained using titanium (IV) tetra (2-propanolate), propan-2-ol, Triton X100 and hydrochloric acid (37%), prepared according to the publication of Lewkowicz et al. [206] was poured into five empty glass flasks; for each glass flask, 1 ml of TiO_2-sol was added.
The five previously prepared dispersion (CNW/DMSO, AC/DMSO, G/DMSO, GO/DMSO, CB/DMSO) was finally added to the glass bottles containing the TiO_2-

precursor in order to obtain solutions with different DMSO-carbon/TiO_2 precursor ratios of 0.1, 0.2 and 0.4 (v/v).
In addition to the five solutions so-obtained, a sixth sample was prepared without carbon, but with the same volume ratio of DMSO in TiO_2, as a reference.
The so-obtained solutions (CNW/TiO_2, AC/TiO_2, G/TiO_2, GO/TiO_2, CB/TiO_2 and pure TiO_2) were sealed with parafilm and sonicated for 30 minutes with the aim of favoring the dispersion of carbon particles in the solvent. Subsequently, each parafilm-cap has been punctured, in order to start the gelation process for 24 hours, with having the sol in contact with air. Subsequently, six laboratory slides were firstly immersed in a piranha solution (H_2SO_4: H_2O_2 = 4:1) with the aim of modifying the glass surface and favoring the uniform dispersion of the prepared carbon-TiO2 solutions. Then, the slides were dried in the oven at a temperature of 105 ° C for 1h.
0.25ml of each solution was spin-coated on the glasses, at a determined speed and duration, in order to To disperse the carbon-TiO_2 solutions uniformly on the surface of the laboratory slides.
The glass slides were then placed in an electric muffle furnace and annealed at 450 °C for 6 hours, at a heating rate of 5°C for a minute.

UV-visible spectroscopy

UV-vis spectroscopy was measured by a double beam spectrophotometer (UV-9000 Metash, China) in the 200-1000nm range, with a scan step of 1 nm and a scan filter of 10.
In order to evaluate the band gap energy (Eg) of the samples, $(\alpha h\nu)^n$ were plotted against the photon energy (hν), according to the well-known relation [15]:

$$(\alpha h\nu)^n = A(h\nu - E_g) \qquad \textit{Equation 15}$$

Where A is a constant, hν is the photon energy, and n depends on the type of allowed transition in the material. It has a value equal to 1/2, 2, 3/2 for direct allowed transitions, indirect allowed transitions, and direct forbidden transitions respectively.

2.3.2.3 Carbon nanowall/Titania composite

Carbon nanowall growth

B-CNW was synthesized using the MicroWave Plasma Enhanced Chemical Vapor Deposition (MWPECVD) system (SEKI Technotron AX5400S, Japan). The base pressure inside the chamber was 10^{-4} Torr. Several B-CNW films have been fabricated using the following process conditions: gas mixtures H_2, CH_4, B_2H_6, and N_2 with a total flow of 328 sccm; process pressure of 50 Torr; microwave power up to 1300 W; microwave radiation of 2.45 GHz. For boron-doped samples was used diborane (B_2H_6) as an acceptor precursor. During the process, the substrate holder was heated up to 700◦C. B-CNW thin films were grown on fused silica, optical grade, substrates (Continental Trade Sp.z.o.o.), before pre-treated by using the same MWPECVD in a hydrogen-rich atmosphere, at 500◦C, 1000W microwave power. Subsequently, substrates were seeded by spin-coating in the diamond slurry [207].

TiO_2 sol-gel deposition

Titanium(IV) tetra(2-propanolate), propan-2-ol, poly(ethylene glycol), Triton X-100 and pentane-2,4-dione were of analytical grade, and they were purchased from Sigma–Aldrich (Germany). Hydrochloric acid was purchased from POCH Company (Gliwice, Poland). Deionized water was obtained from Hydrolab system.
The precursor solution for TiO_2 thin films was obtained using titanium(IV) tetra(2-propanolate), propan-2-ol, Triton X-100 and hydrochloric acid (37%). Detailed procedure on sol preparation can be found in our earlier works [206,208]. Thin films were distributed over the B-CNW using the spin-coating technique.
The sol was applied on the glass/CNWs, and the thin films were dried in air for 24 h. Subsequently, they were annealed for three h at 400°C in air at a speed of 10°C/min.

TG analysis

Simultaneous differential thermal–thermogravimetric (DT-TG) analysis was carried out in a150 µL alumina crucibles with a METTLER TOLEDO TGA/SDTA 851 operating in dry airflow, in a temperature range of 25–1000°C, with a heating rate of 10 C min^{-1}). The accuracy of the balance is 0.1µg. In the experiment, the B-CNW sample was previously conditioned at 25◦C 80% RH for 24 hours, before being put in the crucible.

SEM analysis

Scanning electron microscopy (SEM) FEI Quanta FEG 250 Scanning Electron Microscope using 15kV beam accelerating voltage with SE-ETD detector (secondary electron – Everhart-Thornley detector) working in high vacuum mode (pressure 10^{-4} Pa) was used to observe the structure of the B-CNW surfaces.

Raman spectroscopy

The molecular composition of the deposited films was studied by means of Raman spectroscopy using a Raman microscope (InVia, Renishaw, UK). Spectra were recorded in a range of 200–3500 cm^{-1} with an integration time of 5 s (10 averages), using an argon ion laser emitting at 514nm and operating at 5% of its total power (50mW). Data were smoothed (with a Savitzky-Golay method, 15 points, 2nd polynomial order), the baseline (approximated with a three-degree polynomial) subtracted and normalized.

XRD analysis

The presence of crystallized forms of titanium dioxide in the samples after the heat treatment was examined with X-ray diffraction method (XRD) using BRUKER D2PHASER equipment employing Cu K radiation operated at 30 kV and 10 mA. The XRD patterns were collected from 20◦ to 40◦ 2θ angle range using a scanning step of 0.02◦ and counting time of 0.4 s per step.

UV-visible spectroscopy

The absorbance spectra were recorded by a double beam spectrophotometer (UV-9000 Metash, China) in the 300-1000nm range. The band gap energy (Eg) was estimated by plotting and extrapolating the square of absorption coefficient vs. the bandgap energy (Equation 15).

NOx removal

The experimental apparatus is illustrated in Figure 49-a. The reactor, represented in Figure 49-b, has been 3D-printed by using a UV-cured methacrylate resin. The optical window has been realized by a Fluorine-doped Tin Oxide (FTO) glass. The sample is placed in the lower part of the reactor. The air gap between the sample and the FTO glass is 3mm.

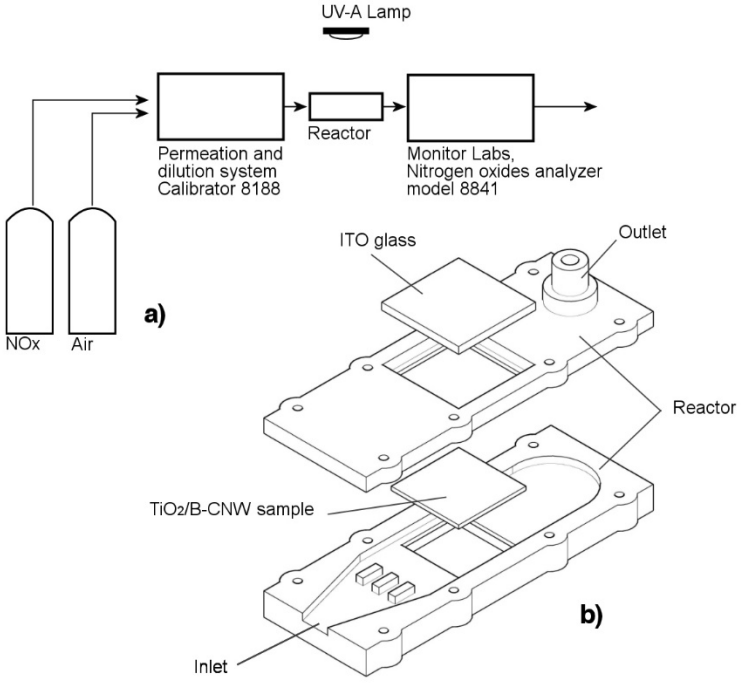

Figure 49 *- Experimental setup.*

The UV lamp is located at the center of the reactor, over the sample, outside the reactor. Lamp, dilution system, NOx tank, and analyzer are the same, described in the previous paragraph.

2.3.2.4 Activated Carbon Cloth/Titania composites

Wet impregnation of TiO_2 on the ACC

Firstly, a dispersion of TiO_2 (P25) in distilled water has been realized. A certain amount of P25 was added to 130ml of DI water, sonicated in an ultrasonic bath for 10 minutes and followed by mixing for three hours on a magnetic stirrer to ensure the homogeneity of suspension. In some sample, GO was added to the solution.

***Table 28** – Amount of TiO_2 and GO inside the solution used for impregnating the ACC*

	DI water (g)	TiO2 (g)	G.O. (g)
Pristine	-	-	-
DI	130	-	-
DI + P25	130	0.17	-
DI + GO	130	-	0.17
DI + GO + P25	130	0.17	0.17
DI + 2GO + P25	130	0.17	0.37
DI + 3GO + P25	130	0.17	0.50
DI + 4GO + P25	130	0.17	0.65
DI + GO + 3P25	130	0.50	0.17
DI + GO + 5P25	130	0.85	0.17

For solutions also containing the graphene oxide, this was added before the TiO_2. ACC samples are immersed in the solution, magnetically stirred for 2 hours and, then, the solvent is evaporated in the oven at 105°C for 48h. So-obtained samples are stored in a desiccator and, before the test, the sample is left at room conditions (temperature of about 22±2°C and relative humidity of 52±10%) for 2 hours, to reach the equilibrium with the environment. A similar procedure was adopted by Nostrati et al. [209] in order to obtain a hydrophilic, photocatalytic and antibacterial additive for polyacrylic based coating. The same impregnation technique was used by Tan et al. [210] for incorporating GO into an O_2-rich TiO_2 with the aim of enhancing stability and shifting the bandgap to the visible region. The photocatalytic efficiency may also be enhanced by a composite prepared with this method; a 4-fold increase was observed for the gas-phase oxidation of ethanol and benzene [211] or nitrogen oxide [212]. In our study, the addition of graphene oxide is primarily aimed to enhance the electrical conductivity of the activated carbon cloth sample and, secondly, to benefit from the GO/TiO_2-coupling.

Determination of gas phase adsorption isotherms

Because of the hydrophobic nature of activated carbon, the copresence of water vapor up to 0.2-0.3 p/p_0 with an organic solvent, doesn't affect the adsorption of the adsorbent. However, if the water vapor concentration exceeds this level, the adsorption of the organic compound is hindered [149].

In order to define the effect of relative humidity on the competitive adsorption with MEK, the adsorption isotherms were determined. A 17cm^2 specimen of ACC were weighted and placed inside a 1L glass jar, together with a specific salt-saturated solution ($MgCl_2$, $Mg(NO_3)_2$, NaCl, KNO_3), in order to maintain a fixed relative humidity ratio (33%, 53%, 75%, 94%), at a specific temperature. At the time t=0, a certain amount of MEK was injected into the jar, and 10µl air samples were taken at fixed time intervals and analyzed through gas chromatography.

Data were fitted according to the linearized term of the equation in Table 29. Langmuir isotherm was chosen because the isotherm fitted the experimental data.

Table 29 *– Linearized equation of different isotherm models*

Isotherm model	Linear form	
Langmuir	$\frac{C_e}{q_e} = \frac{1}{q_m K_L} + \frac{q_e}{q_m}$	*Equation 16*
Freundlich	$\ln q_e = \ln K_F + \frac{1}{n} \ln C_e$	*Equation 17*
Temkin	$q_e = \frac{RT}{b} \ln K_T + \frac{RT}{b} \ln C_e$	*Equation 18*
Elovich	$\ln \frac{q_e}{C_e} = \ln(K_E q_m) - \frac{1}{q_m} q_e$	*Equation 19*
Dubin-Radushkevich	$\ln q_e = \ln q_m - B \left(RT \ln \left(1 + \frac{1}{C_e} \right) \right)^2$	*Equation 20*

Electrical conductivity measurements

Carbon must present an organized "graphitic like" structure to be electrically conductive. This transformation naturally occurs during the thermal manufacturing process. The variation of the electrical conductivity has been already measured and discussed in paragraph 2.2.2.2, where the oxidation of the ACC lead to lower conductivity. Electrical connections, made in stainless steel, were attached to opposite ends of the cloth and were the same length as the cloth sample.

The determination of DC conductivity σ, was calculated by measuring the resistance R and the dimensions of the conductor (l, length and S, cross-sectional area) as follows:

$$\sigma = \frac{l}{RS}$$

To perform the DC conductivity test with the change in VOC concentration a special apparatus was prepared. The reactor consists of a 1L glass jar,
Inside the glass canister, the sample of ACC was anchored at its ends on a special support. Perpendicular to it, at a distance of 3cm, an IR temperature sensor was placed (Melexis MLX90614), in order to record the sample and environmental temperature. A sensor for the relative humidity and temperature has been placed behind the sample. At 10 seconds intervals, a potential of 3V is applied to the sample ends, and through a voltage divider having a known resistance, the resistivity value of the ACC is thus obtained. The reported value is the average of 10 measurements.

2.3.3 Results

2.3.3.1 Silica/Titania composites

Morphology

In Figure 50, the first picture (a) shows the raw silica (RAW) and (b) the AEROXIDE® TiO_2 (P25). It is possible to observe the presence of TiO_2 aggregates, having dimensions of tens of micron, on the silica surface (d) within for the sample W3 obtained by simple mixing. For all the samples obtained with the hydrothermal

method (c), no aggregate of the TiO_2 particle can be detected, but it is possible to observe a more wrinkled surface, with a blueshift in the microscope light scattering. A magnification of sample A3 obtained by SEM is reported in Figure 51, where TiO_2 particles, within the size of hundreds of micrometers, are displaced over the silica surface. The XRD diffractogram for samples A3 and RAW shows the silica amorphous nature, confirming the presence of titanium dioxide, in the anatase form, in sample A3.

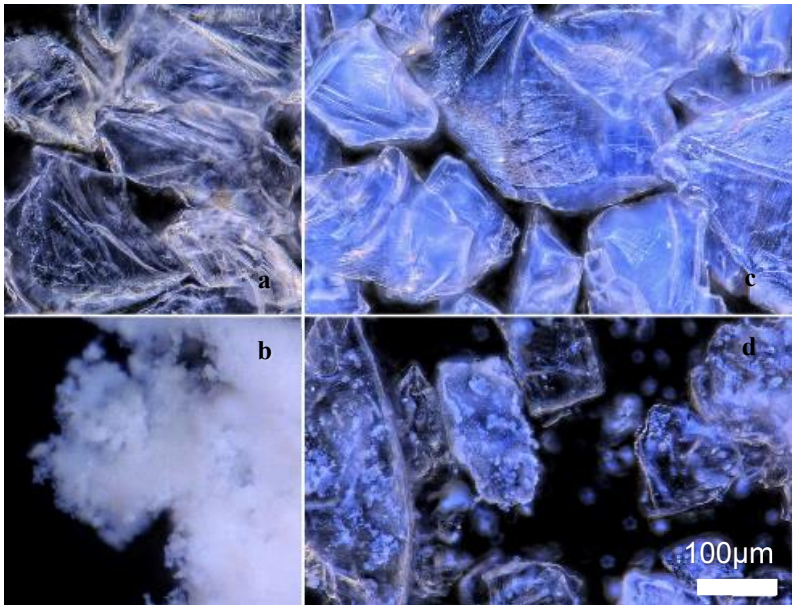

Figure 50 *- Pictures from the digital optical microscope. Magnification of raw silica (a), A3 (b), P25 (c), W3 (d).*

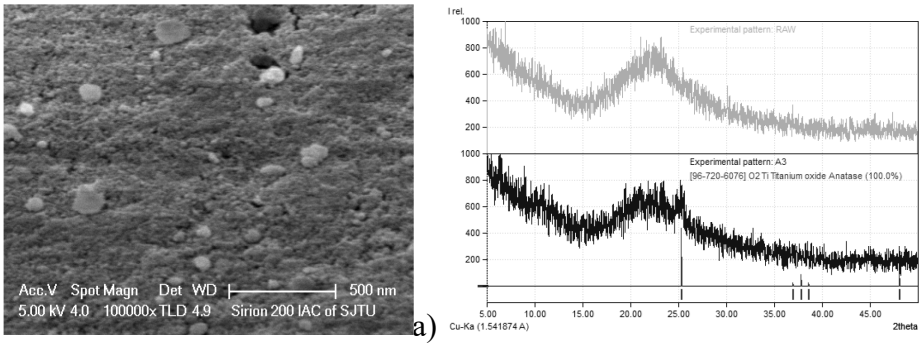

a) b)

Figure 51 *-a) SEM picture of sample A3, b) comparison between the XRD of the sample A3 (black) and the reference (grey)*

Texture properties

Nitrogen adsorption of silica-titania composites was tested, with pure silica and titania as reference samples. Their textural properties such as surface area, pore volumes and average pore size were also analyzed. For silica-titania composites, parameters were calculated on unit mass of the whole composites.

Nitrogen isotherms and pore size distributions were presented in Figure 52 and Figure 53. From Figure 52, Type IV isotherms with hysteresis loops are obtained, and they confirm the dominance of mesopores in these samples. Hysteresis loops of pure silica and titania start near relative pressures of 0.45.

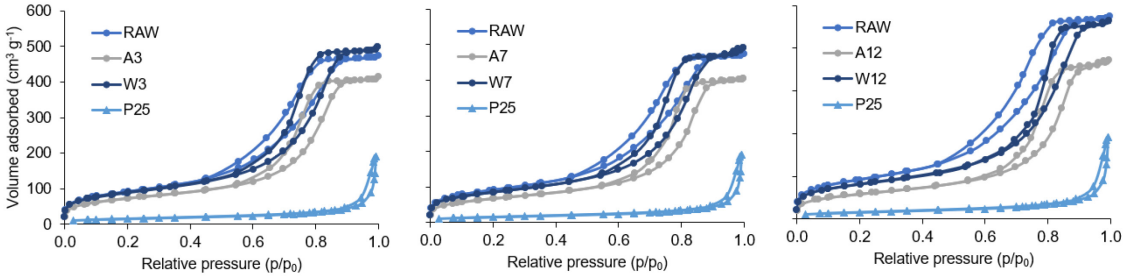

Figure 52 *- Nitrogen adsorption isotherms at 77 K: Wet mixing series (left) and high-temperature hydrolysis series(right).*

In Figure 53, pore size distributions of silica-titania composites tend to that of pure silica, since titania has a much smaller mass portion. Moreover, a lower amount of nitrogen adsorption is observed in samples A (by high-temperature hydrolysis method) than W (by wet mixing procedure).

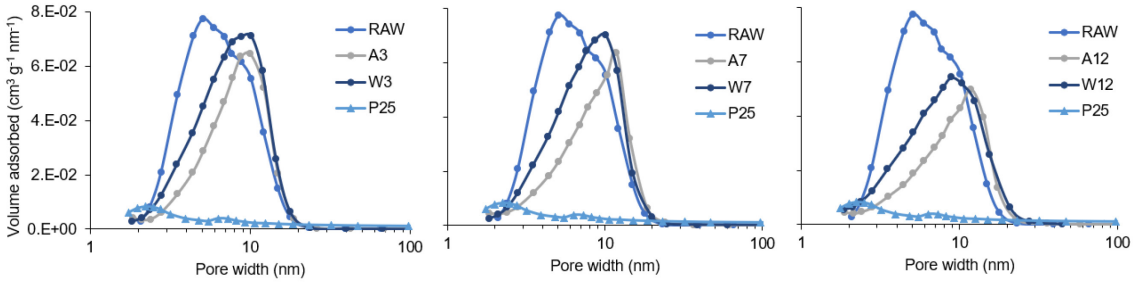

Figure 53 *- Pore size distributions: Wet mixing series (left) and high-temperature hydrolysis series(right).*

BET surface area, total pore volume, and average pore diameter are listed in Table 30. It can be seen that, with the addition of titania, both the surface areas and pore volumes of silica-titania composites are lower than those of pure silica, while average pore sizes become larger than silica. These implied that the properties of silica could be modified by both methods. With high-temperature hydrolysis method, titania plays a more important role in texture properties. For instance, the BET surface area and average pore size of A12 0.57 are 241m^2/g and 10.4nm, while those of W7 are 302m^2/g and 10nm.

Water vapor adsorption kinetic

It can be seen in all the samples that the water vapor adsorbed increases sharply during the initial stage (50% of the total capacity in the first 3 min), while it grows slowly as the samples reach the saturation.

The fastest kinetic of adsorption belongs to the raw silica sample. Modification of the silica samples mainly lead to a decrease of the maximum capacity, q_e, at the equilibrium of water adsorbed. This aspect is also shown by the decrease of the BET surface area, while h, which is related to the rate constant of adsorption, varies between 13 and 30 mg/g min.

***Table 30** - Surface area, pore parameters and water vapor adsorption kinetic parameters of prepared samples.*

Samples	Texture properties			Water vapor adsorption kinetic	
	BET Surface area	Pore volume	Average pore diameter	q_e	h
	m^2/g	cm^3/g	nm	mg/g	mg/g. min
Raw SG	327	0.74	9	222	24
TiO_2	54	0.3	22	42	15
A3	258	0.64	10	98	13
A7	241	0.62	10.4	165	15
A12	210	0.57	10.9	117	27
W3	314	0.77	9.8	165	30
W7	302	0.76	10	111	26
W12	288	0.72	10	152	25

For all the samples, the presence of TiO_2 results in an increase of the average pore diameter and to a decrease in BET surface area, which is stronger for the composite obtained by high-temperature hydrolysis, rather than for the one obtained by simple impregnation.

Photocatalytic activity

Photocatalytic activity of the samples is summarized in Table 31. Experimental data were fitted by using equations Equation 9, Equation 13 and Equation 14, respectively to determine the MEK, NO, and NOx removal rates. The MEK removal rate (h), under both dark and UV conditions, shows its maximum for the two samples having the lowest TiO_2 amount (A3, W3).

***Table 31** – MEK removal rate*

		m	MEK initial concentration	UV		Dark	
				h	q_e	h	q_e
	%	*g*	*mg/l*	*mg/min l*	*mg/l*	*mg/min l*	*mg/l*
RAW	0	0.15	4.0	0.22	3.5	0.29	3.7
A3	3	0.15	4.0	1.06	3.6	0.90	3.9
A7	7	0.15	4.0	0.43	3.7	0.26	3.6
A12	12	0.15	4.0	0.23	3.6	0.23	3.5
W3	3	0.15	4.0	0.87	3.4	0.59	3.6
W7	7	0.15	4.0	0.46	3.7	0.35	3.6
W12	12	0.15	4.0	0.31	3.5	0.30	3.8

Table 32 *– NO and NOx removal efficiencies*

	TiO_2 amount (%)	**ηNO (%)**	**ηNOx (%)**
RAW	0	3.4%	1.5%
A3	3	18.0%	4.9%
A7	7	14.5%	5.6%
A12	12	13.3%	3.8%
W3	3	8.9%	1.2%
W7	7	21.5%	7.6%
W12	12	21.5%	8.7%
P25	99.5	19.9%	8.1%

Observing the NOx photocatalytic activity, two different trends are noticed. The samples obtained by high-temperature hydrolysis show a decreasing trend on the NO photocatalytic index, with increasing the percentage of TiO_2, while for the samples obtained by simple impregnation, the NO photocatalytic index increases jointly with the P25 amount, until reaching a *plateau*. While considering the NO_x removal, efficiencies are halved, since NO_2 is formed as an unwanted product.
It is interesting to compare A3 with W3 and P25. All these samples have the same amount of TiO_2, but they show different photocatalytic activities. W3 is the less active, probably because the same amount of P25 is poorly distributed over the composite surface, while the P25 and A3 activities are comparable. In fact, as seen from the SEM and the optical microscope pictures, TiO_2 is well dispersed on the surface of the silica, for A3. However, this better dispersion, affect mostly the porosity of the silica, resulting in a lower efficiency with higher loads of TiO_2.

2.3.3.2 Carbonaceous nanomaterials/Titania composites

Photocatalytic activity

Adding a solvent (such as DMSO) in the sol may negatively affect the crystallinity of the TiO_2 [213]; for this reason, the same amount was introduced in each sample, but the amount of carbonaceous material in the DMSO was varied. Figure 54 reports the photocatalytic efficiency for the NO removal versus the carbon content of the composite. It is possible to observe how, for most of the composites, not including the graphene oxide, higher addiction negatively affect the photocatalytic activity. CB and CNW are the ones more affected, while for G and AC, the loss in efficiency is comparable to the TiO_2-only sample. Only GO shows an enhancement by its addition into the composite. This effect may be explained by the fact that the GO was well-dispersed both in the DMSO, both on the glass surface, resulting in better incorporation (Figure 55) of the carbonaceous material into the composite.

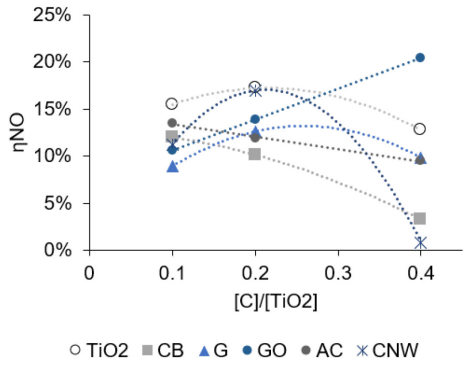

Figure 54 *- Photocatalytic activity of different carbon/TiO_2 composites*

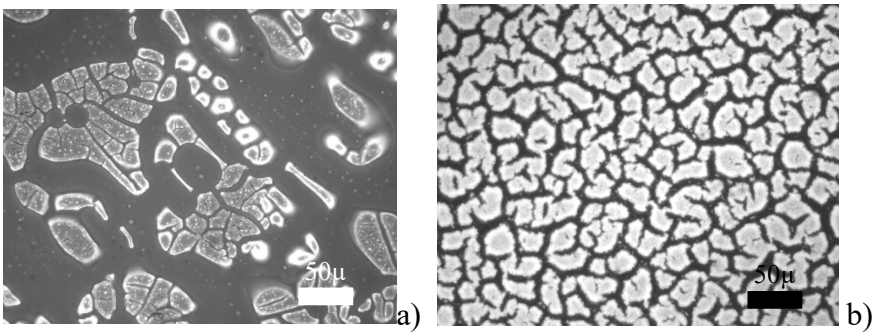

Figure 55 *- Optical microscopy picture of a) TiO_2 and b) G/TiO_2 composite. The white domain is TiO_2.*

UV-visible spectroscopy

The optical bandgap of anatase, reported by Lewkowicz et al., by using the same method, is equal to 3.4eV [206]. In this work, to the precursor was added to the carbon dispersed in DMSO, and the presence of other organic compounds may inhibit the gel formation, limiting the crystallite size and increasing the bandgap [214].

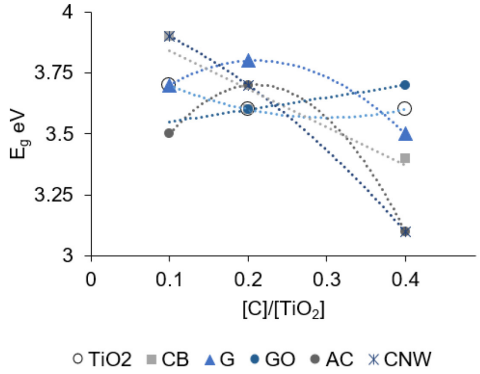

Figure 56 *- Optical bandgap of the C/TiO_2 composites*

The band gap energy of TiO_2 was calculated to be 3.60 eV for the sample with carbon/TiO_2 ratio equal to 0.2. This value is larger than the value measured in bulk for anatase TiO_2 (3.2 eV). Such differences may arise from different phenomena, such as the emergence of a direct transition in the semiconductor or because of the crystallite size [214]. All the calculated bandgaps are close to this value, and the carbon concentration slightly affects it, while for AC and CNW, an increase of the carbon incorporated, lead to a decrease of the E_g, up to 3.1eV.

2.3.3.3 Carbon nanowall/Titania composite

Growth and characterization of B-CNW on glass

Figure 57 shows the SEM images of B-CNW growth, respectively, at 400, 550, 700, 850°C at 2k ppm [B]/[C] ratio and with 0, 2k, 5k, 7.5k ppm [B]/[C] at 700°C. It is found the wall structure only for temperature higher than 700°C, and it is noted that nanowall length increases with increasing temperature.
Boron incorporation into the CNW lattice, in different ratios at the same growth temperature, does not strongly affect the morphology (Fig.1e-h) which can be confirmed in other publications [215].

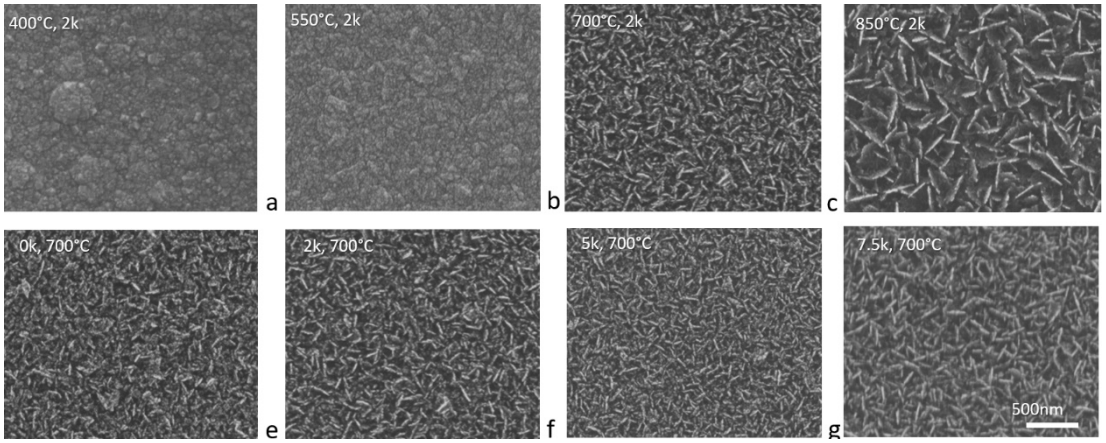

***Figure 57** - SEM picture of B-CNW growth, respectively, at 400°C, 550°C, 700°C, 850°C at 2k ppm [B]/[C] ratio and with 0, 2k, 5k, 7.5k ppm [B]/[C] at 700°C.*

The absorbance spectrum for the sample growth at different temperatures is shown in Figure 58.

The absorbance for wavelengths of between 400 and 700 ranges between 0.2 and 0.8, with increasing growth temperature. In particular, a prominent change in average transmittance has been observed in the 200 nm to 350 nm wavelength region. The absorbance spectrum for the samples with different [B]/[C] ratios are similar, while the trend of visible light absorption for samples initially increases, and then decreases with higher [B]/[C] ratio higher than 5k ppm (Figure 58-b).

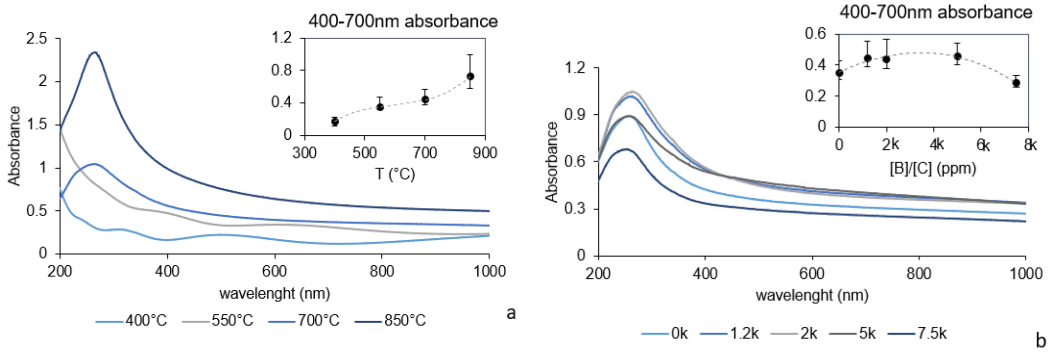

***Figure 58** - a) UV-visible absorbance spectrum for B-CNW growth at 400°C, 550°C, 700°C, 850°C at 2k ppm [B]/[C] ratio and b) UV-visible absorbance spectrum for B-CNW at 0, 2k, 5k, 7.5k ppm [B]/[C] at 700°C.*

Raman spectra of CNWs are analyzed and reported in Figure 59. In all samples, two main bands at ~1580 and ~1350cm^{-1}, are found, which are generally attributed to the G and D band, respectively. In particular, Ferrari and Robertson have suggested that the G and D peaks are due to sp^2 only [158].

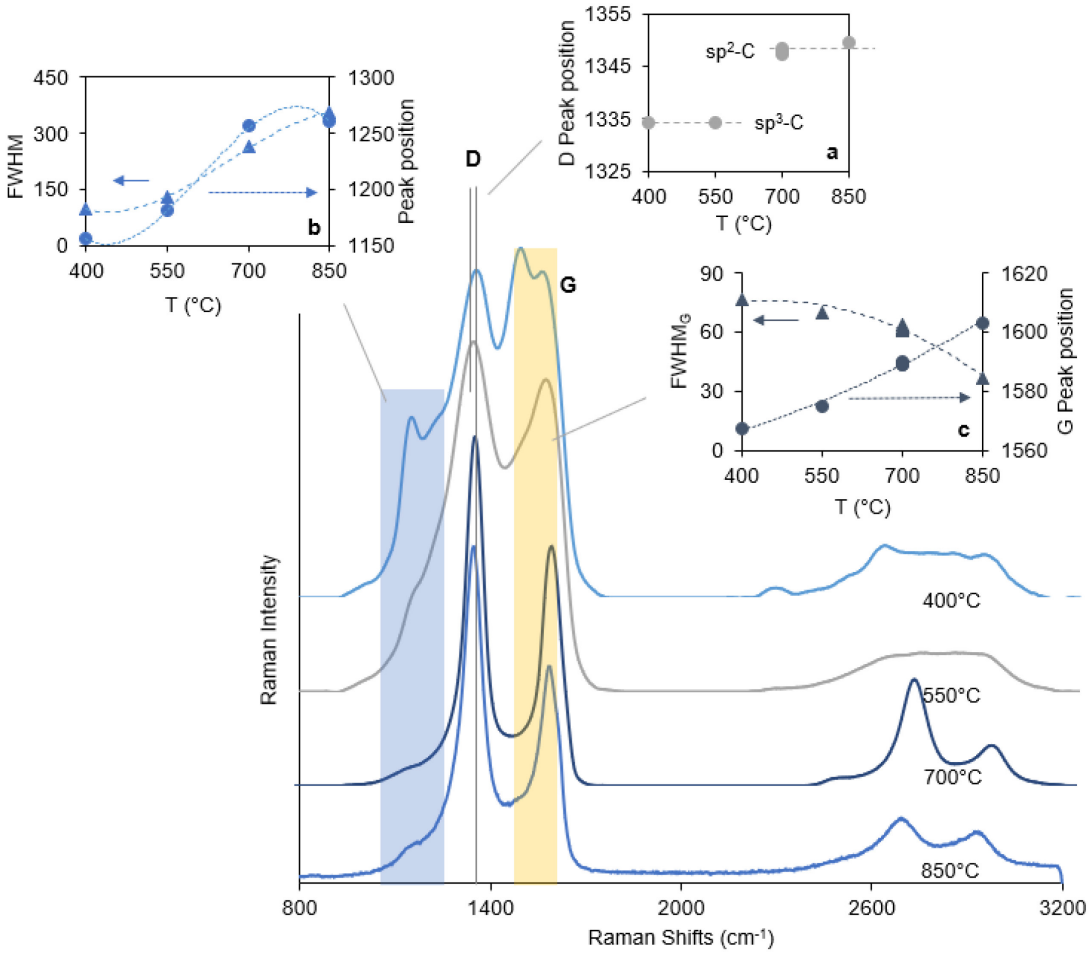

Figure 59 *- Raman Spectrum of the samples growth at 400°C, 550°C, 700°C, 850°C, 2k ppm [B]/[C] ratio*

The peak at around 1350 cm^{-1} corresponds to the breathing mode of sp^2 atoms in a ring (D band, Figure 59-a). The different samples morphology, previously described and reported in Fig.1, is also highlighted by the presence of D-peak, at 1350 cm^{-1} in the Raman spectra, only for the B-CNW growth at higher temperature, which corresponds to distortion of sp^2 crystal structure; while, for the first two samples (at 400 and 550°C), a peak appears before, at 1334 cm^{-1}, which can be attributed, instead, to the diamond structure [216].

The peak at 1580 cm^{-1} is due to bond stretching of sp^2 atoms in rings and chains (G band, Figure 59-b). The G-peak position is shifted to a higher frequency with higher temperatures, and the G-FWHW is also found to decrease with temperature. Marchon *et al*. reported a similar trend, and they linked it to the decrease of sp^3 content [217].

The band at 1220 cm^{-1} is reported to be caused by the effect of boron on the diamond lattice [218]. However, this peak also appears in boron-free CNW, which makes another hypothesis reasonable. Chen *et al*. [219] merged their results with theoretical analysis and experimental results from others to identify two additional Raman peaks

at around 1168 and 1271 cm^{-1}, in tetrahedral amorphous carbon, linked to the sp^3 bonding. In our results, reported in Figure 59-c, it is possible to observe a distinct peak, ahead of the D band, which redshifts with increasing temperature. Moreover, from the Raman spectrum it is observed that when the boron concentration was increased further from 2k ppm [B]/[C], the G-band peak upshifted by $6cm^{-1}$. A similar result was noted by McGuire *et al*. [220] for boron-doped single-walled carbon nanotubes.

The nanowall lengths and the nanowall layer thicknesses, estimated through Spectroscopic Ellipsometry, have been plotted against the different growth temperatures (Figure 60-a/c), jointly with the optical bandgap and electrical conductivity (Figure 60-b/d).

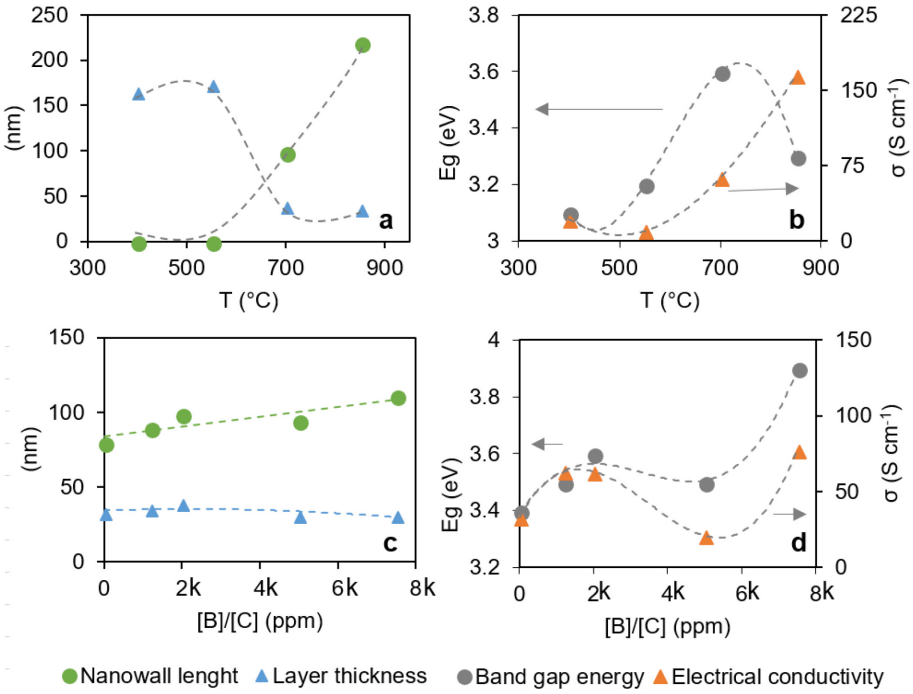

Figure 60 *- a) Nanowall length and layer thickness, b) optical bandgap and electrical conductivity for B-CNW growth at 400°C, 550°C, 700°C, 850°C, 2k ppm [B]/[C] ratio; c) nanowall length and layer thickness, d) optical bandgap and electrical conductivity for B-CNW growth at 0, 2k, 5k, 7.5k ppm [B]/[C] at 700°C.*

Higher electrical conductivity belongs to samples growth at a higher temperature, similarly for the nanowall length, as this parameter particularly affects the charges mobility(Figure 60-a). The longer walls structure delivers higher conductivity mostly due to the minimized effect of carrier scattering at the inter-walls regions and surface defects. Next, the optical bandgap shows a maximum for the sample growth at 700°C (Figure 60-b), which is much larger than values reported by Kawai et al. [221]. This effect is unrevealed, while it could be attributed to the specific molecular structure caused by boron doping. The wall length is slightly positively influenced by the boron level in the gas phase, as previously reported [215], while the B-CNW layer thickness is not, and constant at 34±4nm (Figure 60c). Overall, the incorporation of boron into the CNWs lattice structure induces the unique effect of enhanced electrochemical performance and improved charge transfer [202,203] (Figure 60-d).

Morphology of the B-CNW/TiO_2 composite

The morphology of the B-CNW/TiO_2 composite is shown in Figure 61. Optical microscopy of the composite surface is reported in Figure 61-a, in which it is possible to observe the shading color resulting from interference in titania thickness [222]. The irregular composite surface is better represented by the AFM picture in Figure 61-b, where the roughness is in the order of 10nm, due to the TiO_2 coating. Furthermore, few superficial defects are presents. Figure 61-c,d represents two of those, in which, during the annealing process, the titanium dioxide layer cracked and can be ejected, resulting in the exposure of the B-CNW underlying layer Figure 61-d. Raman spectroscopy (Figure 61-e) confirms the higher amount of crystalline carbon at the defect.

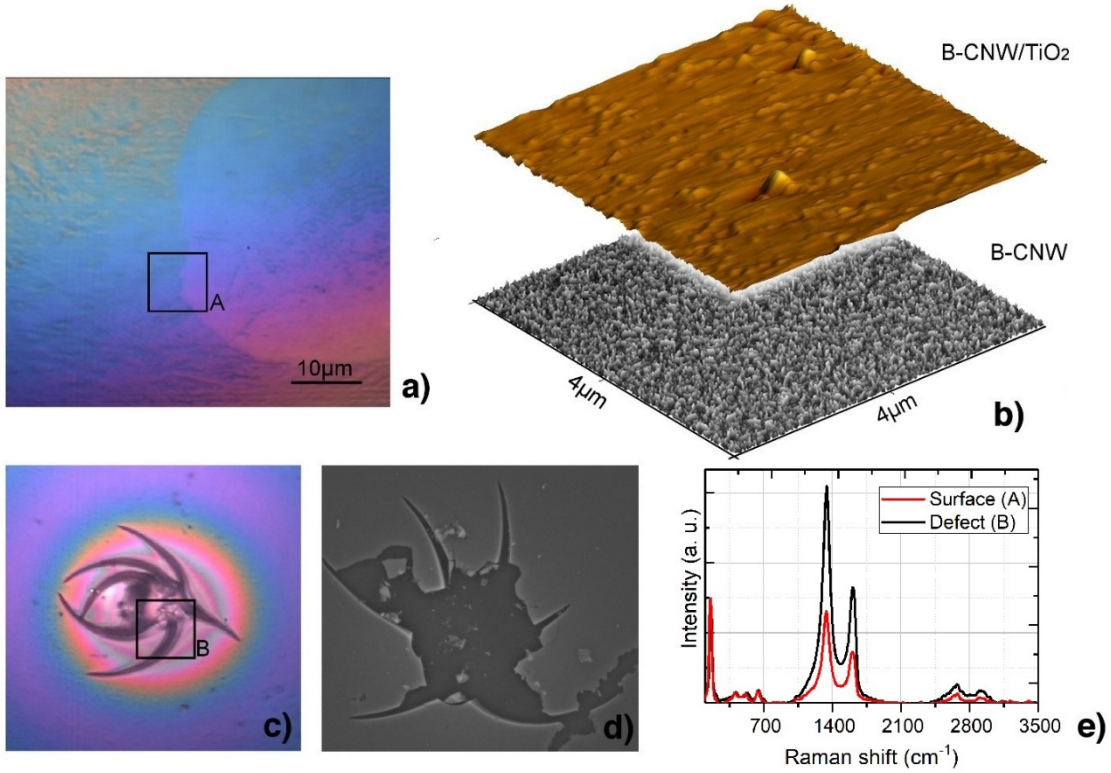

Figure 61 *- a)optical microscopy of the sample surface b) 3D resolution of AFM picture of the composite sample.c-d) defects at the sample surface e)Raman spectra recorded at the clear surface and at the defect*

TG analysis

The TGA shows single combustion of the B-CNW starting at 456°C and finishing at 883°C, with a total mass lost equal to 99.95%. According to this result, calcination of the samples was conducted at 400°C

Raman spectroscopy

Figure 62 shows the comparison of the Raman spectra of TiO_2, CNW, and the TiO_2/CNW composites. A well-resolved TiO_2 Raman peak is observed at about 145 cm^{-1} for the TiO_2 and TiO_2/CNW samples, which is attributed to the main anatase vibration mode, followed by vibration peaks at about 412 cm^{-1}, 522 cm^{-1} and 640

cm^{-1}, may indicate that the anatase crystallites in the materials are the primary species. The other two main bands at ~1580 and ~1350cm^{-1} are attributed to the G and D band of the carbon nanowall, respectively.

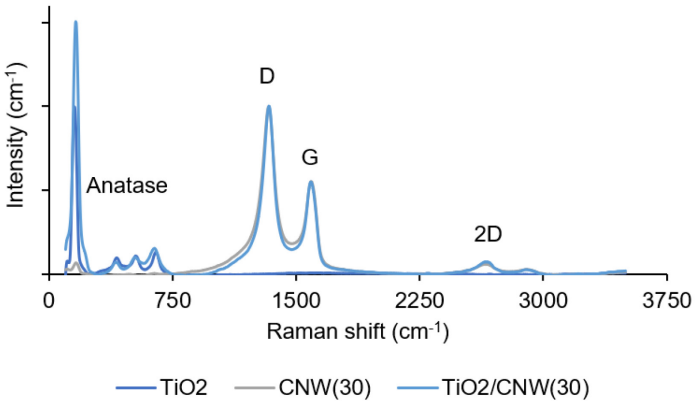

Figure 62- *Raman spectra of the CNW/TiO_2 composites*

XRD analysis

Figure 63 shows the XRD patterns of the samples after heat treatment (400°C, three hours). The signal observed in all cases and located at 24.95 degrees of 2θ angle can be attributed to the most intense reflection of the anatase phase. The presence of this signal confirms the presence of a crystalline form of TiO_2 in obtained thin films. However, the signal is broad and not well resolved. This suggests that the concentration of anatase crystalline domains present in amorphous TiO_2 is relatively small and their average diameter is in nanometer scale.

The intensity of the anatase phase is the same with the increase of the amount of CNW, due to the stable of titanium dioxide with CNW. However, we observe the small intensity of anatase peak, because of their dependence on crystallite size and porosity structure (probably connected with defects in the structure of thin films).

The presence of cristobalite, a high-temperature polymorph of silica, is related to the high-temperature treatment on the quartz substrate. The peak at 2θ= 22, absent in the reference sample which was subjected only at the H_2-pretreatment at 500°C, decreases with increasing B-CNW layer thickness, which indicates a penetration depth of hundreds of nanometers.

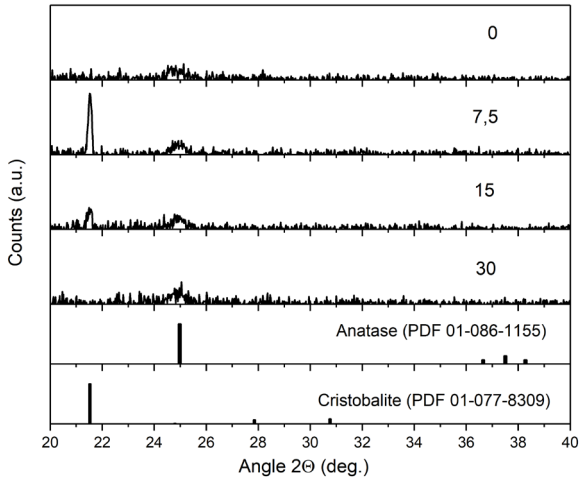

Figure 63 - *Results of XRD analysis.*

UV-vis spectroscopy

UV-vis spectroscopy was conducted in order to estimate the band gap energy of the samples with the Tauc method (Equation 15). Optical bandgaps, reported in Figure 64, show their decrease by increasing the thickness of the BCNW layer, both in the BCNW-only sample and the composite.

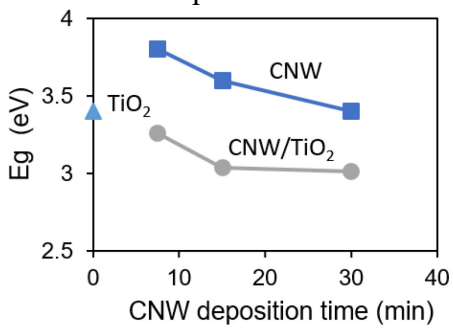

Figure 64 - *The absorbance of the TiO_2/B-CNW samples.*

Photocatalytic activity

The photocatalytic activity of the composite, measured as removal of NOx under UV irradiation, is reported in Figure 65. It was reported that B-CNWs showed no response to light irradiation. Test was performed at two different inlet flow, in order to variate the residence time inside the reactor.

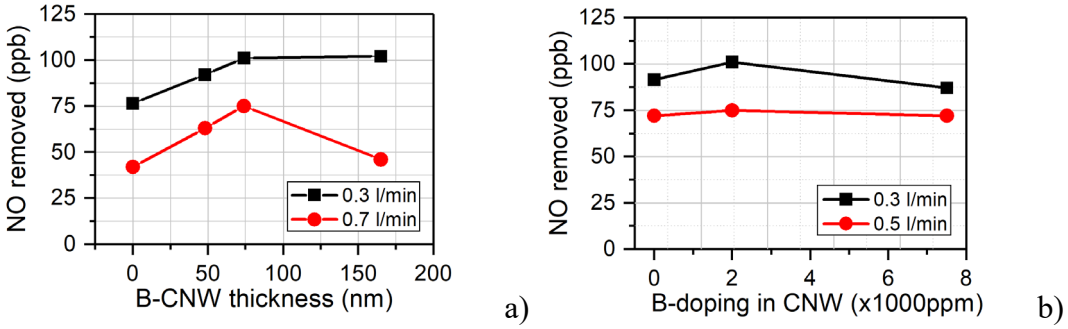

Figure 65 *- NO removed by the different composites, (a) with different carbon nanowall layer thickness and (b) with different B-doping in the CNW.*

It was found that samples are having a thicker CNW thickness show an increased NO removal efficiency, while the boron incorporation slightly affects it, showing a maximum for 2000ppm of B/C ratio. These considerations are consistent with the optical bandgap previously determined.

2.3.3.4 Activated Carbon Cloth/Titania composites

Water vapor isotherm

Effects of the simple impregnation method are reported in Figure 66. In Figure 66-a is reported a simple comparison between the amount of GO and TiO_2 present in the solution, used to impregnate the sample and the final weight of the sample. The slope of the linear correlation suggests that, approximately, 85% of the solute can be

found in the sample. Figure 66-b shows how the electrical conductivity varies according to the amount of GO load in the solution.

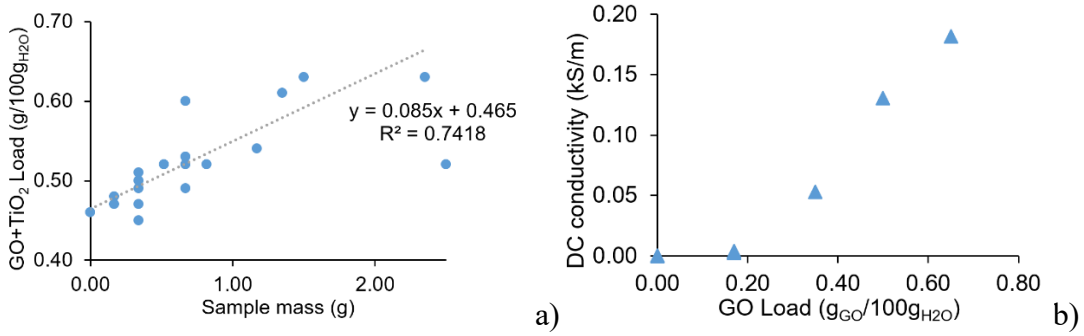

Figure 66 *- a) Correlation between the mass of the sample and the TiO_2+GO load in the solution; b) enhancement of the DC conductivity with increasing the G.O. load in the solution*

Figure 67 shows the water adsorption isotherms, in adsorption and desorption, for the different activated carbon clothes impregnated with P25 and GO and the pore radius distribution. It is possible to observe that the addition of titania and graphene by simple impregnation method does not strongly affect the porosity, like previously described silica/titania composite.

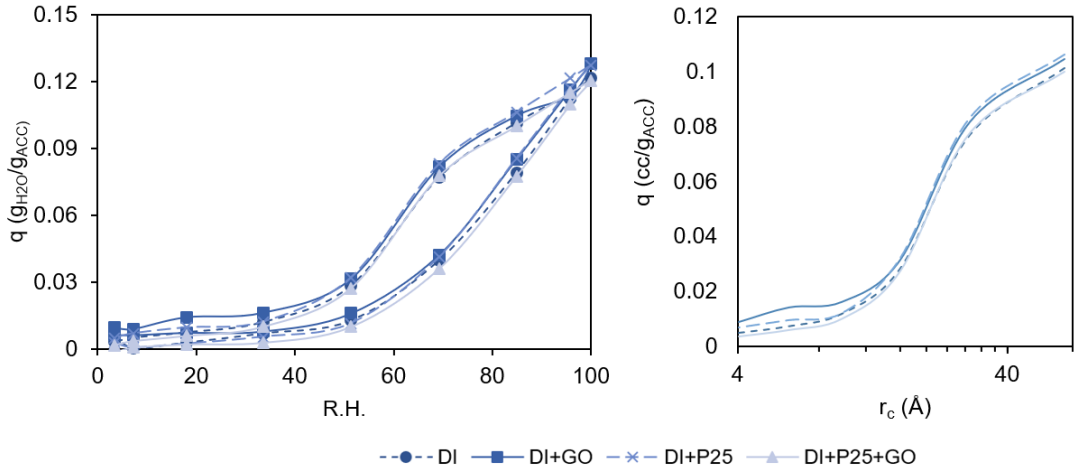

Figure 67 *– Water vapor isotherm of the DI-washed-ACC and impregnated with GO and TiO_2.*

Adsorption isotherms

MEK adsorption on activating carbon cloth has been found to fit a Langmuir model. The isotherms were conducted with the coexistence of a saturated salt solution, in order to control the relative humidity inside the reactor. Figure 68 reports the results of the isotherm fit with a Langmuir model.

U.R.	q_m *mgMEK/gCA*	K_L *l/mgMEK*
94%	25.2	1.5
75%	25.3	3.0
53%	29.3	3.8
33%	26.8	8.4

$$q = \frac{q_m K_L C}{1 + K_L C}$$

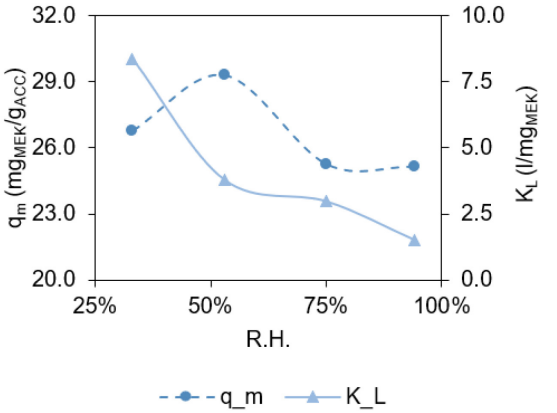

***Figure 68** - Langmuir constant resulting from the data fitting (Equation 16). Effect of the relative humidity on the Langmuir isotherm parameters.*

The Langmuir constant (K_L) indicates the extent of interaction between adsorbate and the surface. The most robust interaction between adsorbate and adsorbent occurs at lower R.H., while the maximum adsorption density is reached for R.H. equal to 53%. q_m, defined as the maximum mass of adsorbate to form a mono-layer, slightly decreases with the RH, showing a maximum for RH=53%. This can be due to cooperative adsorption between the two molecules for medium/low water loading, while it became competitive adsorption for higher concentrations [223].

ACS electrical resistivity

As previously reported, in paragraph 2.2.3.2, activated carbon cloth exhibits a resistive behavior, when exposed to the air. However, its electrical resistivity does not depend only on the presence of functional groups, but also on other parameters: in fact, carbonaceous materials are often used as substrates for sensors, because the adsorption of gases (or water vapor) may result in a variation of the electrical resistivity.
While activated carbons are hydrophobic, they show high affinity to water vapor. A variation of the environmental concentration of water vapor results in a change in the number of water molecules adsorbed, which may reflect into the change of the electrical resistivity of the adsorbent. Table 33 reports the variation in electrical conductivity at different relative humidity level.

***Table 33** - Effect of the relative humidity on the ACC electrical conductivity*

UR %	σ (S/m)
33	3.1E-04
53	2.8E-04
75	2.0E-03
94	1.7E-03

The deposition, by impregnation, of TiO_2, reduces the electrical conductivity of the ACC. Firstly, the only washing with DI water, lye ions and carbon particles that participate in the transmission of charges. For this reason, the coal subjected to washing (DI) has a lower electrical conductivity than the pristine ACC. The only

addition of GO leads to an abrupt increase of the electrical conductivity, which is mitigated by the co-presence of titanium dioxide.

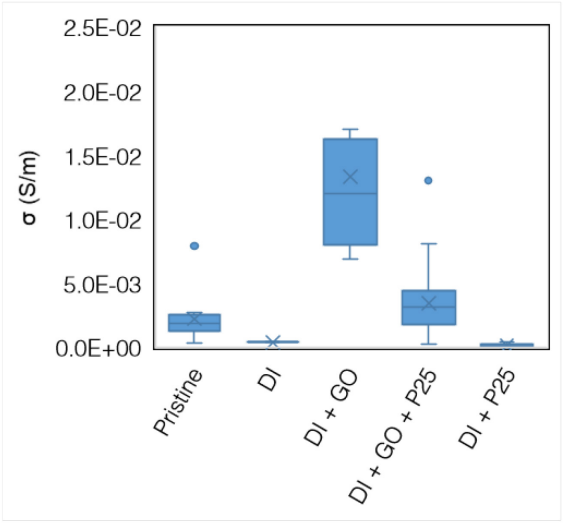

***Figure 69** - Effect of type of treatment on the ACC electrical conductivity*

Maintaining constant the amount of TiO_2 and varying the GO content, it is possible to increase the electrical conductivity of the ACC (Figure 70-a), while maintaining a constant load of GO (Figure 70-b), an increase of the photocatalyst reduces the conductivity.

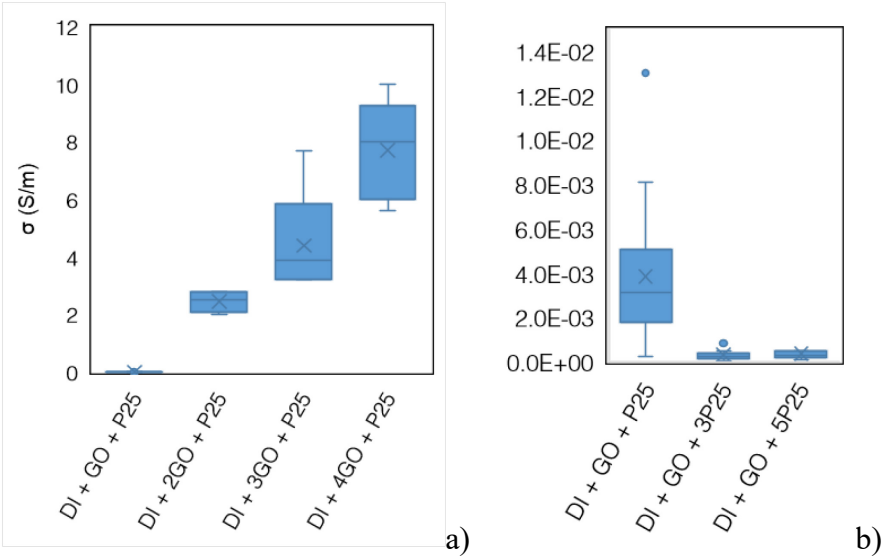

***Figure 70** - Effect of the TiO_2 and GO load on the ACC electrical resistivity*

It has already been reported that the electrical resistance of carbon conductors changes when exposed to an atmosphere of some gas or vapor [224,225].
This behavior is reported in Figure 71 and Figure 72. The grey line is the relative humidity, which ranges between 85 and 88% during the whole test. The crosses are the amount of MEK in the air, not adsorbed, determined by gas chromatography. The difference between injected MEK and this latter one is represented by the blue line, which is also reported in abscissa in Figure 72.

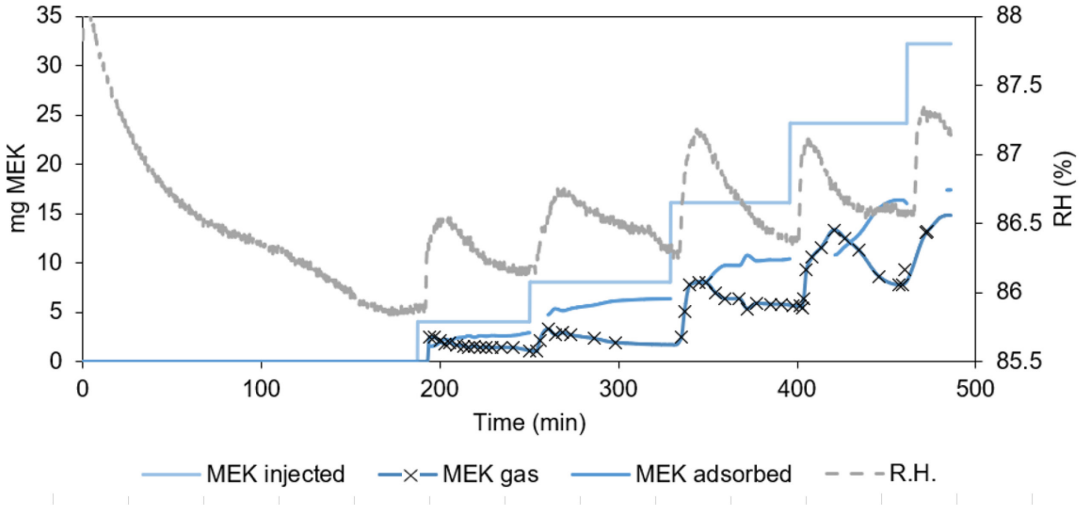

***Figure 71** - Adsorption by ACC of subsequent MEK injection*

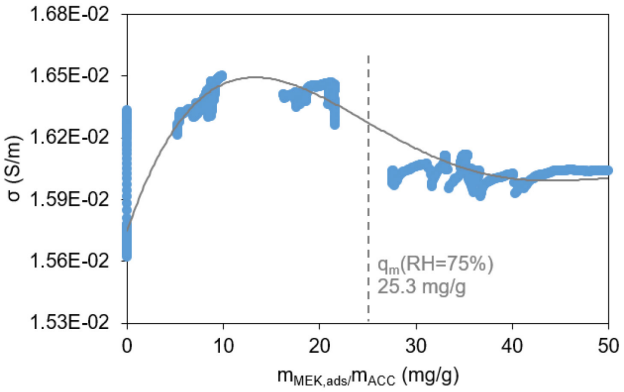

***Figure 72** - Variation of the electrical conductivity by the amount of MEK adsorbed*

After a given amount of MEK has been injected into the reactor, it is possible to observe an increase of the electrical conductivity which is annulled once the capacity of activated carbon has been reached.

2.3.4 Discussion

2.3.4.1 Silica/Titania composite

In this paragraph, starting with the most promising adsorbent materials previously tested, silica and activated carbon were coated with TiO_2. As there are numerous publications in which the above-mentioned composites have been realized, characterized and tested, the first subparagraph, has focused on the realization of a SiO_2/TiO_2 composite starting from metallic titanium.
This choice was justified by the fact of being able to use a waste material as a titania precursor. This method allows obtaining a good covering of the silica, without

excessively affecting the porosity of the adsorbent material, which also acts as a support.
Beyond that it can be considered a simple method for the synthesis of this composite; one drawback of the method is the production of diluted sulfuric acid, as a reaction by-product, which cannot be recovered within the TiO_2 production process. Another problem with this method is the need to reach high temperatures for the production of the mixture.
In the production of a silica-titania composite, while the silica original adsorptive capacity and surface area decrease, the surface area of pure titania significantly increases, playing an essential role in the dispersion and support for the TiO_2. However, the method chosen significantly influences their adsorptive properties:

- the simple mixing of the two oxides, aided by ultrasonication, doesn't strongly affect the surface area and the pore volume, as TiO_2 particles aggregates of tens of microns are placed on the silica surface;
- the hydrothermal method better overlay the silica surface with titanium within the size of hundreds of nanometers, but the surfaces area is negatively affected:
- Both composites show photocatalytic activity toward the degradation of NO_x and MEK. Composites with the lowest amount of TiO_2 (3%) show the best performance and the highest surface area.

The production of silica/titania composites, starting from metallic titanium and commercial-available silica shows a possible new way for a real scale commercial production of such composite.
This method was applied as well for the deposition of TiO_2 on clays, fly ashes and activated carbon; however, the requirement of high temperature to calcinate the catalyst make it not optimal for activated carbons, because of their low thermal stability.

2.3.4.2 Carbonaceous nanomaterial/Titania composite

A carbonaceous material can be coupled with a photocatalyst for many reasons: to operate as support, to increase the concentration of a pollutant in the proximity of the catalyst, to introduce defect or new bonds with the TiO_2, in order to change the bandgap energy or enhance the separation of the photogenerated electron/hole couple. Obtaining a successful junction between carbon and TiO_2 lies both in the deposition technique adopted, both in the type of material. By using the same TiO_2 deposition method (sol-gel technique), different target carbon materials have been tested. Among these, only the addition of graphene oxide showed an increase of the photocatalytic activity, measured as the efficiency of removal of nitrogen oxides, while the other carbonaceous materials were poorly dispersed in the solvent, as well as in the final solution together with the TiO_2 precursor. All the composites exhibited a higher bandgap, compared to the one reported in the literature, but it can be explained by the addition of DMSO into the TiO_2-precursor.

2.3.4.3 Carbon nanowall/Titania composite

In order to study the individual processes effectively and the coupled processes, from a nanometric point of view, instead of a macroscopic scale, an ad-hoc composite was prepared.

To the carbon, nanowall belongs a series of unique properties, which highlight them concerning the other allotropes. Being a vertical sheet of graphene, by varying the geometry and the density, it is possible to modify the porosity of the material. The introduction of impurities within the crystalline structure, such as boron, allows varying the electrical resistivity and the bandgap. The formation of a heterojunction with the TiO_2 allows separating photoinduced couples more effectively, increasing the photocatalytic process efficiency. By varying the gelation time of the organic precursor, it is possible to vary the height of the titanium dioxide layer, thus obtaining different thicknesses and reducing the optical bandgaps.

2.3.4.4 Activated Carbon Cloth/Titania composite

The activated carbon cloths a preferable option as a catalyst support, because of their high surface area, lightweight and self-sustaining property, and they are relatively inexpensive. For these reasons, they have been intensely studied in this work.

The decision to use a commercial photocatalyst and to deposit it using simple wet impregnation lies in the fact that this method does not introduce further variables into the study and because of a broader source of information available in the literature.

The study about the parameters affecting the electrical resistivity of an activated carbon cloth is justified by several points: firstly, since it is a function of the adsorption capacity of a specific adsorbate, it can provide important functions on the state of depletion of the active sites; secondly, dealing with a corona discharge, with the same applied potential, the greater the electrical resistivity, the smaller the electric field will be.

The impregnation of activated carbon cloth with a TiO_2 containing solution results to be a simple and inexpensive method for producing an adsorbent / photocatalytic composite; however, electrical conductivity is penalized both when the ACC is immersed in water and when the P25 is deposited. This problem can be solved by introducing graphene oxide to the solution. The higher is its concentration in the solution, the greater the electrical conductivity will be, but not necessarily its photocatalytic response.

Most of the literature identifies the coupling of "cold plasma" with the photocatalysis with the term "plasma-catalysis." However, often are only considered synergies with a relatively high degree of ionization. In typical configurations, the catalyst is placed together or downstream the plasma region. This combination has been reported to be a promising technique for the removal of gaseous compounds, able to increase the efficiency of the non-thermal plasma and to improve the selectivity towards harmless products.
An unexplored aspect in literature is the effect of weakly ionized gas, close to plasma, applied to a photocatalyst. In this paragraph:

- *Using a corona discharge-configuration, where the photocatalyst covers the electrode, the enhanced removal of VOC and NOx has been studied;*
- *A novel method for the combined photocatalytic activity determination and bandgap estimation has been developed, and it has been used to indirectly estimate the effect of the electric field on the optical bandgap of the semiconductor.*

2.4 Photocatalysis and Electrostatic

2.4.1 Introduction

The synergistic effect between a catalyst and an ionized gas is generally called "plasma-catalysis." The high energy of the electrons produced by the corona discharge, present in the electrostatic filter, allows for a series of electron collision processes with the molecules of the flowing gas, resulting in a range of excited species and positive and negative ions. These excited species have, generally, a short lifetime, so that they cannot play an important role in the process chemistry. Are an exception few states of excited oxygen which contributes to the formation of additional OH radical [226,227] and more stable products, like O_3. Many explanations have been provided to explain this phenomenon, among which the production of ozone, the catalyst activation by the corona production of UV radiation, the plasma-induced adsorption/desorption/oxidation of chemical species and the local heating. Whitehead reported how [95] not only the plasma affect the catalyst, but how also the catalyst affect the plasma: think of the cell capacitance change due to the introduction of the catalyst, and/or the plasma conformation due to the shape - and porosity- of the catalyst. Some author also suggested that the micro discharges, formed inside the catalyst pores may be responsible for the enhanced degradation of chemicals [228], as well as the dielectric constant of the catalyst and the pore size [229] may play an important role.

In the scientific literature, most of the publications concern the application of an NTP through a dielectric barrier discharge configuration, where the dielectric and the catalyst coincide, or the latter is located downstream of the reactor [96,227,230]. A smaller number of publications consider the application of a corona discharge-like configuration to a catalyst [231–233]. Also, this type of synergy is used mostly for the removal of gases, such as exhaust gas, NOx, and volatile organic compounds dangerous for health.

An aspect not covered by the literature is what happens to the catalyst at applied potentials lower than the corona onset voltage, i.e., during the Townsend regime or, even before, during the background ionization.

By means of a First-principle study, Zhao et al. [234] investigated the influence of an external electric field on the electronic structure and optical properties of TiO_2 and they find out that the TiO_2 energy gap became narrower as increasing the electric field was increased, and it reached 0 eV when the electric field was 0.25 eV. For this reason, an application of an external electric field may result in an enhancement of the photocatalytic activity, due to the extension of the absorption edges to the visible region.

Similarly, Futera and English [235] investigated the effects of external electric fields applied to TiO_2/water interfaces using nonequilibrium molecular-dynamics techniques. Interestingly, the static electric field may induce alignment of the water molecules thanks to the water dipoles, and a stronger response of the interfacial hydrogen bonding between TiO_2 and water.

Guo et al. [236] synthesized lithium-doped sulfated titania nanoparticles and tested the photocatalytic activity by methylene blue degradation, in the presence of an electrostatic field. The enhanced degradation of MB was attributed to the Franz–Keldysh effect, which reduced the TiO_2 optical absorption edges with the electric field.

In this paragraph, TiO_2 has been applied over an aluminum electrode, which has been grounded. Photocatalytic degradation of NOx and VOCs by TiO_2 has been investigated in the presence of an external electric field.

2.4.2 Materials and methods

2.4.2.1 Sample Characterization

The catalyst used was TiO_2 P25 Aeroxide®. A TiO_2 paint was obtained mixing a primer, dispersant, and water, and then applied on an aluminum support. The aluminum plate had dimensions of 10x5x0.1cm and the exposed surface was finely grated to achieve better adhesion of the paint on the support.

2.4.2.2 Experimental Procedure

VOC removal

Experiments were run according to a fixed procedure. After washing the TiO_2-coated aluminum support with distilled water, the surface was dried for 15 minutes under an IR-lamp and left outside the reactor until it reached room temperature.

For evaluating the VOC removal efficiency, a batch reactor, inspired by the Italian standard UNI 11848, has been used, in parallelepiped-shape polymethylmethacrylate (PMMA) reactor, having a total volume of 3.8 L (24 cm (L) × 18 cm (W) × 9 cm (H)). Its particular realization allows a tangential flux over the sample (Figure 73).

***Figure 73** - VOC photo-electro catalytic reactor*

After positioning sample inside the reactor, a known volume (corresponding to 33 mmol) of the selected VOC (MEK, acetone, toluene or benzene) was injected into the reactor.
VOC, CO_2, CO measurements, were performed by an infrared photoacoustic analytical instrument (Bruel and Kjaer Multi-gas Monitor Type 1302), while ozone concentration measurements were realized with a UV Photometric Ozone Monitor (API Ozone Monitor Model 450).
Air samples were taken, approximately, every 2 minutes and the concentration curves were approximated as a pseudo-first order kinetic.

$$\frac{dC(t)}{dt} = kC(t) \qquad \textit{Equation 21}$$

Where k is the reaction constant (min^{-1}), and C(t) is the concentration of VOC. Data fitting was obtained by performing least square minimization with the Levenberg-Marquardt algorithm. Efficiencies of VOC removal are expressed as follows:

$$\eta_{PCO} = \frac{k_{PCO} - k_{blank}}{k_{PCO}} \times 100 \qquad \textit{Equation 22}$$

$$\eta_{PCO+ESP} = \frac{k_{PCO+ESP} - k_{blank}}{k_{PCO+ESP}} \times 100 \qquad \textit{Equation 23}$$

blank is referred to a VOC decay within the TiO_2-painted aluminum plate placed inside the box, in the absence of both UV and ESP powered. In *PCO* test setting UV lamp is turned on. Under *PCO+ESP* conditions, both UV lamp and ESP are powered.
To estimate how the combined use of PCO+ESP can improve the PCO process in the VOC removal, the *Increment of VOC removal efficiency* index is introduced:

$$\Delta\eta_{VOC} = \frac{k_{PCO} - k_{PCO+ESP}}{k_{PCO}} \qquad \textit{Equation 24}$$

And are the kinetic constant (k) obtained from Equation 21, for the PCO and PCO+ESP phases. The net CO_2 obtained by coupling the processes is evaluated by the following index:

$$\Delta\eta_{CO_2} = \frac{[CO_2]^{eff}_{PCO+ESP} - [CO_2]^{eff}_{PCO}}{[CO_2]^{th}_{max}} \qquad \textit{Equation 25}$$

Where $\Delta\eta_{CO_2}$ is the difference of CO_2 produced, normalized by the theoretical stoichiometric CO_2 achievable.
The carbon mass balance is computed considering only the first hour of activity. CO and CO_2 production were monitored and compared with the moles of VOC injected.

It is reported that water vapor affects catalysis, and it could be possible to keep it into account by using a Langmuir-Hinshelwood (L-H) competitive species approach (Yu and Lee 2007); however, since in our experiments humidity was kept substantially constant, it was considered possible to adopt a unimolecular reaction kinetic. The Langmuir-Hinshelwood (L-H) kinetics is the most commonly used equation to describe the kinetics of the heterogeneous catalytic processes [237–240].
It is described by the following equation.

$$r = \frac{dC}{dt} = \frac{kKC}{1 + KC} \qquad \textit{Equation 26}$$

Where C is the specific concentration of the considered compound, k the reaction rate constant and K the NO adsorption constant.

NOx removal

The experimental apparatus is illustrated in Figure 74. The photoreactor has a volume of 3L, and it consists of a Pyrex glass cylinder. Inside is placed a thin aluminum plate, coated on one side with the TiO_2 catalyst. This plate is laid on a polymethylmethacrylate (PMMA) support, above which the tungsten wire is placed at a variable distance from the plate. Three PMMA support with a fixed distance between the wire and plate of 1.5cm, 3cm, 4cm were used. Retention time inside the reactor has been imposed between 3 and 1.5min, depending on the inlet flux. The experimental apparatus is coincident with the previously described, except for the ozone monitor, connected through a bypass of the NOx analyzer

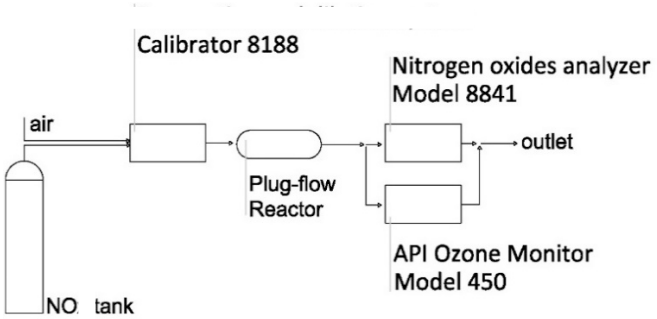

***Figure 74** - Experimental apparatus: NOx and ozone analysis are carried out separately, using a bypass downstream the plug-flow reactor*

Experiments were run according to a fixed procedure; each test is divided into five parts, of different duration.

1) NO, and NO_2 concentrations are stationary;
2) the UV lamp is turned on for 30 minutes, in order to activate the TiO_2 (PCO);
3) the electric potential is applied to the discharge electrode (ESP), without turning off the UV lamp, for the next 30 minutes, in order to have the combined effect (PCO+ESP);

4) the the UV lamp is turned off. Only the ESP is still on (ESP). This phase lasts for 20-40min, depending on the time needed to have constant concentrations;
5) The ESP is turned off. NO and NO_2 stabilize at the initial concentrations.

For each active stage (UV, ESP, UV+ESP), NO removal efficiency was calculated as reported in paragraph 2.3.2.1. Moreover, NO_2 selectivity was evaluated as follows:

$$S_{NO2/NO} = \frac{{NO_2}^{ON} - {NO_2}^{OFF}}{NO^{OFF} - NO^{ON}} \qquad \textit{Equation 27}$$

Where NO^{OFF} , ${NO_2}^{OFF}$ are the initial concentrations of NO and NO_2 while both ESP an UV are turned off (ppb); NO^{ON}, ${NO_2}^{ON}$ are the concentrations of NO and NO_2 while ESP or UV or ESP+UV are turned on (ppb); therefore, a negative selectivity indicates a reduction of NO_2 instead of a production.

2.4.2.3 Multi-LED reactor

NOx apparatus

The apparatus, the test conditions, and the reactor were adopted by the Italian Standard UNI 11247, where a continuous flow test method is used for the determination of the degradation of nitrogen oxides in the air by inorganic photocatalytic materials.
With the same apparatus previously described in paragraph 2.4.2.2, only the light is substituted with an array of LEDs, which are located at the center, outside the reactor, over the sample.
Colloidal samples of various TiO_2-based powders were prepared by sonication of the aqueous slurry for one hour, followed by concentration on a glass surface by slow evaporation under an IR lamp. Obtained samples were stored in a sealed chamber, and they were kept 1hour exposed to laboratory environments, before the test.

LED characterization

LEDs were purchased from Shenzhen Chundaxin Photoelectric Co. (Shenzhen, China) and they were chosen for their different emission peak; their characteristics are reported in Table 34.

Table 34 - LEDs characteristic

	μ, Spectrum peak [nm]		**σ^2, Variance**	**$E_{e,\lambda}$**	**R^2**
	Declared*	**Effective**	[nm^2]	[W m^{-2} nm^{-1}]	
LED 1	blue	467.5	15.2	1.11	0.9860
LED 2	420-430	424.4	10.5	1.10	0.9845
LED 3	400-410	402.4	10.8	0.46	0.9927
LED 4	385-390	378.9	7.2	0.74	0.9848
LED 5	375-380	377.8	6.9	0.43	0.9782
LED 6	365-370	370.6	7.0	0.40	0.9726

* Declared by the producer

LED spectrums were measured in the 200 – 800 nm range by using a spectrometer (model CAS 120, Instrument Systems, Munich, Germany). The CAS 120 is equipped with a crossed Czerny-Turner spectrograph and an array detector. The spectral resolution is 2.7 nm, the data point interval is 0.35nm, the wavelength accuracy is ±0.3 nm, and the integration time is 60 - 870 ms. Spectral irradiance ($E_{e,\lambda}$) was measured at three distances (d) and the follow inverse-squared relation was found:

$$E_{e,\lambda} = \alpha \frac{1}{d^2} \qquad \textit{Equation 28}$$

Spectrum peaks and widths were calculated by approximating spectra to normal distributions:

$$E_{e,\lambda} = \frac{1}{\sqrt{2\pi\sigma^2}} \exp\left(-\frac{1}{2}\left(\frac{\lambda-\mu}{\sigma}\right)^2\right) \qquad \textit{Equation 29}$$

Where μ is the wavelength at which the spectrum is centered (nm) and σ^2 is the variance.
Data fitting was performed with MATLAB *data fit* tool. For the sake of simplicity, Table 34 reports only one set of measurements, at a given distance, with the corresponding data fitting results and goodness.
Measured LEDs relative intensity of emission spectra are reported in Figure 75.

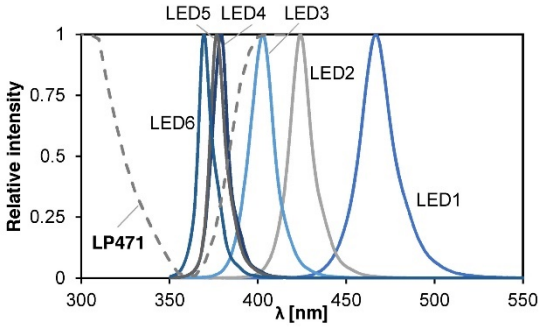

Figure 75 *- LEDs emission spectra.*

This combination of LEDs was chosen to study the 420-365nm region better, as shown by the overlapping region of the different spectrum. It is possible to notice how the emission peaks differ from the central value of the declared interval. Irradiance was also measured with a photoradiometer (Delta Ohm, HD2102.2, Padua, Italy) with a probe centered in the field of the UV-A (LP471), inside the reactor, for keeping into account the effect of the borosilicate glass reactor. This optical window is reported in Figure 75 by the dotted line.
The intensity of the photon energy (E_λ) provided by the different LEDs lights was calculated from the inverse relationship between those:

$$E = \frac{hc}{\lambda} \qquad \textit{Equation 30}$$

Where h is Planck's constant and c is the speed of light. The value of these and other commonly used constants are

$h = 6.626 \times 10^{-34}$ joule·s

$c = 2.998 \times 10^{8}$ m/s

Test procedure description

Once the sample is placed inside the reactor, and the inlet NOx gas concentration is stationary, the first led, characterized by the highest μ, is turned on. After 15 minutes, it is turned off and the second led is turned on for other 15 minutes. Those steps are repeated until the sample has been exposed to all the 6 LEDs. NOx and NO concentrations are monitored during the test. A generic schematic of the test is shown in Figure 76.

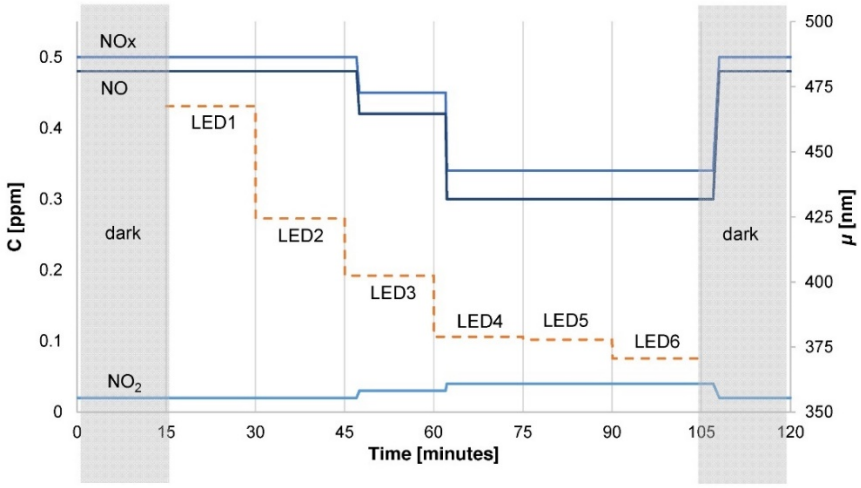

Figure 76 *- NO and NO_2 concentrations during test condition under different LED illumination*

It is possible to observe in Figure 76 the hydraulic residence time of the photocatalytic reactor by the time shift between the moment in which the LED is turned on and the begin of the decrease of the NOx concentration.

NO activity (A_{NO}) is an index to describe the photocatalytic activity toward the degradation of NO, in which C_{NO}^{dark} and C_{NO}^{light} are respectively the averaged concentrations of NO during dark and UV conditions, for each LED.

$$A_{NO} = \frac{C_{NO}^{dark} - C_{NO}^{light}}{C_{NO}^{dark}} \qquad \textit{Equation 31}$$

Similarly, the difference between the NO_2 concentration under light and dark conditions, normalized on the NO concentration, can be considered as an index related to the unwanted NO_2 selectivity. As C_{NO2}^{light} is greater than C_{NO2}^{dark}, the minus in front of the equation is to maintain a positive sign to the index.

$$A_{NO2} = -\frac{C_{NO2}^{dark} - C_{NO2}^{light}}{C_{NO}^{dark}} \qquad \textit{Equation 32}$$

These equations differ from Equation 13 and Equation 14 by the fact that, in this experiment, the light characteristics are not constant over time, so the activity is a function of these, over time.

Data elaboration

By comparing A_{NO} Index, it has been possible to individuate the wavelength at which the photocatalyst activates, so to estimate the bandgap. Two methods are reported:

- by simple observation of which LED interval the photocatalyst activation occurs. It is possible to appreciate it when the activity (A_{NO}) is greater than 0.05 (assumed as a threshold between the minimal observable activity and the background noise). This first method is more intuitive; however, it only provides an interval of reference, which strictly depends on the chosen LEDs.
- The second method is proposed to provide a more accurate estimate of the activation energy, and it is explained in the following way.

As the LED emission spectrum is well represented by a normal distribution, the cumulative distribution function is given by the following equation:

$$E_{e,\bar{\lambda}} = \frac{1}{2}\left(1 + \mathrm{erf}\left(\frac{\bar{\lambda} - \mu}{\sigma\sqrt{2}}\right)\right) \qquad \textit{Equation 33}$$

$E_{e,\bar{\lambda}}$ represent the total irradiance for $\lambda < \bar{\lambda}$, in which $\bar{\lambda}$ is the largest wavelength, at which correspond the minimum energy necessary to activate the photocatalyst. For ease of interpretation, these functions are plotted in Figure 77.

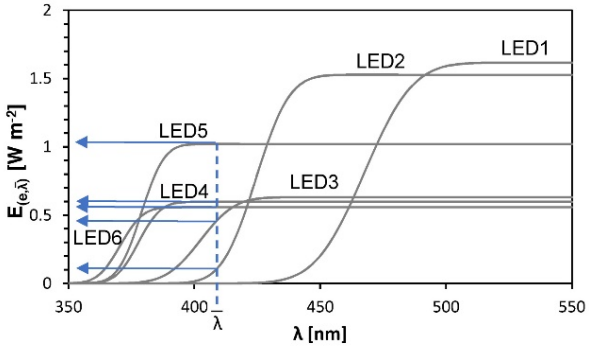

***Figure 77** - Cumulative distribution function adopted for the representation of different LEDs*

Assuming that a generic photocatalyst, having a band gap of E_0, is activated by electromagnetic radiation having a wavelength at $\lambda < \frac{hc}{E_0}$, it will exhibit photocatalytic activity A_{NO}, only when radiated by LEDs 2,3,4,5,6. Moreover, the relation between

photon flow (light irradiance) and photocatalytic activity, for E_e<1 Wm^{-2}, expressed as NO oxidation rate, can be considered linearly dependent [241,242].
By computing the goodness of the linear fit between $E_{e,\bar{\lambda}}$ and A_{NO}, for $A_{NO} > 0$, in the interval $350 < \bar{\lambda} < 500$ [nm], it is possible to estimate the value of λ. The goodness of fit was evaluated by means of maximizing the coefficient of determination, R^2, and minimizing standard error, *se*. To highlight the maximum and minimum of the functions, the first derivative was computed. An example is reported in Figure 78.

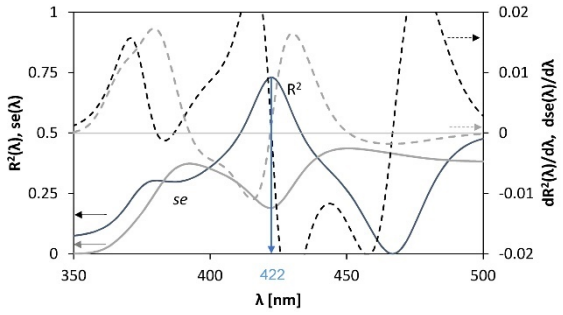

***Figure 78** - Determination of the best correlation between $E_{(e,\lambda)}$ and A_{NO} by computing the coefficient of determination (solid black line), and minimizing the standard error (solid gray line). Minimums and maximums are highlighted by the first derivative (dotted lines).*

Once λ has been estimated, it's possible to plot the relation between the two variables in order to evaluate the fit (Figure 79).

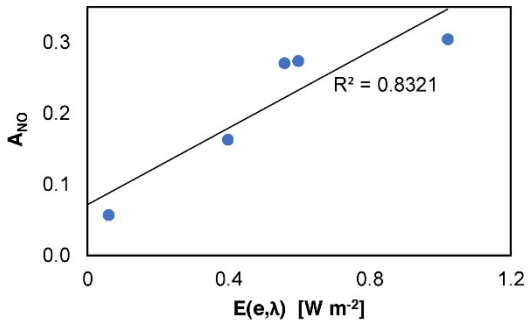

***Figure 79** - Correlation between A_{NO} and E*

2.4.3 Results

2.4.3.1 Enhanced removal of VOC

Employing Equation 21 for fitting the experimental data, an increased efficiency achieved by coupling the two processes appears evident.
It is shown in Table 35 that the decay rates (*Blank,* PCO, PCO+ESP) depend upon the substance considered and by the electrode configuration. Varying the wire to plate distance does not affect the photocatalysis, but the combined process. For instances, increasing the electrode distance, the induced electric field is weakened.

Table 35 *- Values of k (min^{-1}), reaction constant according to Equation 21 for several VOCs in different test conditions.*

	d (cm)	**k_{blank}** (min^{-1})	**k_{PCO}** (min^{-1})	**$k_{PCO+ESP}$** (min^{-1})
Toluene	2	-0.0142	-0.0223	-0.0234
Benzene	2	-0.0240	-0.0301	-0.0302
Acetone	2	-0.0238	-0.0431	-0.0481
Acetaldehyde	2	-0.0402	-0.0893	-0.09824
MEK	2	-0.0206	-0.0474	-0.0523
MEK	1.5			-0.0602
MEK	2.8			-0.0486
MEK	4			-0.0701

From Table 35 it is possible to observe the decrease of the rate by increasing electrode distance, reaching approximately, the same value of the kinetics in the absence of the electric field, with photocatalysis only. Moreover, the higher value found for d=4cm may be because the flow generated by the fan is parallel to the wire, but only a fraction of the air flux, between the wire and the grounded electrode, is under the ESP effect and conveyed over the catalyst. Now, increasing distance between wire to plate the electromagnetic field is weakened, but the whole airflow becomes subjected to it.
This not intuitive aspect is the rationale for the increase observed in MEK removal efficiency. A minimum is reached when the electric field is inadequately strong and more than one-third of the inflow air is conveyed above the ESP control.

CO and CO_2 evolution were continuously followed during tests. Depending on the photoacoustic transducer employed for monitoring, was found that benzene and toluene have interference with CO_2 filter, while acetone and MEK have a minor influence on the CO filter. All cross-correlations were taken into account. Photocatalytic process leads to an incomplete MEK oxidation into CO_2 and CO was also produced. $[CO_2]/[CO]$ ratio is not constant over the time: its maximum is equal to 80, tending to decrease at increasing time. Similar results were obtained and reported by O. Debono *et al.*[243] and Shang *et al.* [239]. The efficiency of conversion to CO and CO_2 is reported in Figure 80.

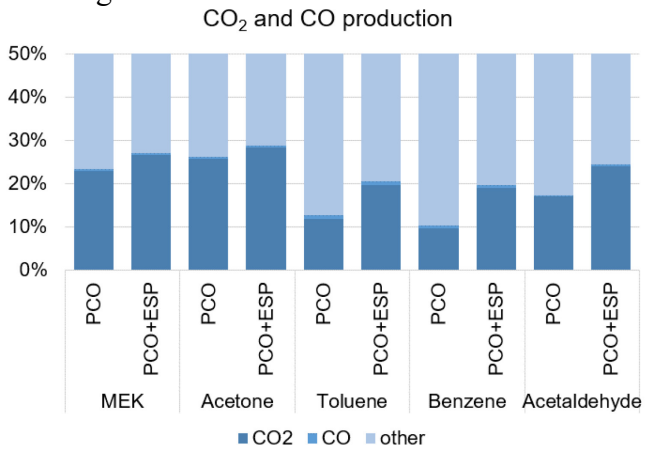

Figure 80 *– Mineralization rate of the different organic compounds under PCO and PCO+ESP conditions.*

Incomplete oxidation to CO_2 is evident by the yields of CO_2 and CO as final products. Although each test was run for approximately 2-hours, only the first hour is taken into account for the mass balance, as it is unlikely that in an indoor full-scale application longer reaction times may be reached.

In Figure 81 are plotted efficiencies of MEK removal along mineralization rate, as defined in Eq. 6. Data suggests that it is possible to increase the efficiency of MEK removal, keeping constant the mineralization rate, by associating the ESP process. The highest value of the mineralization rate belongs to the minimum of the $k_{PCO+ESP}$ curve in Figure 81.

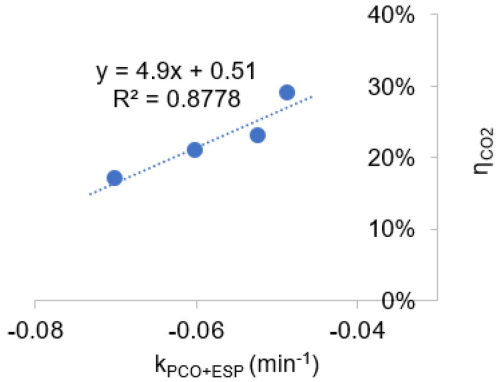

Figure 81 *- In abscissa is reported the rate of MEK removal, versus the enhancement of the mineralization rate, according to Equation 21, for different electrode spacing.*

2.4.3.2 Enhanced removal of NOx

NO removal efficiency and NO_2 production

At first, the NO reduction efficiency will be discussed. Many tests have been conducted, varying: (i) the ESP wire-plate distance; (ii) the inlet NOx mass flux; (iii) the empty bed residence time.

The distance between the plate and wire has been varied keeping constant the applied voltage and the NO massic flow inside the reactor. This modification changed the strength of the electric field and ozone production.

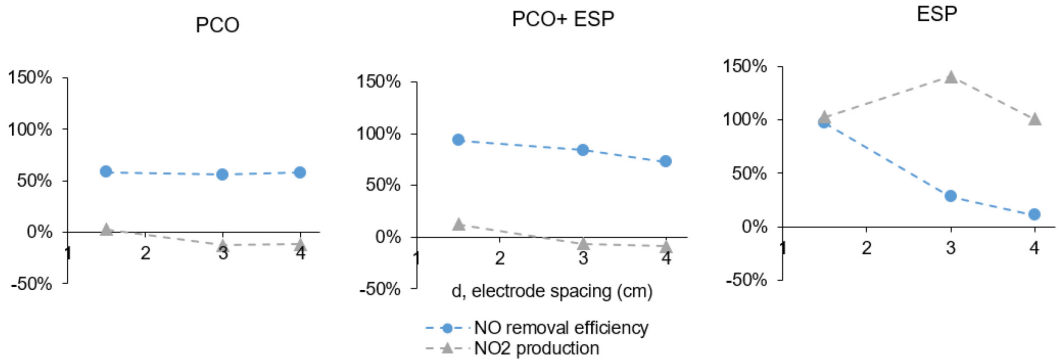

Figure 82 *– Effect of the electrode spacing in the NO removal efficiency and NO_2 production*

In Figure 82 it is possible to observe how during the PCO-only phase, the NO removal efficiency is constant, so to the NO_2 production, while during the ESP-only phase, NO removal efficiency highly increases with decreasing distance between the

wire and plate. With the combined phase, it is possible to reach the highest efficiency of NO removal, with a lower NO_2 production.
Generally, by introducing the ESP, NO_2 selectivity increases. In the case of ESP-only, values higher than 100% are observed. With the combined use of ESP+PCO, selectivity remains close to zero.

In this set of experiments, the inlet mass flow rate was varied in the range 0.82-1.59 μg_{NOx} min^{-1}. Figure 83 illustrates the results obtained.

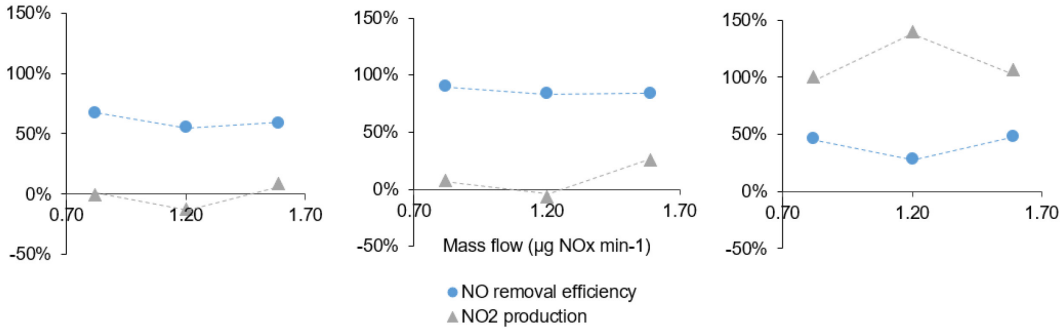

Figure 83 *- Effect of the mass flow in the NO removal efficiency and NO_2 production*

It can be observed that: the overall NOx reduction efficiency is comparable in both cases. As already mentioned, combining ESP with UV gives the best results: high removal rate (in the range of 80-90%) and low NO_2 selectivity (an average of 7%).
The selectivity in ESP-only operating mode reaches and exceeds a value of 100%. The explanation is given by the ESP-generated ozone which reacts with NO to produce NO_2 and by the plasma-generated of oxygen and nitrogen radicals and their recombination in forming nitrogen oxides.

O_3 production

As previously reported in paragraph 1.2.1, the ESP wire-plate configuration generates ozone. Analyses have been conducted with the purpose of determining the ESP ozone production with and without the UV illumination over the TiO_2 catalyst.
As reported in the literature [232,244,245], ozone is destroyed by TiO_2 when exposed to UV irradiation; an explanation was given by Forni et al. [246] which studied the reduction of ozone by hydrated electrons. The reaction results in the formation of the ozonide radical, followed by the production of additional OH• . Table 1 reports the ESP ozone generation rates with and without the presence of PCO. The experiments were conducted varying distance between plate and wire. All generation rates were observed constant with the time.

Table 36 *- Ozone generation rate for every different plate/wire configuration, during ESP-only and ESP+PCO phase.*

Wire-plate distance (cm)	ESP ($\mu g\ min^{-1}$)	ESP+PCO ($\mu g\ min^{-1}$)
1.5	2.53	0.96
3	0.16	0.10
4	0.00	0.00

As we can see from Table 1, at a fixed potential, the increase of the electrode distance affect the ozone production rates, by diminishing them.
Figure 84 shows the ozone concentration at different working conditions, in the presence and absence of NO_x.

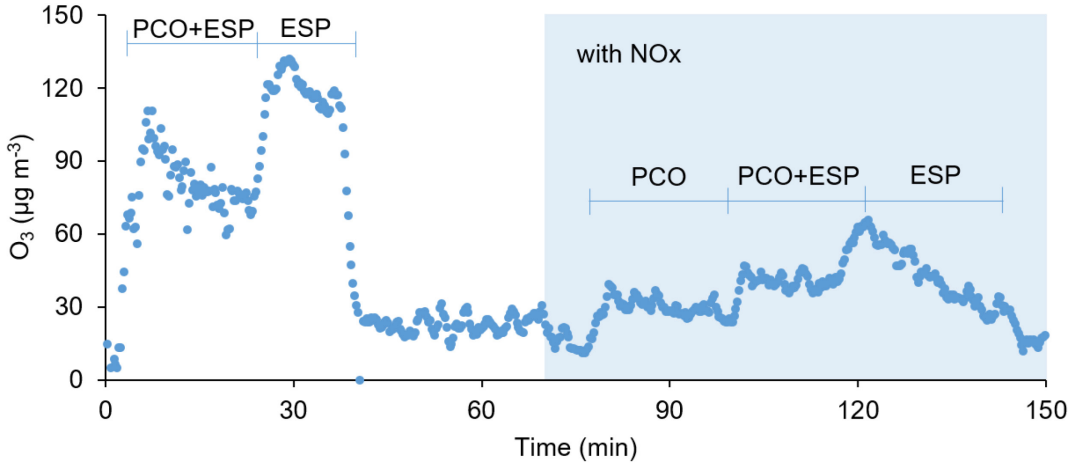

***Figure 84** - UV- only, ESP-only and UV+ESP ozone evolution in the presence or absence of NOx.*

Combining ESP and UV a maximum ozone reduction of 62% could be obtained.
The highest O_3 concentrations are reached during ESP-only mode in the absence of NO_x, while during UV-only mode, ozone levels are comparable to those naturally present in the atmosphere.
Combining ESP and UV the presence of nitrogen oxide halves the O_3 levels (since part of it react with NO to produce NO_2).

NO oxidation by O_3

When the NOx test is protracted for three hours in PCO+ESP conditions, NO_2 concentrations are unstable and tend to rise. For this reason, additional tests were conducted maintaining for 3 hours the active phases (PCO+ESP or PCO). It was found a linear correlation between the amount of O_3 monitored and the NO_2 produced during the active phase.

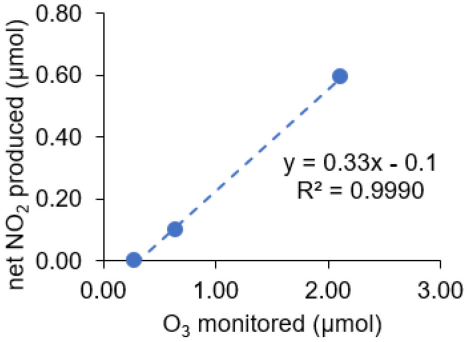

***Figure 85** - Correlation between NO_2 produced and O_3 monitored during a three hours test*

The linear relationship between ozone and nitrogen dioxide produced pointed to ozone as the responsible for the increased reactivity since it constitutes a preferential

path in the oxidation of NO to NO_2, without passing through the intermediate oxidation state of HNO_2 (nitrous acid).

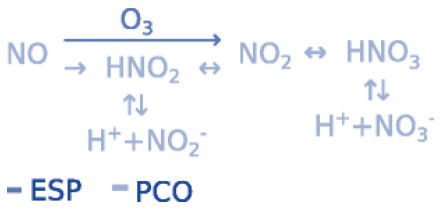

Figure 86 *- Suggested reaction pathway for NO oxidation*

Nitrate effect on TiO_2 catalysis.

As previously suggested, the ozone generated directly oxidizes NO to NO_2 within the gas phase. The shorter pathway avoids the production of NO_2^- characteristic of the photocatalytic process.

Further evidence comes from the nitrates to nitrites ratio found analyzing water extraction of the surface samples. The analyses show that the relationship between nitrate and nitrite depends on the amount of ozone produced: the higher the amount of O_3 produced, the higher is the NO_3^-/NO_2^- ratio (Figure 87).

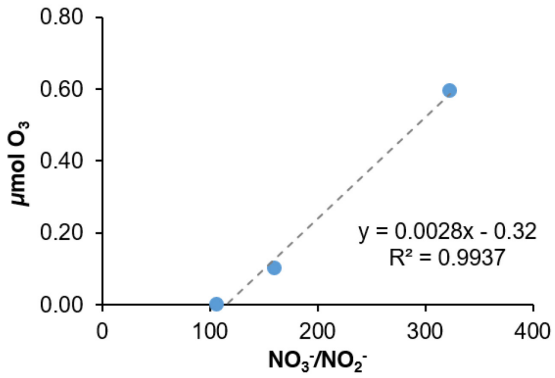

Figure 87 *- O_3 generated by ESP in the presence of TiO_2 under illumination, versus nitrate over nitrite ratio. Nitrate and nitrite have been determined in the water lecheate of the surface of the catalyst*

The effects of nitrate ions (NO_3^-) on the selective catalytic NOx reduction by TiO_2 catalyst were studied, preparing an aqueous solution of $Mg(NO_3)_2$ (840mg/l). The TiO_2-painted surfaces were added with the different amount of the solution and dried using an infrared lamp.

The efficiency and selectivity measured indicate that higher is the number of nitrates added, lower is the NO reduction and higher the NO_2 selectivity as shown in Figure 88.

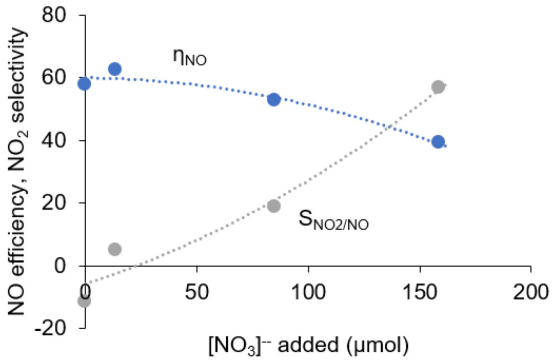

Figure 88 *- Reduction of NO removal efficiency and an increase of NO_2 selectivity related to the catalyst inhibition by the addition of nitrates.*

These findings agree with the work of other authors [247,248] who have reported that the presence of some inorganic salts may reduce the efficiency of the TiO_2 catalyst. This is due to the inhibition of the photocatalyst by the scavenging action of NO_3^- to the •OH radical or due to the characteristic nitrite absorption band, between 270 and 300 nm, which limit the maximum number of photons may reach the photocatalyst surface.

The Langmuir-Hinshelwood (L-H) model

The range of NO_x inlet flow rate was varied from 1.0 to 2.3 l/min. Reynold numbers associated with these inflow values were calculated by the following relation:

$$Re = \frac{d_h v_{air}}{\nu_{air}} = \frac{\frac{4A}{2\pi r}\frac{Q_{in}}{A}}{\nu_{air}} = \frac{2Q_{in}\rho_{air}}{\pi r\, \mu_{air}} \qquad \textit{Equation 34}$$

Where v_{air} is the fluid velocity, d_h is a characteristic linear dimension approximated by the hydraulic diameter of the reactor, r is the radius of the reactor, Q_{in} is the inlet reactor flux and is the air kinematic viscosity assumed equal to 1.58 10^{-5} m^2/s. The Reynolds number obtained ranges from 30 to 70, which indicates a laminar flow inside the reactor.

By assuming that the reactions are not mass-transfer limited and because the reactor chamber can be approximated to a plug-flow reactor, the reaction rate can be written as:

$$r = \frac{dC}{dt} = u\frac{dC}{dx} = \frac{Q}{W}\frac{dC}{dx} \qquad \textit{Equation 35}$$

Where Q is the flow rate, and W is the surface of the catalyst.

Humidity is considered constant for all the experiments, so competitive adsorption by H_2O is not taken into account. Hence, by combining Equation 26 with Equation 35, and integrating, Equation 36 was obtained, and it was linearly interpolated for obtaining k and K [249].

$$\frac{V}{Q(C_{in} - C_{out})} = \frac{1}{kK}\frac{\ln\left(\frac{C_{in}}{C_{out}}\right)}{C_{in} - C_{out}} + \frac{1}{k} \qquad \textit{Equation 36}$$

The goodness of the assumption that PCO and PCO+ESP reactions fit the L-H rate form is underlined by the R-squared coefficient reported in Table 37.

Table 37 *- Reaction rate constant, k, and the adsorption constant, K, calculated for the NO removal by the TiO_2-coated aluminum plate*

	k $mg_{NO}\ m^{-3}\ s^{-1}$	K $m^3\ mg_{NO}^{-1}$	R^2
PCO	0.882	$1.47\ 10^{-3}$	0.736
PCO + ESP	3.37	$1.60\ 10^{-3}$	0.720

As shown, the K adsorption constant, results almost equal for both PCO and PCO+ESP processes, differently from the reaction rate where PCO+ESP results four times higher (3.37 $mg_{NO}\ m^{-3}\ s^{-1}$) than that computed in PCO-only (0.882 $mg_{NO}\ m^{-3}\ s^{-1}$). These values are comparable to the ones found by Hüsken et al. [249]. The enhanced reaction rate observed in the combined process can be due by the formation of ionized reactive species, which intervene in the overall reaction pathway.

2.4.2.3 Multi-LED reactor

Nitrogen Oxides Abatement

Nitrogen oxides removal indexes, obtained according to the Italian Standard UNI11247, have been determined equals to 36%, 41%, 43%, 46%, respectively for $hTiO_2$, $hSiO_2/TiO_2$, P25, KRONOClean7000® samples.
Nitrogen oxides removal indexes, obtained according to the procedure described in Section 2.4, are reported in Table 38. It was found that:

- the amount of NO_2 generated is higher at higher wavelengths;
- to a higher NO activity corresponds to a higher production of NO_2

Table 38 *- Calculated photocatalytic NOx abatement indexes.*

LED		**$hSiO_2/TiO_2$**		**P25**		**KRONOClean7000**		**$hTiO_2$**	
Name	Peak (nm)	A_{NO}	A_{NO}	A_{NO}	A_{NO2}	A_{NO}	A_{NO2}	A_{NO}	A_{NO2}
LED 1	467	0.00	0.00	0.05	0.01	0.27	0.17	0.00	0.00
LED 2	424	0.06	0.00	0.30	0.22	0.27	0.17	0.00	0.00
LED 3	402	0.16	0.05	0.31	0.11	0.29	0.14	0.01	0.00
LED 4	379	0.30	0.08	0.33	0.06	0.30	0.07	0.17	0.05
LED 5	378	0.27	0.10	0.34	0.06	0.30	0.05	0.10	0.06
LED 6	371	0.27	0.11	0.34	0.07	0.30	0.04	0.13	0.06

By plotting values reported in Table 38 and Figure 89, it is possible to have a straightforward view of the material goodness: the score shape describe the sample and the color label the LED used. High A_{NO} scores and low A_{NO2} scores are desirable.

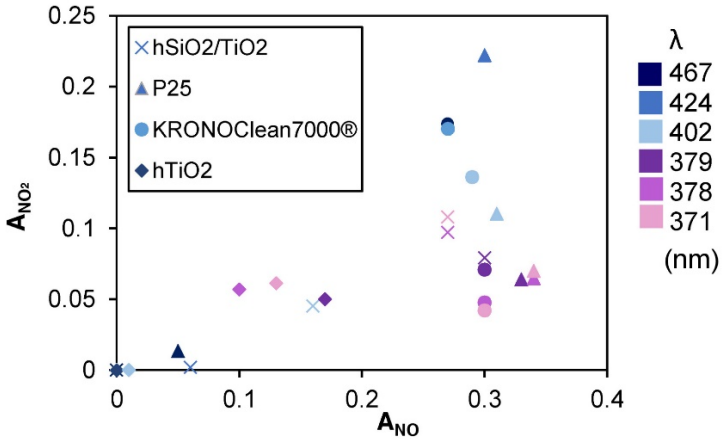

Figure 89 *- Activity indexes grouped by sample and UV light.*

Bandgap Estimation

The band gaps were obtained by plotting $(Kh\nu)^{1/2}$ versus the energy of absorbed light are approximately 3.05 and 3.25 eV, respectively for the P25 and the two titania synthesized by the hydrothermal method. The KRONOClean shows a bandgap of 2.32 eV.

Results of the bandgap estimation, by minimizing the standard error and maximizing the coefficient of determination, are reported in Table 39. Estimated bandgap energies, ($E_{\lambda,ext}$) fall in the determined activation ranges and they are compatible with the values obtained through UV-vis spectroscopy or the one reported in the literature (E_λ).

Table 39 *- Results from the bandgap estimation.*

Sample	Activation Range	λ_{ext} (nm)	$E_{\lambda,ext}$ (eV)	E_λ (eV)	Ref.
P25	LED 1 < λ < LED 2	422	2.94	3.05	[250]
KRONOClean7000®	λ > LED 1	>467	<2.65	2.32	[251]
$hSiO_2/TiO_2$	LED 2 < λ < LED 3	382	3.25	3.20	
$hTiO_2$	LED 3 < λ < LED 4	382	3.25	3.25	
Anatase				3.2	[252]
Rutile				3.0	[252]

Figure 90 shows the comparison between the proposed method and the NOx standard (a) and to the Kubelka-Munk estimation (b). By increasing the number of LEDs having emission peak close to the correspondent expected photocatalyst bandgap, it is possible to estimate its value better. For instance, as KRONOClean7000® exhibits photocatalytic activity since the first LED is turned on, it is not possible to individuate the end of the activation interval, while the method provides a good estimation for $hSiO_2/TiO_2$, $hTiO_2$, P25 with, respectively, 4, 4 and 5 different LED emission spectrum possess enough energy to activate the samples.

The imperfect correspondence between the two procedures, reported in Figure 90-a, is because two different samples were prepared for the two different tests and different lamps were used.

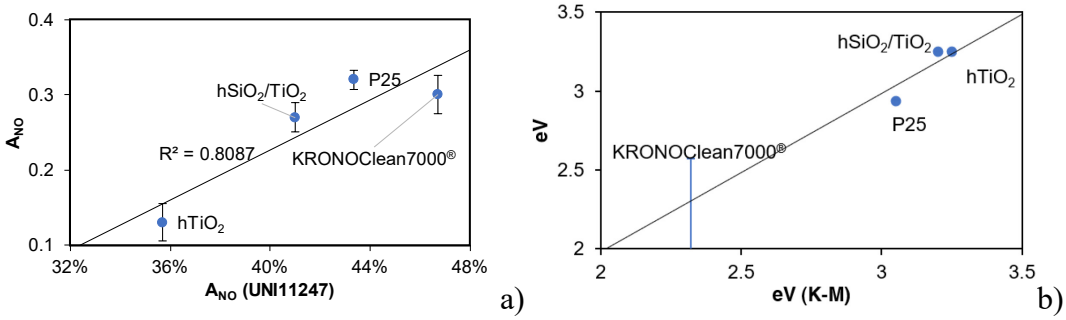

Figure 90 *- (a) Activity indexes grouped by the sample and UV light, (b) relation between the band gap estimated by diffuse UV-visible spectroscopy and the proposed method.*

NO Activity

It is well known that anatase shows a higher photocatalytic activity [253,254] than rutile. At 422 nm (2.94 eV) P25 shows photocatalytic activity, as rutile is reported to activate at 3.0 eV [255,256] and it slightly increases with lowering the wavelength. The silica/titania composite ($hSiO_2/TiO_2$) and the single titania ($hTiO_2$) exhibit similar photocatalytic activity. Despite the amorphous nature of the silica in the composite, XRD diffractogram indicates the presence of anatase, by the peak at 2θ = 25.32. KRONOClean7000 is C-modified anatase, and it was found to be active already at the first LED irradiation, with $\lambda > 467$ nm.

NO_2 Selectivity

The commercial KRONOClean7000, despite its low bandgap making it suitable for indoor applications, exhibits a high production of NO_2 (17.36%) at high wavelengths. At lower wavelengths ($\lambda < 379$ nm) unwanted NO_2 selectivity decreases to 4.2%. A similar behavior belongs to the P25, with the only difference that it activates between 424 and 427 nm. This can be due to the typical ternary composition of P25, where anatase, rutile, and amorphous TiO_2 are present in an average ratio of 78:14:8 [250] and the higher production of NO_2, as well the lower mineralization of organic compounds, it is linked to the presence of rutile [250,257]. However, the increased selectivity into NO_2 by higher wavelengths was also confirmed by Tseng et al. [258]. For the $hSiO_2/TiO_2$ sample, where TiO_2 in anatase form is deposited over a silica substrate, NO_2 production is lower (11%); similarly for the $hTiO_2$ sample obtained through the same hydrothermal method, but without the silica substrate, which shows a lower production of NO_2. However, this aspect is easily explained by the fact that efficiency is also lower.

Bandgap estimation in the presence of an external electric field

Once the previously described method, for the estimation of the bandgap, has been validated, the support carrier, described in paragraph 2.4.2.2, was placed inside the reactor, in order to apply an electric field on the photocatalyst. A potential of 3kV was applied to the discharge electrode.
A proper amount of P25 was deposited on the aluminum support by subsequent drying of the TiO_2/water solution.

Since the presence of ESP generates ozone, which in turn reacts with the NO, the photocatalytic activity has been calculated, point by point, taking into account the NO_x concentration instead. Figure 91shows the trend of the photocatalytic activities, in the presence (light blue) and absence (grey) of the electric field. On the right, in the second ordinate, is reported the peak wavelength of the lit LED.

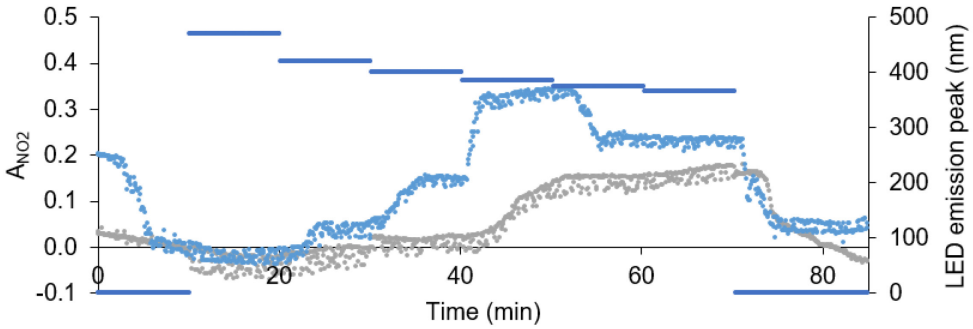

***Figure 91** - Trend of the photocatalytic activities in the presence (light blue) and absence (grey) of the external electric field*

It is possible to notice that, in the presence of the electric field, the P25 shows an increased activity already when illuminated by the second LED (peak at 424 nm). According to the error minimization procedure (reported in Figure 92), the best fit was found for λ_{ext} equal to 377 and 413 nm, respectively for the catalyst in the absence and presence of the electric field. This corresponds to a decrease of the bandgap energy equal to 0.29eV (from 3.29 to 3.00eV).

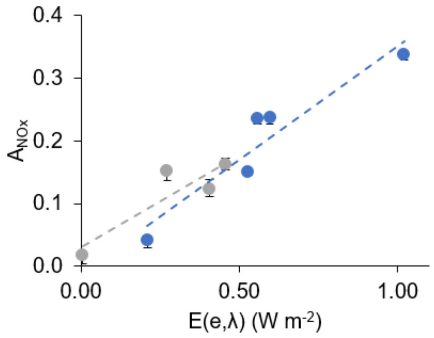

***Figure 92** - Correlation between A_{NOx} and E in the presence (blue) and absence (grey) of the electric field.*

2.4.4 Discussion

Coupling photocatalysis with an external electric field results in an enhancement of the removal rate of gaseous pollutants, such as VOCs and NO_x. Such enhancement depends on the nature of the pollutant, on the reactor geometry, on the intensity of the electric field.

Effect on VOCs

By coupling the use of electrostatic filtration and photocatalysis in situ, it was found that:

- Degradation level of VOC by PCO strictly depends on the substance itself. Aromatic hydrocarbon like benzene and toluene, have the lowest efficiency, aliphatic ketones like MEK and acetone are more easily decomposed.
- Coupling an electromagnetic field can augment photocatalysis. The efficiency increment depends upon the substance, the strength of the electric field and the geometry of the reactor. The highest increase in efficiency belongs to MEK (47.7%), the lowest to benzene (0.4%).
- At the same mineralization rate, the ESP increases VOC removal rate, while slowing down the catalytic reaction consent an increase of the VOC mineralization into final products, such as CO_2.

Effect on NOx

The photocatalytic NO_x conversion to NO_3^- by TiO_2 coated surfaces has been proposed for reducing the environmental pollution. This work aimed to investigate if and how it was possible to increase the efficiency of this process, combining it with the electrostatic process in hybrid technology. The results obtained show that:

- NO removal efficiency by photocatalytic oxidation reached a value of 60% while selectivity into NO_2 is generally disadvantaged; with only-ESP, due to micro discharge, additional NO_2 may be produced from atmospheric N_2. Ozone production, as well as NO_2 production, are strongly related to the intensity of the electric field.
- A linear correlation shows how NO_2 produced and ozone generated are related. Their production over time is constant and is linked to the formation of nitrites and nitrates on the surface of the catalyst. As final products, the accumulation of these anions on the surface of the catalyst, shifts the reaction equilibrium towards the NO_2, such that it is possible to appreciate the increase of its concentration over time. Since ozone oxidizes NO to NO_2, an increase in NO_2 leads to lower consumption of O_3 and an accumulation of the former. This may explain the correlation of these species.
- With the PCO+ESP configuration, only NO_2^- and NO_3^- were observed as final products. Catalyst de-activation and loss of selectivity have been attributed to the accumulation of nitrate on the active surface.

Effect of the electric field on the bandgap

A novel method and protocol to estimate a photocatalyst bandgap, by correlating the photocatalytic efficiency, evaluated as removal of NOx, with the intensity of the irradiation provided by an array of LED characterized by different emission peak, has been developed and tested.

After a good correlation between the estimated values of bandgap and those obtained using the Tauc method has been demonstrated, the developed protocol was used to evaluate the change in the TiO_2 bandgap, in the presence and absence of an applied electric field.

Numerically, it has been modeled that the application of an electric field can reduce the bandgap of the TiO_2 to zero for an electric field strength equal to 0.25 eV [234].

Experimentally, in this study, the application of an electric field to the TiO_2 has shown photocatalytic activity when irradiated with light having a longer wavelength, than in the absence of an electric field. This increase may be due to the Franz-Keldysh effect, which turns in a narrowing of the band by 0.29eV.

After studying the synergistic effects of each coupled process, all three processes were applied simultaneously in the same reactor. Since it is well known that the goal of the electrostatic precipitation is the removal of particulate matter, this aspect will be omitted in the discussion, to focus on the synergistic effect operating to the gaseous pollutants. This final paragraph about the study and optimization of the synergies will discuss the following points:

- *The choice of material influences both the configuration (and intensity) of the electric field and its stability over time. In particular, the greater is the permittivity of the support material, the greater is the effectiveness of NOx removal; the greater is the adsorbent capacity of the material, the longer the process will be stable, avoiding the formation of unwanted by-products;*
- *The application of TiO_2 on an activated carbon cloth by simple impregnation proved to be the simplest and most effective technique at the same time. The addition of graphene oxide can improve the electrical conductivity of the composite and increase the efficiency of pollutant removal;*
- *As the application of the electric field constitutes an additional external force toward the adsorbent material, its application may enhance the adsorption, as inhibit the desorption of the reaction products.*

2.5 Combined process

2.5.1 Introduction

2.5.1.1 Appraisal of the hybrid combined process

The purpose of this paragraph is to study the combination of the TiO_2 photocatalysis with the electrostatic and adsorption processes, in order to improve efficiency and reliability. Operating these three techniques in a single “hybrid” stage may be possible to achieve higher and durable removal efficiency and increase oxidation into harmless compounds [259–261].

To get an overview of the process, four different support materials were used, with the aim to highlight which features are the most important to take into account in assessing the effectiveness of the process. In order to apply the same amount of TiO_2, homogeneously and durable, on all the supports, a solution composed of TiO_2, water, and dispersant was prepared ad hoc, and then applied with a brush on the various supports.

2.5.1.2 Activated carbon cloth/TiO_2 composite

After having carried out the previous tests, the activated carbon cloth was chosen as adsorbent material and support on which deposit the photocatalyst, due to the high adsorption capacity, good electrical properties, and the self-supporting characteristic.

The aim is to capture the adsorptive effectively, and then further decompose the adsorbate by the action of the photocatalyst so that the original adsorption site of the active carbon can be regenerated.

Activated carbon-supported TiO_2 composite coupled with plasma has been used by few Authors in order to study the degradation of toluene [262], ethylene [263], phenol [264], NOx [265], chloroform [266] and chlorinated-VOC [267].

In order to increase the electrical conductivity of the ACC and to enhance the TiO_2 activity [268], in this last part of the study, graphene oxide, was added to the aqueous TiO_2 solution, before impregnating the ACC. The effect of the catalyst and the graphene loadings on the oxidation of MEK and NOx was evaluated.

2.5.2 Materials and methods

2.5.2.1 Appraisal of the hybrid combined process

TiO_2 (Degussa P-25) (40g), a primer (30g) and deionized water (400ml) were mixed to make a slurry used for painting plate supports. An aluminum (Al) and graphite (G) plates, a commercial activated carbon fabric sample (AC) and polyethylene support (PE), all having 10x10cm dimension, are coated with the described slurry and air-dried for two days. The average coating load is approximately 4.0±0.3 mg cm^{-2}.

Two reactors were used to evaluate the single and combined processes. For monitoring the ozone production and evaluating the NOx removal efficiency, a plug-flow reactor described by the Italian standard UNI 11247 has been used (previously described in paragraph 2.3.2). The only difference, is the presence of a tungsten wire, on which is applied a specified electric potential, over the sample.

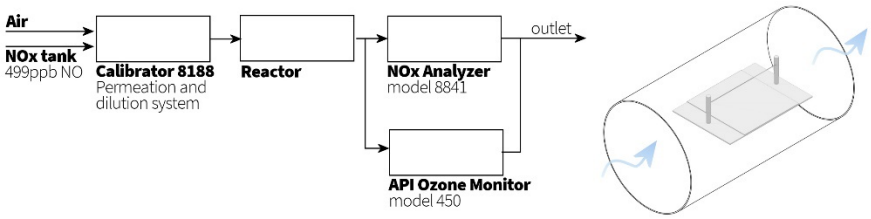

Figure 93 *– NOx photo-electro catalytic reactor*

Test procedures were fully described previously (Paragraph 2.4.2). Briefly, for the NOx removal test, every single test runs continuously for 3h and it is divided into 5 different phases: (I) NO and NO_2 reach constant concentrations, (II) UV lamp is turned on, to activate the TiO_2 photocatalysis (PCO), (III) ESP is turned on jointly with the UV lamp, (IV) UV lamp is turned off while ESP remains still on, (V) ESP is turned off with the NO and NO_2 stabilizing at the initial concentrations.

The NO removal rate (k_{NO}) and the NO_2 production rate (k_{NO_2}), were calculated as follows:

$$k_{NO} = Q\frac{C_{NO}^{off} - C_{NO}^{on}}{A} \qquad \textit{Equation 37}$$

$$k_{NO_2} = -Q\frac{C_{NO}^{off} - C_{NO}^{on}}{A} \qquad \textit{Equation 38}$$

Where, Q is the inlet flux, constant and equal to 1.5 l min^{-1}, C_i^{off} is the concentration of the i-specie in stationary condition without electric field and irradiation, C_i^{on} is the concentration of the i-specie with the electric field and/or UV irradiation and A is the sample exposed surface.

As selectivity is an important parameter to take into account, the production of NO_2, as an unwanted product, was monitored. Visible-light photocatalysts have been under great observation because of their possible application in indoor conditions; however, their effective beneficial provision must be questioned. Bloh et al. [257] arbitrarily assigned a relative toxicity ratio of 1:3, for NO and NO_2. For this reason, systems characterized by high activity, but low selectivity into final products (nitrates) could potentially increase the indoor air toxicity by the formation of NO_2. The application of photocatalytic materials in cement matrices can occur by the combined use of materials with high adsorbent capacity [65].
Each singular test, for a specific process, is represented as a point characterized by the coordinates (k_{NO}, k_{NO_2}). The location in the lower-right side of the plot is considered favorable, as it denotes high efficiency in NO conversion together with low NO_2 production. The color of the point score represents the process, while the shape is associated of the support material.

2.5.2.2 Activated carbon cloth/TiO_2 composite

The procedure to prepare the ACC/GO/TiO_2 composite method was described in paragraph 2.3.2.4. The list of the different combinations between TiO_2 and GO is reported Table 40.

Table 40 *– Description of the ACC/GO/TiO_2 composite*

Sample name	mGO (g)	mTiO2 (g)
REF	0	0
GO	0.17	0
GO	0.17	0
P25	0	0.17
P25	0	0.17
GO+P25	0.17	0.17
GO+P25	0.17	0.17
GO+P25	0.17	0.17
GO+P25	0.17	0.17
GO+P25	0.17	0.17

Sample name	mGO (g)	mTiO2 (g)
GO+P25	0.17	0.17
GO+P25	0.17	0.17
GO+3P25	0.17	0.5
GO+5P25	0.17	1
GO+11P25	0.17	2
3GO+P25	0.5	0.17
2GO+P25	0.35	0.17
2GO+5P25	0.35	1
2GO+11P25	0.35	2
3GO+5P25	0.5	1
3GO+11P25	0.5	2

After the NOx removal efficiency was evaluated, six 50x100mm ACC composites, with the optimal amount of GO and P25 previously determined, were tested to determine the augmented removal efficiency of MEK. Table 41 reports the test conducted. It is possible to notice the absence of the PCO+ESP test, because of the ACC use, which makes it impossible to isolate the adsorption. Only for this test, the ACC from REMA Filtration was used.

Table 41 *- Summary of the MEK removal tests conducted with the ACC/TiO_2/GO composite*

	0kV	**7kV (ESP)**
Only ACC	blank	blank+ESP
ACC+MEK	ADS	ADS+ESP
ACC/P25/GO/MEK	ADS+PCO	ADS+PCO+ESP

The same instrumentation (SEM, FTIR and Raman spectroscopy) was used to characterize the samples. Moreover, to quantify the amount of adsorbed species in the ACC and to ascertain the presence of eventual reaction byproducts, a Gas Chromatography (GC) analysis has been conducted.

Two small stripes of ACC (approximately 150mg) were weighed and introduced into a 2ml glass container, which was filled with a known amount of CS_2 in order to desorb the organic compounds previously adsorbed in the ACC. After a sufficient contact time, 2µl of the solution were collected by a micro-syringe and analyzed with a Carlo Erba gas chromatograph (Flame Ionization Detector, injector split 1:15, carrier flow 2 mL/min, capillary column, 25 m × 0.32 mm, 0.52 µm cross-linked methyl siloxane, isotherm condition 50 °C).

2.5.3 Results

2.5.3.1 Appraisal of the hybrid combined process

Scatter plot of NOx efficiencies

The scatter plot of NOx efficiencies is reported in Figure 94. Conversion efficiency by the process (PCO-only, ESP-only, PCO+ESP) and by support materials are represented by a point in the plot.

All supports (activated Carbon, aluminum, graphite, PVC) have been superficially treated with the same TiO_2 slurry. Their photocatalytic behavior appears similar, as highlighted by their clustered position in the plot (blue), while the ESP-only phase process is characterized by a larger dispersion (grey). The black score cluster on the bottom right of the plot shows the combined PCO + ESP phase.

The higher dispersion observed is explained by Figure 95, where a third parameter, the electrodic distance, is introduced.

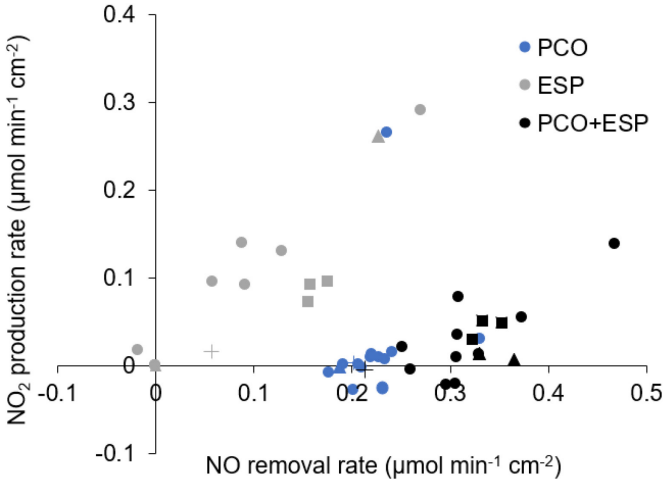

Figure 94 *– Scatter plot of NOx efficiencies. Colors are indicative of the process, the shape of the support material; ●Aluminium, ■Activated carbon, ▲Graphite, + PVC*

Effect of the electric field intensity

Coupling the PCO+ESP leads to higher NO conversion efficiencies (Figure 95-left) and a lower NO_2 production when compared to ESP-only process (Figure 95-right). The highest NO conversion efficiency achieved with the AC, Al and G support is found between 90% and 94%. None electrodes distance effect was observed with the PE support material; probably this may be due to the dielectric property of this material.

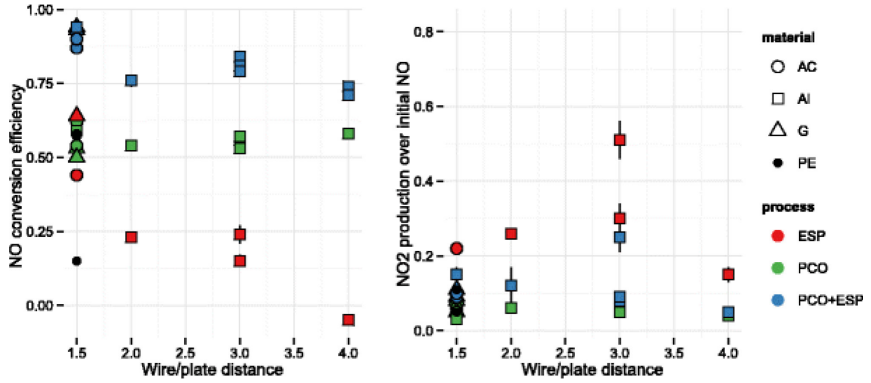

Figure 95 *- NO conversion efficiency and the NO_2/NO ratio at different electrodes distance*

Effect of the electrode material

With the aim to distinguish the effect of the different support material, longer tests were realized. In Figure 96 the NO, NO_2, NOx concentrations at the reactor outlet of the PCO+ESP phase during 6 hours of continuous observation are reported.
It is interesting to note the temporal NO_2 drift when using the aluminum support: its final concentration value (0.240ppm), is five times higher than the initial (0.049ppm). Differently, a slighter concentration increase is observed when using graphite, with a NO_2 doubling at the end of the test. No visible increase is found with the activated carbon support. The adsorptive capacity of support materials can explain the differences observed: higher adsorption capacity can hold the NO_2 produced or the

photocatalytic end-products of the reactions, like nitrates, may lower the inhibitory effect [269].

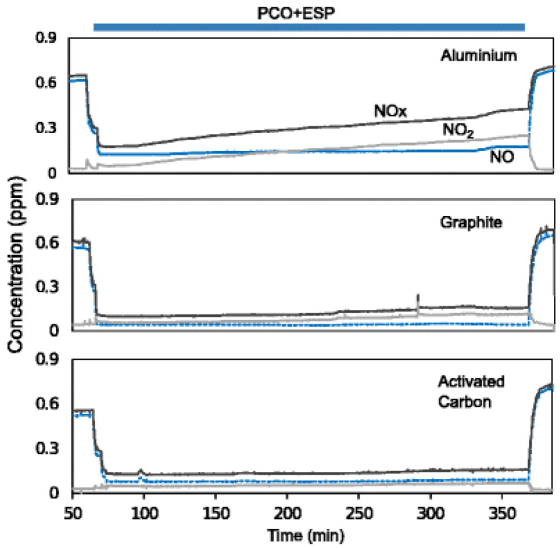

***Figure 96** - NOx, NO, NO_2 concentration, during the PCO+ESP phase, at the reactor outlet*

O_3 removal

The ozone production was monitored in the same plug-flow reactor used for the NOx test, varying the support material and the test conditions. After having reached a stationarity concentration of the ozone generated by the ESP-process, illuminating with the UV light, a sharp decrease is observed.

It is also found that the ozone generated by the ESP configuration is congruent to the wire to plate distance ratio: shorter distance increases the electric field strength and the ozone production. Moreover, when the same TiO_2-coated media is activated by UV light, with the same ESP configuration, lower ozone levels are detected.

Ozone reduction obtained by the different coated material is reported in Table 42. It is worth noting that the ozone generation with the ESP process varies between the different support material employed (0.195–0.336µg/min), while it is reduced at a constant value with the combined ESP+PCO process (0.112–0.165µg/min).

***Table 42** - Ozone production for the different materials coated with the TiO_2 mixture*

	Ozone generation (µg/min)						Ozone reduction (%)
	Environmental concentration		ESP-only		PCO + ESP		
	Mean	SD	Mean	SD	Mean	SD	
Aluminum	0.017	0.013	0.336	0.011	0.112	0.005	67
Activated carbon			0.195	0.005	0.157	0.004	20
Graphite			0.227	0.01	0.165	0.007	28

According to Guo et al. (2006), ozone can increase photons efficiency of the photocatalytic process, and it can react with other active species in order to produce additional $^{\bullet}OH$ radical and to reduce the ozone output.

2.5.3.2 Activated carbon cloth/TiO_2 composite

Adsorbent morphology

Figure 97 and Figure 98 collects the samples SEM picture at different magnification. For a better comparison, they have been reported separately. SEM observations confirmed the absence of remarkable modification in the activated carbon morphology between the raw sample with the application of the electric field (a,b), as previously reported in paragraph 2.2. The presence of MEK does not affect the morphology as well (c-d).

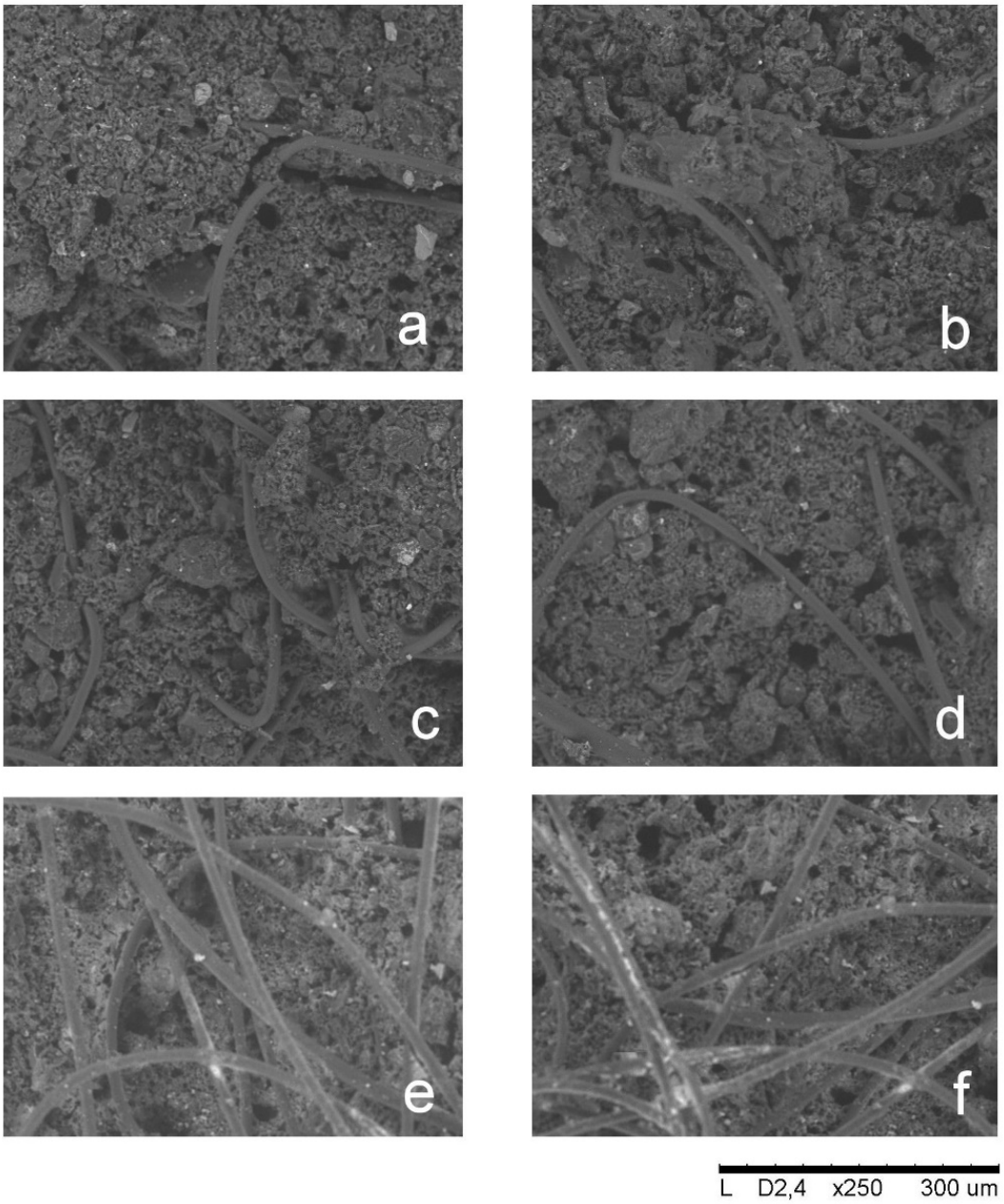

Figure 97 *- SEM pictures of the ACC (a) blank, (b) blank+ESP, (c)ADS, (d)ADS+ESP, (e)ADS+PCO, (f)ADS+PCO+ESP at 250x magnification*

TiO_2 has a characteristic particle diameter of between tens and several hundred nm. The agglomeration of bigger TiO_2 particles is observable on the activated carbon surface and over the fibers (e-f). The photocatalyst covering results in a smoother surface so that smaller holes are hardly observable. For this reason, the porosity may be negatively affected by such coverage.

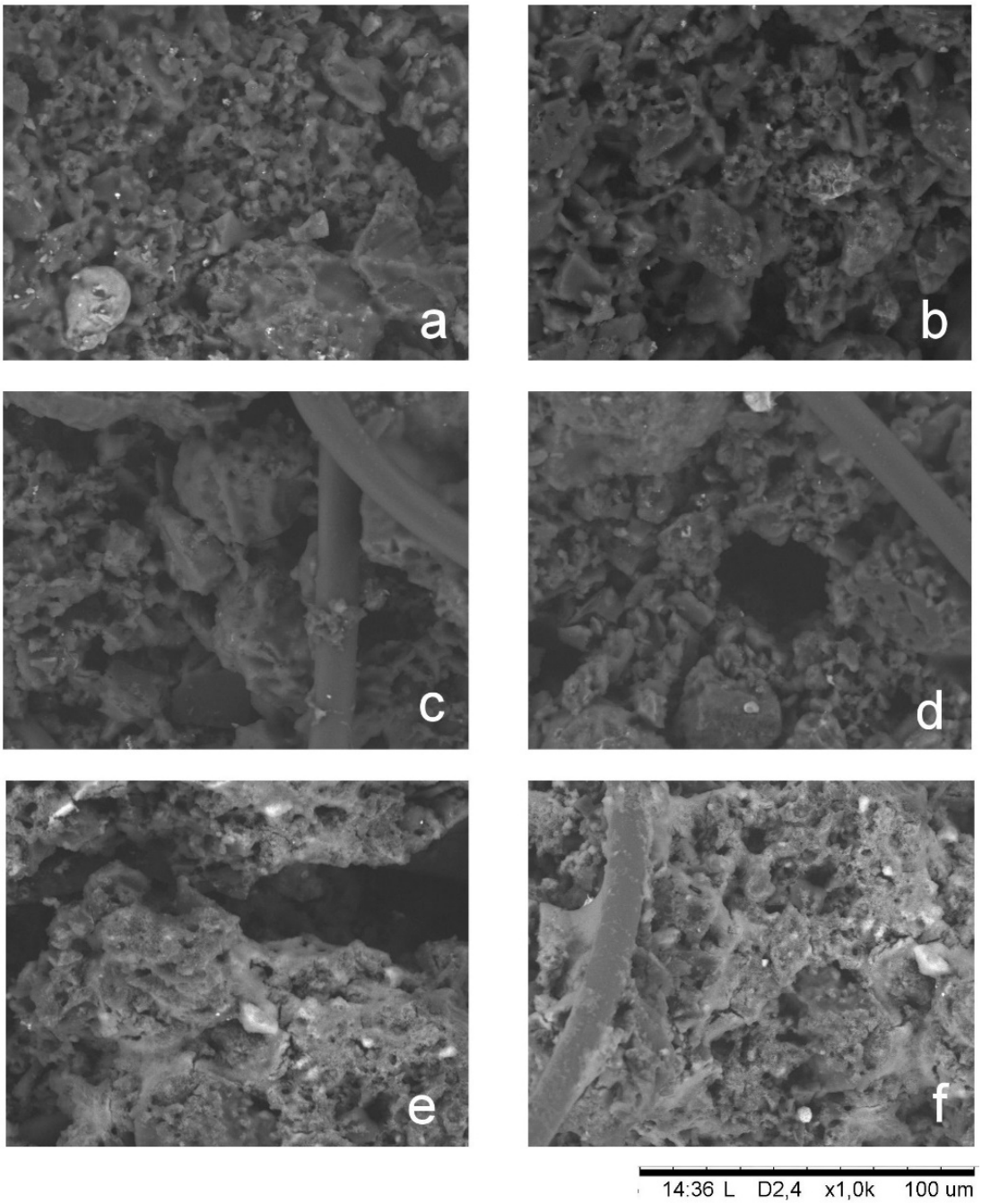

***Figure 98** - SEM pictures of the ACC (a) blank, (b) blank+ESP, (c)ADS, (d)ADS+ESP, (e)ADS+PCO, (f)ADS+PCO+ESP at 1000x magnification*

Raman spectroscopy

The Raman spectra of composites ACC+P25+GO is presented in Figure 99. The specific vibration modes are located at around 159 cm^{-1}, 400 cm^{-1}, 510 $cm^{-1,}$ and 630 cm^{-1}, indicating the presence of the anatase phase in all of these samples, together with two peaks at 220 cm^{-1} and 610 cm^{-1} assigned to the rutile phase. It is known that P25 contains both phases in the different amount [250]. The D and G peaks belonging to the activated carbon are not as sharp as for the bare ACC (paragraph 2.2.3), but they overlap with other two peaks, probably related to the graphene oxide.
A plasma can create oxygen vacancies into TiO_2 and electrons may be trapped on these vacancies, enhancing the electron-hole separation process [270]. However, the different peaks in the 100-850cm^{-1} region may be due to inhomogeneities of the catalyst, while the D and G peaks shifts are attributable to the application of the electric field, as reported previously in paragraph 2.2.3.

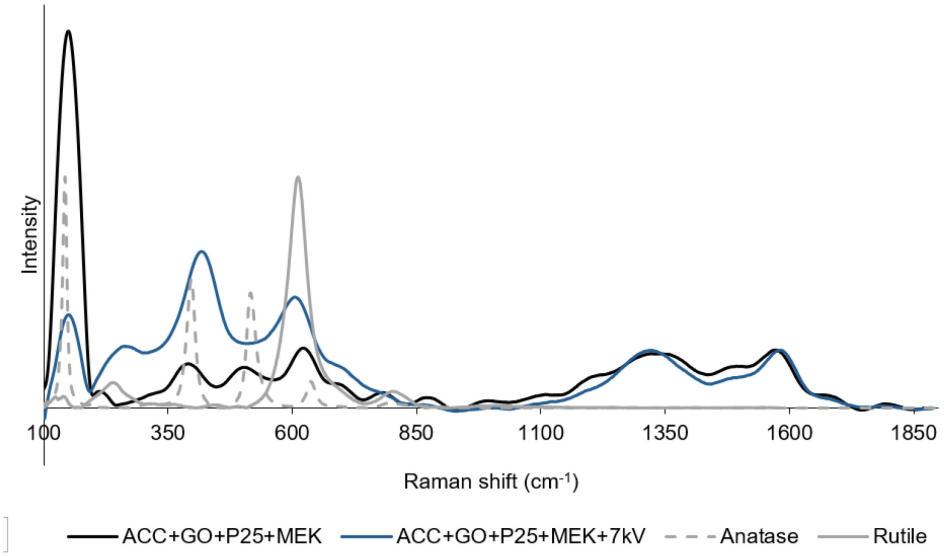

***Figure 99** - Raman spectra of the composite samples, with and without the application of the* electric field

FTIR spectroscopy

Figure 100 shows the FTIR spectrum of the fresh composite after the MEK adsorption and degradation and the composite with the same treatment with applied the electric field. A major band is clear around 1715 cm^{-1}, which is related to the C=O stretching, characteristic both from the activated carbon surface, both from the MEK adsorbed. It is interesting to see that with the application of the electric field, this intensity is lower, perhaps because of the mineralization of the MEK.

As a consequence of the application of the electric field, this peak should increase of intensity, as new functional groups are formed on the carbon surface. However, since the surface is covered with TiO_2, the formation of functional groups is hindered. A weak peak is reported at about 1450cm^{-1}, due to the C-H bending of the methyl group. Also this peak decreases with the application of the combined process. A similar trend is reported in between 1145 and 1200 cm^{-1}, which can be attributed to the C-O stretching.

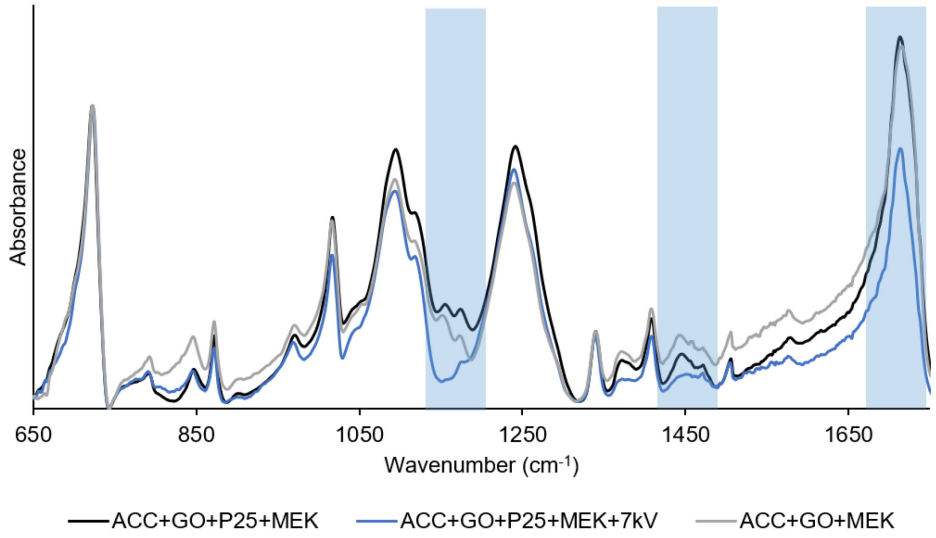

Figure 100 *- FTIR spectra of the composite with and without the application of the electric field*

GC analysis

Peaks height were multiplied by the CS_2 volume used to extract the organic compounds from the ACC and normalized on the ACC weight. These values are reported in Table 43.

Table 43 *– Peak area of GC analysis.*

Peak ID	**X1**	**ACC**	**X2**	**X3**	**CS_2**	**MEK**	**X4**	**X5**
Retention time (min)	**1.18**	**1.26**	**1.33**	**1.39**	**1.55**	**1.71**	**1.86**	**2.07**
				Area x1000				
ADS+PCO+ESP	39.2	46.6	10.8	13.3	6329	3973	53.4	9.2
ADS+PCO	11.7	49.7	3.0	8.1	5591	3809	35.3	5.2
ADS+ESP	24.6	9.5	8.7	6.5	7408	3818	34.2	5.6
ADS	12.3	13.9	6.0	8.1	5843	2990	58.5	8.8
blank+ESP	0.0	12.1	1.2	2.8	2134	0	19.7	0.0
blank	0.0	16.2	2.0	16.8	3177	0	31.3	0.0

*STD peak heights were not normalized on the ACC weight

It is possible to identify two main peaks: the solvent peak (CS_2) at 1.55 min and the MEK peak just after, at 1.71 min. The peak at 1.26 is due to some compound present in the ACC, as it is not present in the standards. All the other peaks are may be due to the presence of other impurities in the solvent or be adsorbed reaction products. It is interesting to see that the higher amounts of MEK and X1 were found in the samples with the electric field applied. The peak at 1.55, attributed to the CS_2, shows a similar trend; while it is representative of the solvent used for the extraction, due to its large relative amount, it may overlap other peaks produced by the MEK oxidation. Another interesting feature is the peak at 1.26min, attributed to the ACC, but it may depend as well by the GO presence or by other lighter oxidation products.

Photocatalytic activity: NOx removal

NO_x degradation by photocatalytic activity of the composite was evaluated by varying the GO and TiO_2 ratio.

In assessing the photocatalytic efficiency by the nitrogen oxides removal test, it can be stated that it depends on both the TiO_2 and the GO content. In particular, a photocatalyst increase leads to an increase in the removal efficiency of NO, up to an asymptotic level for TiO_2 concentration greater than 0.5 g/100 ml in aqueous solution. This finding is common in heterogeneous catalysis [271]; however, an increase of the graphene oxide content, can slightly penalize the photocatalytic efficiency, probably because it covers the photocatalyst surface and occludes the porosity of the adsorbent.

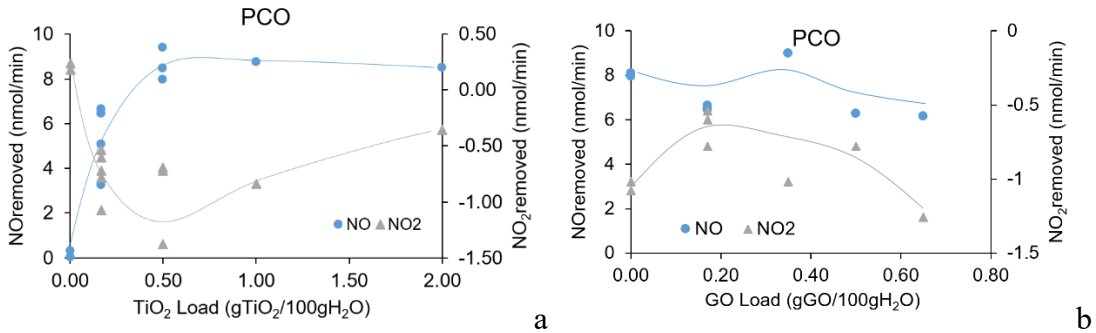

a b

Figure 101 *- NOx removal efficiency under PCO for different composition ratio of the ACC/P25/GO composite*

Both GO, and P25 concentrations do not affect the NOx removal efficiency significantly under ESP conditions (Figure 102), while they are important for the PCO+ESP process (Figure 103). In particular, the TiO_2 follows a similar observed behavior to the PCO-only process, where the efficiency reaches a plateau for the same threshold concentration. The GO addition, instead, does not seem to bring benefit to the NOx removal efficiency.

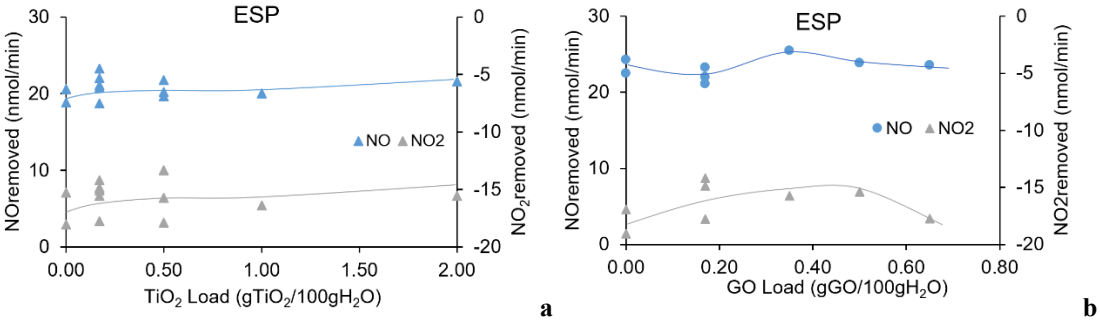

a b

Figure 102 *- NOx removal efficiency under ESP for different composition ratio of the ACC/P25/GO composite*

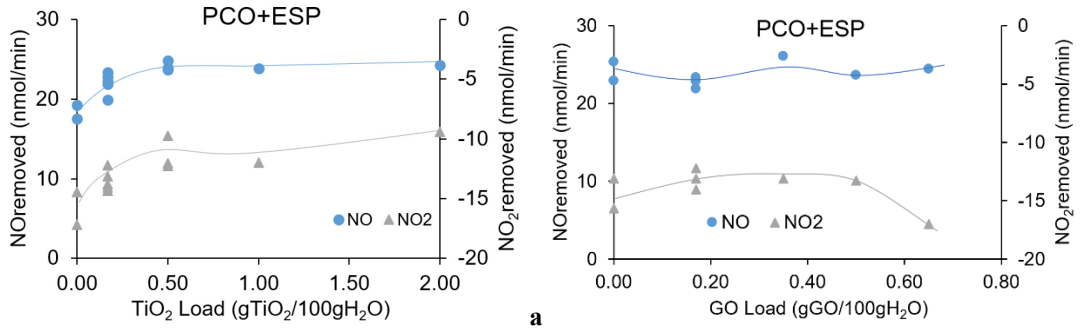

Figure 103 *- NOx removal efficiency under PCO+ESP for different composition ratio of the ACC/P25/GO composite*

For comparison, the individual and combined processes are reported in Figure 104. The highest NO_x removal efficiency belongs to the combined process, with a TiO_2 load higher than 0.5 and an optimal concentration of GO of 35g/l.

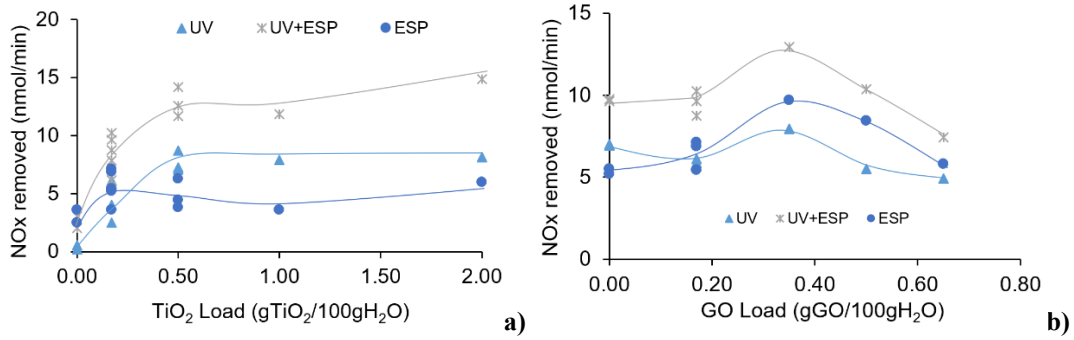

Figure 104 *- Comparison of the different efficiency*

The scatter plot of NOx efficiencies (paragraph 2.5.2.1) is reported in Figure 105. It is straightforward to notice that by using the combined process, a three-fold increase of the NO removal rate. The NO_2 production increases, but not as much as with the ESP only.

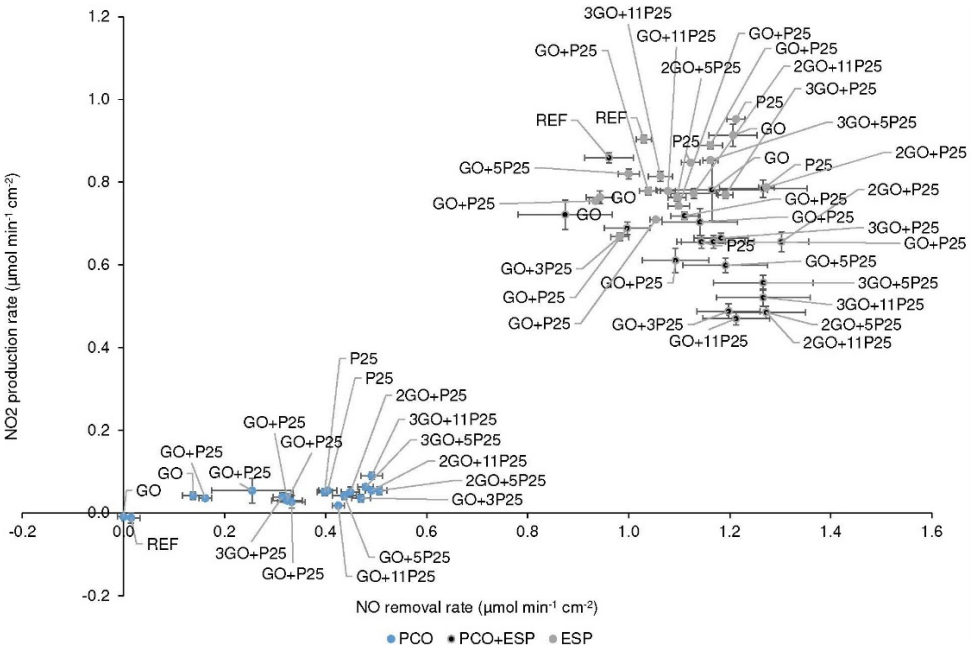

Figure 105 *- Scatterplot of NO_x removal by the ACC+GO+P25 composites*

Photocatalytic activity: VOC removal

VOC removal was studied using the apparatus described in paragraph 2.4.2.2. It has been found that the application of the electric field enhances the adsorption. However, on the other side, with augmented adsorption, the chemical reactions on the catalyst surface take place faster and then slow down thus the desorption of the products is inhibited. For this reason, in Figure 106, it is possible to notice how the final concentration of MEK inside the reactor is greater in the presence of the electric field if compared with photocatalysis only.

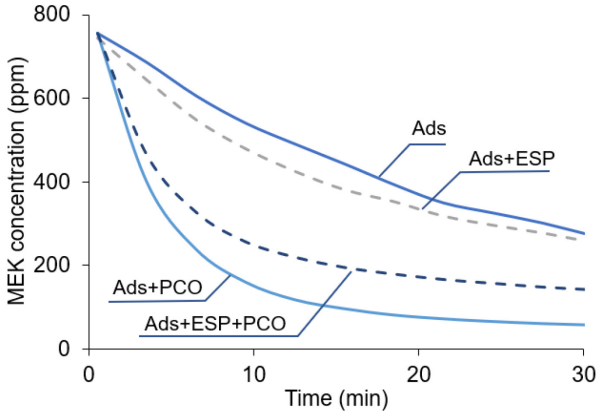

Figure 106 *- Removal of MEK under different test conditions by the composite under Ads, Ads+ESP, Ads+PCO, Ads+ESP+PCO conditions.*

This aspect is well evidenced by the tail of the MEK concentration in a test in which the electric field was applied at first and then turned off (Figure 107). What is possible to notice, is that once the electric field is removed, the concentration of MEK tends to rise again not following the original decay, reported by the dashed line.

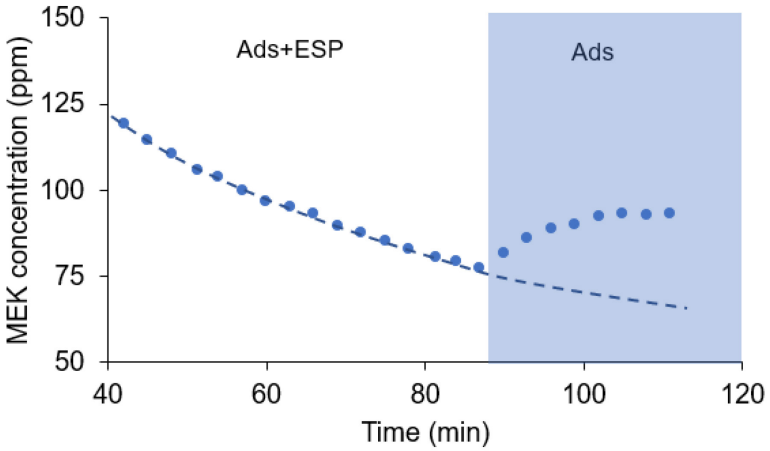

Figure 107 *- Test in which the electric field was first switched on and then off in order to evaluate the neighboring effect.*

2.5.3 Discussion

2.5.3.1 Appraisal of the hybrid process

This work combined electrostatic and adsorptive processes with TiO_2-photocatalysis, in order to build a hybrid air cleaning system and improve the overall removal efficiency. Different support materials coated with an aqueous TiO_2-slurry were submitted to single or combined processes of PCO, ESP, and PCO+ESP.
The fact that the photocatalytic oxidation occurred only on adsorbed compounds implies that the mass transfer to the active surface and the adsorptive process are critical steps in the PCO process.
It is found that coupling ESP with PCO achieves high NO conversion (up to 98%), much higher than the PCO alone; moreover, NO_2 generation is lower for PCO+ESP than ESP-only.
The support materials used in the coupled process (PCO+ESP) revealed of great importance for the coupled process. Particularly, the dielectric property of the polyethylene support, attenuate the electric field, leading to no appreciable differences between PCO and PCO+ESP configuration, within the electric potential employed. Conversely, when aluminum, activated carbon cloth, and graphite are used, the enhanced activity is much higher. It was also found that the choice of the material affects reliability over time.
By fitting the experimental data with the Langmuir-Hinshelwood kinetic, it was determined a fourfold increase of the kinetic rate constant by the combined process, while the adsorption constant remains unchanged.
The mineralization of organic gaseous pollutants is positively affected by the coupling of the processes. It was found that PCO+ESP could increase up to the 12 % the overall removal, with an increase of the CO_2 produced.
The ESP ozone production, in the presence of TiO_2 and under UV lamp, was found fourt times lower than in dark conditions and can be implemented to limit the unwanted ozone production by the electrostatic precipitators.

2.5.3.2 Effect on the ACC

Activated carbons clothes, impregnated with a solution of TiO_2 and GO constitutes good support and adsorbent to perform the synergistic process. However:

- The formation of NO_2, as a byproduct by the reaction of the NO with O_3, has to be kept into account. Higher efficiencies may be obtained, and a lower selectivity to NO_2 may be accomplished by choosing a proper adsorbent material as support;
- As the electric field enhances the adsorption, it limits the desorption of the reaction products. This aspect, if properly managed, can result in a higher retention time of the pollutants onto the catalyst, and to a higher chance to attain complete mineralization to CO_2 and H_2O

Chapter 3
Conclusions

In this last chapter, are reported the conclusion emerging from the previous Chapter, plus few considerations about the implementation of the hybrid process previously described and studied.

- *In paragraph 3.1 the meanings of the adjectives “novel” and “hybrid” are explained in the light of the process investigated and of the obtained results. This is comprehensive of the overall conclusion emerging from the previous paragraphs;*
- *In paragraph 3.2 a summary of the most important remarks affecting the process in its complexity is presented;*
- *In paragraph 3.3 few considerations about the strength and weaknesses of the process are reported, jointly some economic consideration about the process implementation;*
- *In paragraph 3.4 future developments are suggested.*

3.1 A novel hybrid air cleaning process

This paragraph presents the practical consequences that differentiate this process from those reported in the literature.

3.1.1 Why a “hybrid” process?

As presented in paragraph 1.2, a large part of the air purifier market uses different technologies for the removal of pollutants. The simplest and the most controlled method to succeed is to apply the different technologies in series. This aspect allows single processes to be optimized independently, and the choice of the materials and the process parameters affect only the process considered. According to this aspect, it is difficult to define as "hybrid" such processes proceeding simultaneously but in different successive stages, because each process maintains its characteristics and it is not affected by the previous one.

Instead of operating multiple processes in the same stage and simultaneously it is possible to develop new mechanisms and synergies affecting the single processes. The characteristics of a material can be altered both by the same process and by another operating simultaneously and in the same place. However, at the same time, the characteristics of material have repercussions on the processes that interest it.
This type of interaction, more complex than having different processes in series, gives unique properties to the new "hybrid" process, otherwise not obtainable, or allows to achieve similar results, regarding depollution efficiency, to the conventional tandem technologies, with a lower expenditure of energy or materials.

Adsorption is a process used since ancient times, and the first systematic study dates the XVII century [272]. The study of the electrostatic precipitation was subsequent to the industrial revolution, and the first patent, describing an apparatus for charging and the collecting particulate, dates 1907 [273]. Environmental photocatalysis is a newly-born remediation technique, still under intense studies [274].

The only difference in maturity of these technologies explains how it is possible that certain applications can still be partially unexplored or completely new. Moreover, the multiplicity of methods and configurations available to couple different materials and processes results in a more fragmented discussion of the topic. All these aspects show how difficult it is to provide a description of the occurring phenomena exhaustively, and how to optimize processes parameters and materials in a way that they actively participate in a positive synergy.

3.1.2 The novelty of the process

The main findings, emerging from the experimental section in Paragraph 2, are here listed. They are the main conclusions of the experimental part.

3.1.2.1 Gas removal by electrostatic precipitation

Electrostatic precipitation is an established technology for removing suspended particles from an air stream, by charging and transporting them toward a collecting plate. One of the most important features, of such process, is the absence of considerable pressure drops, due to the fact that the air flow is parallel to collecting plate, therefore making possible to handle large flow without having considerable load losses. The ozone production and the ionic wind are two secondary effects of the electrostatic precipitation. Coating the collecting electrode with an adsorbent, it is possible to adsorb the gases transported by the electrohydrodynamic force. The ozone generated may react with the gas or with the adsorbent, causing alterations of the surface, and advantaging (or disadvantaging) the adsorption of certain classes of pollutants.

3.1.2.2 Adsorption enhancement by an external-applied electric field

The ionic wind does not only enhance the diffusion of the adsorptive toward the surface of the adsorbent, but the applied force distribution results in an increase of the relative pressure, leading to a higher amount of gas adsorbed. This aspect was evident in Figure 107 where it is possible to appreciate the reversibility and the instantaneousness of the process once the electric field is turned off. Besides the enhancement in the capacity, from this intuitive explanation, the electric field may promote the adsorption kinetic as well, depending on the type of the pollutant considered.

3.1.2.3 Earlier activation of a photocatalyst due to the corona effect

It was found that a photocatalyst may exhibit photocatalytic activity, when irradiated with light having energy lower than the bandgap, if inserted within an external electric field. The full explanation of the phenomena was not provided; however, it was supposed that it could be due to the shortening of the bandgap edges, due to the displacement of the electrical charges in the semiconductor.

3.1.2.4 Enhancement and inhibition of the heterogeneous photocatalysis by the hybrid process

The heterogeneous photocatalysis consists of five different steps:

1. diffusion of the reactants to the surface;
2. adsorption of reactants;
3. reaction;
4. desorption of products;
5. diffusion of the products away from the surface.

As the presence of an electric field may affect adsorption and diffusion, therefore the steps 1 and 2 should be enhanced, while steps 4 and 5 should be inhibited. This would have a consequence on step 3, as the retention time on the catalyst surface would increase.

Indeed, the removal kinetics of MEK, by the ESP-only or by the ESP+PCO, are similar for the first minutes (the photocatalytic oxidation of MEK by TiO_2 is slower than its adsorption over the ACC; for this reason it is difficult to separate the two single contributions) while, for longer times, the combined process became slower, due to the accumulation of the reaction products on the adsorbent. However, this phenomena increases the retention time over the catalyst, leading to higher mineralization of the pollutant (Figure 80).

3.2 Materials and processes

The choice of the materials constitutes a fundamental point to evaluate the final process efficiency. In fact, because of the existence of a combined process shared characteristic should be promoted, while discordant parameters should be balanced out.

In order to optimize the final process, Table 44 summarizes the most important material characteristic and process variables, for each technology, individually considered.

Table 44 *– Parameters affecting each single technology*

	PCO	ESP	Ads
Material	Low bandgap Good charge separation High stability	High conductivity Electrodes material Low wire diameter	High surface area High capacity High affinity Fast kinetic
Process	Diffusion to the surface Diffusion from the surface Light absorption High efficiency Low selectivity to by-products High contact time	Electric potential Flow velocity Electrode spacing Low retention time	Diffusion to the surface Competitive adsorption Exhaustion Medium/high contact time

It is clear that the choice of materials, for being implemented into the hybrid process, must take into account every single aspect. Therefore, only the *ad-hoc* realization of a composite can satisfy multiple requirements at the same time.

As well the operational parameters should result from a compromise between the facilitate a process and disadvantage another (i.e., find the minimum of the applied voltage to the discharge electrode in order not to produce an excess of ozone which can damage the adsorbent or react with the pollutants).

It has been reported in Chapter 1.2, which pollution control techniques are more appropriate for a specific pollutant. Table 45 summarize them.

Table 45 *– Effect of the single process on the target pollutant*

Single processes	Ads	ESP	PCO
VOC	Good	No effect	Poor°
NOx	Poor/Good[#]	No effect*	Good
O_3	Poor/Good[#]	No effect*	Poor/Good[@]
PM	Poor[§]	Good	No effect

°Considering a full degradation into CO_2, H_2O, with a typical purifier-contact time, [#]Depends on the adsorbate (NO or NO_2) and the adsorbent *Produced by ESP [@]Good with TiO_2 [§]Depends on the type and the morphology of the adsorbent, acting as a filter.

However, by coupling the processes, the final efficiency is not only inherited from the best efficiency of the selected ones, but it may results to be better than that. A summary of the obtainable results are reported in Table 46.

Table 46 *– Effect of the coupled process on the target pollutant*

Coupled processes	Ads+ESP	ESP+PCO	PCO+Ads	Ads+ESP+PCO
VOC	Good	Poor/Good	Good	Good
NOx	Poor/Good[#]	Good	Good	Good
O_3	Poor/Good[#]	Poor/Good[@]	Good	Good
PM	Good	Good	Poor[§]/ No effect	Good

3.3 Final considerations for the implementation

As a final step, the hybrid process has been implemented into several air cleaner prototypes. Geometries and internal arrangements have been chosen and modified according to not only the results presented in this work but also to the engineering of the process. Without going into details, due to a patent pending application, the choice of materials, geometries and process variables must also take into account the feasibility and ease in engineering the elements.
The following bullet points report critical considerations on the implemented process.

3.3.1 Strengths

- The lack of a transversal crossing of the filtering media allows having a less powerful air handling unit since the pressure drops are reduced. This turns into lower cost, lower noise and reduced power consumption.
- By controlling the geometries and optimizing the materials, it is possible to reduce the potential applied to the discharge electrode, limiting the production of ozone and NOx and electrical consumption.
- The presence of the photocatalyst regenerates the adsorbent.
- The electric field-induced flux enhances the adsorption and the contact time with the TiO_2. Selectivity is enhanced as well.

3.3.2 Weaknesses

- The optimal electric field strength is a function of the air velocity through the adsorbent/collecting plates.
- NO_x generated by the corona discharge may be adsorbed by the adsorbent and accelerate its exhaustion.
- It is more effective at lower concentrations of pollutants.

3.3.3 Economic considerations

Cost/efficiency is a key aspect for the practical implementation of the process. Costs for the implementation of the process considered in an indoor air purifier are subdivided into fixed cost, such as the cost of the equipment and in variable costs, including the filtering material (which must be replaced once exhausted) and the electricity consumption.

System setup (electrical transformer and drivers) is higher than a common fan-filter unit, due to presence of an high voltage transformer and a LED (including the constant current supplying circuit). However, the cost of the fan is lower, as the pressure drop across the filter is an order of magnitude lower than traditional fan filter unit or HEPA filters.

Filter media costs are largely dependent on the quality of the adsorbent material used and on the manufacturing process. As reported in Chapter 2.3.1.1, it is possible to functionalize the adsorbent material, starting from a non-lab grade quality metallic titanium powder. By using this method, it is possible to deposit directly a photocatalyst on a target adsorbent with low costs. The choice made in Chapter 2.5, to functionalize

an activated carbon cloth by simple impregnation with an aqueous dispersion of nano-TiO_2 is meaningful in term of easiness, repeatability but it is strongly influenced by the cost of the catalyst.

Energy consumption costs are lower than conventional fan filter units, as the power adsorbed by the fan is lower due to absence of a significant pressure drop. With using LEDs, to activate the photocatalyst, and with a proper high-voltage transformer, the overall power consumption ranges between 10-20W for 200m^3/h.

3.4 Future developments

It has been shown that the application of an electric field can be used to enhance the kinetics and to increase the adsorption capacity of a pollutant. However, the same method could also be used to control the partial desorption of an adsorbed species, by switching off the electric field.

Another aspect that will be investigated is the effect of the electric field on the adsorption, investigating the nanometric scale, instead of the indirect effect on the gases. Tailoring a composite, with a specific characteristic (bandgap, conductivity, porosity, etc..) opens the way to a scenario where is it possible to investigate the effect of every single parameter, in order to optimize the composite. The choice of deposit B-CNW on a transparent substrate lies in fact to conduct a new series of analysis where the variations of the optical parameters of the material are measured in the presence and absence of an electric field.

Measurements using spectroscopic ellipsometry and Fabry-Perot interferometry were conducted, despite the difficulty of electrically insulating the existing setups and apparatus from the tested samples. However, the results obtained are not of univocal interpretation, and further studies are necessary.

References

1. Chen, C. Searching for intellectual turning points: progressive knowledge domain visualization. *Proc. Natl. Acad. Sci. U. S. A.* **2004**, *101 Suppl 1*, 5303–10, doi:10.1073/pnas.0307513100.
2. (WHO), W. H. O. *WHO Guidelines for Indoor Air Quality: Selected Pollutants*; 2010;
3. Kleinberg; Jon Bursty and hierarchical structure in streams. *Proc. eighth ACM SIGKDD Int. Conf. Knowl. Discov. data Min.* **2002**, 91–101, doi:10.1145/775047.775061.
4. Molina, C.; Pickering, A. C.; Valjbjorn, O.; De Bartoli, M. Sick Building Syndrome. A practical Guide. **1989**, 36.
5. Skov, P.; Valbjorn, O.; Pedersen, B. V Influence of indoor climate on the sick building syndrome in an office environment. The Danish Indoor Climate Study Group. *Scand. J. Work. Environ. Health* **1990**, *16*, 363–371, doi:10.5271/sjweh.1772.
6. Spengler, J. D. Buildings operations and ETS exposure. *Environ. Health Perspect.* **1999**, *107 Suppl 2*, 313–7.
7. Hodgson, M. J. Environmental tobacco smoke and the sick building syndrome. *Occup. Med. 4*, 735–40.
8. Rousseeuw, P. J. Silhouettes: A graphical aid to the interpretation and validation of cluster analysis. *J. Comput. Appl. Math.* **1987**, *20*, 53–65, doi:10.1016/0377-0427(87)90125-7.
9. Chen, C.; Ibekwe-SanJuan, F.; Hou, J. The Structure and Dynamics of Co-Citation Clusters: A Multiple-Perspective Co-Citation Analysis. **2010**, doi:10.1002/asi.21309.
10. Dunning, T. Accurate Methods for the Statistics of Surprise and Coincidence. *Comput. Linguist.* **1993**, *19*, 61--74.
11. Wieslander, G.; Norbäck, D.; Nordström, K.; Wålinder, R.; Venge, P. Nasal and ocular symptoms, tear film stability and biomarkers in nasal lavage, in relation to building-dampness and building design in hospitals. *Int. Arch. Occup. Environ. Health* **1999**, *72*, 451–461, doi:10.1007/s004200050398.
12. Wieslander, G.; Norbäck, D.; Wålinder, R.; Erwall, C.; Venge, P. Inflammation markers in nasal lavage, and nasal symptoms in relation to relocation to a newly painted building: a longitudinal study. *Int. Arch. Occup. Environ. Health* **1999**, *72*, 507–515, doi:10.1007/s004200050408.
13. Brooks, B. O.; Utter, G. M.; DeBroy, J. A.; Schimke, R. D. Indoor Air Pollution: An Edifice Complex. *J. Toxicol. Clin. Toxicol.* **1991**, *29*, 315–374, doi:10.3109/15563659109000363.
14. Nordström, K.; Norbäck, D.; Wieslander, G. Subjective Indoor Air Quality in Geriatric Hospitals. *Indoor Built Environ.* **1999**, *8*, 49–57, doi:10.1177/1420326X9900800105.
15. WESCHLER, C. J. Ozone in Indoor Environments: Concentration and Chemistry. *Indoor Air* **2000**, *10*, 269–288, doi:10.1034/j.1600-0668.2000.010004269.x.
16. Wolkoff, P. How to measure and evaluate volatile organic compound emissions from building products. A perspective. *Sci. Total Environ.* **1999**, *227*, 197–213, doi:10.1016/S0048-9697(99)00019-4.
17. Drakou, G.; Zerefos, C.; Ziomas, I. A Sensitivity Study of Parameters in the Nazaroff-

Cass IAQ Model with Respect to Indoor Concentrations of O_3, NO, NO_2. *Environ. Technol.* **2000**, *21*, 483–503, doi:10.1080/09593330.2000.9618931.

18. WOLKOFF*, P.; CLAUSEN, P. A.; WILKINS, C. K.; NIELSEN, G. D. Formation of Strong Airway Irritants in Terpene/Ozone Mixtures. *Indoor Air* **2000**, *10*, 82–91, doi:10.1034/j.1600-0668.2000.010002082.x.

19. Feng, Y.; Wen, S.; Wang, X.; Sheng, G.; He, Q.; Tang, J.; Fu, J. Indoor and outdoor carbonyl compounds in the hotel ballrooms in Guangzhou, China. *Atmos. Environ.* **2004**, *38*, 103–112, doi:10.1016/J.ATMOSENV.2003.09.061.

20. Bahadori, T.; Suh, H.; Koutrakis, P. Issues in Human Particulate Exposure Assessment: Relationship between Outdoor, Indoor, and Personal Exposures. *Hum. Ecol. Risk Assess. An Int. J.* **1999**, *5*, 459–470, doi:10.1080/10807039.1999.10518871.

21. Janssen, N. A.; Hoek, G.; Brunekreef, B.; Harssema, H. Mass concentration and elemental composition of PM10 in classrooms. *Occup. Environ. Med.* **1999**, *56*, 482–7, doi:10.1136/OEM.56.7.482.

22. Micallef, A.; Colls, J. J.; Caldwell, J. Measurement of vertical concentration profiles of airborne particulate matter in indoor environments: Implications for refinement of models and monitoring campaigns. *Int. J. Environ. Health Res.* **1999**, *9*, 5–18, doi:10.1080/09603129973317.

23. Braniš, M.; Šafránek, J. Characterization of coarse particulate matter in school gyms. *Environ. Res.* **2011**, *111*, 485–491, doi:10.1016/J.ENVRES.2011.03.010.

24. Braniš, M.; Šafránek, J.; Hytychová, A. Indoor and outdoor sources of size-resolved mass concentration of particulate matter in a school gym—implications for exposure of exercising children. *Environ. Sci. Pollut. Res.* **2011**, *18*, 598–609, doi:10.1007/s11356-010-0405-0.

25. Fuoco, F.; Stabile, L.; Buonanno, G.; Trassiera, C.; Massimo, A.; Russi, A.; Mazaheri, M.; Morawska, L.; Andrade, A. Indoor Air Quality in Naturally Ventilated Italian Classrooms. *Atmosphere (Basel).* **2015**, *6*, 1652–1675, doi:10.3390/atmos6111652.

26. Mejía, J. F.; Choy, S. L.; Mengersen, K.; Morawska, L. Methodology for assessing exposure and impacts of air pollutants in school children: Data collection, analysis and health effects – A literature review. *Atmos. Environ.* **2011**, *45*, 813–823, doi:10.1016/J.ATMOSENV.2010.11.009.

27. Pacitto, A.; Stabile, L.; Viana, M.; Scungio, M.; Reche, C.; Querol, X.; Alastuey, A.; Rivas, I.; Álvarez-Pedrerol, M.; Sunyer, J.; van Drooge, B. L.; Grimalt, J. O.; Sozzi, R.; Vigo, P.; Buonanno, G. Particle-related exposure, dose and lung cancer risk of primary school children in two European countries. *Sci. Total Environ.* **2018**, *616–617*, 720–729, doi:10.1016/J.SCITOTENV.2017.10.256.

28. Pacitto, A.; Stabile, L.; Moreno, T.; Kumar, P.; Wierzbicka, A.; Morawska, L.; Buonanno, G. The influence of lifestyle on airborne particle surface area doses received by different Western populations. *Environ. Pollut.* **2018**, *232*, 113–122, doi:10.1016/J.ENVPOL.2017.09.023.

29. Jones, A. P. Indoor air quality and health. *Atmos. Environ.* **1999**, *33*, 4535–4564, doi:10.1016/S1352-2310(99)00272-1.

30. KLEPEIS, N. E.; NELSON, W. C.; OTT, W. R.; ROBINSON, J. P.; TSANG, A. M.; SWITZER, P.; BEHAR, J. V; HERN, S. C.; ENGELMANN, W. H. The National Human Activity Pattern Survey (NHAPS): a resource for assessing exposure to environmental pollutants. *J. Expo. Sci. Environ. Epidemiol.* **2001**, *11*, 231–252,

doi:10.1038/sj.jea.7500165.

31. Daisey, J. M.; Angell, W. J.; Apte, M. G. Indoor air quality, ventilation and health symptoms in schools: an analysis of existing information. *Indoor Air* **2003**, *13*, 53–64, doi:10.1034/j.1600-0668.2003.00153.x.

32. World Health Organization WHO Air quality guidelines for particulate matter, ozone, nitrogen dioxide and sulfur dioxide: global update 2005: summary of risk assessment. *Geneva World Heal. Organ.* **2006**, 1–22, doi:10.1016/0004-6981(88)90109-6.

33. Mendell, M. J.; Heath, G. A. Do indoor pollutants and thermal conditions in schools influence student performance? A critical review of the literature. *Indoor Air* **2005**, *15*, 27–52, doi:10.1111/j.1600-0668.2004.00320.x.

34. Sundell, J.; Levin, H.; Nazaroff, W. W.; Cain, W. S.; Fisk, W. J.; Grimsrud, D. T.; Gyntelberg, F.; Li, Y.; Persily, A. K.; Pickering, A. C.; Samet, J. M.; Spengler, J. D.; Taylor, S. T.; Weschler, C. J. Ventilation rates and health: multidisciplinary review of the scientific literature. *Indoor Air* **2011**, *21*, 191–204, doi:10.1111/j.1600-0668.2010.00703.x.

35. Chen, C.; Zhao, B. Review of relationship between indoor and outdoor particles: I/O ratio, infiltration factor and penetration factor. *Atmos. Environ.* **2011**, *45*, 275–288, doi:10.1016/J.ATMOSENV.2010.09.048.

36. Salthammer, T.; Mentese, S.; Marutsky, R.; Marutzky, R.; Marutsky, R. Formaldehyde in the Indoor Environment. *Chem. Rev.* **2010**, *110*, 2536–2572, doi:10.1021/cr800399g.

37. Chow, J. C. Health Effects of Fine Particulate Air Pollution: Lines that Connect. *J. Air Waste Manage. Assoc.* **2006**, *56*, 707–708, doi:10.1080/10473289.2006.10464484.

38. Freeman, L. C. A Set of Measures of Centrality Based on Betweenness. *Sociometry* **1977**, *40*, 35, doi:10.2307/3033543.

39. Brown, S. K.; Sim, M. R.; Abramson, M. J.; Gray, C. N. Concentrations of Volatile Organic Compounds in Indoor Air – A Review. *Indoor Air* **1994**, *4*, 123–134, doi:10.1111/j.1600-0668.1994.t01-2-00007.x.

40. Wallace, L. Indoor Particles: A Review. *J. Air Waste Manage. Assoc.* **1996**, *46*, 98–126, doi:10.1080/10473289.1996.10467451.

41. Bornehag1,9*, C.-G.; Blomquist2, G.; Gyntelberg3, F.; Jarvholm4, B.; Malmberg5, P.; Nordvall6, L.; Nielsen7, A.; Pershagen8, G.; Sundell9, J. Dampness in Buildings and Health. Nordic Interdisciplinary Review of the Scientific Evidence on Associations between Exposure to "Dampness" in Buildings and Health Effects (NORDDAMP). *Indoor Air* **2001**, *11*, 72–86, doi:10.1034/j.1600-0668.2001.110202.x.

42. Chen, C. The CiteSpace Manual. *Coll. Comput. Informatics* **2014**, 1–84, doi:10.1007/s11192-015-1576-8.

43. Yu, C. W. F.; Jeong Tai Kim, J. T. Building Pathology, Investigation of Sick Buildings — VOC Emissions. *Indoor Built Environ.* **2010**, *19*, 30–39, doi:10.1177/1420326X09358799.

44. Yu, C. W. F.; Jeong, T. K. Building environmental assessment schemes for rating of IAQ in sustainable buildings. *Indoor Built Environ.* **2011**, *20*, 5–15, doi:10.1177/1420326X10397780.

45. Dimitroulopoulou, C. Ventilation in European dwellings: A review. *Build. Environ.* **2012**, *47*, 109–125, doi:10.1016/J.BUILDENV.2011.07.016.

46. Zhang, Y.; Mo, J.; Li, Y.; Sundell, J.; Wargocki, P.; Zhang, J.; Little, J. C.; Corsi, R.; Deng, Q.; Leung, M. H. K.; Fang, L.; Chen, W.; Li, J.; Sun, Y. Can commonly-used fan-driven air cleaning technologies improve indoor air quality? A literature review. *Atmos. Environ.* **2011**, *45*, 4329–4343, doi:10.1016/J.ATMOSENV.2011.05.041.

47. Almeida, S. M.; Canha, N.; Silva, A.; Freitas, M. do C.; Pegas, P.; Alves, C.; Evtyugina, M.; Pio, C. A. Children exposure to atmospheric particles in indoor of Lisbon primary schools. *Atmos. Environ.* **2011**, *45*, 7594–7599, doi:10.1016/J.ATMOSENV.2010.11.052.

48. Lim, S. S.; Vos, T.; Flaxman, A. D.; Danaei, G.; Shibuya, K.; Adair-Rohani, H.; AlMazroa, M. A.; Amann, M.; Anderson, H. R.; Andrews, K. G.; Aryee, M.; Atkinson, C.; Bacchus, L. J.; Bahalim, A. N.; Balakrishnan, K.; Balmes, J.; Barker-Collo, S.; Baxter, A.; Bell, M. L.; Blore, J. D.; Blyth, F.; Bonner, C.; Borges, G.; Bourne, R.; Boussinesq, M.; Brauer, M.; Brooks, P.; Bruce, N. G.; Brunekreef, B.; Bryan-Hancock, C.; Bucello, C.; Buchbinder, R.; Bull, F.; Burnett, R. T.; Byers, T. E.; Calabria, B.; Carapetis, J.; Carnahan, E.; Chafe, Z.; Charlson, F.; Chen, H.; Chen, J. S.; Cheng, A. T.-A.; Child, J. C.; Cohen, A.; Colson, K. E.; Cowie, B. C.; Darby, S.; Darling, S.; Davis, A.; Degenhardt, L.; Dentener, F.; Des Jarlais, D. C.; Devries, K.; Dherani, M.; Ding, E. L.; Dorsey, E. R.; Driscoll, T.; Edmond, K.; Ali, S. E.; Engell, R. E.; Erwin, P. J.; Fahimi, S.; Falder, G.; Farzadfar, F.; Ferrari, A.; Finucane, M. M.; Flaxman, S.; Fowkes, F. G. R.; Freedman, G.; Freeman, M. K.; Gakidou, E.; Ghosh, S.; Giovannucci, E.; Gmel, G.; Graham, K.; Grainger, R.; Grant, B.; Gunnell, D.; Gutierrez, H. R.; Hall, W.; Hoek, H. W.; Hogan, A.; Hosgood, H. D.; Hoy, D.; Hu, H.; Hubbell, B. J.; Hutchings, S. J.; Ibeanusi, S. E.; Jacklyn, G. L.; Jasrasaria, R.; Jonas, J. B.; Kan, H.; Kanis, J. A.; Kassebaum, N.; Kawakami, N.; Khang, Y.-H.; Khatibzadeh, S.; Khoo, J.-P.; Kok, C.; Laden, F.; Lalloo, R.; Lan, Q.; Lathlean, T.; Leasher, J. L.; Leigh, J.; Li, Y.; Lin, J. K.; Lipshultz, S. E.; London, S.; Lozano, R.; Lu, Y.; Mak, J.; Malekzadeh, R.; Mallinger, L.; Marcenes, W.; March, L.; Marks, R.; Martin, R.; McGale, P.; McGrath, J.; Mehta, S.; Memish, Z. A.; Mensah, G. A.; Merriman, T. R.; Micha, R.; Michaud, C.; Mishra, V.; Hanafiah, K. M.; Mokdad, A. A.; Morawska, L.; Mozaffarian, D.; Murphy, T.; Naghavi, M.; Neal, B.; Nelson, P. K.; Nolla, J. M.; Norman, R.; Olives, C.; Omer, S. B.; Orchard, J.; Osborne, R.; Ostro, B.; Page, A.; Pandey, K. D.; Parry, C. D.; Passmore, E.; Patra, J.; Pearce, N.; Pelizzari, P. M.; Petzold, M.; Phillips, M. R.; Pope, D.; Pope, C. A.; Powles, J.; Rao, M.; Razavi, H.; Rehfuess, E. A.; Rehm, J. T.; Ritz, B.; Rivara, F. P.; Roberts, T.; Robinson, C.; Rodriguez-Portales, J. A.; Romieu, I.; Room, R.; Rosenfeld, L. C.; Roy, A.; Rushton, L.; Salomon, J. A.; Sampson, U.; Sanchez-Riera, L.; Sanman, E.; Sapkota, A.; Seedat, S.; Shi, P.; Shield, K.; Shivakoti, R.; Singh, G. M.; Sleet, D. A.; Smith, E.; Smith, K. R.; Stapelberg, N. J.; Steenland, K.; Stöckl, H.; Stovner, L. J.; Straif, K.; Straney, L.; Thurston, G. D.; Tran, J. H.; Van Dingenen, R.; van Donkelaar, A.; Veerman, J. L.; Vijayakumar, L.; Weintraub, R.; Weissman, M. M.; White, R. A.; Whiteford, H.; Wiersma, S. T.; Wilkinson, J. D.; Williams, H. C.; Williams, W.; Wilson, N.; Woolf, A. D.; Yip, P.; Zielinski, J. M.; Lopez, A. D.; Murray, C. J.; Ezzati, M. A comparative risk assessment of burden of disease and injury attributable to 67 risk factors and risk factor clusters in 21 regions, 1990–2010: a systematic analysis for the Global Burden of Disease Study 2010. *Lancet* **2012**, *380*, 2224–2260, doi:10.1016/S0140-6736(12)61766-8.

49. Hospodsky, D.; Qian, J.; Nazaroff, W. W.; Yamamoto, N.; Bibby, K.; Rismani-Yazdi, H.; Peccia, J. Human Occupancy as a Source of Indoor Airborne Bacteria. *PLoS One* **2012**, *7*, e34867, doi:10.1371/journal.pone.0034867.

50. Satish, U.; Mendell, M. J.; Shekhar, K.; Hotchi, T.; Sullivan, D.; Streufert, S.; Fisk, W. (Bill) J. Is CO2 an Indoor Pollutant? Direct Effects of Low-to-Moderate CO2

Concentrations on Human Decision-Making Performance. *Environ. Health Perspect.* **2012**, doi:10.1289/ehp.1104789.

51. Geiss, O.; Giannopoulos, G.; Tirendi, S.; Barrero-Moreno, J.; Larsen, B. R.; Kotzias, D. The AIRMEX study - VOC measurements in public buildings and schools/kindergartens in eleven European cities: Statistical analysis of the data. *Atmos. Environ.* **2011**, *45*, 3676–3684, doi:10.1016/J.ATMOSENV.2011.04.037.

52. Pegas, P. N.; Alves, C. A.; Evtyugina, M. G.; Nunes, T.; Cerqueira, M.; Franchi, M.; Pio, C. A.; Almeida, S. M.; Verde, S. C.; Freitas, M. C. Seasonal evaluation of outdoor/indoor air quality in primary schools in Lisbon. *J. Environ. Monit.* **2011**, *13*, 657, doi:10.1039/c0em00472c.

53. Guo, H.; Morawska, L.; He, C.; Zhang, Y. L.; Ayoko, G.; Cao, M. Characterization of particle number concentrations and PM2.5 in a school: influence of outdoor air pollution on indoor air. *Environ. Sci. Pollut. Res.* **2010**, *17*, 1268–1278, doi:10.1007/s11356-010-0306-2.

54. Logue, J. M.; McKone, T. E.; Sherman, M. H.; Singer, B. C. Hazard assessment of chemical air contaminants measured in residences. *Indoor Air* **2011**, *21*, 92–109, doi:10.1111/j.1600-0668.2010.00683.x.

55. Pegas, P. N.; Evtyugina, M. G.; Alves, C. A.; Nunes, T.; Cerqueira, M.; Franchi, M.; Pio, C.; Almeida, S. M.; Freitas, M. do C. Outdoor/indoor air quality in primary schools in Lisbon: a preliminary study. *Quim. Nova* **2010**, *33*, 1145–1149, doi:10.1590/S0100-40422010000500027.

56. Qian, J.; Hospodsky, D.; Yamamoto, N.; Nazaroff, W. W.; Peccia, J. Size-resolved emission rates of airborne bacteria and fungi in an occupied classroom. *Indoor Air* **2012**, *22*, 339–351, doi:10.1111/j.1600-0668.2012.00769.x.

57. Wichmann, J.; Lind, T.; Nilsson, M. A.-M.; Bellander, T. PM2.5, soot and NO2 indoor–outdoor relationships at homes, pre-schools and schools in Stockholm, Sweden. *Atmos. Environ.* **2010**, *44*, 4536–4544, doi:10.1016/J.ATMOSENV.2010.08.023.

58. Pegas, P. N.; Alves, C. A.; Evtyugina, M. G.; Nunes, T.; Cerqueira, M.; Franchi, M.; Pio, C. A.; Almeida, S. M.; Freitas, M. C. Indoor air quality in elementary schools of Lisbon in spring. *Environ. Geochem. Health* **2011**, *33*, 455–468, doi:10.1007/s10653-010-9345-3.

59. Pegas, P. N.; Nunes, T.; Alves, C. A.; Silva, J. R.; Vieira, S. L. A.; Caseiro, A.; Pio, C. A. Indoor and outdoor characterisation of organic and inorganic compounds in city centre and suburban elementary schools of Aveiro, Portugal. *Atmos. Environ.* **2012**, *55*, 80–89, doi:10.1016/J.ATMOSENV.2012.03.059.

60. Annesi-Maesano, I.; Baiz, N.; Banerjee, S.; Rudnai, P.; Rive, S.; the SINPHONIE Group, on behalf of the S. Indoor Air Quality and Sources in Schools and Related Health Effects. *J. Toxicol. Environ. Heal. Part B* **2013**, *16*, 491–550, doi:10.1080/10937404.2013.853609.

61. Fabi, V.; Andersen, R. V.; Corgnati, S.; Olesen, B. W. Occupants' window opening behaviour: A literature review of factors influencing occupant behaviour and models. *Build. Environ.* **2012**, *58*, 188–198, doi:10.1016/J.BUILDENV.2012.07.009.

62. Mendell, M. J.; Eliseeva, E. A.; Davies, M. M.; Spears, M.; Lobscheid, A.; Fisk, W. J.; Apte, M. G. Association of classroom ventilation with reduced illness absence: a prospective study in California elementary schools. *Indoor Air* **2013**, *23*, 515–528, doi:10.1111/ina.12042.

63. Pierpaoli, M.; Fava, G. A passive opportunity for improving air quality in the schools environment: A real-world scale testing. *Am. J. Environ. Sci.* **2016**, *12*, 206–212, doi:10.3844/ajessp.2016.206.212.

64. Pierpaoli, M.; Giosuè, C.; Ruello, M. L.; Fava, G. Appraisal of a hybrid air cleaning process. *Environ. Sci. Pollut. Res.* **2017**, *24*, 12638–12645, doi:10.1007/s11356-016-7880-x.

65. Giosuè, C.; Pierpaoli, M.; Mobili, A.; Ruello, M. L.; Tittarelli, F. Influence of binders and lightweight aggregates on the properties of cementitious mortars: From traditional requirements to indoor air quality improvement. *Materials (Basel).* **2017**, *10*, doi:10.3390/ma10080978.

66. Pichat, P.; Disdier, J.; Hoang-Van, C.; Mas, D.; Goutailler, G.; Gaysse, C. Purification/deodorization of indoor air and gaseous effluents by TiO2 photocatalysis. *Catal. Today* **2000**, *63*, 363–369, doi:10.1016/S0920-5861(00)00480-6.

67. Chen, W.; Chen, W.; Zhang, J. S. Performance of air cleaners for removing multi-volatile organic compounds in indoor air. *ASHRAE Trans.* **2005**, 1101–1114.

68. Pierpaoli, M.; Ruello, M.; Fava, G. Enhanced Adsorption of Organic Compounds over an Activated Carbon Cloth by an External-Applied Electric Field. *Environments* **2017**, *4*, 33, doi:10.3390/environments4020033.

69. Zikova, N.; Hopke, P. K.; Ferro, A. R. Evaluation of new low-cost particle monitors for PM2.5concentrations measurements. *J. Aerosol Sci.* **2017**, doi:10.1016/j.jaerosci.2016.11.010.

70. Morawska, L.; Thai, P. K.; Liu, X.; Asumadu-Sakyi, A.; Ayoko, G.; Bartonova, A.; Bedini, A.; Chai, F.; Christensen, B.; Dunbabin, M.; Gao, J.; Hagler, G. S. W.; Jayaratne, R.; Kumar, P.; Lau, A. K. H.; Louie, P. K. K.; Mazaheri, M.; Ning, Z.; Motta, N.; Mullins, B.; Rahman, M. M.; Ristovski, Z.; Shafiei, M.; Tjondronegoro, D.; Westerdahl, D.; Williams, R. Applications of low-cost sensing technologies for air quality monitoring and exposure assessment: How far have they gone? *Environ. Int.* **2018**, *116*, 286–299, doi:10.1016/j.envint.2018.04.018.

71. Ali, A. S.; Zanzinger, Z.; Debose, D.; Stephens, B. Open Source Building Science Sensors (OSBSS): A low-cost Arduino-based platform for long-term indoor environmental data collection. *Build. Environ.* **2016**, *100*, 114–126, doi:10.1016/j.buildenv.2016.02.010.

72. Cannistraro, G.; Cannistraro, M.; Cannistraro, A. Analysis of air pollution in the urban center of four cities Sicilian. *Int. J. HEAT Technol.* **2016**.

73. Delgoshaei, P.; Heidarinejad, M.; Austin, M. Semantic Frameworks for Model-based Assessment and Management of Indoor Air Quality. In *Indoor Air 2018*; 2018.

74. Gordon, S. B.; Bruce, N. G.; Grigg, J.; Hibberd, P. L.; Kurmi, O. P.; Lam, K. H.; Mortimer, K.; Asante, K. P.; Balakrishnan, K.; Balmes, J.; Bar-Zeev, N.; Bates, M. N.; Breysse, P. N.; Buist, S.; Chen, Z.; Havens, D.; Jack, D.; Jindal, S.; Kan, H.; Mehta, S.; Moschovis, P.; Naeher, L.; Patel, A.; Perez-Padilla, R.; Pope, D.; Rylance, J.; Semple, S.; Martin, W. J. Respiratory risks from household air pollution in low and middle income countries. *Lancet Respir. Med.* **2014**, *2*, 823–860, doi:10.1016/S2213-2600(14)70168-7.

75. Schluger, N. Household air quality in high-income countries: forgotten but not gone. *Lancet Respir. Med.* **2014**, *2*, 781–783, doi:10.1016/S2213-2600(14)70183-3.

76. EUR-Lex - 32004L0042 - EN. *Off. J. L 143 , 30/04/2004 P. 0087 - 0096;* .

77. US EPA, O. Technical Overview of Volatile Organic Compounds.

78. Gallego, E.; Roca, X.; Perales, J. F.; Guardino, X. Determining indoor air quality and identifying the origin of odour episodes in indoor environments. *J. Environ. Sci.* **2009**, *21*, 333–339, doi:10.1016/S1001-0742(08)62273-1.

79. Salthammer, T.; Mentese, S.; Marutzky, R. Formaldehyde in the Indoor Environment. *Chem. Rev.* **2010**, *110*, 2536–2572, doi:10.1021/cr800399g.

80. Krzyzanowski, M. WHO Air Quality Guidelines for Europe. *J. Toxicol. Environ. Heal. Part A* **2008**, *71*, 47–50, doi:10.1080/15287390701557834.

81. Greta, S. D. M.; STYLIANOS, K.; Juhani, R.; Matti, J. Personal Carbon Monoxide Exposure in Helsinki, Finland. **2005**.

82. Morawska, L. (Lidia); Salthammer, T. *Indoor environment : airborne particles and settled dust*; Wiley-VCH, 2003; ISBN 9783527305254.

83. Salthammer, T.; Uhde, E. *Organic Indoor Air Pollutants. Occurrence, Measurement, Evaluation*; 2010; Vol. 72; ISBN 9783527319596.

84. Parker, K. R. *Applied Electrostatic Precipitation*; Springer Netherlands, 1996; ISBN 9789400915534.

85. Mizuno, A. Electrostatic precipitation. *IEEE Trans. Dielectr. Electr. Insul.* **2000**, *7*, 615–624, doi:10.1109/94.879357.

86. Boelter, K. J.; Davidson, J. H. Ozone Generation by Indoor, Electrostatic Air Cleaners. *Aerosol Sci. Technol.* **1997**, *27*, 689–708, doi:10.1080/02786829708965505.

87. Fann, N.; Lamson, A. D.; Anenberg, S. C.; Wesson, K.; Risley, D.; Hubbell, B. J. Estimating the National Public Health Burden Associated with Exposure to Ambient PM2.5 and Ozone. *Risk Anal.* **2012**, *32*, 81–95, doi:10.1111/j.1539-6924.2011.01630.x.

88. Ruthven, D. M. Adsorption, Fundamentals. *Kirk-Othmer Encycl. Chem. Technol.* **2001**, *1*, 582–617, doi:10.1002/0471238961.0104191518212008.a01.pub2.

89. Metts, T. A.; Batterman, S. A. Effect of VOC loading on the ozone removal efficiency of activated carbon filters. *Chemosphere* **2006**, *62*, 34–44, doi:10.1016/j.chemosphere.2005.04.049.

90. FUJISHIMA, A.; HONDA, K. Electrochemical Photolysis of Water at a Semiconductor Electrode. *Nature* **1972**, *238*, 37–38, doi:10.1038/238037a0.

91. Schneider, J.; Matsuoka, M.; Takeuchi, M.; Zhang, J.; Horiuchi, Y.; Anpo, M.; Bahnemann, D. W. Understanding TiO2 Photocatalysis: Mechanisms and Materials. *Chem. Rev.* **2014**, *114*, 9919–9986, doi:10.1021/cr5001892.

92. Anpo, M.; Kamat, P. V. *Environmentally benign photocatalysts : applications of titanium oxide-based materials*; Springer, 2010; ISBN 9780387484440.

93. Schneider, J.; Bahnemann, D. (Detlef); Ye, J.; Puma, G. L.; Dionysiou, D. D. *Photocatalysis : fundamentals and perspectives*; ISBN 1782620419.

94. Kim, H.-H. Nonthermal Plasma Processing for Air-Pollution Control: A Historical Review, Current Issues, and Future Prospects. *Plasma Process. Polym.* **2004**, *1*, 91–110, doi:10.1002/ppap.200400028.

95. Whitehead, J. C. Plasma – catalysis : the known knowns , the known unknowns and the unknown unknowns. *J. Phys. D. Appl. Phys.* **2016**, *49*, 243001, doi:10.1088/0022-3727/49/24/243001.

96. Kim, H. H.; Teramoto, Y.; Negishi, N.; Ogata, A. A multidisciplinary approach to understand the interactions of nonthermal plasma and catalyst: A review. *Catal. Today* **2015**, *256*, 13–22, doi:10.1016/j.cattod.2015.04.009.

97. Waring, M. S.; Siegel, J. A.; Corsi, R. L. Ultrafine particle removal and generation by portable air cleaners. *Atmos. Environ.* **2008**, *42*, 5003–5014, doi:10.1016/J.ATMOSENV.2008.02.011.

98. Alshawa, A.; Russell, A. R.; Nizkorodov, S. A. Kinetic analysis of competition between aerosol particle removal and generation by ionization air purifiers. *Environ. Sci. Technol.* **2007**, *41*, 2498–504.

99. McGregor, F. R.; Piscaer, P. J.; Aieta, E. M. Economics of Treating Waste Gases from an Air Stripping Tower Using Photochemically Generated Ozone. *Ozone Sci. Eng.* **1988**, *10*, 339–351, doi:10.1080/01919518808552389.

100. Bhowmick, M.; Semmens, M. J. Ultraviolet photooxidation for the destruction of vocs in air. *Water Res.* **1994**, *28*, 2407–2415, doi:10.1016/0043-1354(94)90057-4.

101. Chen, F.; Yang, Q.; Pehkonen, S. O.; Ray, M. B. Modeling of Gas-Phase Photodegradation of Chloroform and Carbon Tetrachloride. *J. Air Waste Manage. Assoc.* **2004**, *54*, 1281–1292, doi:10.1080/10473289.2004.10470991.

102. Koh, L.-H.; Kuhn, D. C.; Mohseni, M.; Allen, D. G. Utilizing ultraviolet photooxidation as a pre-treatment of volatile organic compounds upstream of a biological gas cleaning operation. *J. Chem. Technol. Biotechnol.* **2004**, *79*, 619–625, doi:10.1002/jctb.1030.

103. Kang, I.-S.; Xi, J.; Hu, H.-Y. Photolysis and photooxidation of typical gaseous VOCs by UV Irradiation: Removal performance and mechanisms. *Front. Environ. Sci. Eng.* **2018**, *12*, 8, doi:10.1007/s11783-018-1032-0.

104. Heindel, T. H.; Streib, R.; Botzenhart, K. [Effect of ozone on airborne microorganisms]. *Zentralbl. Hyg. Umweltmed.* **1993**, *194*, 464–80.

105. Fontes, B.; Cattani Heimbecker, A. M.; de Souza Brito, G.; Costa, S. F.; van der Heijden, I. M.; Levin, A. S.; Rasslan, S. Effect of low-dose gaseous ozone on pathogenic bacteria. *BMC Infect. Dis.* **2012**, *12*, 358, doi:10.1186/1471-2334-12-358.

106. R Core Team R: A language and environment for statistical computing. 2013.

107. Baker, C. An R Client to the "PatentsView" API • patentsview Available online: https://ropensci.github.io/patentsview/index.html (accessed on Nov 4, 2018).

108. Chiang, H. L.; Chiang, P. C.; Huang, C. P. Ozonation of activated carbon and its effects on the adsorption of VOCs exemplified by methylethylketone and benzene. *Chemosphere* **2002**, *47*, 267–275, doi:10.1016/S0045-6535(01)00216-8.

109. Che, Y.; Zhou, J.; Wang, Z. Plasma Modification of Activated Carbon Fibers for Adsorption of SO_2. *Plasma Sci. Technol.* **2013**, *15*, 1047–1052, doi:10.1088/1009-0630/15/10/16.

110. Grevillot, G.; France, N. Laboratoire des Sciences du Genie Chimique ELECTRICAL. **1989**, 193–221.

111. Su, X.; Hatton, T. A. Electrosorption. In *Kirk-Othmer Encyclopedia of Chemical Technology*; John Wiley & Sons, Inc.: Hoboken, NJ, USA, 2016; pp. 1–11.

112. Oren, Y. Capacitive deionization (CDI) for desalination and water treatment — past, present and future (a review). *Desalination* **2008**, *228*, 10–29, doi:10.1016/J.DESAL.2007.08.005.

113. Porada, S.; Zhao, R.; van der Wal, A.; Presser, V.; Biesheuvel, P. M. Review on the science and technology of water desalination by capacitive deionization. *Prog. Mater. Sci.* **2013**, *58*, 1388–1442, doi:10.1016/J.PMATSCI.2013.03.005.

114. Li, H.; Zou, L.; Pan, L.; Sun, Z. Novel Graphene-Like Electrodes for Capacitive Deionization. *Environ. Sci. Technol.* **2010**, *44*, 8692–8697, doi:10.1021/es101888j.

115. Tsouris, C.; Mayes, R.; Kiggans, J.; Sharma, K.; Yiacoumi, S.; DePaoli, D.; Dai, S. Mesoporous Carbon for Capacitive Deionization of Saline Water. *Environ. Sci. Technol.* **2011**, *45*, 10243–10249, doi:10.1021/es201551e.

116. Lota, G.; Fic, K.; Frackowiak, E. Carbon nanotubes and their composites in electrochemical applications. *Energy Environ. Sci.* **2011**, *4*, 1592, doi:10.1039/c0ee00470g.

117. Frackowiak, E.; Abbas, Q.; Béguin, F. Carbon/carbon supercapacitors. *J. Energy Chem.* **2013**, *22*, 226–240, doi:10.1016/S2095-4956(13)60028-5.

118. Ponton, L. M.; Porter, M. D. High-speed electrochemically modulated liquid chromatography. *Anal. Chem.* **2004**, *76*, 5823–8, doi:10.1021/ac049257w.

119. Gileadi, E. *Electrosorption*; 1967; ISBN 9788578110796.

120. Bockris, J. O. *Modern Aspects of Electrochemistry No. 4*; Springer US, 1966; ISBN 9781468409130.

121. Chue, K. T.; Grévillot, G.; Tondeur, D. Electrosorption an Activated Carbon Bed. *Stud. Surf. Sci. Catal.* **1993**, *80*, 97–104, doi:10.1016/S0167-2991(08)63503-X.

122. Doll, T. *Advanced Gas Sensing - The Electroadsorptive Effect and Related Techniques*; Doll, T., Ed.; Springer US: Boston, MA, 2003; Vol. 6; ISBN 978-1-4020-7433-2.

123. Wolkenstein, T. The Electron Theory of Catalysis on Semiconductors. *Adv. Catal.* **1960**, *12*, 189–264, doi:10.1016/S0360-0564(08)60603-3.

124. Peek, F. W. *Dielectric phenomena in high voltage engineering :*; McGraw-Hill Book Company, Inc., 1915;

125. Chen, J.; Davidson, J. H. Ozone Production in the Positive DC Corona Discharge: Model and Comparison to Experiments. *Plasma Chem. Plasma Process.* **2002**, *22*, 495–522, doi:10.1023/A:1021315412208.

126. Qu, G.-Z.; Li, J.; Li, G.-F.; Wu, Y.; Lu, N. DBD regeneration of GAC loaded with acid orange 7. *ASIA-PACIFIC J. Chem. Eng. Asia-Pac. J. Chem. Eng* **2009**, *4*, 649–653, doi:10.1002/apj.310.

127. Wu, Z.; Cong, Y.; Zhou, M.; Tan, T. p-Nitrophenol abatement by the combination of electrocatalysis and activated carbon. *Chem. Eng. J.* **2005**, *106*, 83–90, doi:10.1016/J.CEJ.2004.10.009.

128. Ma, S.; Yao, J.; Gao, L.; Ma, X.; Zhao, Y. Experimental study on removals of SO_2 and NO_X using adsorption of activated carbon/microwave desorption. *J. Air Waste Manage. Assoc.* **2012**, *62*, 1012–1021, doi:10.1080/10962247.2012.695320.

129. Shi, S.; Hwang, J.-Y.; Li, X.; Sun, X.; Lee, B. I. Enhanced hydrogen sorption on carbonaceous sorbents under electric field. *Int. J. Hydrogen Energy* **2010**, *35*, 629–631, doi:10.1016/j.ijhydene.2009.11.008.

130. Cab, C.; Medina-Esquivel, R.; Acosta, C.; Mendez-Gamboa, J.; Peñuñuri, F.; Tapia, A. Influence of Electric Field in the Adsorption of Atomic Hydrogen on Graphene. *Adv. Condens. Matter Phys.* **2015**, *2015*, 1–9, doi:10.1155/2015/847804.

131. Finamore, N. K.; Liu, C.; Mohanty, P.; Moore, D. T.; Landskron, K. *Electric Field Swing Adsorption for Carbon Capture Applications*; 2011;

132. Zhang, W.-J.; Bagreev, A.; Rasouli, F. Reaction of NO $_2$ with Activated Carbon at Ambient Temperature. *Ind. Eng. Chem. Res.* **2008**, *47*, 4358–4362, doi:10.1021/ie800249s.

133. Pierpaoli, M.; Giosuè, C.; Ruello, M. L.; Fava, G. Appraisal of a hybrid air cleaning process. *Environ. Sci. Pollut. Res.* **2017**, *24*, 12638–12645, doi:10.1007/s11356-016-7880-x.

134. Strobel, M.; Jones, V.; Lyons, C. S.; Ulsh, M.; Kushner, M. J.; Dorai, R.; Branch, M. C. A Comparison of Corona-Treated and Flame-Treated Polypropylene Films. *Plasmas Polym.* **2003**, *8*, 61–95, doi:10.1023/A:1022817909276.

135. Townsend Brown, T. A method of and an apparatus or machine for producing force and motion. *GB Pat.* 1928, 300311.

136. Cagnoni, D.; Agostini, F.; Christen, T.; Parolini, N.; Stevanovi??, I.; De Falco, C. Multiphysics simulation of corona discharge induced ionic wind. *J. Appl. Phys.* **2013**, *114*, 1–24, doi:10.1063/1.4843823.

137. Jewell-larsen, N. E.; Karpov, S. V; Krichtafovitch, I. A.; Jayanty, V. Modeling of corona-induced electrohydrodynamic flow with COMSOL multiphysics. **2008**, 1–13.

138. Mantach, S. Simplified Numerical Models in Simulating Corona Discharge and EHD Flows. **2018**.

139. Bouazza, M. R.; Yanallah, K.; Pontiga, F.; Chen, J. H. A simplified formulation of wire-plate corona discharge in air: Application to the ion wind simulation. *J. Electrostat.* **2018**, *92*, 54–65, doi:10.1016/j.elstat.2018.02.001.

140. Boeuf, J. P.; Pitchford, L. C. Electrohydrodynamic force and aerodynamic flow acceleration in surface dielectric barrier discharge. *J. Appl. Phys.* **2005**, *97*, 103307, doi:10.1063/1.1901841.

141. Debien, A.; Benard, N.; Moreau, E. Streamer inhibition for improving force and electric wind produced by DBD actuators. *J. Phys. D. Appl. Phys.* **2012**, *45*, doi:10.1088/0022-3727/45/21/215201.

142. Lee, D.; Hee, S.; Paek, K.; Ju, W. Adsorbability enhancement of activated carbon by dielectric barrier discharge plasma treatment. **2005**, *200*, 2277–2282, doi:10.1016/j.surfcoat.2004.11.027.

143. Kodama, S.; Habaki, H.; Sekiguchi, H.; Kawasaki, J. Surface modification of adsorbents by dielectric barrier discharge. **2002**, *407*, 151–155.

144. Chiang, H. L.; Huang, C. P.; Chiang, P. C. The surface characteristics of activated carbon as affected by ozone and alkaline treatment. *Chemosphere* **2002**, *47*, 257–265, doi:10.1016/S0045-6535(01)00215-6.

145. Deitz, V. R. The rates of adsorption and desorption of water vapor from air flows through activated carbons. *Carbon N. Y.* **1991**, *29*, 569–573, doi:10.1016/0008-6223(91)90122-Y.

146. General Admixtures MICRO-POZZ® PFA - cenere volante selezionata e controllata migliora tutte le prestazioni del calcestruzzo Available online: https://www.gageneral.com/pdf/Micro-Pozz_CenereVolante_IT.pdf.

147. Fava, G.; Naik, T.; Pierpaoli, M.; Fava, G.; Naik, T. R.; Pierpaoli, M. Compressive Strength and Leaching Behavior of Mortars with Biomass Ash. *Recycling* **2018**, *3*, 46,

doi:10.3390/recycling3030046.

148. Bansal, R. C.; Donnet, J.; Stoeckli, F. *Activated Carbon*; 1998; ISBN 0080444636.

149. Suzuki, M. *Fundamentals of adsorption : proceedings of the Fourth International Conference on Fundamentals of Adsorption, Kyoto, May 17-22, 1992*; Kodansha, 1993; ISBN 9780080887722.

150. Brunauer, S. The Adsorption of Gases and Vapors. Physical Adsorption. *Princet. Univ. Press* **1943**, *1*, 528.

151. Boehm, H.-P.; Diehl, E.; Heck, W.; Sappok, R. Surface Oxides of Carbon. *Angew. Chemie Int. Ed. English* **1964**, *3*, 669–677, doi:10.1002/anie.196406691.

152. Kim, Y. S.; Yang, S. J.; Lim, H. J.; Kim, T.; Park, C. R. A simple method for determining the neutralization point in Boehm titration regardless of the CO2 effect. *Carbon N. Y.* **2012**, *50*, 3315–3323, doi:10.1016/J.CARBON.2011.12.030.

153. Qiu, H.; Lv, L.; Pan, B.; Zhang, Q. Q.; Zhang, W.; Zhang, Q. Q. Critical review in adsorption kinetic models. *J. Zhejiang Univ. A* **2009**, *10*, 716–724, doi:10.1631/jzus.A0820524.

154. Ho, Y. S.; McKay, G. Pseudo-second order model for sorption processes. *Process Biochem.* **1999**, *34*, 451–465, doi:10.1016/S0032-9592(98)00112-5.

155. Ghasemi, N.; Tamri, P.; Khademi, A.; Nezhad, N. S.; Alwi, S. R. W. Linearized Equations of Pseudo Second-order Kinetic for the Adsorption of Pb(II) on Pistacia Atlantica Shells. *IERI Procedia* **2013**, *5*, 232–237, doi:10.1016/j.ieri.2013.11.097.

156. Srinivasan, N. R.; Shankar, P. A.; Bandyopadhyaya, R. Plasma treated activated carbon impregnated with silver nanoparticles for improved antibacterial effect in water disinfection. *Carbon N. Y.* **2013**, *57*, 1–10, doi:10.1016/J.CARBON.2013.01.008.

157. Barkauskas, J.; Dervinyte, M. An investigation of the functional groups on the surface of activated carbons. *J. Serbian Chem. Soc.* **2004**, *69*, 363–375, doi:10.2298/JSC0405363B.

158. Ferrari, A. C.; Robertson, J.; Ferrari, O.; Robertson, J. O. H. N. Raman spectroscopy of amorphous, nanostructured, diamond-like carbon, and nanodiamond. **2004**, doi:10.1098/rsta.2004.1452.

159. Lota, G.; Krawczyk, P.; Lota, K.; Sierczyńska, A.; Kolanowski, Ł.; Baraniak, M.; Buchwald, T. The application of activated carbon modified by ozone treatment for energy storage. *J. Solid State Electrochem.* **2016**, *20*, 2857–2864, doi:10.1007/s10008-016-3293-5.

160. Thomas, K.; Hoggan, P. E.; Mariey, L.; Lamotte, J.; Lavalley, J. C. Experimental and theoretical study of ozone adsorption on alumina. *Catal. Letters* **1997**, *46*, 77–82, doi:10.1023/A:1019017123596.

161. Lasne, J.; Romanias, M. N.; Thevenet, F. Ozone Uptake by Clay Dusts under Environmental Conditions. *ACS Earth Sp. Chem.* **2018**, *2*, 904–914, doi:10.1021/acsearthspacechem.8b00057.

162. H. Valdés, *,†; M. Sánchez-Polo, ‡; J. Rivera-Utrilla, ‡ and; Zaror†, C. A. Effect of Ozone Treatment on Surface Properties of Activated Carbon. **2002**, doi:10.1021/LA010920A.

163. Anderson, C.; Bard, A. J. An Improved Photocatalyst of TiO_2/SiO_2 Prepared by a Sol-Gel Synthesis. *J. Phys. Chem.* **1995**, *99*, 9882–9885, doi:10.1021/j100024a033.

164. Gao, X.; Wachs, I. E. Titania–silica as catalysts: molecular structural characteristics

and physico-chemical properties. *Catal. Today* **1999**, *51*, 233–254, doi:10.1016/S0920-5861(99)00048-6.

165. Guan, K. Relationship between photocatalytic activity, hydrophilicity and self-cleaning effect of TiO2/SiO2 films. *Surf. Coatings Technol.* **2005**, *191*, 155–160, doi:10.1016/j.surfcoat.2004.02.022.

166. Jansson, I.; Suárez, S.; Garcia-Garcia, F. J.; Sánchez, B. Zeolite-TiO2 hybrid composites for pollutant degradation in gas phase. *Appl. Catal. B Environ.* **2015**, *178*, 100–107, doi:10.1016/j.apcatb.2014.10.022.

167. Huang, M.; Xu, C.; Wu, Z.; Huang, Y.; Lin, J.; Wu, J. Photocatalytic discolorization of methyl orange solution by Pt modified TiO2 loaded on natural zeolite. *Dye. Pigment.* **2008**, *77*, 327–334, doi:10.1016/j.dyepig.2007.01.026.

168. Chong, M. N.; Tneu, Z. Y.; Poh, P. E.; Jin, B.; Aryal, R. Synthesis, characterisation and application of TiO2–zeolite nanocomposites for the advanced treatment of industrial dye wastewater. *J. Taiwan Inst. Chem. Eng.* **2015**, *50*, 288–296, doi:10.1016/J.JTICE.2014.12.013.

169. Shimizu, K.-I.; Kaneko, T.; Fujishima, T.; Kodama, T.; Yoshida, H.; Kitayama, Y. Selective oxidation of liquid hydrocarbons over photoirradiated TiO2 pillared clays. *Appl. Catal. A Gen.* **2002**, *225*, 185–191, doi:10.1016/S0926-860X(01)00863-8.

170. Sterte, J. Synthesis and Properties of Titanium Oxide Cross-Linked Montmorillonite. *Clays Clay Miner.* **1986**, *34*, 658–664, doi:10.1346/CCMN.1986.0340606.

171. Ding, Z.; Zhu, H. Y.; Lu, G. Q.; Greenfield, P. F. Photocatalytic Properties of Titania Pillared Clays by Different Drying Methods. *J. Colloid Interface Sci.* **1999**, *209*, 193–199, doi:10.1006/jcis.1998.5857.

172. Mogyorósi, K.; Dékány, I.; Fendler, J. H. Preparation and Characterization of Clay Mineral Intercalated Titanium Dioxide Nanoparticles. *Langmuir* **2003**, *19*, 2938–2946, doi:10.1021/la025969a.

173. Ao, C. H.; Lee, S. C. Enhancement effect of TiO2 immobilized on activated carbon filter for the photodegradation of pollutants at typical indoor air level. *Appl. Catal. B Environ.* **2003**, *44*, 191–205, doi:10.1016/S0926-3373(03)00054-7.

174. Leary, R.; Westwood, A. Carbonaceous nanomaterials for the enhancement of TiO2 photocatalysis. *Carbon N. Y.* **2011**, *49*, 741–772, doi:10.1016/j.carbon.2010.10.010.

175. Araña, J.; Doña-Rodríguez, J. M.; Tello Rendón, E.; Garriga I Cabo, C.; González-Díaz, O.; Herrera-Melián, J. A.; Pérez-Peña, J.; Colón, G.; Navío, J. A. TiO2 activation by using activated carbon as a support: Part I. Surface characterisation and decantability study. *Appl. Catal. B Environ.* **2003**, *44*, 161–172, doi:10.1016/S0926-3373(03)00107-3.

176. Li, Y.; Li, X.; Li, J.; Yin, J. Photocatalytic degradation of methyl orange by TiO2-coated activated carbon and kinetic study. *Water Res.* **2006**, *40*, 1119–1126, doi:10.1016/j.watres.2005.12.042.

177. Lu, Y.; Wang, D.; Ma, C.; Yang, H. The effect of activated carbon adsorption on the photocatalytic removal of formaldehyde. *Build. Environ.* **2010**, *45*, 615–621, doi:10.1016/j.buildenv.2009.07.019.

178. Guan, K.; Lu, B.; Yin, Y. Enhanced effect and mechanism of SiO2 addition in super-hydrophilic property of TiO2 films. *Surf. Coatings Technol.* **2003**, *173*, 219–223, doi:10.1016/S0257-8972(03)00521-8.

179. Hirano, M.; Ota, K. Direct Formation and Photocatalytic Performance of Anatase (TiO2)/Silica (SiO2) Composite Nanoparticles. *J. Am. Ceram. Soc.* **2004**, *87*, 1567–1570, doi:10.1111/j.1551-2916.2004.01567.x.

180. Masanori Hirano, *,†; Keisuke Ota, † and; Iwata‡, H. Direct Formation of Anatase (TiO2)/Silica (SiO2) Composite Nanoparticles with High Phase Stability of 1300 °C from Acidic Solution by Hydrolysis under Hydrothermal Condition. **2004**, doi:10.1021/CM040055Q.

181. Houmard, M.; Riassetto, D.; Roussel, F.; Bourgeois, A.; Berthomé, G.; Joud, J. C.; Langlet, M. Morphology and natural wettability properties of sol-gel derived TiO2-SiO2 composite thin films. *Appl. Surf. Sci.* **2007**, *254*, 1405–1414, doi:10.1016/j.apsusc.2007.06.072.

182. Smitha, V. S.; Manjumol, K. A.; Baiju, K. V.; Ghosh, S.; Perumal, P.; Warrier, K. G. K. Sol–gel route to synthesize titania-silica nano precursors for photoactive particulates and coatings. *J. Sol-Gel Sci. Technol.* **2010**, *54*, 203–211, doi:10.1007/s10971-010-2178-9.

183. Stöber, W.; Fink, A.; Bohn, E. Controlled growth of monodisperse silica spheres in the micron size range. *J. Colloid Interface Sci.* **1968**, *26*, 62–69, doi:10.1016/0021-9797(68)90272-5.

184. Montes, M.; Getton, F. P.; Vong, M. S. W.; Sermon, P. a. Titania on silica. A comparison of sol-gel routes and traditional methods. *J. Sol-Gel Sci. Technol.* **1997**, *8*, 131–137, doi:10.1007/BF02436830.

185. Dong, W.; Sun, Y.; Lee, C. W.; Hua, W.; Lu, X.; Shi, Y.; Zhang, S.; Chen, J.; Zhao, D. Controllable and Repeatable Synthesis of Thermally Stable Anatase Nanocrystal−Silica Composites with Highly Ordered Hexagonal Mesostructures. *J. Am. Chem. Soc.* **2007**, *129*, 13894–13904, doi:10.1021/ja073804o.

186. Yu, J.; Zhao, X.; Yu, J. C.; Zhong, G.; Han, J.; Zhao, Q. The grain size and surface hydroxyl content of super-hydrophilic TiO2/SiO2 composite nanometer thin films. *J. Mater. Sci. Lett.* **2001**, *20*, 1745–1748, doi:10.1023/A:1012458411717.

187. Paušová, Š.; Krýsa, J.; Jirkovský, J.; Prevot, V.; Mailhot, G. Preparation of TiO2-SiO2 composite photocatalysts for environmental applications. *J. Chem. Technol. Biotechnol.* **2014**, *89*, 1129–1135, doi:10.1002/jctb.4436.

188. Xu, H.; Zhu, P.; Wang, L.; Jiang, Z.; Zhao, S. Structural characteristics and photocatalytic activity of ambient pressure dried SiO2/TiO2 aerogel composites by one-step solvent exchange/surface modification. *J. Wuhan Univ. Technol. Sci. Ed.* **2016**, *31*, 80–86, doi:10.1007/s11595-016-1334-7.

189. Alaoui, O. T.; Nguyen, Q. T.; Rhlalou, T. Preparation and characterization of a new TiO2/SiO2 composite catalyst for photocatalytic degradation of indigo carmin. *Environ. Chem. Lett.* **2009**, *7*, 175–181, doi:10.1007/s10311-008-0154-1.

190. Hirano, M.; Ota, K. Preparation of photoactive anatase-type TiO2/silica gel by direct loading anatase-type TiO2 nanoparticles in acidic aqueous solutions by thermal hydrolysis. *J. Mater. Sci.* **2004**, *39*, 1841–1844, doi:10.1023/B:JMSC.0000016199.85213.0b.

191. Zhang, Z.; Lim, S. H.; Li, B.; Wang, X.; Liu, Z. Dual-Phase Spinel MnCo2O4 and Spinel MnCo2O4 /Nanocarbon Hybrids for Electrocatalytic Oxygen Reduction and Evolution. *Appl. Mater. interfaces* **2014**, 4–11, doi:10.1149/2.029405jes.

192. Wei, J.; Liang, Y.; Hu, Y.; Kong, B.; Zhang, J.; Gu, Q.; Tong, Y.; Wang, X.; Jiang, S.

P.; Wang, H. Hydrothermal Synthesis of Metal–Polyphenol Coordination Crystals and Their Derived Metal/N-doped Carbon Composites for Oxygen Electrocatalysis. *Angew. Chemie - Int. Ed.* **2016**, *55*, 12470–12474, doi:10.1002/anie.201606327.

193. Chen, M.; Wang, L.; Yang, H.; Zhao, S.; Xu, H.; Wu, G. Nanocarbon/oxide composite catalysts for bifunctional oxygen reduction and evolution in reversible alkaline fuel cells: A mini review. *J. Power Sources* **2018**, *375*, 277–290, doi:10.1016/j.jpowsour.2017.08.062.

194. Liu, X.; Liu, W.; Ko, M.; Park, M.; Kim, M. G.; Oh, P.; Chae, S.; Park, S.; Casimir, A.; Wu, G.; Cho, J. Metal (Ni, Co)-Metal Oxides/Graphene Nanocomposites as Multifunctional Electrocatalysts. *Adv. Funct. Mater.* **2015**, *25*, 5799–5808, doi:10.1002/adfm.201502217.

195. Cai, W.; Luo, X.; Jiang, Y.; Liu, Z.; Li, J.; Ma, L.; Xiong, J.; Yang, Z.; Cheng, H. Nitrogen-doped carbon active sites boost the ultra-stable hydrogen evolution reaction on defect-rich MoS2nanosheets. *Int. J. Hydrogen Energy* **2017**, *43*, 2026–2033, doi:10.1016/j.ijhydene.2017.12.059.

196. Samanta, A.; Raj, C. R. Catalyst Support in Oxygen Electrocatalysis: A Case Study with CoFe Alloy Electrocatalyst. *J. Phys. Chem. C* **2018**, *122*, 15843–15852, doi:10.1021/acs.jpcc.8b02830.

197. Ekspong, J.; Sharifi, T.; Shchukarev, A.; Klechikov, A.; WÃ¥gberg, T.; Gracia-Espino, E. Stabilizing Active Edge Sites in Semicrystalline Molybdenum Sulfide by Anchorage on Nitrogen-Doped Carbon Nanotubes for Hydrogen Evolution Reaction. *Adv. Funct. Mater.* **2016**, *26*, 6766–6776, doi:10.1002/adfm.201601994.

198. Sobaszek, M.; Siuzdak, K.; Ryl, J.; Sawczak, M.; Gupta, S.; Carrizosa, S. B.; Ficek, M.; Dec, B.; Darowicki, K.; Bogdanowicz, R. Diamond Phase (sp3-C) Rich Boron-Doped Carbon Nanowalls (sp2-C): Physicochemical and Electrochemical Properties. *J. Phys. Chem. C* **2017**, *121*, 20821–20833, doi:10.1021/acs.jpcc.7b06365.

199. Hosu, I. S.; Sobaszek, M.; Ficek, M.; Bogdanowicz, R.; Drobecq, H.; Boussekey, L.; Barras, A.; Melnyk, O.; Boukherroub, R.; Coffinier, Y. Carbon nanowalls: a new versatile graphene based interface for the laser desorption/ionization-mass spectrometry detection of small compounds in real samples. *Nanoscale* **2017**, *9*, 9701–9715, doi:10.1039/C7NR01069A.

200. Siuzdak, K.; Ficek, M.; Sobaszek, M.; Ryl, J.; Gnyba, M.; Niedziałkowski, P.; Malinowska, N.; Karczewski, J.; Bogdanowicz, R. Boron-Enhanced Growth of Micron-Scale Carbon-Based Nanowalls: A Route toward High Rates of Electrochemical Biosensing. *ACS Appl. Mater. Interfaces* **2017**, *9*, 12982–12992, doi:10.1021/acsami.6b16860.

201. Pierpaoli, M.; Lewkowicz, A.; Ficek, M.; Ruello, M. L.; Bogdanowicz, R. Preparation and characterization of a TiO<inf>2</inf>/carbon nanowall composite on a transparent substrate. *Photonics Lett. Pol.* **2018**, *10*, 54–56, doi:10.4302/plp.v10i2.825.

202. Fudala-Ksiazek, S.; Sobaszek, M.; Luczkiewicz, A.; Pieczynska, A.; Ofiarska, A.; Fiszka-Borzyszkowska, A.; Sawczak, M.; Ficek, M.; Bogdanowicz, R.; Siedlecka, E. M. Influence of the boron doping level on the electrochemical oxidation of raw landfill leachates: Advanced pre-treatment prior to the biological nitrogen removal. *Chem. Eng. J.* **2018**, *334*, 1074–1084, doi:10.1016/j.cej.2017.09.196.

203. Siuzdak, K.; Ficek, M.; Sobaszek, M.; Ryl, J.; Gnyba, M.; Niedziałkowski, P.; Malinowska, N.; Karczewski, J.; Bogdanowicz, R. Boron-Enhanced Growth of Micron-Scale Carbon-Based Nanowalls: A Route toward High Rates of

Electrochemical Biosensing. *ACS Appl. Mater. Interfaces* **2017**, *9*, 12982–12992, doi:10.1021/acsami.6b16860.

204. Nidzworski, D.; Siuzdak, K.; Niedziałkowski, P.; Bogdanowicz, R.; Sobaszek, M.; Ryl, J.; Weiher, P.; Sawczak, M.; Wnuk, E.; Goddard, W. A.; Jaramillo-Botero, A.; Ossowski, T. A rapid-response ultrasensitive biosensor for influenza virus detection using antibody modified boron-doped diamond. *Sci. Rep.* **2017**, *7*, 15707, doi:10.1038/s41598-017-15806-7.

205. Wang, H.; Quan, X.; Yu, H.; Chen, S. Fabrication of a TiO2/carbon nanowall heterojunction and its photocatalytic ability. *Carbon N. Y.* **2008**, *46*, 1126–1132, doi:10.1016/j.carbon.2008.04.016.

206. Lewkowicz, A.; Synak, A.; Grobelna, B.; Bogdanowicz, R.; Karczewski, J.; Szczodrowski, K.; Behrendt, M. Thickness and structure change of titanium(IV) oxide thin films synthesized by the sol–gel spin coating method. *Opt. Mater. (Amst).* **2014**, *36*, 1739–1744, doi:10.1016/J.OPTMAT.2014.02.033.

207. Sobaszek, M.; Siuzdak, K.; Ryl, J.; Sawczak, M.; Gupta, S.; Carrizosa, S. B.; Ficek, M.; Dec, B.; Darowicki, K.; Bogdanowicz, R. Diamond Phase (sp3-C) Rich Boron-Doped Carbon Nanowalls (sp2-C): Physicochemical and Electrochemical Properties. *J. Phys. Chem. C* **2017**, *121*, 20821–20833, doi:10.1021/acs.jpcc.7b06365.

208. Lewkowicz, A.; Bojarski, P.; Synak, A.; Grobelna, B.; Akopova, I.; Gryczyński, I.; Kułak, L. Concentration-Dependent Fluorescence Properties of Rhodamine 6G in Titanium Dioxide and Silicon Dioxide Nanolayers. *J. Phys. Chem. C* **2012**, *116*, 12304–12311, doi:10.1021/jp3022562.

209. Nosrati, R.; Olad, A.; Shakoori, S. Preparation of an antibacterial, hydrophilic and photocatalytically active polyacrylic coating using TiO2 nanoparticles sensitized by graphene oxide. *Mater. Sci. Eng. C* **2017**, *80*, 642–651, doi:10.1016/J.MSEC.2017.07.004.

210. Tan, L.-L.; Ong, W.-J.; Chai, S.-P.; Goh, B. T.; Mohamed, A. R. Visible-light-active oxygen-rich TiO2 decorated 2D graphene oxide with enhanced photocatalytic activity toward carbon dioxide reduction. *Appl. Catal. B Environ.* **2015**, *179*, 160–170, doi:10.1016/J.APCATB.2015.05.024.

211. Andryushina, N. S.; Stroyuk, O. L. Influence of colloidal graphene oxide on photocatalytic activity of nanocrystalline TiO2 in gas-phase ethanol and benzene oxidation. *Appl. Catal. B Environ.* **2014**, *148–149*, 543–549, doi:10.1016/J.APCATB.2013.11.044.

212. Suave, J.; Amorim, S. M.; Ângelo, J.; Andrade, L.; Mendes, A.; Moreira, R. F. P. M. TiO2/reduced graphene oxide composites for photocatalytic degradation in aqueous and gaseous medium. *J. Photochem. Photobiol. A Chem.* **2017**, *348*, 326–336, doi:10.1016/J.JPHOTOCHEM.2017.08.064.

213. Brinker, C. J.; Frye, G. C.; Hurd, A. J.; Ashley, C. S. Fundamentals of sol-gel dip coating. *Thin Solid Films* **1991**, *201*, 97–108, doi:10.1016/0040-6090(91)90158-T.

214. Elizalde-González, M. P.; García-Díaz, E.; Sabinas-Hernández, S. A. Novel preparation of carbon-TiO2 composites. *J. Hazard. Mater.* **2013**, *263*, 73–83, doi:10.1016/J.JHAZMAT.2013.07.059.

215. Sobaszek, M.; Siuzdak, K.; Ryl, J.; Sawczak, M.; Gupta, S.; Carrizosa, S. B.; Ficek, M.; Dec, B.; Darowicki, K.; Bogdanowicz, R. Diamond Phase (sp3-C) Rich Boron-Doped Carbon Nanowalls (sp2-C): Physicochemical and Electrochemical Properties. *J. Phys. Chem. C* **2017**, *121*, 20821–20833, doi:10.1021/acs.jpcc.7b06365.

216. Haubner, R.; Moritz, R. Raman characterisation of diamond coatings using different laser wavelengths. In *Nineteenth European Conference on Chemical Vapor Deposition, (EUROCVD*; 2013; pp. 71–78.

217. Marchon, B.; Gui, J.; Grannen, K.; Rauch, G. C. Photoluminescence and ramana Spectroscopy in hydrogenated carbon films. *IEEE Trans. Magn.* **1997**, *33*.

218. Krivchenko, V. A.; Lopaev, D. V.; Minakov, P. V.; Pirogov, V. G.; Rakhimov, A. T.; Suetin, N. V. Study of polycrystalline boron-doped diamond films by Raman spectroscopy and optical absorption spectroscopy. *Tech. Phys.* **2007**, *52*, 1471–1474, doi:10.1134/S106378420711014X.

219. Chen, Z. Y.; Zhao, J. P.; Yano, T.; Ooie, T.; Yoneda, M.; Sakakibara, J. Observation of sp3 bonding in tetrahedral amorphous carbon using visible Raman spectroscopy. *J. Appl. Phys.* **2000**, *88*, 2305–2308, doi:10.1063/1.1288160.

220. McGuire, K.; Gothard, N.; Gai, P.; Dresselhaus, M.; Sumanasekera, G.; Rao, A. Synthesis and Raman characterization of boron-doped single-walled carbon nanotubes., doi:10.1016/j.carbon.2004.11.001.

221. Kawai, S.; Kondo, S.; Takeuchi, W.; Kondo, H.; Hiramatsu, M.; Hori, M. Optical properties of evolutionary grown layers of carbon nanowalls analyzed by spectroscopic ellipsometry. *Jpn. J. Appl. Phys.* **2010**, *49*, 0602201–0602203, doi:10.1143/JJAP.49.060220.

222. Skowroński, Ł.; Trzcinski, M.; Antończak, A. J.; Domanowski, P.; Kustra, M.; Wachowiak, W.; Naparty, M. K.; Hiller, T.; Bukaluk, A.; Wronkowska, A. A. Characterisation of coloured TiOx/Ti/glass systems. *Appl. Surf. Sci.* **2014**, *322*, 209–214, doi:10.1016/J.APSUSC.2014.10.050.

223. Qi, N.; LeVan, M. D. Coadsorption of Organic Compounds and Water Vapor on BPL Activated Carbon. 5. Methyl Ethyl Ketone, Methyl Isobutyl Ketone, Toluene, and Modeling. *Ind. Eng. Chem. Res.* **2005**, *44*, 3733–3741, doi:10.1021/ie049109w.

224. McIntosh, R.; Haines, R. S.; Benson, G. C. The Effect of Physical Adsorption on the Electrical Resistance of Activated Carbon. *J. Chem. Phys.* **1947**, *15*, 17–27, doi:10.1063/1.1746280.

225. Johnsen, D. L.; Zhang, Z.; Emamipour, H.; Yan, Z.; Rood, M. J. Effect of isobutane adsorption on the electrical resistivity of activated carbon fiber cloth with select physical and chemical properties. *Carbon N. Y.* **2014**, *76*, 435–445, doi:10.1016/J.CARBON.2014.05.010.

226. Holzer, F.; Roland, U.; Kopinke, F.-D. Combination of non-thermal plasma and heterogeneous catalysis for oxidation of volatile organic compounds: Part 1. Accessibility of the intra-particle volume. *Appl. Catal. B Environ.* **2002**, *38*, 163–181, doi:10.1016/S0926-3373(02)00040-1.

227. Mei, D.; Zhu, X.; Wu, C.; Ashford, B.; Williams, P. T.; Tu, X. Plasma-photocatalytic conversion of CO2 at low temperatures: Understanding the synergistic effect of plasma-catalysis. *Appl. Catal. B Environ.* **2016**, *182*, 525–532, doi:10.1016/J.APCATB.2015.09.052.

228. Zhang, Y.-R.; Van Laer, K.; Neyts, E. C.; Bogaerts, A. Can plasma be formed in catalyst pores? A modeling investigation. *Appl. Catal. B Environ.* **2016**, *185*, 56–67, doi:10.1016/J.APCATB.2015.12.009.

229. Zhang, Y.-R.; Neyts, E. C.; Bogaerts, A. Influence of the Material Dielectric Constant on Plasma Generation inside Catalyst Pores. *J. Phys. Chem. C* **2016**, *120*, 25923–

25934, doi:10.1021/acs.jpcc.6b09038.

230. Chen, H. L.; Lee, H. M.; Chen, S. H.; Chang, M. B.; Yu, S. J.; Li, S. N. Removal of volatile organic compounds by single-stage and two-stage plasma catalysis systems: A review of the performance enhancement mechanisms, current status, and suitable applications. *Environ. Sci. Technol.* **2009**, *43*, 2216–2227, doi:10.1021/es802679b.

231. Feng, F.; Ye, L.; Liu, J.; Yan, K. Non-thermal plasma generation by using back corona discharge on catalyst. *J. Electrostat.* **2013**, *71*, 179–184, doi:10.1016/J.ELSTAT.2012.11.034.

232. Fava, G.; Pierpaoli, M. A hybrid photocatalytic-electrostatic reactor for nitrogen oxides removal. *Am. J. Environ. Eng. Sci.* **2015**, *2*, 7–13.

233. Dors, M.; Mizeraczyk, J. NOx removal from a flue gas in a corona discharge-catalyst hybrid system. *Catal. Today* **2004**, *89*, 127–133, doi:10.1016/J.CATTOD.2003.11.031.

234. Zhao, C.; Huang, D.; Chen, J.; Li, Y.; Du, Z. First-principle study for influence of an external electric field on the electronic structure and optical properties of TiO $_2$. *RSC Adv.* **2016**, *6*, 98908–98915, doi:10.1039/C6RA21025B.

235. Futera, Z.; English, N. J. Electric-Field Effects on Adsorbed-Water Structural and Dynamical Properties at Rutile- and Anatase-TiO2Surfaces. *J. Phys. Chem. C* **2016**, *120*, 19603–19612, doi:10.1021/acs.jpcc.6b01907.

236. Guo, Y.; Chen, J.; Ding, Z.; Guo, T.; Wei, J.; Ye, X.; Xu, W.; Zhou, Z. Simple synthesis of lithium-doped sulfated titania nanoparticles and their high visible light photocatalytic activity under negative bias electrostatic field. *RSC Adv.* **2016**, *6*, 101714–101724, doi:10.1039/C6RA19815E.

237. Asenjo, N. G.; Santamaría, R.; Blanco, C.; Granda, M.; Álvarez, P.; Menéndez, R. Correct use of the Langmuir–Hinshelwood equation for proving the absence of a synergy effect in the photocatalytic degradation of phenol on a suspended mixture of titania and activated carbon. *Carbon N. Y.* **2013**, *55*, 62–69, doi:10.1016/J.CARBON.2012.12.010.

238. Devahasdin, S.; Fan, C.; Li, K.; Chen, D. H. TiO2 photocatalytic oxidation of nitric oxide: Transient behavior and reaction kinetics. *J. Photochem. Photobiol. A Chem.* **2003**, *156*, 161–170, doi:10.1016/S1010-6030(03)00005-4.

239. Shang, J.; Du, Y.; Xu, Z. Photocatalytic oxidation of heptane in the gas-phase over TiO2. *Chemosphere* **2002**, *46*, 93–99, doi:10.1016/S0045-6535(01)00115-1.

240. Yu, Q. L.; Brouwers, H. J. H. Indoor air purification using heterogeneous photocatalytic oxidation. Part I: Experimental study. *Appl. Catal. B Environ.* **2009**, *92*, 454–461, doi:10.1016/j.apcatb.2009.09.004.

241. Bengtsson, N.; Oxidation, M. C.-J. of A.; 2010, undefined Photocatalytic Activity for NO Degradation by Construction Materials: Parametric Study andMultivariable Correlations. *degruyter.com*.

242. Herrmann, J. M. Photocatalysis fundamentals revisited to avoid several misconceptions. *Appl. Catal. B Environ.* **2010**, *99*, 461–468, doi:10.1016/j.apcatb.2010.05.012.

243. Debono, O.; Thévenet, F.; Gravejat, P.; Héquet, V.; Raillard, C.; Le Coq, L.; Locoge, N. Gas phase photocatalytic oxidation of decane at ppb levels: Removal kinetics, reaction intermediates and carbon mass balance. *J. Photochem. Photobiol. A Chem.* **2013**, *258*, 17–29, doi:10.1016/J.JPHOTOCHEM.2013.02.022.

244. Bulanin, K. M.; Lavalley, J. C.; Tsyganenko, a a Infrared Study of Ozone Adsorption on TiO2 (Anatase). *J. Phys. Chem.* **1995**, *99*, 10294–10298, doi:10.1021/j100025a034.

245. Huang, H.; Ye, D. Combination of photocatalysis downstream the non-thermal plasma reactor for oxidation of gas-phase toluene. *J. Hazard. Mater.* **2009**, *171*, 535–541, doi:10.1016/j.jhazmat.2009.06.033.

246. Forni, L.; Bahnemann, D.; Hart, E. J. Mechanism of the hydroxide ion-initiated decomposition of ozone in aqueous solution. *J. Phys. Chem.* **1982**, *86*, 255–259, doi:10.1021/j100391a025.

247. Guillard, C.; Puzenat, E.; Lachheb, H.; Houas, A. Why inorganic salts decrease the TiO2 photocatalytic efficiency. *academia.edu*.

248. Wang, K.-H.; Hsieh, Y.-H.; Wu, C.-H.; Chang, C.-Y. The pH and anion effects on the heterogeneous photocatalytic degradation of o-methylbenzoic acid in TiO2 aqueous suspension. *Chemosphere* **2000**, *40*, 389–394, doi:10.1016/S0045-6535(99)00252-0.

249. Hüsken, G.; Hunger, M.; Ballari, M. M.; Brouwers, H. J. H. The Effect of Various Process Conditions on the Photocatalytic Degradation of NO.

250. Ohtani, B.; Prieto-Mahaney, O. O.; Li, D.; Abe, R. What is Degussa (Evonic) P25? Crystalline composition analysis, reconstruction from isolated pure particles and photocatalytic activity test. *J. Photochem. Photobiol. A Chem.* **2010**, *216*, 179–182, doi:10.1016/j.jphotochem.2010.07.024.

251. Tobaldi, D. M.; Seabra, M. P.; Otero-Irurueta, G.; de Miguel, Y. R.; Ball, R. J.; Singh, M. K.; Pullar, R. C.; Labrincha, J. A. Quantitative XRD characterisation and gas-phase photocatalytic activity testing for visible-light (indoor applications) of KRONOClean 7000®. *RSC Adv.* **2015**, *5*, 102911–102918, doi:10.1039/C5RA22816F.

252. Chen, Y.; Lee, C.; Yeng, M.; growth, H. C.-J. of crystal; 2003, undefined The effect of calcination temperature on the crystallinity of TiO2 nanopowders. *Elsevier*.

253. Blöß, S. P. Visible Light Photo-catalysts Based on Titanium Dioxide and their Potential Applications – an Introduction. *Tenside Surfactants Deterg.* **2007**, *44*, 266–269, doi:10.3139/113.100346.

254. Hurum, D.; Agrios, A.; Gray, K.; … T. R.-T. J. of; 2003, undefined Explaining the Enhanced Photocatalytic Activity of Degussa P25 Mixed-Phase TiO2 Using EPR. *ACS Publ.*

255. Tanaka, K.; Capule, M. F. V; Hisanaga, T. Effect of crystallinity of TiO2 on its photocatalytic action. *Chem. Phys. Lett.* **1991**, *187*, 73–76, doi:10.1016/0009-2614(91)90486-S.

256. Tang, H.; Prasad, K.; Sanjinès, R.; Schmid, P. E.; Lévy, F. Electrical and optical properties of TiO_2 anatase thin films. *J. Appl. Phys.* **1994**, *75*, 2042–2047, doi:10.1063/1.356306.

257. Bloh, J. Z.; Folli, A.; Macphee, D. E. Photocatalytic NO_x abatement: why the selectivity matters. *RSC Adv.* **2014**, *4*, 45726–45734, doi:10.1039/C4RA07916G.

258. Tseng, Y. H.; Kuo, C. S.; Huang, C. H.; Li, Y. Y.; Chou, P. W.; Cheng, C. L.; Wong, M. S. Visible-light-responsive nano-TiO2 with mixed crystal lattice and its photocatalytic activity. *Nanotechnology* **2006**, *17*, 2490–2497, doi:10.1088/0957-4484/17/10/009.

259. Zhou, R.; Zhou, R.; Zhang, X.; Li, J.; Wang, X.; Chen, Q.; Yang, S.; Chen, Z.; Bazaka, K.; (Ken) Ostrikov, K. Synergistic Effect of Atmospheric-pressure Plasma and TiO2

Photocatalysis on Inactivation of Escherichia coli Cells in Aqueous Media. *Sci. Rep.* **2016**, *6*, 39552, doi:10.1038/srep39552.

260. Jérôme Taranto, †,‡,§; Didier Frochot, *,† and; Pierre Pichat*, ‡ Combining Cold Plasma and TiO2 Photocatalysis To Purify Gaseous Effluents: A Preliminary Study Using Methanol-Contaminated Air. **2007**, doi:10.1021/IE0700967.

261. Assadi, A. A.; Bouzaza, A.; Vallet, C.; Wolbert, D. Use of DBD plasma, photocatalysis, and combined DBD plasma/photocatalysis in a continuous annular reactor for isovaleraldehyde elimination – Synergetic effect and byproducts identification. *Chem. Eng. J.* **2014**, *254*, 124–132, doi:10.1016/j.cej.2014.05.101.

262. Sun, R.-B.; Xi, Z.-G.; Chao, F.-H.; Zhang, W.; Zhang, H.-S.; Yang, D.-F. Decomposition of low-concentration gas-phase toluene using plasma-driven photocatalyst reactor. *Atmos. Environ.* **2007**, *41*, 6853–6859, doi:10.1016/j.atmosenv.2007.04.041.

263. Ye, S.; Liang, J.; Song, X.; Luo, S.; Liang, J. Modeling intrinsic kinetics in a reactor of corona discharge coupled with TiO 2 -activated carbon fibre for ethylene degradation and ozone regulation. *Biosyst. Eng.* **2016**, *150*, 123–130, doi:10.1016/j.biosystemseng.2016.07.010.

264. Tang, S.; Lu, N.; Li, J.; Shang, K.; Wu, Y. Improved phenol decomposition and simultaneous regeneration of granular activated carbon by the addition of a titanium dioxide catalyst under a dielectric barrier discharge plasma. *Carbon N. Y.* **2013**, *53*, 380–390, doi:10.1016/j.carbon.2012.11.028.

265. Wang, T.; Zhang, X.; Liu, J.; Liu, H.; Sun, B. Comparison of NO conversion over Cu/M (M = TiO2, Al2O3, ZSM-5, carbon nanotubes, activated carbon) catalysts assisted by plasma. *React. Kinet. Mech. Catal.* **2018**, *124*, 587–601, doi:10.1007/s11144-018-1358-4.

266. Abedi, K. ad-D.; Ghorbani-Shahna, F.; Bahrami, A.; Ebrahimi, H.; Maleki, A.; Madjidi, F.; Musavi, S.; Mohammadi, E.; Giahi, O. Effect of TiO2/GAC and water vapor on chloroform decomposition in a hybrid plasma-catalytic system. *Environ. Technol.* **2018**, *39*, 2041–2050, doi:10.1080/09593330.2017.1349185.

267. Abedi, K.; Ghorbani-Shahna, F.; Jaleh, B.; Bahrami, A.; Yarahmadi, R.; Haddadi, R.; Gandomi, M. Decomposition of chlorinated volatile organic compounds (CVOCs) using NTP coupled with TiO2/GAC, ZnO/GAC, and TiO2–ZnO/GAC in a plasma-assisted catalysis system. *J. Electrostat.* **2015**, *73*, 80–88, doi:10.1016/j.elstat.2014.10.008.

268. Zhang, H.; Lv, X.; Li, Y.; Wang, Y.; Li, J. P25-Graphene Composite as a High Performance Photocatalyst. *ACS Nano* **2010**, *4*, 380–386, doi:10.1021/nn901221k.

269. Wang, H.; Wu, Z.; Zhao, W.; Guan, B. Photocatalytic oxidation of nitrogen oxides using TiO2 loading on woven glass fabric. *Chemosphere* **2007**, *66*, 185–190, doi:10.1016/j.chemosphere.2006.04.071.

270. Nakamura, I.; Negishi, N.; Kutsuna, S.; … T. I.-J. of M.; 2000, undefined Role of oxygen vacancy in the plasma-treated TiO2 photocatalyst with visible light activity for NO removal. *Elsevier*.

271. Herrmann, J. M. Fundamentals and misconceptions in photocatalysis. *J. Photochem. Photobiol. A Chem.* **2010**, *216*, 85–93, doi:10.1016/j.jphotochem.2010.05.015.

272. Robens, E. Some intriguing items in the history of adsorption. *Stud. Surf. Sci. Catal.* **1994**, *87*, 109–118, doi:10.1016/S0167-2991(08)63070-0.

273. Art of separating suspended particles from gaseous bodies. 1907.

274. Hashimoto, K.; Irie, H.; Fujishima, A. TiO2 Photocatalysis: A Historical Overview and Future Prospects. *Jpn. J. Appl. Phys.* **2005**, *44*, 8269–8285, doi:10.1143/JJAP.44.8269.

Annex

Annex A:

Patent analysis of the Lens.org dataset

Data collection

Dataset was obtained in a single day (1/11/2018) by using the following query:

abstract: indoor AND (classification_cpc: (B01D OR (B03C* OR (B04B* OR B04C*))) OR (title: indoor AND classification_cpc: (B01D* OR (B03C* OR (B04B* OR B04C*)))))*

The results table, consisting of 283 references was then analyzed with R [106] and results plotted by the package ggplot2.

Temporal and geographical patent distribution

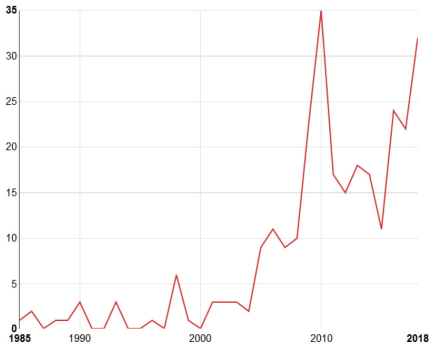

Top assignee

Number of patents within the dataset	Assignee
66	Daikin Ind Ltd
32	Enverid System Inc.
25	Mitsubishi Electric Corp
13	Sakashita Akihiko
13	Toshiba Carrier Corp.
11	Okada Morimichi
9	Yokomizo Tsuyoshi

Process used

The process of removal of a pollutant is identified by the CPC group.

- # **B01D2251** Reactants
- # **B01D2252** Absorbents, i.e. solvents and liquid materials for gas absorption
- # **B01D2253** Adsorbents used in seperation treatment of gases and vapours
- # **B01D2255** Catalysts
- # **B01D2273** Operation of filters specially adapted for separating dispersed particles from gases or vapours

- # **B01D2279** Filters adapted for separating dispersed particles from gases or vapours specially modified for specific uses
- # **B01D46** Filters , i.e. particle separators or filtering processes specially modified for separating dispersed particles from gases or vapours
- # **B01D53** Separation of gases or vapours; Recovering vapours of volatile solvents from gases; Chemical or biological purification of waste gases, e.g. engine exhaust gases, smoke, fumes, flue gases, aerosols,
- # **B03C3** Separating dispersed particles from gases or vapour, e.g. air, by electrostatic effect

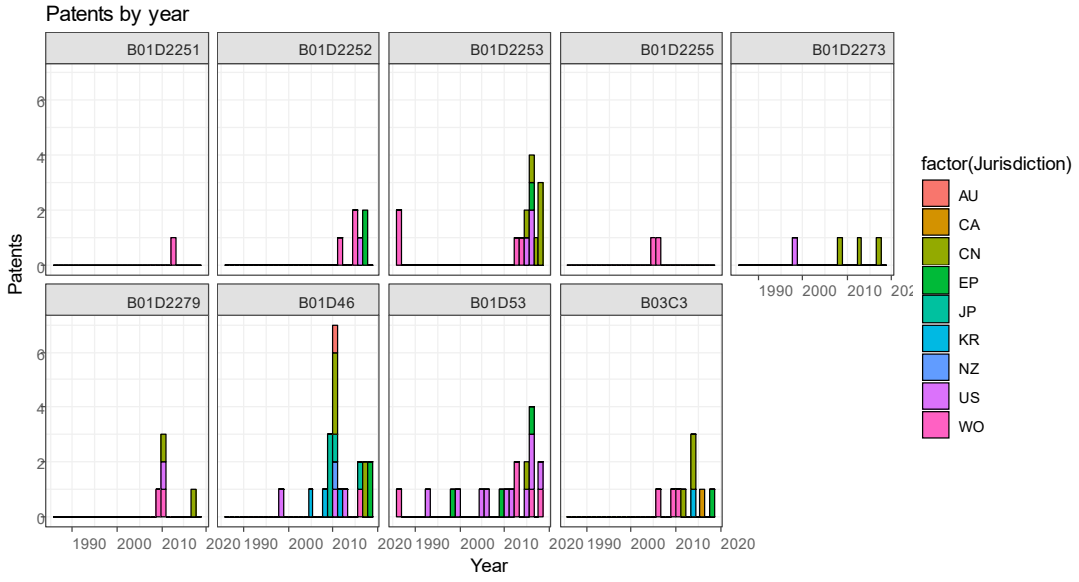

Target pollutant

The Components to be removed are identified by the CPC group code B01D2257. In particular:

- B01D2257/**106**: . . Ozone
- B01D2257/**11**: . . Noble gases
- B01D2257/**302**: . . Sulfur oxides
- B01D2257/**304**: . . Hydrogen sulfide
- B01D2257/**308**: . . Carbonoxysulfide COS
- B01D2257/**402**: . . Dinitrogen oxide
- B01D2257/**404**: . . Nitrogen oxides other than dinitrogen oxide
- B01D2257/**502**: . . Carbon monoxide
- B01D2257/**504**: . . Carbon dioxide
- B01D2257/**70**: . Organic compounds not provided for in groups
- B01D2257/**7027**: . . . Aromatic hydrocarbons
- B01D2257/**708**: . . Volatile organic compounds V.O.C.'s
- B01D2257/**90**: . Odorous compounds not provided for in groups B01D2257/00 B01D2257/708
- B01D2257/**91**: . Bacteria; Microorganisms
- B01D2257/**93**: . Toxic compounds not provided for in groups B01D2257/00 B01D2257/708

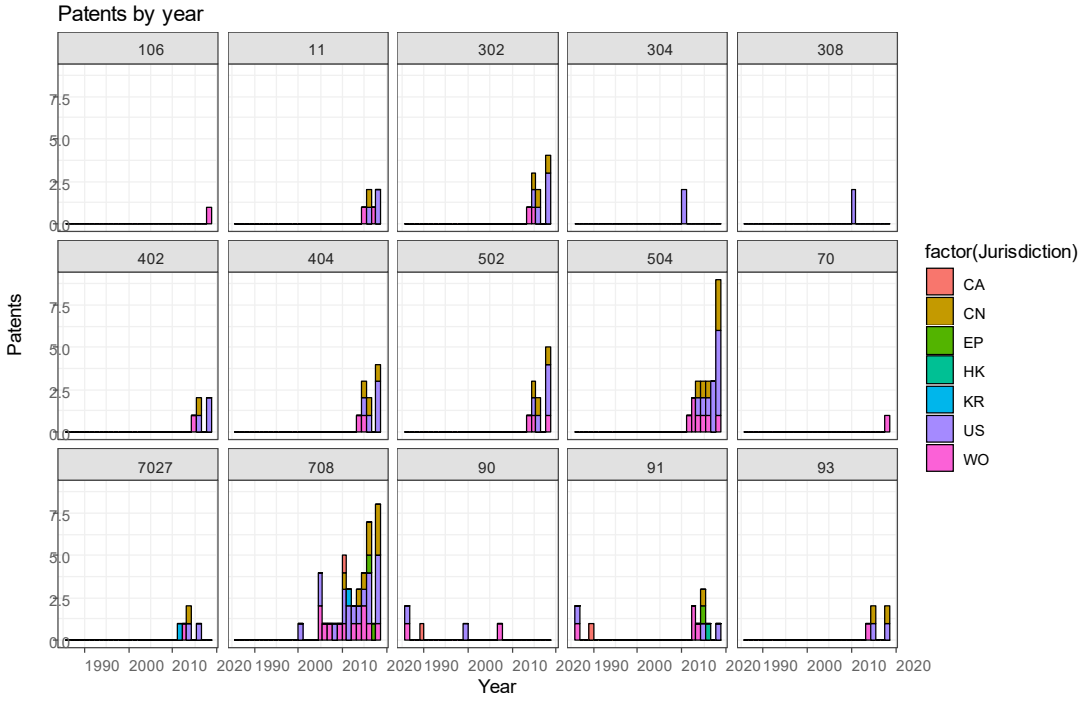

Type of treatment

- B01D2259/**10**: . Gas phase, e.g. by using aerosols
- B01D2259/**40083**: . . Regeneration of adsorbents in processes other than pressure or temperature swing adsorption
- B01D2259/**40086**: . . . by using a purge gas (B01D2259/4009 takes precedence)
- B01D2259/**4009**: . . . . using hot gas
- B01D2259/**40098**: . . . . with other heating means
- B01D2259/**414**: . . using different types of adsorbents
- B01D2259/**4143**: . . . . arranged as a mixture
- B01D2259/**4145**: . . . . arranged in series
- B01D2259/**45**: . Gas separation or purification devices adapted for specific applications
- B01D2259/**4508**: . . for cleaning air in buildings
- B01D2259/**4541**: . . for portable use, e.g. gas masks
- B01D2259/**455**: . . for transportable use (portable devices B01D2259/4541
- B01D2259/**4566**: . . for use in transportation means
- B01D2259/**4575**: . . . in aeroplanes or space ships
- B01D2259/**65**: . Employing advanced heat integration, e.g. Pinch technology

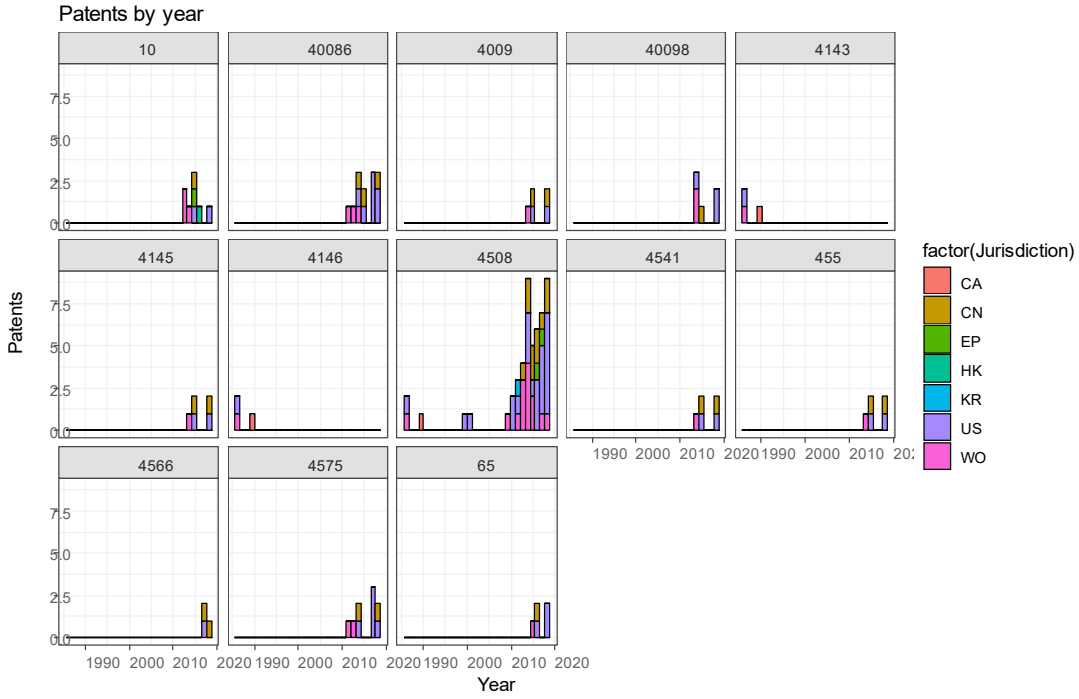
Patents by year
10
40086
4009
40098
4143
4145
4146
4508
4541
455
4566
4575
65
Patents
Year
factor(Jurisdiction)
CA
CN
EP
HK
KR
US
WO

Annex B:

Patents classifier algorithm

```
N is the dataframe containing the patent data


N<-mutate(N, Filter =
  if_else(
             str_detect(TI, fixed("HEPA", ignore_case = TRUE)) |
      str_detect(ID, fixed("HEPA", ignore_case = TRUE)) |
      str_detect(TI, fixed("ULPA", ignore_case = TRUE)) |
      str_detect(ID, fixed("ULPA", ignore_case = TRUE)) |
      str_detect(TI, fixed("FILTRATION", ignore_case = TRUE)) |
      str_detect(ID, fixed("FILTRATION", ignore_case = TRUE)) |
      str_detect(TI, fixed("FILTER", ignore_case = TRUE)) |
      str_detect(ID, fixed("FILTER", ignore_case = TRUE)),
  "Filter", ""))
N<-mutate(N, Dyna =
  if_else(
     str_detect(TI, fixed("Cyclone", ignore_case = TRUE)) |
      str_detect(ID, fixed("Cyclone", ignore_case = TRUE)) |
     str_detect(TI, fixed("wash", ignore_case = TRUE)) |
      str_detect(ID, fixed("wash", ignore_case = TRUE)) |
      str_detect(TI, fixed("Scrubber", ignore_case = TRUE)) |
      str_detect(ID, fixed("Scrubber", ignore_case = TRUE)),
  "Dyna", ""))
N<-mutate(N, ESP =
  if_else(
    str_detect(TI, fixed("electrostatic filtration", ignore_case = TRUE)) |
      str_detect(ID, fixed("electrostatic filtration", ignore_case = TRUE)) |
    str_detect(TI, fixed("electric-field", ignore_case = TRUE)) |
      str_detect(ID, fixed("electric-field", ignore_case = TRUE)) |
      str_detect(TI, fixed("electrostatic precipitation", ignore_case = TRUE)) |
      str_detect(ID, fixed("electrostatic precipitation", ignore_case = TRUE)) |
      str_detect(TI, fixed("electrostatic filter", ignore_case = TRUE)) |
      str_detect(ID, fixed("electrostatic filter", ignore_case = TRUE)),
  "ESP", ""))
N<-mutate(N, Ads =
  if_else(
    str_detect(TI, fixed("adsorption", ignore_case = TRUE)) |
    str_detect(ID, fixed("adsorption", ignore_case = TRUE))|
    str_detect(TI, fixed("sorbent", ignore_case = TRUE)) |
    str_detect(ID, fixed("sorbent", ignore_case = TRUE))|
           str_detect(TI, fixed("adsorbent", ignore_case = TRUE)) |
           str_detect(ID, fixed("adsorbent", ignore_case = TRUE)) |
           str_detect(TI, fixed("carbon", ignore_case = TRUE)) |
           str_detect(ID, fixed("carbon", ignore_case = TRUE)) |
           str_detect(TI, fixed("zeolite", ignore_case = TRUE)) |
           str_detect(ID, fixed("zeolite", ignore_case = TRUE)) |
           str_detect(TI, fixed("adsorbing", ignore_case = TRUE)) |
           str_detect(ID, fixed("adsorbing", ignore_case = TRUE)),
  "Ads", ""))
N<-mutate(N, PCO =
  if_else(
    str_detect(TI, fixed("catalysis", ignore_case = TRUE)) |
    str_detect(ID, fixed("catalysis", ignore_case = TRUE))|
    str_detect(TI, fixed("photocatalytic", ignore_case = TRUE)) |
    str_detect(ID, fixed("photocatalytic", ignore_case = TRUE))|
           str_detect(TI, fixed("catalyst", ignore_case = TRUE)) |
           str_detect(ID, fixed("catalyst", ignore_case = TRUE)) |
           str_detect(TI, fixed("semiconductor", ignore_case = TRUE)) |
           str_detect(ID, fixed("semiconductor", ignore_case = TRUE)),
  "PCO", ""))
```

```
 N<-mutate(N, UV =
  if_else(
    str_detect(TI, fixed("UVGI", ignore_case = TRUE)) |
    str_detect(ID, fixed("UVGI", ignore_case = TRUE))|
           str_detect(TI, fixed("photolysis", ignore_case = TRUE)) |
           str_detect(ID, fixed("photolysis", ignore_case = TRUE)) |
           str_detect(TI, fixed("UV-C", ignore_case = TRUE)) |
           str_detect(ID, fixed("UV-C", ignore_case = TRUE)),
  "UV", ""))
N<- mutate(N, NTP =
  if_else(
    str_detect(TI, fixed("NTP", ignore_case = TRUE)) |
    str_detect(ID, fixed("NTP", ignore_case = TRUE))|
           str_detect(TI, fixed("plasma", ignore_case = TRUE)) |
           str_detect(ID, fixed("plasma", ignore_case = TRUE)) |
           str_detect(TI, fixed("barrier discharge", ignore_case = TRUE)) |
           str_detect(ID, fixed("barrier discharge", ignore_case = TRUE)),
  "NTP", ""))
N<- mutate(N, Ion =
  if_else(
    str_detect(TI, fixed("ionizer", ignore_case = TRUE)) |
    str_detect(ID, fixed("ionizer", ignore_case = TRUE))|
    str_detect(TI, fixed("ions", ignore_case = TRUE)) |
    str_detect(ID, fixed("ions", ignore_case = TRUE))|
           str_detect(TI, fixed("ionization", ignore_case = TRUE)) |
           str_detect(ID, fixed("ionization", ignore_case = TRUE)) |
           str_detect(TI, fixed("brush", ignore_case = TRUE)) |
           str_detect(ID, fixed("brush", ignore_case = TRUE)),
  "Ion", ""))
 N<-mutate(N, Plant =
   if_else(
    str_detect(TI, fixed("plant", ignore_case = TRUE)) |
    str_detect(ID, fixed("plant", ignore_case = TRUE))|
    str_detect(TI, fixed("biomass", ignore_case = TRUE)) |
    str_detect(ID, fixed("biomass", ignore_case = TRUE))|
           str_detect(TI, fixed("botanical", ignore_case = TRUE)) |
           str_detect(ID, fixed("botanical", ignore_case = TRUE)) |
           str_detect(TI, fixed("plants", ignore_case = TRUE)) |
           str_detect(ID, fixed("plants", ignore_case = TRUE)),
  "Plant", ""))
```

Annex C:

Numerical simulation of an electro-enhanced adsorption process

Apparatus

The apparatus adopted is the one reported in paragraph 2.2.2. Briefly, the sample holder on which the specimens are placed is represented below. A thin (180µm diameter) wire (discharge electrode) is set to positive polarity, whereas the opposite electrode, (collector), is earthed trough two grounded connections at the ends of the activated carbon cloth sample. A fan induces a quasi-parallel air flux in the z-direction. The sample holder is placed into a 13L glass box.

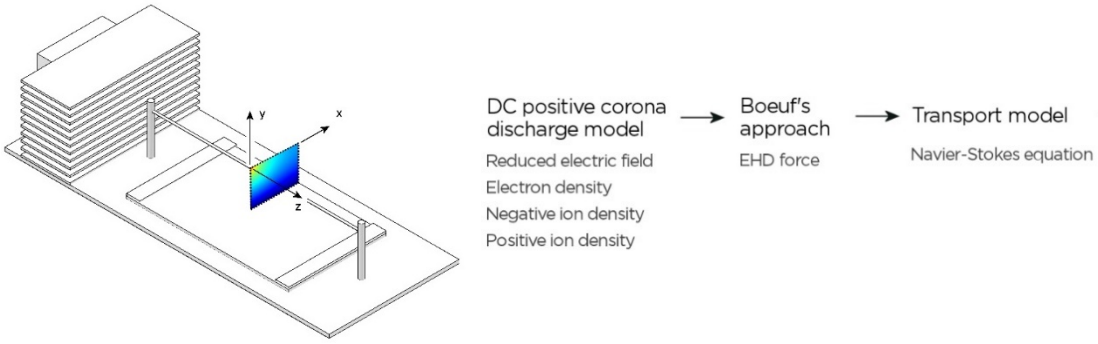

DC positive corona discharge model

(Spatial distribution of the charged species, for 10kV applied)

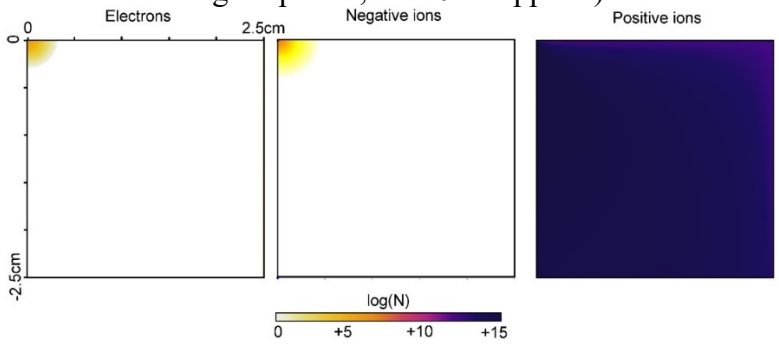

Beuf's approach

(Electroinduced force in the considered domain; along the y-axis)

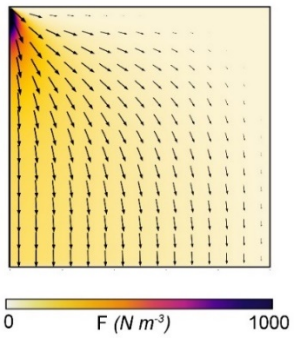

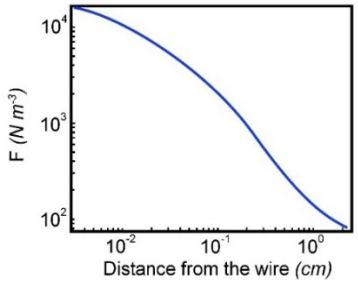

Transport (Navier-Stokes equations)

Velocity fields at different horizontal velocity. Pressure distribution on the collecting electrode.